Universidad de Alcalá

Programa de Doctorado en Electrónica: Sistemas Electrónicos Avanzados. Sistemas Inteligentes

3D Positioning System with Optical Sensors using Encoding Techniques

Ph.D. Thesis Presented by

Elena Aparicio Esteve

2022

Universidad de Alcalá

Programa de Doctorado en Electrónica: Sistemas Electrónicos Avanzados. Sistemas Inteligentes

3D Positioning System with Optical Sensors using Encoding Techniques

Ph.D. Thesis Presented by

Elena Aparicio Esteve

Advisors

Dr. Jesús Ureña Ureña

Dr. Álvaro Hernández Alonso

Alcalá de Henares, 2022

Acknowledgements

Quiero comenzar agradeciendo este trabajo a mis padres y hermana. A mis padres, no puedo agradecerles suficiente todo lo que han hecho por mi y todo el apoyo que he recibido en cada paso que he dado a lo largo de mi vida. A mi hermana, gracias por todos esos mensajes de ánimo y por estar ahí siempre que lo he necesitado. No me puedo olvidar de tí, Miguel. Gracias por tu paciencia, tu apoyo y estar ahí tanto en los momentos buenos como en los malos. Simplemente, gracias por todo.

Quiero continuar agradeciendo este trabajo a mis tutores Jesús Ureña y Álvaro Hernández. Gracias por haberme dado la oportunidad de hacer esta tesis con vosotros y haberme guiado durante el desarrollo de la misma, haciendo posible que esta sea una realidad. Gracias por todo el apoyo, conocimiento, ilusión y tiempo que me han dedicado a lo largo de estos años.

También agradecer al grupo de investigación GEINTRA al completo por todo lo que me han aportado y en especial al profesorado Mª Carmen Pérez, José M. Villadangos, Juan Jesús García, Ana Jiménez. No me olvido de todos aquellos que están o han estado en el grupo GEINTRA: Sara, Laura, Alejandro, Sergio, David, Mario, Javier, Rubén, Andrés, Sergio, David, Rubén, Álvaro, Santi, Khaoula y un largo etcétera.

I would also like to thank the supervisor of my research stay at the KU Leuven Technologie Campus of Gent, Dr. Nobby Stevens, for welcome me at the DRAMCO research group, for his support and for enriching my knowledge to complete this work. I do not forget of all the DRAMCO members for their support during my stay: Willem, Jorik, Bert, Chesney, François, Jona, Daan, etc.

No puedo acabar sin antes mencionar a todos aquellos que me han ayudado a evadirme de la tesis tanto online como presencialmente: Noelia, Ana, Sara, Iris, Casillas, Álvaro, Luisfer, Sergio, Fran, Raúl, María ... Gracias por haber estado ahí presentes a lo largo de esta etapa.

Dicen que siempre queda alguien pendiente al cuál no has mencionado en los agradecimientos...a todos vosotros: gracias.

Resumen

Esta tesis doctoral se centra en el desarrollo y la mejora de los Sistemas de Posicionamiento Locales (LPS) en interiores, los cuales se utilizan en entornos no compatibles con señales GNSS (Global Navigation Satellite Systems) para localizar, seguir y guiar a personas, objetos o vehículos. Se han realizado numerosos estudios para llevar a cabo un sistema de posicionamiento en entornos interiores, donde las personas pasan aproximadamente el 80 % de su tiempo. Algunas de las técnicas propuestas emplean diversas señales, como acústicas, de radiofrecuencia, mecánicas u ópticas, entre otras. Por su bajo coste, facilidad de integración en el entorno de trabajo y ausencia de riesgos para la salud, la tecnología óptica es una alternativa viable que ha comenzado a expandirse rápidamente.

Esta tesis aporta propuestas que permiten establecer las bases para el desarrollo de un LPS óptico basado en técnicas de codificación y sensores QADA. Se han propuesto dos diseños: un LPS orientado a la privacidad, basado en un conjunto de cuatro LEDs transmisores, aunque fácilmente extensible a más emisores, que actúan como balizas en ubicaciones conocidas y un único sensor QADA que actúa como el receptor a posicionar; y un LPS centralizado basado en un conjunto de transmisores móviles y al menos dos receptores QADA colocados en ubicaciones conocidas.

Se han estudiado los módulos transmisor y receptor. En concreto, se propone un esquema de codificación para la emisión del transmisor, que proporciona capacidad de acceso múltiple, así como robustez frente a bajas relaciones señal a ruido y condiciones adversas como los efectos de multicamino y cerca-lejos. Además, para mejorar las prestaciones de la propuesta sin aumentar significativamente el tiempo de emisión, se han analizado diferentes secuencias y sus longitudes, como los códigos LS (Loosely Synchronized) o las secuencias pseudoaleatorias (Kasami).

Por otro lado, el módulo receptor está compuesto por un sensor QADA, una apertura cuadrada y una etapa de filtrado para reducir las interferencias no deseadas. El sensor QADA y la apertura se han modelado para, en primer lugar, analizar la influencia de la longitud de la apertura en la linealidad de las ecuaciones de estimación del punto imagen y, en segundo lugar, determinar los parámetros intrínsecos que modelan el receptor (longitud, altura, desalineación y descentrado de la apertura respecto al sensor QADA), de forma que se pueda implementar un algoritmo de calibración para mejorar la precisión del sistema propuesto.

El LPS tiene como objetivo estimar la posición 3D de un objeto estático o en movimiento. Para ello, se diseñan varios algoritmos basados en técnicas de triangulación con determinación de ángulos de llegada (AoA) y técnicas homográficas que resuelven el problema de la perspectiva de n puntos (PnP) del sistema pin-hole propuesto.

Todas las propuestas han sido verificadas mediante simulaciones y pruebas experimentales en una gran variedad de situaciones: utilizando luz visible o infrarroja, secuencias LS o Kasami, diferentes

longitudes de apertura, distintas distancias entre transmisores y receptores, diferentes algoritmos de posicionamiento y varias rotaciones del receptor. Finalmente, las pruebas experimentales han demostrado que es posible posicionar con errores de menos de 5 centímetros.

Abstract

This PhD thesis focuses on the development and improvement of indoor Local Positioning Systems (LPS), which are used in non-GNSS (Global Navigation Satellite Systems) environments to locate, track, and guide people, objects, or vehicles. Numerous studies have been carried out to implement a positioning system in indoor environments, where people spend approximately 80% of their time. Some of the proposed techniques employ a variety of signals, including acoustic, radiofrequency, mechanical, and optical, among others. Because of its low cost, ease of integration into the work environment, and lack of health risks, optical technology is a feasible alternative that has begun to expand.

This thesis aims to provide proposals that can establish the basis for the development of an optical LPS based on encoding techniques and QADA (Quadrant Photodiode Angular Diversity Aperture) sensors. In this way, two designs have been proposed: a privacy-oriented LPS based on a set of four LEDs (easily extendable to more emitters) at known locations and a single QADA sensor acting as the receiver to be positioned; and a centralized LPS based on a set of mobile transmitters and at least two stationary QADA receivers at known locations.

Both the transmitter and receiver modules have been studied. In particular, an encoding scheme is proposed for the transmitter's emission, providing multiple access capability and robustness against low signal-to-noise ratios and harsh conditions such as multipath and near-far effects. Furthermore, in order to improve the proposal's performance without significantly increasing the emission time, different sequences and their lengths, such as Loosely Synchronized (LS) codes or pseudo-random sequences (Kasami), have been analysed.

On the other hand, the receiver's module is composed of a QADA sensor, a square aperture, and a filtering stage to reduce undesired interference. The QADA sensor and the aperture have been modelled in order to firstly analyse the influence of the aperture length on the linearity of the equations in the estimation of the image point, and, secondly, to determine the intrinsic parameters that model the receiver (aperture length, height, misalignment, and centre with respect to the QADA sensor). In that way, a calibration algorithm can be implemented to improve the accuracy of the proposed system.

The proposed optical LPS aims to estimate the 3D position of a stationary or moving target. To accomplish this, various algorithms are designed, based on triangulation techniques with Angles of Arrival (AoA) detection and on homographic techniques that solve the Perspective-n-Point (PnP) problem of the proposed pin-hole system.

All of the aforementioned proposals have been verified by simulations and experimental tests in a variety of situations: using visible or infrared light, LS or Kasami sequences, different aperture lengths, different distances between transmitters and receivers, various positioning algorithms and receiver rotations. Finally, experimental tests have proved that positioning accuracy with errors

below 5 centimetres is possible.

Contents

List of Figures

List of Tables

Glossary

List of mathematical symbols

A_k	Illuminated area in quadrant k on the receiver
$\mathbf{A}$	Constant transition matrix on Chapters 5-6. Derivative of $f(\hat{\mathbf{X}}_{k-1})$ with respect to the state vector $\hat{\mathbf{X}}_k^-$
b_i	3D position of transmitter i
c_i	Transmitted code of the i-th transmitter
d	Distance between QADAs
d_{ij}	Distance between the transmitter i and receiver j in the plane where the receiver is placed
d_r	Distance between pairs of image points
D	Distance between pairs of transmitters
E_d	Euclidean distance error of the estimated position with respect to the ground-truth
f_c	Carrier frequency of the emitters
f_{cSYN}	Carrier frequency of the synchronization beacon
f_s	Sampling frequency
h_{ap}	Expected height at which the aperture is located (focal length)
h'_{ap}	Actual height at which the aperture is located
H_i	Distance between the transmitter's and the receiver's plane
$\mathbf{H}_k$	Constant transition matrix on Chapters 5-6. Derivative of $h(\hat{\mathbf{X}}_k^-)$ with respect to the state vector $\hat{\mathbf{X}}_k^-$
i	Index. Number of transmitters
i_k	Current obtained by the different quadrants k on the receiver
I	Total number of transmitters
j	Index. Number of QADAs in the receiver
J	Total number of QADAs
$\mathbf{J}$	Jacobian matrix
k	Index. Number of quadrants in the photoreceiver Current state on Chapters 5-6
$\mathbf{K}$	Kalman Filter gain that minimizes the residual error on Chapters 5-6
l	Length of the aperture
L	Length of the transmitted sequence
M	Samples per period

$m[n]$	Modulated signal in the discrete time domain
n	Discrete time domain
	Number of n points in the PnP algorithm on Chapter 4
N_c	Periods of the carrier
p	Index. Number of mobile targets
$\mathbf{P}$	Covariance matrix of the state vector on Chapters 5-6
P_j	Experimental points used in the calibration of the receiver
$\mathbf{P}_k^-$	A priori estimate covariance matrix of the state vector on Chapters 5-6
(p_x, p_y)	Ratios that relate the image points (x_r, y_r), the correlated signals and the intrinsic parameters of the receiver
$\mathbf{Q}$	Process noise error covariance matrix on Chapters 5-6
Q_1, Q_2, Q_3, Q_4	Corners of the tilted aperture
r	Radius of the QADA photodiode
r_i	Correlated signal of v_{LR} and the transmitted codes c_i
(r_x, r_y)	Residuals of the LLS algorithm at the calibration of the receiver in Chapter 4
$\mathbf{R}$	Rotation matrix R(α, β, γ)
$\mathbf{R}$	Measurement noise error covariance matrix on Chapters 5-6
s	Index. Current state in the NLSE algorithm in Chapter 4
s_i	Correlated signal of v_{sum} and the transmitted codes c_i
$s[n]$	Modulation carrier
t	Continuous time domain
t_i	Correlated signal of v_{BT} and the transmitted codes c_i
$\mathbf{t}$	Translation matrix $\mathbf{t} = (x, y, z)$
T_s	Sampling period
u	Threshold in the NLSE algorithm in Chapter 4
v_k	Output voltages provided by each quadrant k of the receiver in Chapter 3
	Measurements noise at instant k on Chapters 5-6
$v_{f_{BT}}$	Buffer of the acquired v_{BT} signal
$v_{f_{LR}}$	Buffer of the acquired v_{LR} signal
$v_{f_{sum}}$	Buffer of the acquired v_{sum} signal
v_{sum}	Global sum signal of the incident energy on the QADA receiver
v_{BT}	Voltage difference on the Y-axis (bottom-top) on the QADA receiver
v_{LR}	Voltage difference on the X-axis (left-right) on the QADA receiver
w_k	Process noise related to the state vector on Chapters 5-6
$\mathbf{X}_k$	State vector on the current state k on Chapters 5-6
$\hat{\mathbf{X}}_k^-$	Prediction of the state vector in Chapters 5-6
(x_c, y_c)	Optical centre of the aperture (intrinsic parameter)
(x_r, y_r)	Rotated image points on the QADA receiver
(x_r', y_r')	Non-rotated image points on the QADA receiver
$(\hat{x}_r, \hat{y}_r)$	Ideal image point implemented in the calibration algorithm of the receiver in Chapter 4
$(x_{r,\lambda,c,\delta}, y_{r,\lambda,c,\delta})$	Image point coordinates including all the intrinsic parameters in Chapter 4. Each subindex refers to a different intrinsic parameter: λ to the focal length adjustment,

	c to the optical centre, and δ to the aperture misalignment
(x, y, z)	3D Cartesian coordinates. Position of the receiver
$(\widehat{x}, \widehat{y}, \widehat{z})$	3D Cartesian coordinates. Estimated positions of the receiver
(x_p, y_p, z_p)	3D Cartesian coordinates. Position of the mobile target
(x_t, y_t, z_t)	3D Cartesian coordinates. Position of the transmitter
$[X, Y, Z]$	Global axis on the proposed system (m)
$[X_r, Y_r, Z_r]$	Local axis at the QADA receiver (mm)
$[X_r, Y_r, Z_r]_p$	Local axis at the mobile object p (m)
$\mathbf{Z}_k$	Measurements at instant k given by the estimated ratios (p_x, p_y) in Chapters 5-6
α	Rotation angle on the X axis
β	Rotation angle on the Y axis
γ	Rotation angle on the Z axis
δ	Aperture misalignment with respect to the photodiode (intrinsic parameter)
ϵ	Detected error in the non-linear point estimation at the receiver in Chapter 4
η	Angle between the rotated image point and the X_r axis
θ	Angle between the image point and the X_r axis
κ	Angle between the transmitter's projection on plane XY and the X axis
λ	Wavelength
	Focal length adjustment (intrinsic parameter) in Chapter 4
ρ	Angle that define the circular segment on Chapter 4
σ^2	Variances of the measured positions in Chapters 5-6
σ_x	Gaussian noise introduced on coordinate x
σ_y	Gaussian noise introduced on coordinate y
σ_z	Gaussian noise introduced on coordinate z
ψ_i	Angle of incidence of the light on the QADA, for each LED i

List of acronyms

ADC	Analog-to-Digital Converter
AGV	Automatic Guided Vehicle
AoA	Angles of Arrival
APD	Avalanche Photodiodes
ARM	Advanced RISC Machine
BDS	BeiDou Navigation Satellite System
BLE	Bluetooth Low Energy
BPSK	Binary Phase Shift Keying
CDF	Cumulative Distribution Function
CDMA	Code Division Multiple Access
CMD	Cayley-Menger Determinant
CMOS	Complementary Metal–Oxide–Semiconductor
CoO	Cell-of-Origin
CSS	Complementary pair of Sequences
DR	Dead Reckoning
ECC	European Communications Committee
EKF	Extended Kalman Filter
EPnP	Efficient Perspective-n-Point Camera Pose Estimation
FCC	Federal Communications Commission
FDMA	Frecuency Division Multiple Access
FoV	Field of View
FP	Fingerprinting
FPGA	Field-Programmable Gate Array
GLONASS	Global'naya Navigatsionnaya Sputnikovaya Sistema
GNSS	Global Navigation Satellite System
GP	Gaussian Process
GPS	Global Positioning System
GT	Ground-truth
HF	High Frecuency
IFW	Interference Free Window
IM	Intensity Modulation
IMU	Inertial Measurements Unit
INS	Inertial Navigation System
IPPE	Infinitesimal Plane-Based Pose Estimation
IPS	Indoor Positioning Systems
IR	Infrared
IRLPS	Infrared Light Positioning System
ISI	Inter-Symbol Interference
KF	Kalman Filter

LBS	Location Based Services
LED	Light-Emitting Diode
LF	Low Frecuency
LLS	Linear Least Squares
LoS	Line of Sight
LPS	Local Positioning System
LS	Loosely Synchronous
LSE	Least Squares Estimator
MAC	Media Access Control
MAI	Multiple Access Interference
MLP	Multi Layer Perceptron
MEMS	Microelectromechanical Systems
NFER	Near-Field Electromagnetic Ranging
NLoS	Non-Line of Sight
NLSE	Non-Linear Least Squares Estimator
OFDM	Orthogonal Frequency-Division Multiplexing
OOK	On-Off Keying
PD	Photodiode
PDE	Partial Differential Equation
PnP	Perspective-n-Point
PDoA	Phase Difference of Arrival
PPM	Pulse Position Modulation
PR	Pseudorandom
PSD	Position Sensitive Detectors
PWM	Pulse Width Modulation
QADA	Quadrant Photodiode Angular Diversity Aperture
QPSK	Quadrature Phase-Shift Keying
RADAR	Radio Detection and Ranging
RF	Radio Frecuency
RFID	Radio Frecuency Identification
rMSE	root-Mean-Square Error
RPnP	Robust Non-Iterative Solution of Perspective-n-Point
RSS	Received Signal Strength
RSSI	Received Signal Strength Indicator
SHF	Super High Frequency
SMR	Sidelobe-to-Mainlobe Ratio
SNR	Signal-to-Noise Ratio
SoC	System on a Chip
SPI	Serial Peripheral Interface
SSID	Service Set Identifier
SVM	Support-Vector Machine
T-ZCZ	Three Zero-Correlation Zones

TDoA	Time Differences of Arrival
TDoF	Difference Time of Flight
ToA	Times of Arrival
ToF	Time of Flight
UHF	Ultra High Frecuency
ULPS	Ultrasonic Local Positioning System
US	Ultrasound
USB	Universal Serial Bus
UWB	Ultrawide Band
VL	Visible Light
VLC	Visible Light Communication
VLP	Visible Light Positioning
VLPS	Visible Light Positioning System
vSLAM	Visual Simultaneous Localization and Mapping
WAN	Wide Area Network
WLAN	Wireless Local Area Network
WPS	Wi-Fi-based Positioning Sytstem
2D	2 Dimension
3D	3 Dimension

Chapter 1

Introduction

1.1 Introduction

In recent years, the demand for affordable and accurate positioning systems has increased considerably with the development of different location-based applications and services, as well as the advancement of various technologies that can be used for this purpose. The great development of Global Navigation Satellite Systems (GNSS) has been of enormous benefit to society in recent decades, as they have made it possible to obtain relatively accurate positioning and tracking of people, objects or vehicles [Kol16]. This has led to a large number of applications and, in general, to an improvement of many previously cumbersome or error-prone tasks. This functionality, however, is lost in non-GNSS environments such as indoors, since the accuracy of GNSS is severely reduced due to the multipath effect and the attenuation of the received signal, especially inside buildings with multiple floors, thick walls and areas far from windows. Numerous studies have been carried out to perform this task in indoor environments, where people spend approximately 80% of their time, as the information can be used as an enabler of indoor location-based services (LBS) (e.g., guiding people inside a building, receive indications to find a certain product, navigation of Automatic Guided Vehicle, AGV, and drones, ...).

Ideally, an indoor positioning system must have a low cost and size, high accuracy, long lifetime and a large coverage volume, among other characteristics. Some of the proposed techniques use different types of signals to achieve them: acoustic, radio frequency, mechanical, optical, ... [Mau12]. In general, the choice of positioning systems is determined based on the conditions that must be met and how they will be implemented [Lop14]. As a result, all of the strategies discussed here are applicable to a variety of indoor situations, ranging from moving object control to automated manufacturing environments and warehouses. Acoustic positioning systems are excellent for covering large distances with centimetre-level accuracy. However, they need to consider effects such as channel multipath and their update rate tends to be relatively low [Ure18]. On the other hand, radio frequency positioning systems (Wi-Fi, RFID, UWB, etc.), despite having accuracies in the centimeter range (for the case of UWB), are highly dependent on signal fluctuations, which lead to high errors. Furthermore, they are subject to eavesdropping, jeopardizing link security [Han11]. Mechanical systems have a number of advantages, the most important of which is their low cost and small size. They are, however, very reliant on the object's acceleration and orientation [Lee18].

Finally, indoor positioning systems (IPS) based on optical signals, i.e. visible light (VLP) or infrared (IRLP), are a feasible alternative that has begun to expand due to its low cost, easy integration into the work environment and absence of health risks [Wan15a]. Their rise is driven partly by the recent emergence of a multitude of indoor location-based applications and services, which are being driven by technology advancements and the massive usage of light-emitting diodes (LEDs). Optical systems have major advantages over other technologies, such as the accuracy achieved. Nevertheless, there are still a number of research challenges, mainly related to the robustness of the technology. In addition, although the use of optical cameras is widespread compared to the use of photodiodes in reception, off-the-shelf and smartphone-integrated cameras often pose a low limit on the system's operating speed. Therefore, there is a great research activity in real-time positioning of mobile robots and drones to meet these requirements.

This thesis focuses its research on this field, analysing various problems of positioning with optical signals, in particular the use of different algorithms that allow 3D positioning in situations where the receiver is rotated in one or, even, in any of its axes, as well as the minimisation of positioning errors.

1.2 Motivation and Objectives of the Thesis

The motivation of this thesis is the contribution to the development of an optical LPS that can be complementary to or replace the GNSS in the absence of its signals or in locations where this system is not available (e.g. indoor environments). In this way, there is an interest in having a centimetric 3D optical system covering large distances ($\geq$ 5 m), capable of working in non-ideal situations (ambient light on, open windows) to locate people, robots, drones, *etcetera*. In addition, having a small and compact modular structure is key to facilitate the system's deployment in a room. For this purpose, it is crucial to have centimetric accuracies using a low number of beacons and the fact of not including other types of sensors that might compromise the latency of the proposal. Thus, the purposes of this thesis are:

- Analysis of different geometric configurations of positioning system deployment.
- Study of the coverage available in the working cell.
- Analysis and design of the sequences to be transmitted to minimise undesired interference.
- Study of the aperture length and its dependence on the linearity of the proposed algorithm.
- Design of an algorithm to estimate the incident point of light on the receiver.
- Design of various algorithms for estimating the pose of the mobile object.
- Performing experimental tests of the proposal.

1.3 Thesis Context

This thesis describes the work carried out in the Electronics Department of the University of Alcalá within the GEINTRA (Grupo de Ingeniería Electrónica Aplicada a Espacios Inteligentes y Transporte)

research group. The application areas of the GEINTRA research group are related to intelligent spaces and intelligent transport systems and are organized around eight main research lines: sensory systems; mobile robotics; human-machine interfaces; e-health, independent living and assistive technology; intelligent transport and infrastructure systems; distributed control and automation; and embedded digital systems, System on a Chip (SoC) and codesign; and localization and positioning systems, which is the research line focused by this thesis.

Most research work done within this thesis was developed under the structure of the research projects TARSIUS (ref. TIN2015-71564-c4-1-R), MICROCEBUS (ref. RTI2018-095168-BC51) and Red de Posicionamiento y Navegación en Interiores y Exteriores Delimitados REPNIN+ (ref. TEC2017-90808-REDT) supported by the Spanish Ministry of Economy, Innovation and Competitiveness; PUILPOS (ref. CM/JIN/2019-038), QADIR (ref. CM/JIN/2021-027) and the Youth Employment Program (ref. PEJ2018-003459-A) sponsored by the Community of Madrid.

The thesis was also economically supported by the University of Alcalá through the mobility program, as well as by the NEWFOCUS COST Action (CA19111) through the Short Term Scientific Mission (STSM) to allow a research stay at the Faculty of Engineering Technology, KU Leuven.

1.4 Thesis Structure

This thesis has been divided into the following chapters, in addition to this introductory one:

- Chapter 2: State-of-the-Art.

  This chapter summarizes the current status of research in the areas related to this thesis, highlighting the different positioning systems in use nowadays, describing their advantages and drawbacks. In particular, it focuses on optical positioning systems, comparing camera-based and photodetector-based LPS among previous works. It also summarizes different positioning techniques as well as some encoding sequence techniques.

- Chapter 3: Direct Positioning System: Configuration and Encoding techniques.

  This chapter focuses on the implementation and validation of a privacy-oriented local positioning system based on a set of four transmitting LEDs, acting as beacons at known locations, and a single QADA sensor, acting as the receiver to be positioned. In addition, this chapter analyses different sequences in order to improve the receiver's position estimation and presents some simulated results.

- Chapter 4: Direct Positioning System: Calibration and Positioning algorithms.

  This chapter presents the estimation of the image points at the receiver, by using non-linear and linear equation systems, depending on the size of the aperture. Different solutions are presented to estimate the final estimation of the receiver's position by means of an Angles of Arrival (AoA) algorithm or using homographic techniques that solve the Perspective-n-Point (PnP) problem of the proposed pin-hole system, such as Efficient Perspective-n-Point Camera Pose Estimation (EPnP), Infinitesimal Plane-Based Pose Estimation (IPPE) and Robust Non-Iterative Solution of Perspective-n-Point (RPnP) solutions. A novel calibration algorithm is proposed to estimate the intrinsic parameters of the quadrant photoreceiver and its aperture.

- Chapter 5: Centralized Local Positioning System.

  This chapter focuses on the proposal and validation of a centralized local positioning system, based on a set of mobile emitter LEDs and at least two fixed receivers at known positions in the working space. There is no restriction on the rotational angles that the moving LEDs can have, allowing the system to position 3D mobile objects such as drones using minimal hardware. Using AoA measurements, various solutions are presented to estimate the receiver's position using a Least-Squares estimator and geometrical considerations or using an Extended Kalman Filter (EKF) to increase the robustness of the estimations.

- Chapter 6: Experimental Results.

  In this chapter, we present a set of experimental results that validate the algorithms, techniques and hardware, discussed and evaluated in simulations in previous chapters.

- Chapter 7: Conclusions and Future Works.

  The most important conclusions of this thesis are presented in this chapter, along with the claims to novelty and some suggestions for further research. Finally, the publications derived from this thesis will be shown.

Chapter 2

State-of-the-Art

2.1 Positioning Systems

The need for affordable and accurate positioning systems is increasing due to the development of a great variety of positioning-based applications and services. The two main positioning systems are Global Navigation Satellite Systems (GNSS) and Local Positioning Systems (LPS).

GNSS operate at a global scale with positions referred to the global reference frame (eg. World Geodetic System WGS-84 [Kul00]). GNSS use satellites to provide geospatial positioning (longitude, altitude and latitude) by means of radio signals transmitted along a line of sight (LoS) achieving an accuracy in the order of metres. The main implemented GNSS [Kol16] are: Global Positioning System (GPS) from the United States, China's BeiDou-2 Navigation Satellite System (BDS) [Che10], Russia's GLONASS (Global'naya Navigatsionnaya Sputnikovaya Sistema) [Hac14] and Galileo [Ber08] from the European Union.

The development of GNSS has been of enormous benefit to society in recent decades, as it has made it possible to obtain relatively accurate positioning and tracking of people, objects or vehicles. This has led to a large number of applications, and, in general, to an improvement of many previously tedious or error-prone tasks. However, this functionality is lost in non-GNSS environments such as indoors (especially inside buildings with several floors, in areas far from windows, near thick walls, etc.), where people spend around 80% of their time, and where many automation tasks requiring certain form of positioning (warehouses, factories, *etcetera*) take place.

On the contrary, LPS provide positioning information in the coverage area within transmitters and receivers placed in the working area, with positions referred to local reference frames. Within the applications of indoor positioning systems, two large groups can be established. On the one hand, there are those that search for a contextual location, where a precision of around a few metres may be sufficient (this is the case of guidance or monitoring of people, or opportunistic advertising on mobile devices). On the other hand, there are applications that require greater precision, in the order of decimetres or centimetres, as in the case of unmanned vehicle guidance for automation or inspection tasks; or, in the case of people, when it is required to know with certain precision the position of some parts of the body in order to evaluate the activity being carried out. Together with the aforementioned accuracy, the ease of deployment and associated costs, the degree of coverage, the compatibility with

other systems (including communications systems), the privacy and the accuracy of positioning, even in situations that may be hostile or malicious, mean that various positioning technologies are currently being accommodated.

Fig. 2.1 shows the most commonly used positioning technologies grouped by [Mau12]. In [Lop14], restrictions on accuracy and coverage are applied to meet the conditions of an indoor scenario (coverage below 50 m) and focusing on those applications requiring high accuracies, such as human tracking or unmanned vehicle guidance (accuracy below 1 m). These restrictions reveal that only ten technologies distributed in five categories are eligible to be implemented in an indoor LPS for tracking applications. The classified technologies are: 1) optical, 2) mechanical, 3) magnetic, 4) acoustic, and 5) radio frequency (RF) based systems. A summary of the different technologies in terms of accuracy and coverage is presented in Table 2.1.

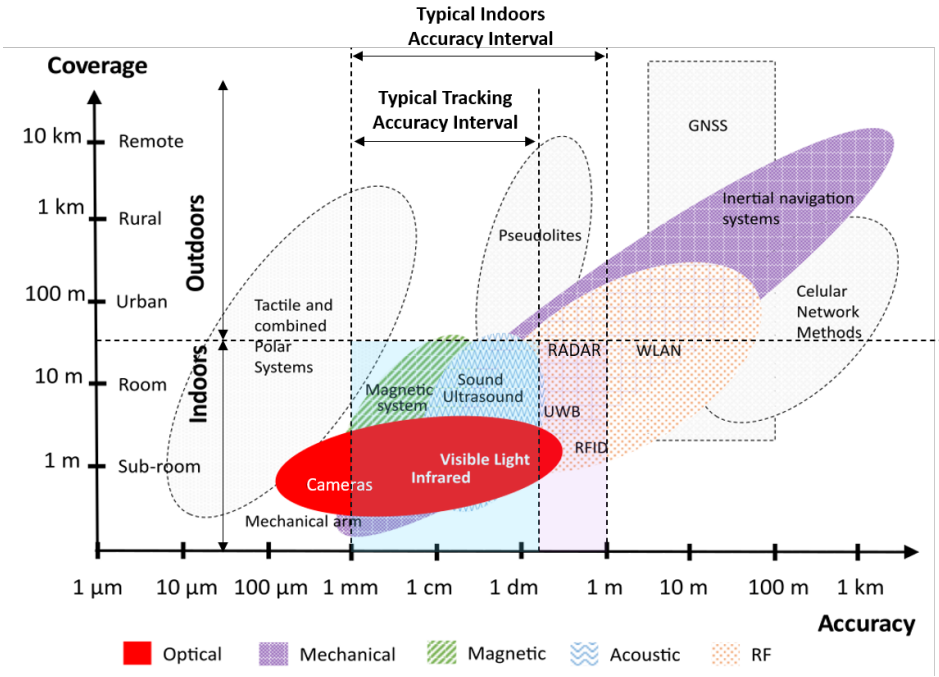

Figure 2.1: Overview of indoor LPS according to accuracy and range (adapted from [Mau12, Lop14, Ure18]).

Table 2.1: Overview of indoor systems according to accuracy and coverage (adapted from [Lop14]).

Category	Technology	Accuracy (m)	Coverage (m)
Optical	Cameras	mm−dm	0.5 − 10
	Infrared/Visible	mm−cm	0.5 − 10
Mechanical	Mechanical arm	0.1mm−1mm	1 − 2
	Inertial Navigation	1%	10 − 100
Magnetic	Magnetic Systems	mm−cm	1 − 20
Acoustic	Sound/Ultrasound	cm	1 − 50
RF	UWB	cm−m	1 − 50
	RADAR	cm−dm	0.5 − 10
	RFID	dm−m	1 − 50
	WLAN/WiFi	cm−m	10 − 100
	Bluetooth	dm−m	10 − 15

2.1.1 Radio Frequency

The majority of LPSs are based on radio frequency technologies that allow the user to obtain position using a radio signal. Within the radio frequency technologies, the following can be distinguished: Wi-Fi/WLAN (Wireless Local Area Networks), Bluetooth, Radio Frequency Identification (RFID), and Ultrawide Band (UWB), among others.

WLAN

Wi-Fi signals (IEEE 802.11) can be implemented alone, in the so-called Wi-Fi-based Positioning Systems (WPS), or they can be combined with other technologies, typically GNSS [Kov14]. WPS is commonly used in low accuracy applications and typically positions by matching the RSS (Received Signal Strength) measurements with the pre-acquired fingerprints (see Section 2.2) previously stored in a database [Kot15, You05]; an overview is presented in Fig. 2.2. Other typical Wi-Fi signal parameters also used are the Service Set Identifier (SSID) and the Media Access Control address (MAC).

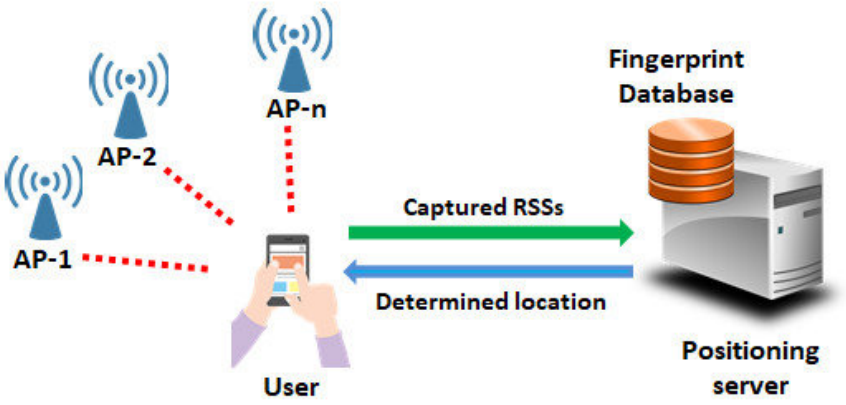

Figure 2.2: General overview of a WLAN positioning system [Hai19].

The main drawback of WPS is the high dependency of its accuracy on signal fluctuation that may occur due to changes in the environment. On the contrary, WLAN access points are readily available in many indoor environments, and positioning can be done with a standard mobile phone [Mau12]. The average error in the location is usually conditioned by the scenario considered for positioning, ranging from centimetres [Che16] up to a meter [Kot15, You05].

RADAR

Radio Detection and Ranging (RADAR) is widely used for radio frequency-based indoor positioning [Par15]. A special case of radar technology typically used for positioning below 1 km is the millimetric radar wave. The mode of application of millimeter waves is through the radar principle: one antenna generates an electromagnetic wave, while another captures the same wave once it is reflected on an item in the environment (see Fig. 2.3). Through the computation of the ToF (Time of Flight), the device that controls the antennas is able to determine the distance to the object (see Section 2.2) [Par21b].

The majority of sensors operate in the radio bands of 24, 60, and 77 GHz. At the moment, the market is focusing on the second and third bands, with bandwidths reaching 4 GHz (60- 64 GHz) [Par21b]. In

general, the use of millimeter wave allows the construction of small-sized antennas, allowing easier integration with the environment [Fer18]. Different works use millemtric radar wave to identify and track humans [Zha19] or drones [Par21a] at distances up to 5 m with positioning errors below 16 cm and 22.86 cm, respectively.

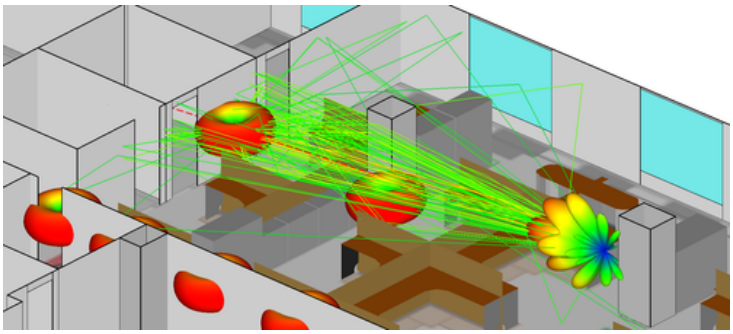

Figure 2.3: General overview of a millimeter wave radar positioning system [Rem21].

Bluetooth

Bluetooth (IEEE 802.15) operates in the 2.4 GHz ISM band. It overcomes the weaknesses of GNSS or Wi-Fi in areas where its accuracy decreases, typically using trilateration methods and RSS measurements (see Section 2.2) within a short range (10 - 15 m) [Kal16]. Other advantages are its high security, low cost, low power and small size. In addition, it is a technology highly embedded in most intelligent mobile phones; an overview of a Bluetooth indoor positioning system is presented in Fig. 2.4. In fact, in 2013, Apple launched iBeacon for iOS, a new technology based on Bluetooth Low Energy (BLE) that extended the range of positioning up to 50 m [App21].

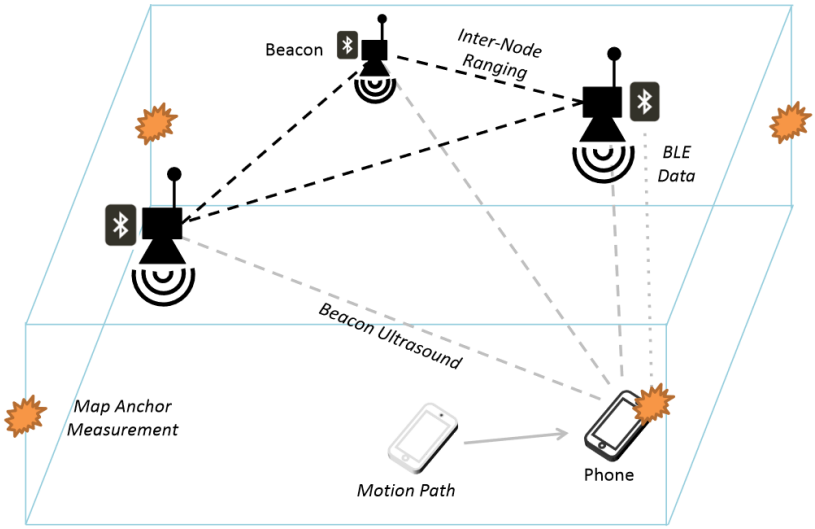

Figure 2.4: General view of a Bluetooth positioning system [Laz15].

RFID

An RFID system consists of a reader with an antenna that interrogates, via radio waves, nearby active transceivers or passive RFID tags attached to objects, in the pavement or walls [Sch15]; an overview of an RFID positioning system is presented in Fig. 2.5.

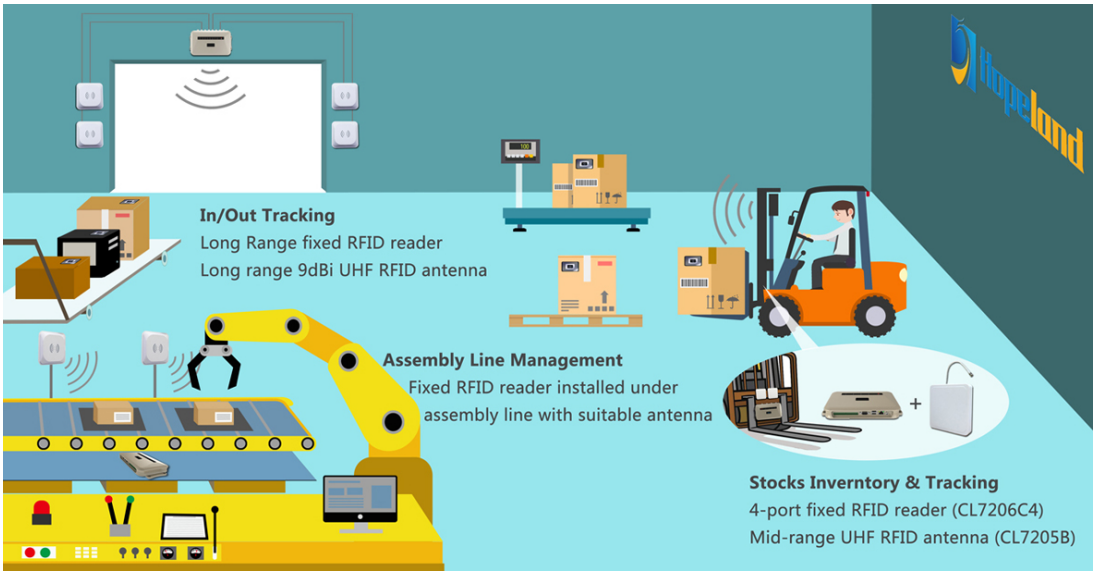

Figure 2.5: General view of a RFID positioning system [Tec21].

The most widely used positioning principle with RFID is the principle of proximity, also known as Cell-of-Origin (CoO) [Mau12]. The information contained in the tag (code or serial number) is associated with the position in which the tag is located, and by extension, with the position in which the user is located. Thereby, the accuracy of an RFID system will be determined by the density of tag deployment and the maximal reading ranges. Other implemented techniques rely on times of arrival (ToA) or time differences of arrival (TDoA) [Abd14], AoA or Phase Difference of Arrival (PDoA) [Bes19], fingerprinting (FP) and RSS [Liu17a] (see Section 2.2).

In addition, four types of RFID systems can be distiguished depending on the frequency range they use: low frequency (LF: 30 kHz to 500 kHz), High Frequency (HF: 3 MHz to 30 MHz), Ultra High Frequency (UHF: 433 MHz & 868 MHz to 930 MHz); and microwave (SHF: 2.4 GHz to 2.5 GHz & 5.8 GHz). The higher the frequency, the more the signal suffers from attenuation [Mau12].

The most widespread criteria for classifying RFID systems is the one that has to do with how these tags offer information to the user. From this point of view, we can distinguish between passive and active tags [Agu16]. Passive tags rely on the inductive coupling that allows the tags to receive sufficient energy, in the form of RF waves from the nearby RFID scanner, to operate the integrated circuit that it possesses and transmit their codes back to the scanner [Lop14]. Their main advantages over active tags are the lack of a power supply, small size, robustness, low cost and low maintenance. Their main drawback is that the detection range is usually from about 10 mm to 6 m, demanding a dense deployment of tags. On the other hand, active tags emit RF emissions autonomously using power supplied by an integrated battery. The fact that they need to use batteries makes them heavier and more expensive but enables long distance measurements in ranges of more than 30 m that allow positioning typically by fingerprinting on RSS measurements [Agu16].

Summing it up, RFID is a widely deployed technology in manufacturing; however, it derives serious security concerns from unauthorised eavesdropping without notice to the user [Han11]. Some of the proposed solutions in the literature regarding passive tags are related to inventory control [Kan17], while others focus on clothing integration for people tracking [He19] or drone tracking [Buf17]. In addition, applications that use active tags focus on hospitals [Fri19] or vehicle and pedestrian navigation [Pen11].

UWB

UWB uses radio signals over short distances to position by using ToF measurements (see Section 2.2). Its main advantages are its robustness against interference and that it usually works with low power signals [Sch18, Ure18]; an overview of an UWB indoor positioning system is presented in Fig. 2.6. In particular, an emitted radio wave is considered UWB if either the bandwidth is higher than 500 MHz or 20% of the carrier frequency [Mau12]. Thus, it has a high coverage and range capability, with the possibility to partially penetrate walls and obstacles, although its accuracy and maximum range are considerably reduced in practice when operating indoors ($10 - 30$ cm) [Tie16], especially due to the NLoS (Non-Line of Sight) effect and the influence of obstacles and metallic equipment [Gua19].

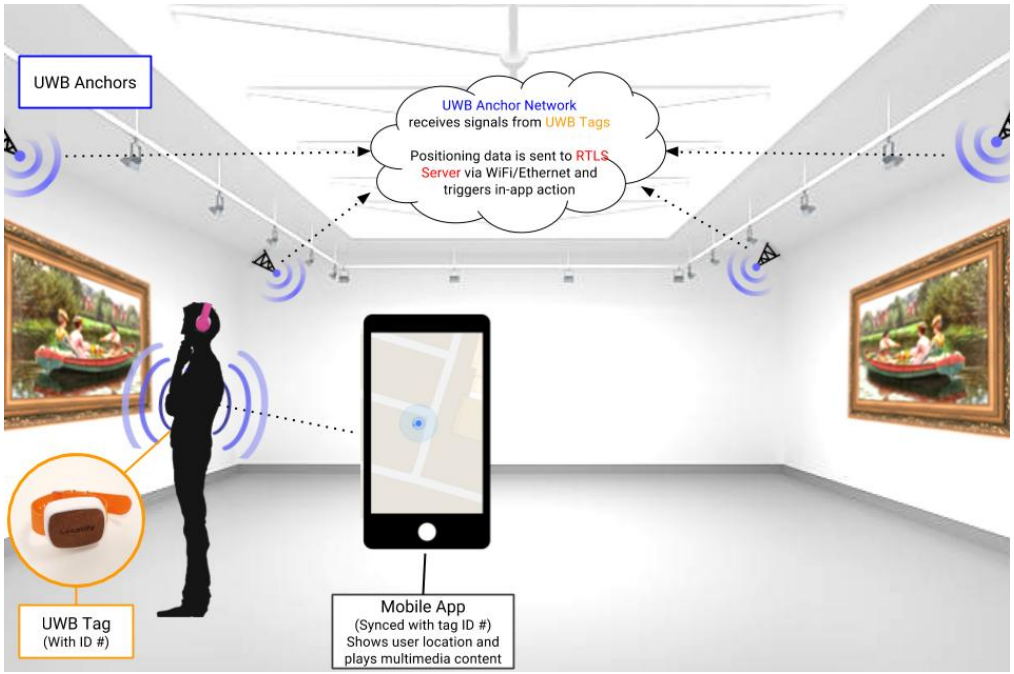

Figure 2.6: General view of an UWB positioning system [Loc21].

In order to avoid interference with other radio signals, the frequency range for UWB emissions has been legalised between 3.1 GHz and 10.6 GHz in the case of the Federal Communications Commission (FCC) in the USA and between 6.0 GHz and 8.5 GHz, according to the European Communications Committee (ECC) in Europe. In both cases, the isotropically radiated power density has also been limited to -41.3 dBm/MHz to avoid possible harmful effects on the human body [FCC21]. Nowadays, its use is widespread indoors due to its easy implementation in already installed infrastructure (thanks to the development of particular chipsets [Dec21]) and it has already started to be implemented in advanced versions of smartphones [Sam21].

2.1.2 Mechanical

Mechanical positioning systems typically use Inertial Measurement Units (IMUs) based on MEMS to position due to their small size and low cost [Bis09]. IMUs are often incorporated into Inertial Navigation Systems (INS) which use the IMU angle measurements to determine position, linear velocity and altitude. The main operating principle of these systems is based on knowledge of the user's initial position to estimate successive positions according to variations in the direction and speed of his movements. This technique is known as Dead Reckoning (DR). It is really useful in indoor environments where it is impossible to install any positioning infrastructure (see Fig. 2.7).

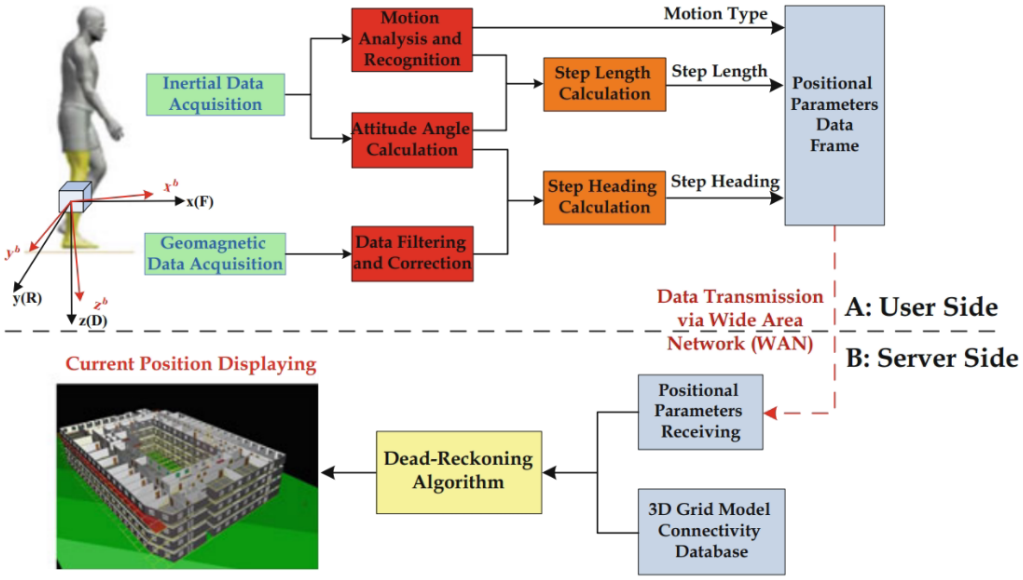

Figure 2.7: Block diagram of a INS [Wan14a].

However, IMUs are highly affected by stability and drifts and they have a strong dependence on the object's acceleration and orientation in the three axes over time [Lee18]. In order to correct those weaknesses, they are often combined with other systems, such as a barometer [Per14].

2.1.3 Magnetic

Magnetic systems use the generation of artificial electric and magnetic fields to determine the user's position (see Fig. 2.8). Positioning systems based on electromagnetic fields can be classified as systems using the Antenna Near Field, systems using magnetic fields from currents (coils of AC magnetics), systems using permanent magnets and systems using magnetic fingerprinting [Mau12]. Some of the advantages of these systems are that they can be used in conditions without LoS; they are not affected by multipath nor reflection and they can track moving objects due to their high measurement acquisition rate, meanwhile the drawbacks are that these systems suffer high interference with external magnetic objects, such as metal objects, and thus, their coverage tends to be small [Lop14].

Near-Field Electromagnetic Ranging (NFER) uses the phase relation between the electric and the magnetic field components of an electro-magnetic field to estimate the distance from a small transmitter antenna achieving average positioning errors of 34 cm over ranges up to 23.4 m [Sch11].

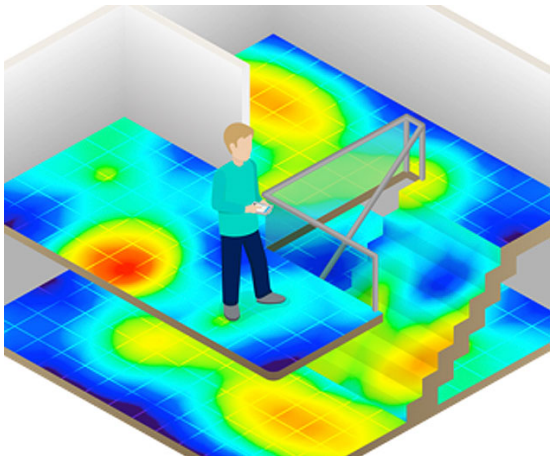

Figure 2.8: General view of a magnetic positioning system [Atl21].

Systems using magnetic fields from currents (i.e. coils) are based on the fact that the magnetic field created by a coil can be modelled. Thus, if multiple coils generate magnetic fields at known locations, the relative 3D position of the sensor can be determined with a high degree of accuracy. A similar approach is developed when using permanent magnets where multiple static magnetic sensors at known locations measure the magnetic flux density of a mobile magnet to locate it. An example of a coil-based system is LIBERTY, where more than 16 coils were used to obtain millimetre accuracy with operating ranges up to 4 m [Lib21].

On the other hand, a different approach using magnetic systems is that a fingerprinting method can be applied under the assumption that the magnetic field inside a building is approximately static and that each location has the unique signature of its magnetic flux density. The location to be estimated is determined by comparing the current flux density with the previously stored values in the database achieving accuracies in the range of decimetres [Hav09].

2.1.4 Acoustic

Acoustic positioning systems use audible sound (below 20 kHz) or ultrasound signals (above 20 kHz) to position by using Difference Time of Flight (TDoF), Time of Flight (ToF) and phase coherence methods (see Section 2.2). These systems typically deploy a set of transmitting and receiving ultrasonic beacons in the localisation environment and, by measuring the distance between them and applying positioning algorithms, the position of the person or object to be located can be estimated. A general view of an acoustic LPS is presented in Fig. 2.9. They provide accuracies in the range of centimetres with coverages of tens of meters [Lin15, Par18]. In addition, although their update rate is relatively low and they have a considerable channel multipath [Jim05, Hol05], they can provide robustness and security compared to the RF technology, as they can be used in spaces confined by room walls, and do not suffer from external electromagnetic interference (even those that could be malicious), which could lead to loss of confidence in the positioning system. Besides, they can take advantage of their lower cost, new technological developments in transducers or non-radio communications, or the avoidance of radio spectrum saturation.

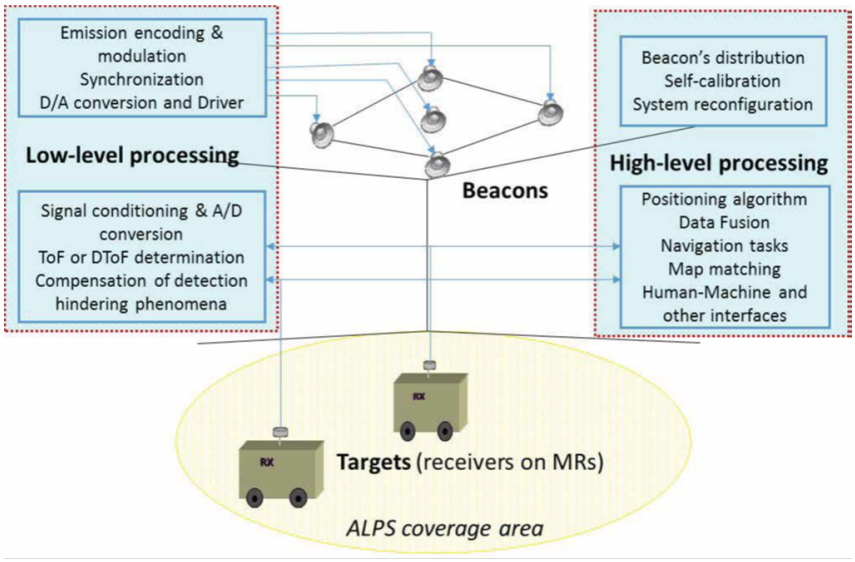

Figure 2.9: General view of an acoustic positioning system [Ure18].

2.1.5 Optical

Camera-based positioning systems are among the most widely used positioning systems since they achieve good accuracies with large coverage ranges. However, they require a good calibration, they have to be used in environments where the illumination is adequate and the computation time is high.

One possible solution of camera-based positioning systems is that one or multiple cameras are used to detect active or passive markers (e.g. using reflective materials) that are attached to the object being tracked by using infrared light. In these conditions, the image processing algorithm is reduced to a simple point detection in a grayscale image, see the Optitrack system example in Fig. 2.10. These systems are typically used for human body tracking in the movie industry and are very expensive.

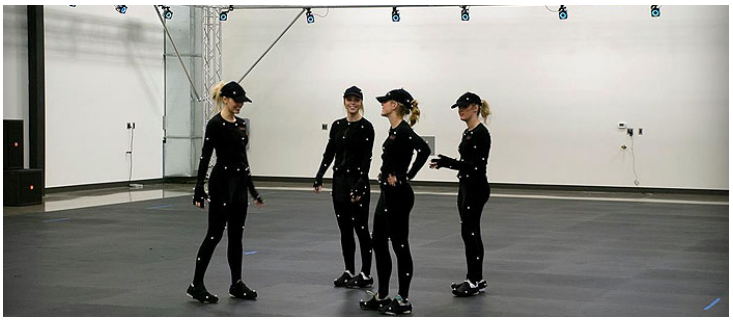

Figure 2.10: General view of the Optitrack Motion Capture Positioning system [Opt21].

On the other hand, if the camera is fixed to the agent to be positioned, it can obtain its position from the captured images. This type of system use landmarks, which can be artificial (developed and conveniently placed for a particular application) or natural (detected as particular features of the environment). For instance, Visual Simultaneous Localization and Mapping (vSLAM) is a technology introduced in [Kar05] to create a visual landmark map (see Fig. 2.11). They use an object recognition algorithm on a camera image captured by a mobile device. This technology does not require installing additional infrastructure or auxiliary devices, but it has to deal with large landmark databases and significant computational times.

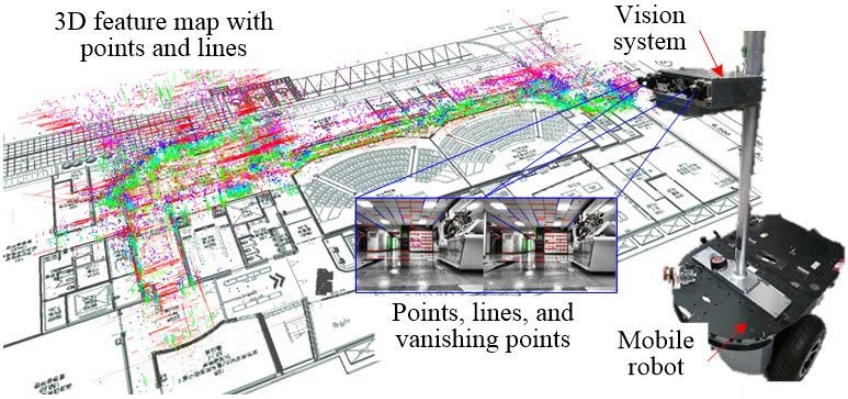

Figure 2.11: General view of a VSLAM system [Cha20].

Indoor positioning systems (IPS) based on optical signals, visible light (VL) or infrared (IR), are a feasible alternative that has begun to expand due to their easy integration into the work environment [Wan15a], low cost and absence of health risks [Do16b]. Its expansion is partly due to the recent emergence of a multitude of indoor location-based applications and services, which are driven by technological improvement and the massive use of Light-Emitting Diodes (LEDs). Optical Positioning Systems are used both in indoor and outdoor areas. Although most work focuses on indoor applications due to the high influence from ambient light [Do16b], interesting outdoor applications can also be found [Son21]. In the case of indoor positioning, whereas the transmitter is usually a LED array or a single LED, it is possible to distinguish positioning systems based on imaging sensors and simple photodetectors at the receiver.

In general, positioning systems based on imaging sensors typically use Complementary Metal Oxide Semiconductor (CMOS) cameras [G S17]-[Kaz14] or the camera of conventional smartphones [Raj14] (see Fig. 2.12). Although the use of optical cameras is widespread compared to the use of photodiodes in reception, off-the-shelf and smartphone-integrated cameras often pose a low boundary on the system's operating speed due to the required complex image processing algorithms [Pat15]. The majority of previous works implement the RSS technique achieving a decimetre positioning error [Zha17, Zac16] with an average of positioning time of 3 seconds in [Fan17]. In order to cover large distances, they require a high number of beacons; in [Fan17], a corridor is proposed as the operation area, so that 20 beacons are placed over a distance of 30 m to accurately position the receiver. Some previous works combine the CMOS camera with accelerometers to improve their accuracy [Huy16].

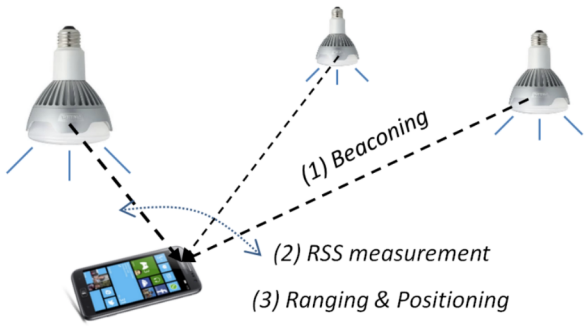

Figure 2.12: General overview of a camera-based Optical LPS [Hu13].

On the contrary, positioning systems whose receptor is a photodetector, use either photodiodes [Cai17, Wan13a] or an array of photodiodes [Cin18a, Yan14], to generate a current corresponding to a light impact on the photodiode, from which the position of the receiver can be estimated (see Fig. 2.13). It is worth noting that the vast majority of manufactured photosensors have their maximum responsivity at the near-infrared region (around 910 nm), so the use of visible light is usually penalized. A more in-depth analysis of the existing optical positioning systems using photodiodes is detailed in Section 2.4.

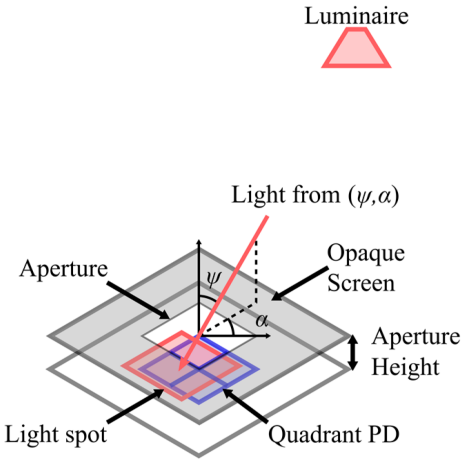

Figure 2.13: Block diagram of an aperture-based Optical LPS [Cin19].

2.2 Positioning Techniques

The most commonly used positioning techniques in Visible Light Positioning Systems (VLPS) or Infrared Light Positioning Systems (IRLPS) are fingerprinting, triangulation, trilateration or multilateration with times of flight measurements (ToA, Times of Arrival; TDoA, Time Difference of Arrival) [Wan13b], signal attenuation measurements (RSS, Received Signal Strength) [Ala19, Ste17] or angles of arrival measurements (AoA, Angle of Arrival) [Wan15a]; although other methods such as proximity [Xie18] are also used (see Fig. 2.14). These methods can be combined or used separately.

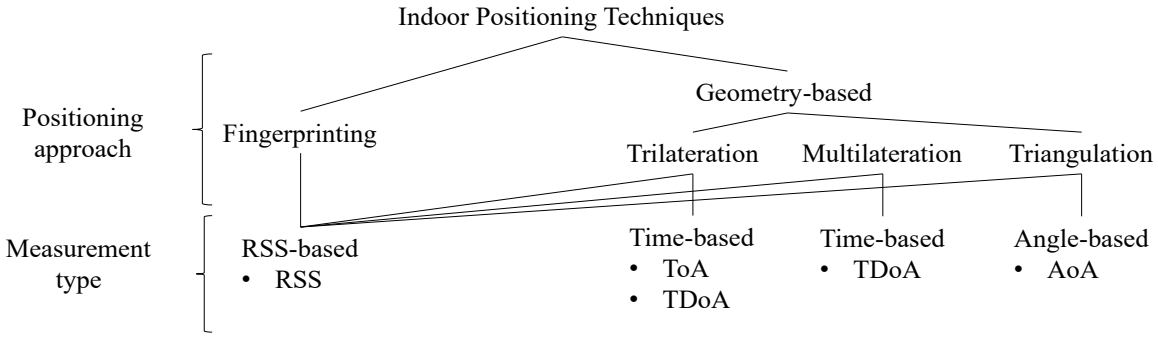

Figure 2.14: Summary of some positioning techniques (adapted from [Lop14]).

Fingerprinting (FP) is usually divided into two stages: 1) training and 2) positioning. The training stage consists of building a database of empirical fingerprints by taking exhaustive RSS measurements in the area of interest. In the positioning stage, a position is estimated by matching the obtained

measurements with the best position in the database [Che18]. In order to improve the accuracy of this technique, different restrictions can be included by adding maps of the surroundings.

Geometry-based positioning systems use geometric relations (distances or angles) to estimate a position. Trilateration estimation of 3D positions can be implemented if three or more non-collinear beacons are involved [Cha19], while multilateration requires at least four measurements as one of them is used as reference. These method uses the distance between beacons to obtain the target position, as presented in Fig. 2.15. Similarly, triangulation estimation can be used if at least three angles between beacons and the object to position can be measured, typically using AoA measurements.

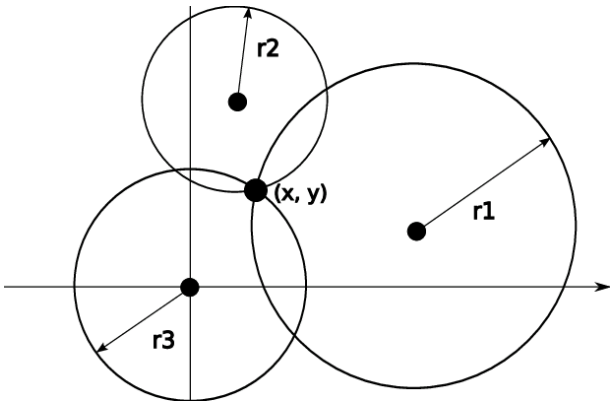

Figure 2.15: Trilateration positioning schematic [Gol10].

Positioning using RSS measurements implies taking into account the reflections of light on different surfaces and the consequent multipath effect, which increases the difficulty of the positioning algorithm [Lla20]. In practice, RSS is used for short distances in VLPS (from a few millimetres up to 1 m) due to the strong influence of ambient light. Other aspects, such as the tilting of the transmitter or its radiation pattern, must be handled [Ste19] often by implementing Machine Learning algorithms in order to enhance the VLP distances (up to 5 m while having centimetric positioning errors [Rae21]).

TDoA is based on the measurement of the time difference between the signal arrivals at the receiver, whereas ToA uses the absolute time of arrival. The distance between transmitter and receiver is calculated by knowing the length of the transmitted signal, the speed of light in the medium and the measured time between the transmission and the reception. The main disadvantages of TDoA and ToA measurements are the required synchronisation between beacons (and also with the tag for Time of Flights) and the high value of the speed of light, which implies that 1 ns time estimation error becomes a 30 cm positioning error [Dan12]. Therefore, these techniques are typically used in long distances ($>$ 50m) when a laser is used as transmitter [Ber12].

Finally, the AoA-based positioning algorithm uses the estimation of angles of arrival from several LEDs to position. Its main advantages are its robustness against source and environmental fluctuations (fumes, dust, etc.), as well as the fact that synchronisation between transmitters is not necessary [Ste17]. In addition, if the image plane coordinates of the point of incidence of the central ray of the beam are determined, homography techniques or Perspective-n-Point (PnP) solutions could be applied [Apa21c]. The main disadvantages of AoA measurements are that at least three measurements are required to position in three dimensions by triangulation [Do16a] and that obstruction in the LoS will deteriorate the link.

2.3 Medium Access and Encoding Techniques

Another key aspect is the medium access technique, often related to the modulation scheme implemented in the transmissions. Several works rely on Pulse Position Modulation (PPM) or Pulse Width Modulation (PWM) [Kes18, Ala19] since they are the most robust modulations against Inter-Symbol Interference (ISI), whereas others use On-Off Keying (OOK) modulation [Ste18, Li17] due to its simplicity [Lv17a]. On the contrary, in [Ste17], an OOK modulation is compared to a Binary Phase Shift Keying (BPSK), with the last one having the best performance in visible light communications.

Furthermore, several applications require encoding schemes that allow simultaneous interference-free transmissions. In these cases, Barker and Walsh codes cannot be used due to the lack of low cross-correlation functions and to the strict synchronism required between transmitters and receivers [Per09]. Thus, in order to overcome these drawbacks, there is a previous trend in the use of pseudorandom sequences (PR), such as Kasami [Apa19a] or Gold codes [Yan18], as well as complementary pair of sequences (CSS) or sequences derived from them, such as Three Zero-Correlation Zones codes (T-ZCZ) [Zha05] or Loosely Synchronous (LS) [Gar12].

It is worth remarking that the encoding technique often has a significant influence on the final performance of the system, since, when simultaneous transmissions are carried out, the Multiple Access Interference (MAI) may imply a systematic error in the estimation of the position. Furthermore, sequences with more robust behavior against MAI often require complex transmission and reception schemes. Their complexity directly affects the transmission time, and may increase the computational load on the receiver due to the algorithms involved in the calculation of correlation functions and, therefore, it may decrease the position-updating rates. These correlations are often characterized by massive and parallel data processing, which makes them especially suitable for specific architectures designed in FPGAs (Field-Programmable Gate Arrays) devices, as in the case of Visible Light Communication (VLC) [Far17]. Other architectures are also used: in [Agu17] an Arduino Nano is combined with an AD9850 signal generator circuit; in [Wan15b] an Advanced RISC Machine (ARM) structure is implemented; and in [Liu17b] an STM32 is used, among others. The choice of an optimal final architecture for the implementation of these techniques remains to be a key aspect in the design of this type of positioning systems.

2.4 Photodiode-based Optical Positioning Systems

The main receiving systems employed in visible and near infrared light detection use either a single photodiode or several photodiodes.

2.4.1 Using a Single Photodiode as the Receiver

Regarding works that implement a single photodiode, they typically use RSS measurements to estimate the position of a certain target. In order to deploy more robust systems they use multiplexing techniques (CDMA, Code Division Multiple Access [Cai17], FDMA, Frecuency Division Multiple Access [Knu20], Quadrature Phase-Shift Keying, QPSK [Hua21]), deploy several LEDs [Li17], use Avalanche Photodiodes (APD) [Hua21], include an analysis of the multipath and the emission pattern [Ste19, Alm19] or implement machine learning techniques [Knu20, Hua21], among others.

An Environment-Aware RSSI based positioning algorithm for Visible Light Positioning (VLP) that uses a multi-SVM (Support-Vector Machine) classifier was proposed in [Hua21]. They placed an APD receiver at a distance of 1 m from the transmitter's plane and, the transmitters implement a QPSK modulation scheme and an Intensity Modulation (IM). Different points were analyzed in a grid of 0.60×0.60 m^2 finding absolute 3D errors of 12 cm in 90% of cases.

More machine learning techniques are compared in [Knu20], where a FDMA VLP system is proposed. Authors compare a Gaussian Process (GP) regression with a Multi Layer Perceptron (MLP) technique and a trilateration algorithm to estimate the position of a receiver in an area of 3.5×3.5 m^2 and a height of 1.4 m, finding the GP to be the best solution with p95 errors below 17.07 cm in a setting where only a limited amount of training data is available.

Finally, the authors of [Alm19] demonstrate the degrading effect of multipath reflections on VLPS and highlighting the need to take it into consideration when evaluating VLPS. RSS signals and two trilateration algorithms (Cayley-Menger Determinant, CMD, and the Linear Least Square, LLS, method) are used to estimate the receiver's position in an area of 4×4 m^2 and a height range of $0.64 - 2.55$ m. The p95 obtained results are 20.4 and 23.5 cm for the CMD and the LLS algorithm, respectively. Multipath reflections increased the median positioning errors by 112% in 2D systems and by 69% for 3D systems.

2.4.2 Using an Array of Photodiodes as the Receiver

Those works that use arrays of photodiodes can be classified into four broad categories [Cin19]: aperture-based, lens-based, prism-based, and tilted photodiode-based designs. Those based on prisms [Wan14b] or tilted photodiodes [Zhu19] are larger in size and typically provide limited resolution in AoA measurement (sometimes quantified ranges of angles). Aperture-based designs using quadrant photodiodes (see Fig. 2.13) allow higher resolution in AoA estimation, but with Field of View (FoV) limitations [Apa20d]. The use of a Quadrant Photodiode Angular Diversity Aperture (QADA) is highlighted due to its better angular diversity [Cin18a]. Finally, lens-based systems (e.g., with a hemispherical lens) typically use Position Sensitive Detectors (PSD) to provide higher FoV [Wan13a], achieving higher refresh rates than cameras, but they have smaller bandwidths than QADA sensors and photodiodes [Lla20]. They must also consider the effects of the lens on the photosensor to achieve a high accuracy [DLLC21].

On the other hand, there are other works that while using an array of photodiodes, do not use apertures, lens, prism or tilted designs. [Hos20] proposes a 2D positioning algorithm based on a single LED and one to four photodiodes. The proposal implements a RSS and fingerprinting method that achieves $5 - 25$ cm of positioning errors in an area of operation of 0.5×0.5 m^2 at heights from 1.5 to 3 m. [Zhu19] proposes a 3D positioning algorithm based on 2 APDs and a reference detector. It uses RSS measurements to estimate the pose of the receiver in a grid of 1×1 m^2 at heights of 1.5 m achieving less than 10 cm of positioning error. Finally, [Lv17b] proposes a 3D positioning algorithm based on 8 photodiodes with apertures. It uses AoA measurements to estimate the pose of the receiver in a larger operation area of 5×5 m^2 at heights of 2 m achieving less than 20 cm of positioning error.

In general, the use of multiple photodiodes with apertures is increasing due to their good performance using AoA instead of RSS and thus neglecting errors due to the multipath effect, as well as undesired reflections.

2.4.3 Sensor Fusion

Finally, several works attempt to combine information from multiple sensors for positioning. Different technologies are combined to compensate for each other's potential drawbacks, increasing the operating area while decreasing the positioning error. The main limitation of sensor fusion is the need for an algorithm capable of fusing the data efficiently and accurately with low computational time. Some examples found in the literature are:

- Optical + mechanical: [Li17] adds an IMU, while [Yas16] adds an accelerometer to the proposed VLP, achieving positioning errors below 10 cm at distances up to 2.5 m. In [Ber20] a 2D VLPS based on three photodiodes and an IMU is proposed. The system estimates the receiver's position using radiometry and AoA measurements. The proposal is experimentally tested in a small area of 0.6×0.6 m^2 with a distance between transmitters and receiver of 3 m and it reaches positioning errors in the range of 5 cm.

- Optical + ultrasound: [Apa21d] fuses the positioning results from an infrared and ultrasound LPS to improve the availability of the system achieving positioning errors below 10 cm at distances over 4 m. [Rab17] uses the received ultrasound and optical pulses to estimate the receiver's position at distances of up to 80 cm achieving positioning errors below 5 cm.

- Optical + optical: [Cin19, Cin18b] develop a VLPS that combines a camera with a QADA receiver achieving simulated errors below 20 cm.

2.4.4 Comparison of Photodiode-based Optical LPSs

A comparison of some existing photodiode-based VLPSs and IRLPSs is presented in Table 2.2. The parameters to be compared in the literature are the dimensionality of the proposed system; the number of beacons required in the implementation and their electrical power; the modulation or encoding of the transmitted signals, if used; the ceiling height at which the emitters are placed; the type of receiver including any additional non-optical hardware; the coverage area at which the proposed system can operate and the position accuracy achieved in it; and, finally, the implemented positioning technique. All of them consider a Lambertian profile at the LED emitter and Gaussian noise.

Summing it up, there is an interest in having a centimetric 3D optical system covering large distances ($\geq$ 5 m), capable of working in non-ideal situations (ambient light on, open windows) to locate people, robots, drones, etcetera. In addition, having a small and compact modular structure is key to facilitate the system's deployment in a room. For this purpose, it is crucial to have centimetric accuracies using a low number of beacons and the fact of not including other types of sensors that might compromise the latency of the proposal.

2.5 Problem Statement and Thesis Objectives

As described in the previous sections of this chapter, there are several proposals for indoor 3D positioning. Each of them has different drawbacks as for example the dependence on the object orientation in mechanical systems; the multipath effect of the channel in acoustic positioning systems;

and the strong dependence on signal fluctuations of radio frequency signals, in addition to unauthorized eavesdropping that can compromise the security of the link.

Compared to other technologies, optical systems can provide significant advantages, such as the accuracy achieved. Nevertheless, there are still a number of research challenges, mainly related to the robustness of the technology. In addition, although the use of optical cameras is widespread compared to the use of photodiodes in reception, off-the-shelf and smartphone-integrated cameras often have a low system operating speed.

Therefore, the main objective of this thesis is the implementation of a centimetric 3D optical positioning system using photodiodes and LED transmitters in environments at working distances of up to 5 m. A coded sequence will be transmitted and different possible geometrical and deployment structures of the system will be studied. An analysis is needed to determine which structure and coding sequence to use, as well as the advantages of synchronising the positioning system or part of it, in order to select the most suitable one. In order to achieve this global objective, a list of partial objectives has been drawn up, which will have to be addressed throughout the development of the doctoral thesis:

- Search, study and analysis of the existing literature on the topics, in order to have a knowledge of the state of the art, the developments made and the corresponding contributions. In this way, possible improvements or extensions to already available systems will be evaluated.
- Modeling of the complete positioning system used to estimate the position of a desired mobile. In order to accomplish this, it will be necessary to:
  - Analyse and implement different geometric configurations of positioning system deployment. In particular, two designs will be studied theoretically to achieve the functionality of the proposed objectives. The first is a privacy-oriented 3D positioning system where the receiver will be mobile and the transmitters will be fixed, and the second is a centralized 3D positioning system where the transmitter will be mobile and the receivers will be stationary.
  - The coverage available in the working cell will be studied to determine the physical limitations of the system. The use of a larger number of transmitters can lead to an improvement in the accuracy of the receiver position estimation; it is therefore of great interest to optimise the number of transmitters and their arrangement in the cell.
  - Study of the aperture length and its dependence on the linearity of the proposed algorithm. Design of an algorithm to estimate the incident point of light on the receiver (image point), under non-linear and linear constraints, to enlarge the emitter-receiver range, thus increasing the total coverage space.
  - Design of various algorithms to optimally estimate the pose of the mobile object using trilateration techniques with Angle of Arrival (AoA) signal detection and homographic techniques. A comparison of the performance of the different approaches will be carried out, so an intensive experimental characterization might allow to determine an optimal solution by combining the various aforementioned techniques.
- Analysis and design of the sequences to be transmitted to identify each transmitter and minimise undesired interference. The use of CDMA (Code Division Multiple Access) will be evaluated to

uniquely identify the signal from each transmitter. Different sequences and their lengths will be analysed, such as Loosely Synchronized (LS) codes or pseudo-random sequences (Kasami), to determine which one has better behaviour in our proposal.

- Implementation of the proposed systems and validation of the different structures in a real prototype through experimental tests and simulations. This point covers all the stages of transmission, reception, including filtering, acquisition of the signals and processsing to obtain an estimation of the final position.

Table 2.2: Comparison of previous VLPSs and IRLPSs.

Ref.		Number of beacons	Power of each beacon	Modulation/ Codification	Receiver's height	Type of receiver	Area of operation	Position accuracy	Positioning technique
[Cai17]	3D	4	9 W	CDMA	1.1/0.7/0.3 m	1 PIN	0.9×0.9 m^2	4 cm (average)	RSS
[Alm19]	3D	4	13.3 – 16.6 W	IM	0.64 – 2.55 m	1 PIN	4×4 m^2	20.4 / 23.5 cm (p95)	RSS + CMD/LLS
[Knu20]	2D	4		FDMA	1.4 m	1 PD	3.5×3.5 m^2	17.07 cm (p95)	RSS + GP / MLP
[Hua21]	3D	4		QPSK + IM	1 m	1 PD	0.6×0.6 m^2	12 cm (p95)	RSSI + SVM
[Hos20]	2D	1			1.5 – 3 m	1 – 4 PDs	0.5×0.5 m^2	5 – 25 cm (average)	RSS + FP
[Zhu19]	3D	1	3.6 W		0.45 m	4 tilted PDs	0.3×0.3 m^2	2 cm (average)	AoA
[Kes18]	2D	4			5 m	2 PD	10×10 m^2	$<$ 60 cm (average)	RSS
[Lv17b]	3D	3	1 W		1.5 m	2 APD + reference detector	1×1 m^2	$<$ 10 cm (average)	RSS
[Ste18]	3D	4	1 W	OFDM	2 m	8 PDs with apertures	5×5 m^2	$<$ 20 cm (rMSE)	AoA

Chapter 3

Direct Positioning System: Configuration and Encoding Techniques

This chapter is focused on the implementation and the validation of a privacy-oriented Local Positioning system based on a set of four transmitting LEDs, acting as beacons at known positions, and on a unique QADA sensor, acting as the receiver to be positioned. This system has been intended for long-distance measurements (more than 3 m) and includes an ad hoc synchronization module that allows the receiver module to acquire only when new data are available, thus facilitating real-time operation. It is worth mentioning that it is not really necessary to perform a synchronisation between emitters and receiver, since it is only used to simplify the acquisition process. Instead of using it, we could identify that there is a signal to analyse when a change in the output sum signal of the QADA receiver is detected. The system is based on the reception and further processing of different encoded signals, emitted simultaneously by the aforementioned beacons.

The use of coding techniques is associated with an increase in the computational load of the receiving system due to the algorithms involved in the calculation of the correlation functions. In this way, the receiver system should be fast enough to acquire those signals and process them, as well as light, compact, of low consumption, and easy to transport. Therefore, the use of solutions based on ARM or STM32 architectures is interesting, compared to specific architectures designed with field-programmable gate arrays (FPGAs) devices, since, although the last ones are ideal for massive and parallel data processing, they usually present higher power consumption.

In the search for a centimetre-precise positioning system, it is important to consider the implemented medium access technique, often related to the modulation scheme used in the transmissions. Whereas there is a majority of works that uses On-Off Keying (OOK) modulations due to their simplicity, in [Shi15] a better performance in Visible Light Communications was obtained by using Binary Phase Shift Keying (BPSK) modulation.

In addition, several applications require encoding schemes, besides the modulation used, that allow simultaneous interference-free transmission so that the receiver is able to identify and separate each of the encoded signals. In this way and to overcome those drawbacks, there is a previous trend in the use

of pseudorandom sequences (PR), such as Gold [Yan18] or Kasami codes, as well as in complementary pairs of sequences (CSS) or sequences derived from them, such as LS (Loosely Synchronous) [Gar12] or T-ZCZ (Three Zero-Correlation Zones) [Zha05] codes.

In different works [Apa20b] [Apa19a], a systematic error in the estimation of the indoor location of the receiver appeared due to the Multiple Access Interference (MAI) effect. The MAI effect is generated due to the interference between the cross-correlation functions in the simultaneous reception of the codes. Different sequences are analysed in this chapter so that the MAI effect is minimized and hence the estimation of the receiver's location is improved. This analysis is underpinned by a successful validation of the proposal with simulated results.

This chapter is organized as follows: the first section provides the proposed system description including an in-depth detail of the transmitters' and receiver's modules, as well as the synchronization module implementation; the second section analyses different sequences in order to improve the receiver's location estimation and provides some simulated results; and the last section discusses some conclusions.

3.1 Proposed System

The proposed optical positioning system is based on a set of four LEDs (infrared or visible light) at 3D positions $\mathbf{b}_i$, located at known points in the environment, as well as a receiver and a synchronization module. The overall system is shown in Fig. 3.1.

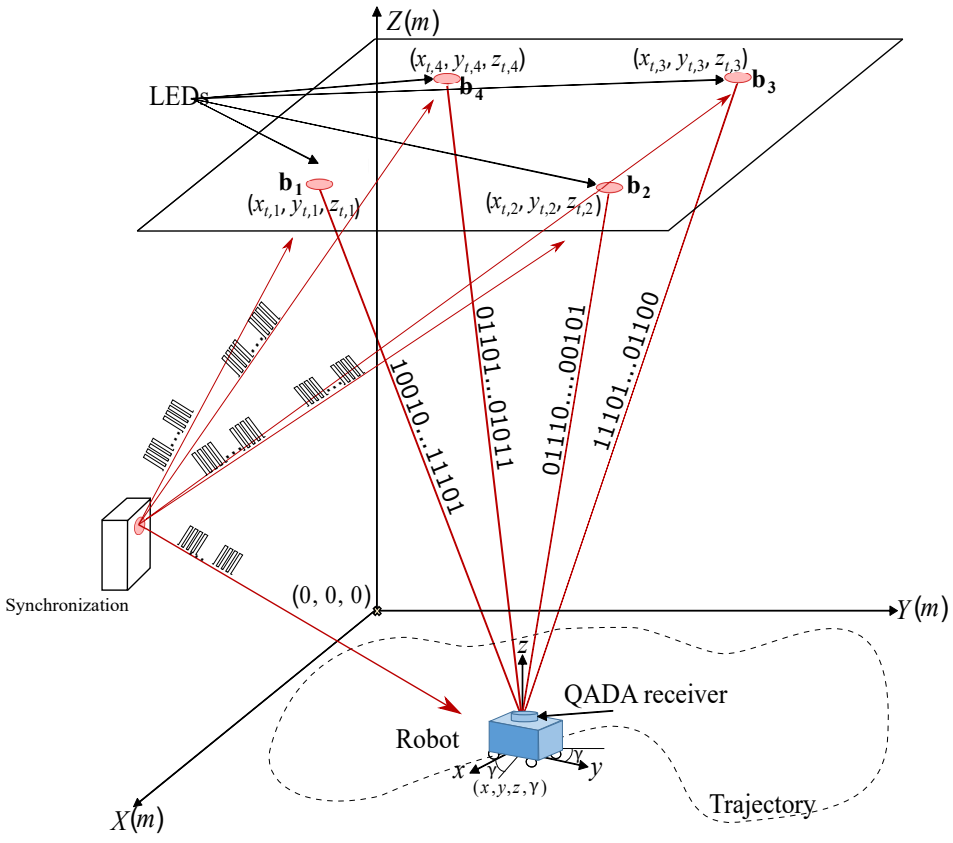

Figure 3.1: General diagram of the proposed positioning system.

The system consists of a synchronization system (a special beacon), which emits a 455 kHz IR carrier during 1 ms, periodically every 0.5 s. This signal is received by each one of the beacons, as well as by the reception module. The synchronization system easily covers large spaces with a single high-power LED emitter and a PLL receiver, since the receiver detects both LoS and NLoS signals. When a synchronization pulse is captured by both systems, transmissions and acquisition start simultaneously. Note that, as the speed of the light is very high, the transmissions from the beacons and the corresponding acquisition at the receiver happen at the same time for practical purposes. After the signal is acquired, it is transmitted through an Universal Serial Bus (USB) port to a computer, where it is processed to estimate the position of the receiver. This procedure allows the system to update the receiver position every 0.5 s.

The infrared synchronization module consists of a beacon (which emits a 1 ms - long pulse every 0.5 s) and of the photodetectors located both in the receiver and in the transmitters. The infrared transmitter located in the synchronization beacon is the ILH-IW01–85NL–SC201-WIR200 [Osl15], which has a 150 ° radiation angle and a central wavelength response of 850 nm. On the other hand, the receivers are based on the TSOP7000 infrared detector [Tel01], which is centered at a frequency f_{cSYN} = 455 kHz. After receiving the carrier from the synchronization beacon, the detector generates a pulse with the same length (1 ms). This pulse is received by the transmitters' and the receiver's module allowing simultaneous transmission and acquisition.

3.1.1 Transmitter Module

The transmitter's module consists of four beacons LED distributed in a certain space. Two types of emitted light are considered: visible and infrared light. It is assumed that transmitters present a Lambertian radiation pattern [Kah97], typical of LEDs and that they do not present any angle of rotation or inclination. In our case, LEDs are oriented so that their radiance is normal to the ceiling surface.

Both modules (infrared and visible light transmitters) use a BPSK (Binary Phase Shift Keying) modulation with a square carrier signal. The modulated signal emitted by the i-th emitter is given by (3.1):

$$\begin{aligned} m_i[n] &= c_i\left[\frac{n}{N_c \cdot M}\right] \cdot s[n] \\ for \quad n &= 0, 1, \ldots N_c \cdot M \cdot L - 1 \end{aligned} \tag{3.1}$$

Where $m_i[n]$ is the modulated signal in the discrete time domain n; $c_i[n]$ is the binary sequence used to encode the emission; L is the length of this sequence; and $s[n] = sin(2 \cdot \pi \cdot f_c \cdot n \cdot T_s)$ is the modulation carrier, with a symbol formed by N_c periods of the carrier, and $M = f_s / f_c$ samples per period. Note that f_c is the carrier frequency, whereas $f_s = 1/T_s$ is the sampling frequency.

Although all the transmitted codes are merged at the receiver, the use of a different code per beacon (see Fig. 3.2), with suitable cross-correlation properties, allows the later processing algorithm to discriminate the signals coming from each emitter and obtain the corresponding angle of incidence, intensity of the signal, *etcetera*, related to each beacon. In order to eliminate the effect of flickering with its consequent negative effects on health, a much higher carrier frequency than 200 Hz has been selected. In particular, the carrier frequency of the BPSK modulation is $f_c = 25$ kHz.

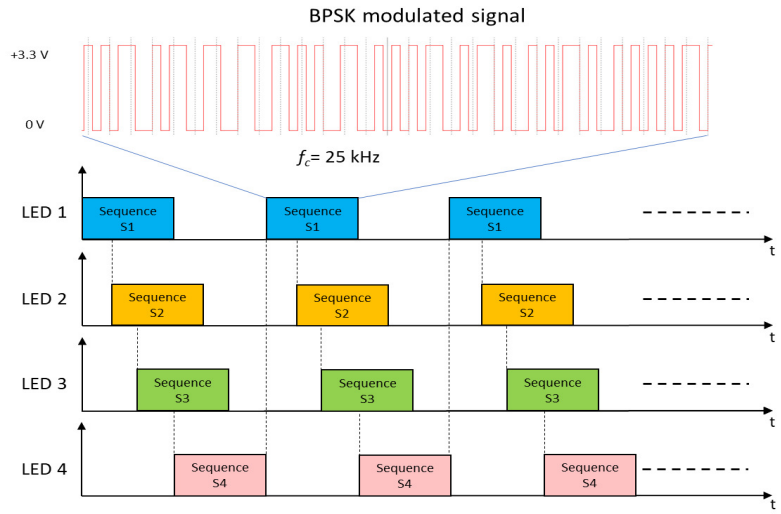

Figure 3.2: Global view of the transmission scheme for the codes c_i.

The transmission has been defined by using an oversampling of $M = f_s/f_c = 10$ samples for a carrier cycle (sampling frequency of $f_s = 250\,\text{kHz}$) and sequence shifting, which improves the cross-correlation properties of the codes at the receiver by minimizing the Multiple Access Interference (MAI) effect, produced by the simultaneous transmission and reception of all the sequences. The suitability of each sequence will be discussed in Section 3.2.

Visible Light Transmitters

On one hand, the visible light emitters are composed of five modules OVM12F3W7 (white, typical illumination 4 lx at 1 m and 1 lx at 2 m, 5000-7000 K) [Tec16] connected in parallel; each module has three LEDs in series. With a beam angle of 120 °, they emit 1.5 W whether a typical voltage of 12 V is applied. Hereinafter the LED lamp modules are going to be modelled as a point-like source. Those LED modules are excited individually with a particular 1023-bit Kasami code. This code c_i is transmitted to the LED lamp $\mathbf{b}_i$ by using a Blueboard LPC1768-H platform as presented in Fig. 3.3. Every resulting modulated signal is generated by a pin of a microcontroller port and drives each LED lamp through the VNP10N07FI [STM13] driver, based on a MOSFET capable of switching up to 50 kHz, as can be observed in Fig. 3.3. An AC/DC converter LD05-20B12 [Mor15] is included in every LED lamp, which allows the system to be directly connected to the electrical mains, and which provides a 12 V output, used to supply the LED lamps, as well as the microcontroller in the case of LED $i = 1$.

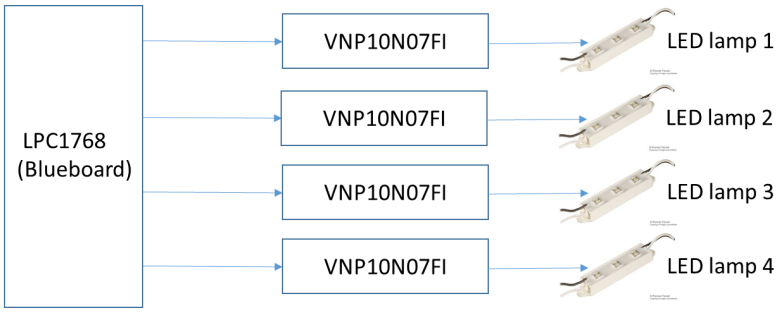

Figure 3.3: Block diagram of the VL transmission system.

Infrared Transmitters

On the other hand, the infrared emitters located in the transmission system are the same as those used in the synchronization module [Osl15]. In this case, the general operation of the system for beacon $\mathbf{b}_i$ is presented in Fig. 3.4, where each transmitter is individually driven by a microprocessor [Sem17], whose input signal is the pulse generated by the infrared detector whereas the output is the modulated sequence c_i to be transmitted. Every time the synchronization detector receives the carrier from the synchronization beacon, the transmission begins. The code c_i used for the i-th LED beacon is an 1151 bit LS sequence. The four codes c_i are emitted simultaneously by each LED, with a relative delay of 10 samples regarding the previous one, giving a total duration of 46.04 ms (1151 bits $\cdot \frac{1}{25kHz}$) for the whole transmitted signal (see Fig. 3.2).

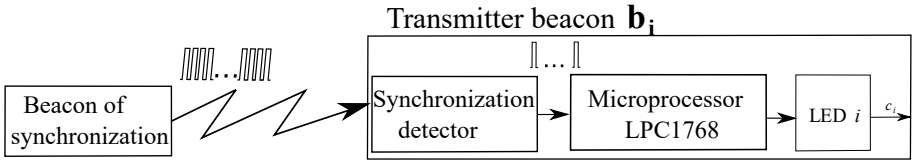

Figure 3.4: Block diagram of the IR transmission system.

3.1.2 Receiver Module

The reception module consists of a QADA circular photoreceptor QP50–6–18u–TO8 [Inc12], a filtering system, a synchronization signal detector and an acquisition system STM32F469I Discovery [STM15]. The general operation of the receiver system is shown in Fig. 3.5. Note that the acquisition system starts acquiring at the instant it receives the synchronization pulse from the corresponding detector. The signals to be acquired come from the signals measured by the QADA after being filtered. The acquired signals are sent through an USB port for further processing on a computer.

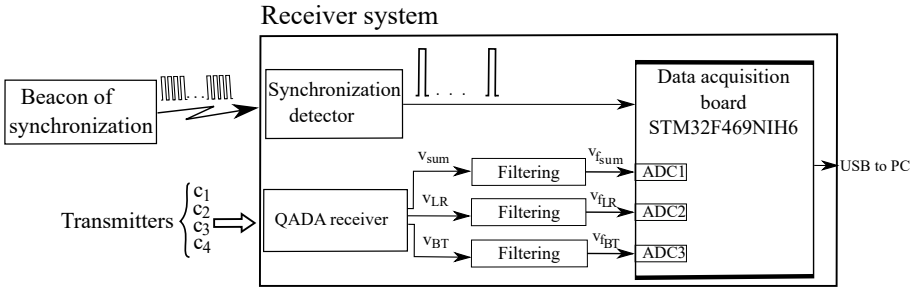

Figure 3.5: Block diagram of the reception system.

The QADA receiver is mounted in the QP50-6-18u-SD2 board [Inc12], it has a radius r = 3.9 mm, and an effective area of 11.78 mm^2. Its responsivity is 0.4 A/W and 0.65 A/W at a wavelength λ = 625 nm and λ = 950 nm, respectively; and the theoretical noise is 15 nV/$\sqrt{Hz}$ with a 15 V input signal. A square aperture made by 3D printing has been added to the photodiode array. Note that the aperture is fully aligned with the QADA sensor, so the centre of the aperture perfectly matches the centre of the QADA. The shape of the aperture has been chosen for the sake of simplifying the equations related to the estimation of the angle of incidence (compared to a circular aperture, for instance).

The operation principle of the proposal is based on the fact that the light coming from the emitters goes through the centre of the square aperture placed on the receiver and illuminates the array of photodiodes (see Fig. 3.6).

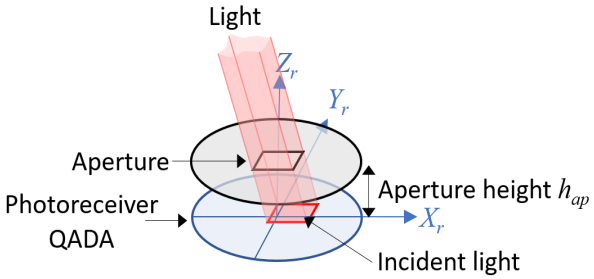

Figure 3.6: Geometrical representation of the quadrature angular diversity aperture (QADA) receiver.

The QADA is a photoreceptor divided into four quadrants, so that it generates three output signals according to the area illuminated in each of the quadrants, which depend on the angle of incidence from the received signal. These three signals are the global sum of the incident energy, v_{sum}; the voltage difference on the X axis (left-right), v_{LR}; and the voltage difference on the Y axis (bottom-top), v_{BT}.

A filtering and amplification stage is required before starting the acquisition process, with the aim of maximizing the amplitude of the received signals, as well as to reduce possible interference in the desired signal with the light coming from the windows and the room's own illumination. An inverted band-pass filter has been selected to eliminate undesired signals below 2 kHz and beyond 75 kHz. The diagram of the filtering and amplification stage for the signal v_{sum} can be observed in Fig. 3.7. Similar circuits are used for the signals v_{LR} and v_{BT}.

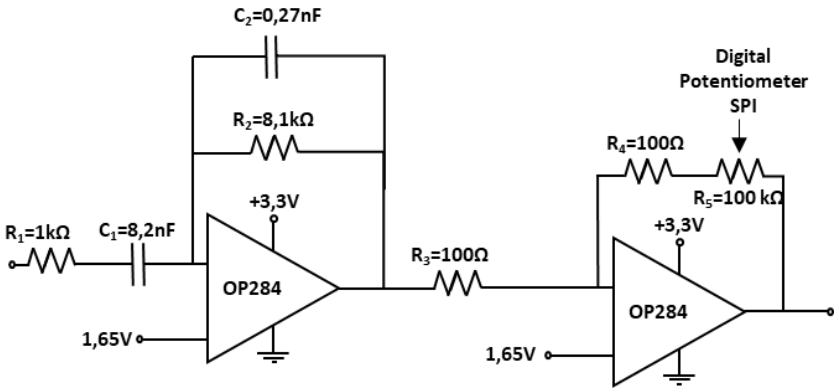

Figure 3.7: Circuit for the amplification and filtering of the received signal v_{sum}.

The acquisition system is based on a microcontroller STM32F469NIH6U, which manages an adjustable potentiometer [Inc03] included in the filtering and amplification system. Depending on the received signal amplitude ($maxValue$), the circuit gain is adjusted with this digital potentiometer controlled by a Serial Peripheral Interface (SPI) bus, increasing or decreasing the internal resistance ($StepValue$). As was shown in Fig. 3.5, three 12-bit Analog-to-Digital Converters (ADCs) are used in the acquisition of the signals, which have a maximum dynamic range of 4096, reduced to 4000 for security and to avoid introducing higher voltages than the maximum allowed at the input of the acquisition system.

With this objective, three ranges are defined to increase the gain of the signal to be filtered: the first range covers signal amplitudes up to 3000, where *StepValue* is increased by 20; the second range covers amplitudes from 3000 to 3500, where *StepValue* is increased by 10; and, finally, the third range contains amplitudes between 3500 and 4000, where *StepValue* is increased by 1. This process is independent for each channel, $v_{f_{sum}}$, $v_{f_{LR}}$ and $v_{f_{BT}}$, and is implemented in order to maximize the dynamic range of the used acquisition module. Note that the acquisition does not start and, therefore, the programmable resistance does not vary until the pulse of synchronization is detected. The flowchart explaining the interrupt service routine is presented in Fig. 3.8.

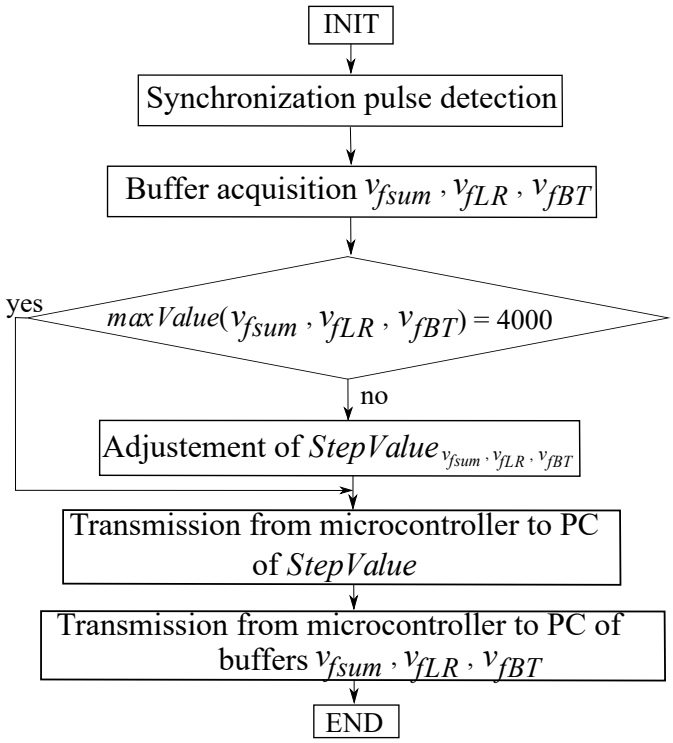

Figure 3.8: Flowchart of the acquisition process at the receiver.

The complete reception system has a power consumption of 0.23 A, with a voltage supply of 5 V. It is worth mentioning that, when the acquired signals are transmitted via the USB, the value of the gain used in the capture of those signals is also transmitted.

3.2 Encoding Techniques

The reception of the sequences can be altered by the MAI effect, as a result from the simultaneous transmission and reception, as well as due to limitations in the channel or the transmitters' bandwidth, interferences in the correlation of signals, *etcetera*. Furthermore, not all the sequences have the same correlation scheme (see Fig. 3.9), hence they behave differently against the MAI effect. Therefore, it is important to analyse those sequences that may minimize the MAI effect at reception, so that the final estimation of the receiver's position is improved.

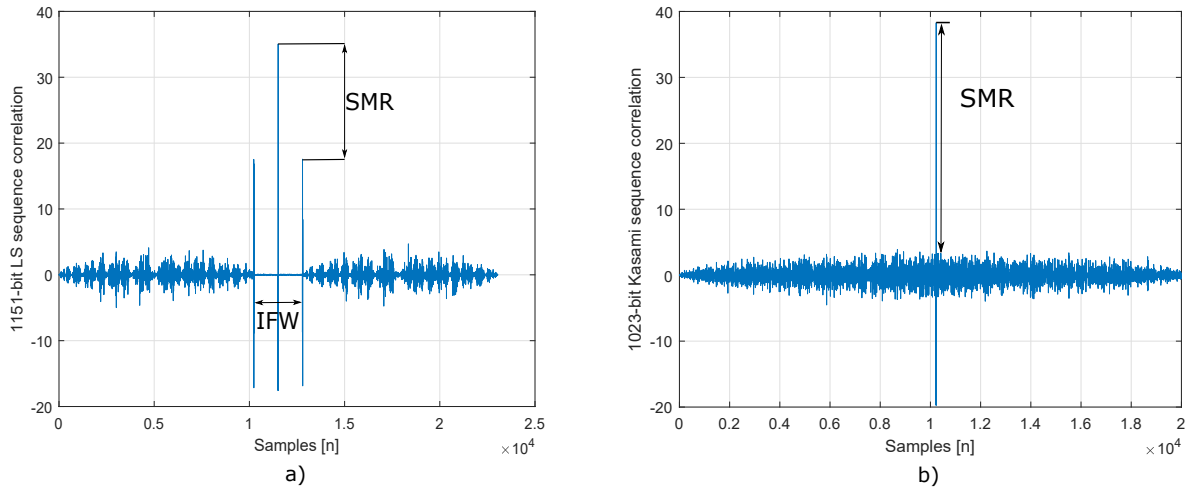

Figure 3.9: Example of auto-correlation functions: a) 1151-bit LS and b) 1023-bit Kasami.

It is worth mentioning that those sequences with more robust behaviour will often require complex transmission and reception schemes. The complexity of the schemes directly affects the time required for transmitting all the codes c_i and thus, the updating rate of positioning. Therefore, in order to be able to implement a real-time Local Positioning System, hereinafter complex sequences, such as Zadoff-Chu [Mur18], or multilevel [Gar12] sequences are not analysed.

In order to enhance the receiver's position estimation, it is essential to have a suitable correlation function. The Sidelobe-to-Mainlobe Ratio (SMR) is a parameter commonly related to the correlation functions (see Fig. 3.9) that is of great interest in the design of a sequence. A high value of SMR indicates that the main lobe may be confused with a sidelobe, thus resulting in inaccurate results. The behaviour of pseudo-random sequences, such as Kasami, as well as complementary pairs of sequences, such as LS sequences, is studied from the point of view of the SMR parameter, in order to determine their performance in the proposed system.

LS sequences have, in addition to low SMR, another relevant feature to consider: the Interference Free Window (IFW), which is a zone where the auto correlations and cross correlations are null. In particular, LS sequences present a zero-correlation zone around the origin (see Fig. 3.9.a). On the other hand, Kasami sequences have higher SMR than LS sequences (see Fig. 3.9.b). However, if not only the samples within the IFW are considered, then LS sequences present a higher SMR. In order to accurately determine the IFW of the sequence in a transmission, it is crucial to have a pseudo-synchronization between emitters and receivers.

The length of the IFW depends on the design of the sequence; for example, the 1151-bit LS sequence is based on two sets of 512-bits with 127 zeros in between [Per09], so the IFW is 127 long. There is a trade-off between maximizing the IFW and having an extremely long sequence. A consistent localization of the IFW is key to clearly detect the mainlobe of the correlation signal and, hence, have a low SMR. Note that there is a significant sidelobe at both ends of the IFW.

3.3 Experiments and Results

Hereinafter, Kasami and LS sequences are used in the estimation of the receiver's position. In simulations, the volume under analysis is $2 \times 2 \times 3.4\,\mathrm{m}^3$ (a distance of 3.4 m between transmitters and the plane where the receiver moves), the number of measurements per analysed point is 50 with a grid of points every 10 cm, and the Signal-to-Noise Ratio (SNR) is 10 dB. This value has been selected since it has been checked, in the experimental tests, that typical values of SNR in the environment are around 10 dB. The transmitters' positions are presented in Table 3.1. The receiver's position is estimated using angles of arrival measurements as detailed in Chapter 4.

Table 3.1: LED's coordinates considered in simulations.

LED i	**Coordinates** $(x_{t,i}, y_{t,i}, z_{t,i})$
LED 1	(1.33 m, 0.66 m, 3.40 m)
LED 2	(1.33 m, 1.33 m, 3.40 m)
LED 3	(0.66 m, 1.33 m, 3.40 m)
LED 4	(0.66 m, 0.66 m, 3.40 m)

A general analysis is detailed in Fig. 3.10, where the Cumulative Distribution Function (CDF) of the absolute position error for the three coordinates is presented for Kasami and LS sequences, according to their lengths L (255 and 1023 for Kasami, and 71, 287 and 1151 for LS). The 255-bit Kasami code results in the worst sequence to use. The 1023-bit Kasami code obatins absolute errors for coordinates x and y of almost 10 cm, whereas coordinate z has errors of 40 cm in the 90% of cases. On the other hand, it can be observed how the 1151-bit LS sequences achieve the best performance, where errors below 3 cm are achieved in the 90% of cases for coordinates x and y.

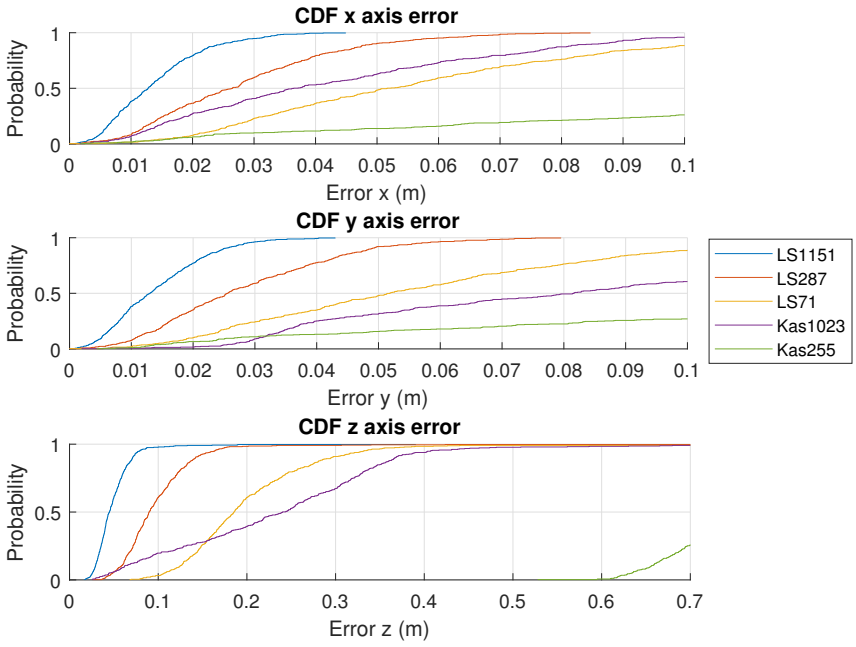

Figure 3.10: CDF for the absolute error in the estimation of the receiver's position in coordiantes x, y and z for different types of sequences.

It is worth mentioning that a sequence shifting or displacement can improve the cross-correlation properties of the codes at the receiver, as the time of arrival is considered to be the same for all the emissions. This sequence shifting actually implies a displacement of a certain number of samples in the emission from a LED c_i with regard to the previous one, thus avoiding a fully simultaneous transmission by all the transducers.

In order to clearly select the most suitable displacement for the 1151-bit LS sequence, the SMR of the different correlated signals with respect to the number of displaced samples is presented in Fig. 3.11 for each emitted code $i = \{1, 2, 3, 4\}$. The SMR parameter analysed in Fig. 3.11 is coming from the sum of the auto-correlation of code i plus the cross-correlations of the other three codes. Therefore, the SMR is obtained over the received signal involving the four LED transmissions. In this proposal, we have considered the whole sequence (not only the IFW) in the estimation of the SMR, which is the worst possible scenario. Anyway, this LPS application deals with transmissions arriving inside the IFW, which means that normal operation conditions are more favourable than those shown in Fig. 3.11. It can be observed that whether the selected displacement is ten samples or higher, the SMR remains constant at SMR $= 0.5$.

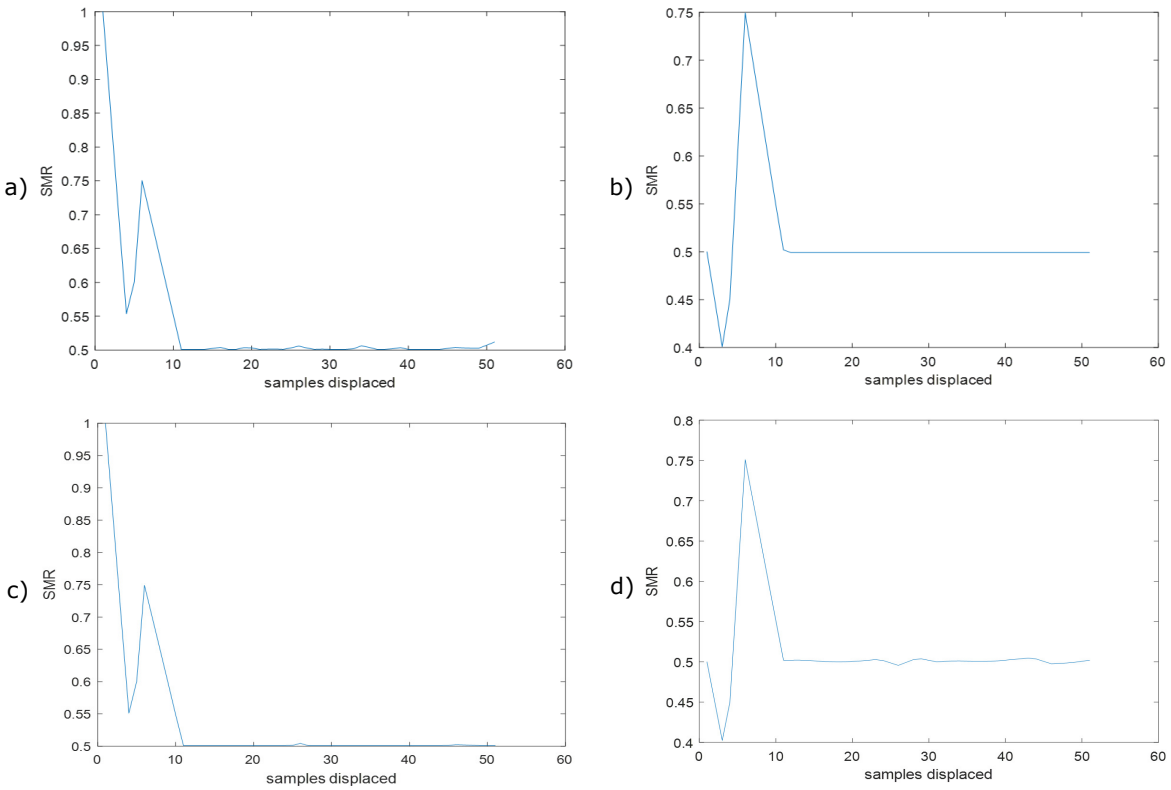

Figure 3.11: SMR analysis for 1151-bit LS codes with different displacements for codes i: a) $i = 1$; b) $i = 2$; c) $i = 3$; d) $i = 4$.

On the other hand, the number of zeros within the IFW of the LS sequence can also be varied. In this way, Fig. 3.12 presents the SMR of code $i = 4$ when the number of zeros in the IFW is varied from 1 up to 127 (which is the so called 1151-bit LS sequence) with respect to the number of displaced samples. There is no substantial difference between the simulated curves.

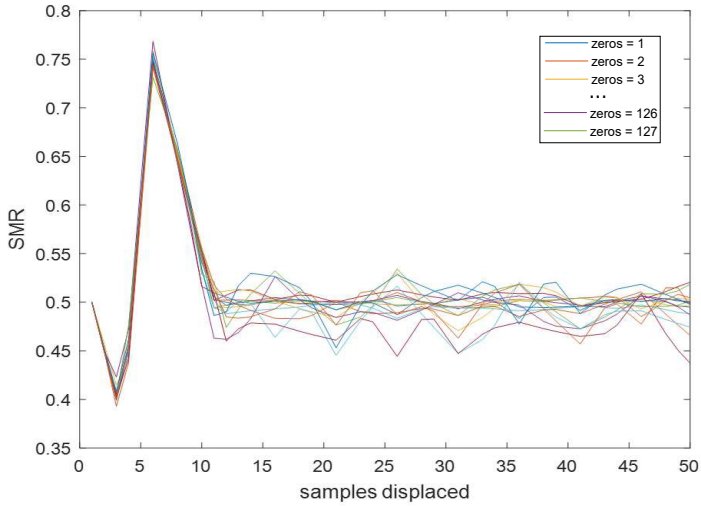

Figure 3.12: SMR analisis for code $i = 4$ varying the number of zeros in the LS sequence.

In addition to the previous analysis, in Fig. 3.13 an 1151-bit LS sequence with displacements of 3, 4, 10, 12 and 15 samples is considered to estimate the receiver's position. Fig. 3.13.a) plots the global CDF, whereas Fig. 3.13.b) is a particular zoom. It can be observed that at the 90% of the CDF the obtained absolute error values are 1.8 - 2 cm, achieving the best performance when the sequence is shifted ten samples. Therefore, hereinafter a 1151-bit LS sequence with a displacement of ten samples is considered. This encoding scheme has been applied to every transmission coming from each LED lamp, so that they can be identified by the receiver, thus providing multiple access capability and a significant improvement of the system to deal with low SNR, and different types of hindering phenomena, such as multipath and near-far effect. The receiver's position is estimated using the AoA algorithm described in Chapter 4.

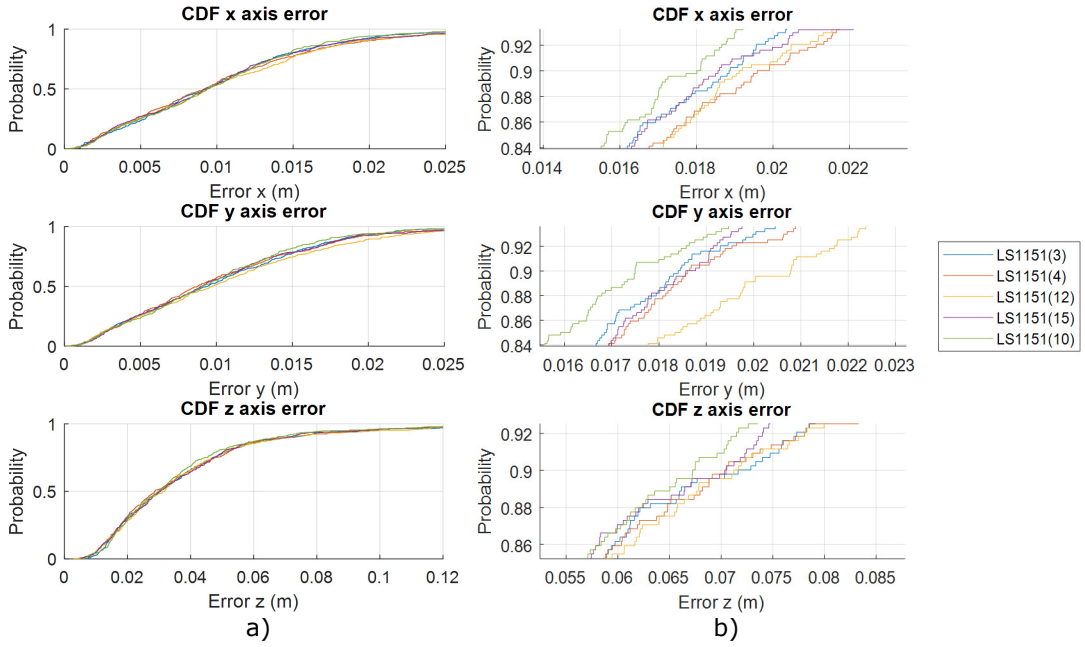

Figure 3.13: CDF for the absolute error in the estimation of the receiver's position in coordinates x, y and z using a 1151-bit LS sequence with a displacement of 3, 4, 10, 12 and 15 samples.

A similar analysis has been performed for the Kasami sequences. In Fig. 3.14 the CDF is presented for the absolute errors for coordinates x and y, where the displacement in the transmission of sequences is varied from the full code ($M \cdot L$) up to a thirty second part of $M \cdot L$ ($M \cdot L/32$). Only the 1023-bit Kasami sequence has been analysed in this work since those Kasami sequences with lower lengths had a remarkably worst behaviour (see Fig. 3.10). It is worth nothing that there is no correspondence between more displacement and less absolute error. Note that a displacement of $M \cdot L/32$ requires a shift of 319 samples for a 1023-Kassami sequence with an oversampling $M = 10$. Five samples (half a modulation symbol, $M/2$) have been considered to be a suitable trade-off between minimizing the positioning error and having a simultaneous transmission.

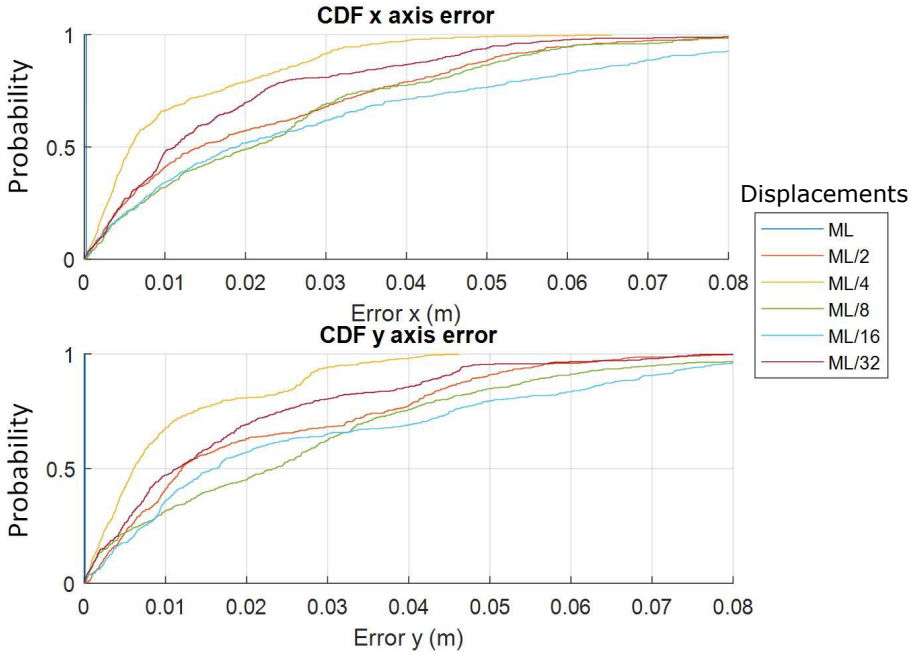

Figure 3.14: CDF of the absolute errors in the analysis of samples displacement for coordinates x and y using a 1023-bit Kasami sequence.

On the other hand, in Section 4.3 it will be shown that the lowest and the highest errors in the estimation of the receiver's position, whether there is a rotation in the Z axis, occurs when the receiver is rotated 5° and 45° for the first quadrant, respectively. The study of a quadrant in the proposed scenario can be extended to the rest of the grid due to the symmetry existing in the transmitters' arrangement. Therefore, six points have been analysed in the proposed scenario when the transmitters are located at $z_t = \{2\,\text{m}, 3.4\,\text{m}\}$ and for both rotational angles $\gamma = 5°, 45°$. Figs. 3.15 and 3.16 depict the position estimates, using a 1151-bit LS sequence with a displacement of 10 samples and a 1023-bit Kasami with a displacement of 5 samples, respectively. The SNR is 10 dB. The black crosses represent the projection of the LED's coordinates; the red crosses are the ground-truth of the measurements; and the coloured point clouds are the estimated receiver's position. An error ellipsoid is also plotted with 95% of confidence for every test point.

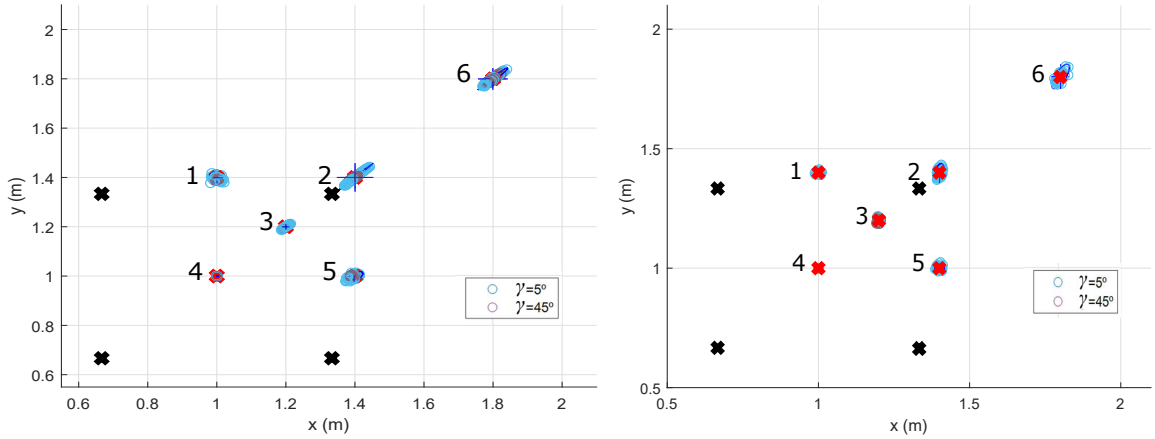

Figure 3.15: Simulated position estimates for $\gamma = 5°, 45°$ with the transmission of a 1151-bit LS sequence with a displacement of 10 samples for: a) $z_t = 2\,\text{m}$; and b) $z_t = 3.4\,\text{m}$.

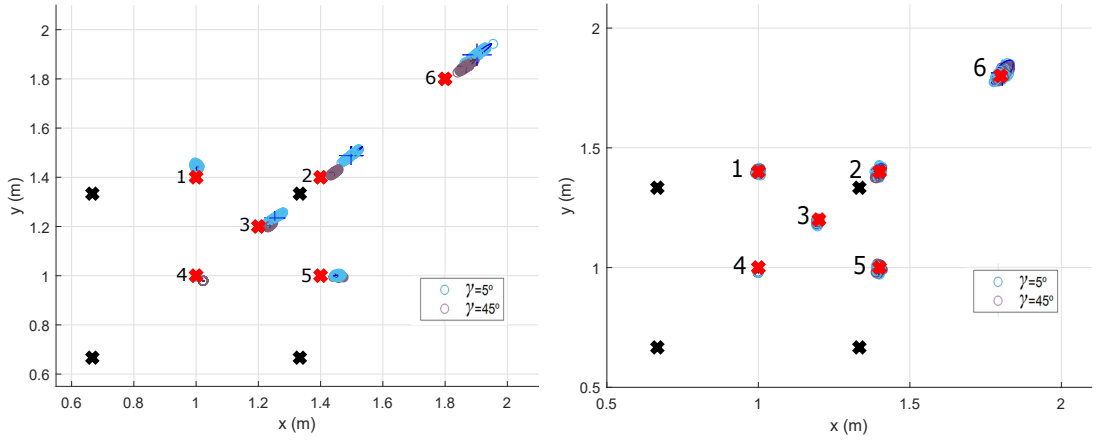

Figure 3.16: Simulated position estimates for $\gamma = 5°, 45°$ with the transmission of a 1023-bit Kasami sequence with a displacement of 5 samples for: a) $z_t = 2\,\text{m}$ and b) $z_t = 3.4\,\text{m}$.

It can be observed that the centres of the error ellipsoids in the estimated points in Fig. 3.16.a) do not match the ground-truth (GT) in any of the proposed polar angles. In fact, the absolute errors in the corners of the grid are noticeable compared to those obtained in the centre of the grid (see point 6 versus point 4). On the other hand, in Fig. 3.15 the absolute error is highly decreased and, thus, the MAI effect present in Fig. 3.16 is nearly discarded. This improvement has been achieved through the use of a robust sequence against MAI, such as the 1151-bit LS sequence with a displacement of 10 samples. The values of the average absolute error and the standard deviation for the six points analysed for every angle and every sequence are further detailed in Tables 3.2 to 3.5 and in the box diagram presented in Fig. 3.17. It is noticeable that, although the standard deviation remains very similar in both cases, whether the LS sequence is used in the transmission, the absolute errors in the estimation of the different coordinates are highly decreased. In particular, the proposal achieves average absolute positioning errors at a height of 3.40 m of 0.07 cm and 0.28 cm; 0.10 cm and 0.89 cm; and 0.75 cm and 11.36 cm for the LS and the Kasami sequences in the coordinates x, y and z, respectively. The standard deviations are similar, achieving values of 0.50 cm and 0.85 cm in coordinates x and y for both sequences, and, 6.4 cm and 6.2 cm in coordinate z for the LS and the Kasami sequences, respectively.

Table 3.2: Simulated average absolute error and standard deviation for the analysed points with a 1023-bit Kasami sequence for $z_t = 2\,\text{m}$.

		Average absolute error			**Standard deviation**		
Points	γ**(º)**	***X (cm)***	***Y (cm)***	***Z (cm)***	***X (cm)***	***Y (cm)***	***Z (cm)***
Point 1	5º	0.27	4.55	14.92	0.22	0.49	1.44
	45º	0.40	4.26	18.42	0.23	0.64	2.37
Point 2	5º	9.63	8.66	39.20	1.37	1.30	11.25
	45º	4.50	2.04	5.25	0.58	0.52	3.96
Point 3	5º	5.52	3.68	16.62	1.32	1.11	5.82
	45º	3.69	0.35	18.61	0.34	0.25	3.84
Point 4	5º	0.40	0.38	14.13	0.02	0.02	1.73
	45º	2.27	2.09	14.63	0.02	0.02	1.73
Point 5	5º	5.45	0.23	15.34	0.54	0.18	1.58
	45º	5.75	0.31	20.17	0.58	0.20	2.28
Point 6	5º	10.59	10.07	25.58	1.58	1.58	4.26
	45º	6.86	5.26	14.46	1.00	0.94	2.77
Total		4.61	3.49	18.11	0.65	0.60	3.59

Table 3.3: Simulated average absolute error and standard deviation for the analysed points with a 1023-bit Kasami sequence for $z_t = 3.4\,\text{m}$.

		Average absolute error			**Standard deviation**		
Points	γ**(º)**	***X (cm)***	***Y (cm)***	***Z (cm)***	***X (cm)***	***Y (cm)***	***Z (cm)***
Point 1	5º	0.01	0.16	20.39	0.42	0.66	5.34
	45º	0.01	0.21	20.78	0.39	0.51	4.40
Point 2	5º	0.21	0.12	14.24	0.59	1.18	12.52
	45º	0.20	0.20	17.62	0.51	1.04	11.36
Point 3	5º	0.33	0.72	18.96	0.28	0.60	6.77
	45º	0.36	0.79	18.58	0.25	0.61	6.65
Point 4	5º	0.07	2.01	9.31	0.05	0.06	4.65
	45º	0.07	2.01	8.13	0.05	0.06	3.95
Point 5	5º	0.25	0.89	0.12	0.54	0.87	4.42
	45º	0.29	0.56	0.03	0.49	1.01	3.82
Point 6	5º	0.50	1.30	3.18	1.28	1.89	6.98
	45º	1.03	1.69	4.97	1.16	1.68	5.90
Total		0.28	0.89	11.36	0.50	0.85	6.40

Table 3.4: Simulated average absolute error and standard deviation for the analysed points with a 1151-bit LS sequence for $z_t = 2\,\text{m}$.

		Average absolute error			**Standard deviation**		
Points	γ(°)	***X (cm)***	***Y (cm)***	***Z (cm)***	***X (cm)***	***Y (cm)***	***Z (cm)***
Point 1	5°	0.56	0.71	1.79	0.53	0.51	1.25
	45°	0.22	0.52	1.88	0.16	0.37	1.41
Point 2	5°	1.58	1.73	32.00	1.05	1.12	43.00
	45°	0.44	0.41	13.06	0.33	0.31	18.27
Point 3	5°	0.41	0.37	3.27	0.35	0.33	2.63
	45°	0.29	0.28	2.33	0.20	0.19	1.62
Point 4	5°	0.01	0.01	1.40	0.01	0.01	1.02
	45°	0.01	0.01	1.23	0.01	0.01	1.02
Point 5	5°	0.64	0.60	1.58	0.50	0.55	1.27
	45°	0.39	0.21	1.42	0.30	0.16	1.09
Point 6	5°	1.44	1.39	3.73	0.90	0.86	2.56
	45°	0.79	0.81	2.20	0.55	0.54	1.53
Total		0.57	0.59	5.49	0.41	0.41	6.39

Table 3.5: Simulated average absolute error and standard deviation for the analysed points with a 1151-bit LS sequence for $z_t = 3.4\,\text{m}$

		Average absolute error			**Standard deviation**		
Points	γ(°)	***X (cm)***	***Y (cm)***	***Z (cm)***	***X (cm)***	***Y (cm)***	***Z (cm)***
Point 1	5°	0.09	0.11	0.96	0.36	0.52	4.24
	45°	0.11	0.01	0.02	0.41	0.51	4.19
Point 2	5°	0.03	0.12	1.30	0.61	1.01	15.16
	45°	0.02	0.06	0.39	0.69	1.17	12.47
Point 3	5°	0.11	0.06	1.94	0.28	0.62	4.50
	45°	0.07	0.07	0.50	0.31	0.66	4.79
Point 4	5°	0.01	0.01	0.65	0.01	0.01	3.47
	45°	0.01	0.00	0.52	0.01	0.01	3.53
Point 5	5°	0.01	0.09	0.15	0.45	0.67	3.73
	45°	0.03	0.07	0.28	0.50	0.62	4.23
Point 6	5°	0.12	0.16	0.88	1.22	2.13	7.03
	45°	0.25	0.47	1.35	1.14	2.05	7.01
Total		0.07	0.10	0.77	0.50	0.83	6.20

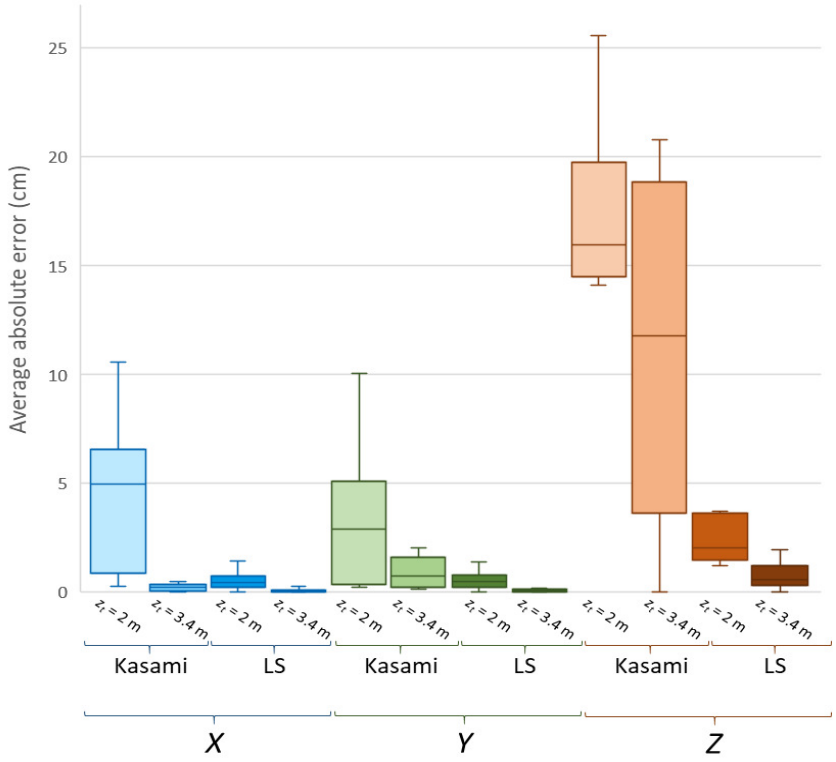

Figure 3.17: Average absolute error for the analysed points in simulation with a 1023-bit Kasami and 1151-bit LS sequence for $z_t = 2\,\text{m}$ and $z_t = 3.4\,\text{m}$.

3.4 Conclusions

In this chapter, the implementation of the direct 3D Infrared or Visible Light Positioning system has been described. Here some partial conclusions are listed:

- The proposed system is based on a set of four LEDs (infrared or visible light), located at known points in the environment, as well as a receiver and a synchronization module.
  - The transmitter system is based on four transmitter beacons, each one of them emitting a particular BPSK modulated signals using either Kasami or LS sequences. The carrier frequency has been established at 25 kHz, which is much higher than the detectable by human eyes (200 Hz), in order to eliminate any possible flickering.
  - The reception module consists of a QADA photoreceptor, a filtering system and an acquisition system. The filtering system eliminates undesired signals below 2 kHz and beyond 75 kHz. Regarding the acquisition system, the circuit gain is adjusted with a digital potentiometer controlled by a SPI bus to maximize the dynamic range of the used acquisition module.
  - The synchronism system is based on a particular IR beacon and a photodetector. These synchronism detectors are located in the receiving module and in every transmitting beacon, thus allowing a simultaneous reception and transmission.
- The behaviour of different sequences has been analysed to improve the performance of the proposal and with the final aim of decreasing the MAI effect that can alter the reception of the

sequences. In this way, the SMR and the IFW have been studied for Kasami and LS sequences in a scenario of $2 \times 2\,\mathrm{m}^2$. Sequence shifting has also been analysed to improve the cross-correlation properties of the codes. In particular, a 1023-bit Kasami sequence with a displacement of 5 samples and a 1151-bit LS sequence with a displacement of 10 samples have been considered to be a suitable trade-off between minimizing the positioning error and having a simultaneous transmission.

- The proposal achieves average absolute positioning errors at a height of 3.40 m of 0.07 cm and 0.28 cm; 0.10 cm and 0.89 cm; and 0.75 cm and 11.36 cm for the LS and the Kasami sequences in the coordinates x, y and z, respectively. The standard deviations are similar for both sequences, achieving values below 1 cm in the x and y coordinates, and below 6.4 cm in the z coordinate.

The next chapter will detail different algorithms to estimate first, the image points of the transmitters' projection onto the QADA receiver and, later, the receiver's pose by means of AoA measurements and an algorithm based on trilateration and another based on homographic techniques. Some simulated results will also be presented and discussed.

Chapter 4

Direct Positioning System: Calibration and Positioning Algorithms

In the previous chapter, we analysed the implementation of a 3D Infrared or Visible Light Positioning system based on a set of four LEDs, located at known points in a large indoor environment, as well as a receiver and a synchronization module. It is worth noting that these systems face important challenges, such as very high dynamic ranges with low Signal-to-Noise Ratios (SNR) when the coverage area is increased, Multiple Access Interference (MAI), multipath and near-far effects, calibration issues (misalignments in the receiver and other intrinsic parameters), and so on. In this way, it is crucial that the implemented algorithms deal with those challenges. In order to improve the performance of the proposal, we studied the use of encoding techniques to deal with the simultaneous emission of all the transmitted signals at the receiver's processing stage. In particular, the behaviour of Kasami and LS sequences were analysed finding the use of an 1151-bit LS sequence with a displacement of 10 samples to be a suitable trade-off between minimizing the positioning error and having a simultaneous transmission.

In this chapter, we present the estimation of the image points at the receiver, under non-linear and linear constraints, depending on the aperture size, to enlarge the emitter-receiver range, thus increasing the total coverage space, while dealing with the aforementioned challenges. This chapter also describes different solutions to estimate the final receiver's position by means of an Angles of Arrival (AoA) algorithm or using homographic techniques that solve the Perspective-n-Point (PnP) problem of the proposed pin-hole system. Regarding the homographic techniques, we have analysed the implementation of Efficient Perspective-n-Point Camera Pose Estimation (EPnP), Infinitesimal Plane-Based Pose Estimation (IPPE) and Robust Non-Iterative Solution of Perspective-n-Point (RPnP) solutions.

As for the system characterization, the different measurements and analysis carried out here assume that the transmitters are placed on the ceiling, whereas the receiver can move on a certain plane (e.g. the floor). Thus, the transmitters are neither rotated nor tilted, and the receiver is supposed to be parallel to plain containing the transmitters, although it can have any rotation in the Z axis. Besides, in order to properly position the receiver, at least three emitters must be detected in the QADA receiver. In this way, the proposed system might be applied in its current configuration as a 2D IRLPS to obtain the pose

of a mobile robot moving on a horizontal floor (x, y, γ) in large spaces in the XY plane, thus reducing the complexity of estimating the coordinate z, where a high uncertainty is expected due to the configuration of emitters. Nevertheless, further improvements in terms of more degrees of freedom can also be derived. In particular, in the current configuration, the transmitters are located on the same plane, what can be released if homographic algorithms are used. For instance, the EPnP and RPnP algorithms can deal with non-planar cases, although at the cost of increasing the number of transmitters. Similarly, another possible enhancement is related to the plane where the receiver is located. The proposed 2D IRPS or VLPS can be extended to obtain the 3D pose of a mobile drone $(x, y, z, \alpha, \beta, \gamma)$ by using planar or non-planar PnP algorithms, but at the expense of decreasing the accuracy, due to the low number of emitters used.

The studies presented in this chapter are carried out at two different heights depending on the experimental environment in which they have been validated. The first scenario is a room of $2\times\ 2\,\mathrm{m}^2$ and the transmitters are placed at a height of 1 or 2 meters, whereas the second scenario is a room of $2\times\ 2\,\mathrm{m}^2$ and the transmitters are located at a height of 3.4 m.

This chapter is organized as follows: the first section provides an introduction to the global processing block diagram proposed for estimating the receiver's position; the second section details the proposed non-linear algorithm, and the constraints to linearize it, to estimate the image points at the receiver; the third section provides the proposed algorithm to estimate the final coordinates of the receiver using an AoA algorithm or homographic techniques, as well as the simulated results for both solutions; the fourth section details the calibration algorithm; and the last section concludes the chapter.

4.1 General Processing Diagram

Fig. 4.1 details the general processing block diagram proposed for the receiver's position estimation. The LEDs located on the ceiling emit an LS sequence. Each LED transmits its own code so that the emitted signals can be identified at the receiver. Note that between each transmission there is a slight displacement to reduce the MAI effect, as detailed in Chapter 3.

At the receiver, all the emitted codes are detected. The receiver is a quadrant photodiode QADA QP50–6–18u–TO8 [Inc12] that has four output signals, one per quadrant. These four signals are combined to provide the sum of all quadrant signals (v_{sum}) and two difference signals for the X axis, left-right, (v_{LR}) and the Y axis, bottom-top, (v_{BT}). Those three output signals are filtered, amplified and then acquired with the module STM32F469I Discovery [STM15], and finally stored.

Each of the stored signals (v_{sum}, v_{BT} and v_{LR}) passes through a correlation bank where they are correlated with each of the emitted LS sequences c_i (match filtering), which are also stored in the receiver, being i the i-th emitter. The correlated signals coming from the correlation of v_{sum}, v_{BT} and v_{LR} with the emitted codes are defined as s_i, t_i and r_i, respectively.

Each correlated signal (s_i, t_i and r_i) has a maximum peak per LED i. In order to clearly detect all the maximum peaks, we first select the maximum peaks of the sum signals s_i and, later, the other maximum peaks of the signals t_i and r_i are obtained according to the displacements between the transmitted codes.

Afterwards, the image points $(x_{r,i}, y_{r,i})$ are estimated by means of a non-linear or a linear algorithm, where the use of each one depends on the length of the aperture, which is highly dependent on the volume coverage. It is worth noting that the linear algorithm estimate the image points using the ratios

$p_{x,i}$ and $p_{y,i}$ obtained from the peaks of the correlated signals and the intrinsic parameters of a pin-hole system, such as the optical centre, the height at which the aperture is located, the aperture misalignment and the length of the aperture.

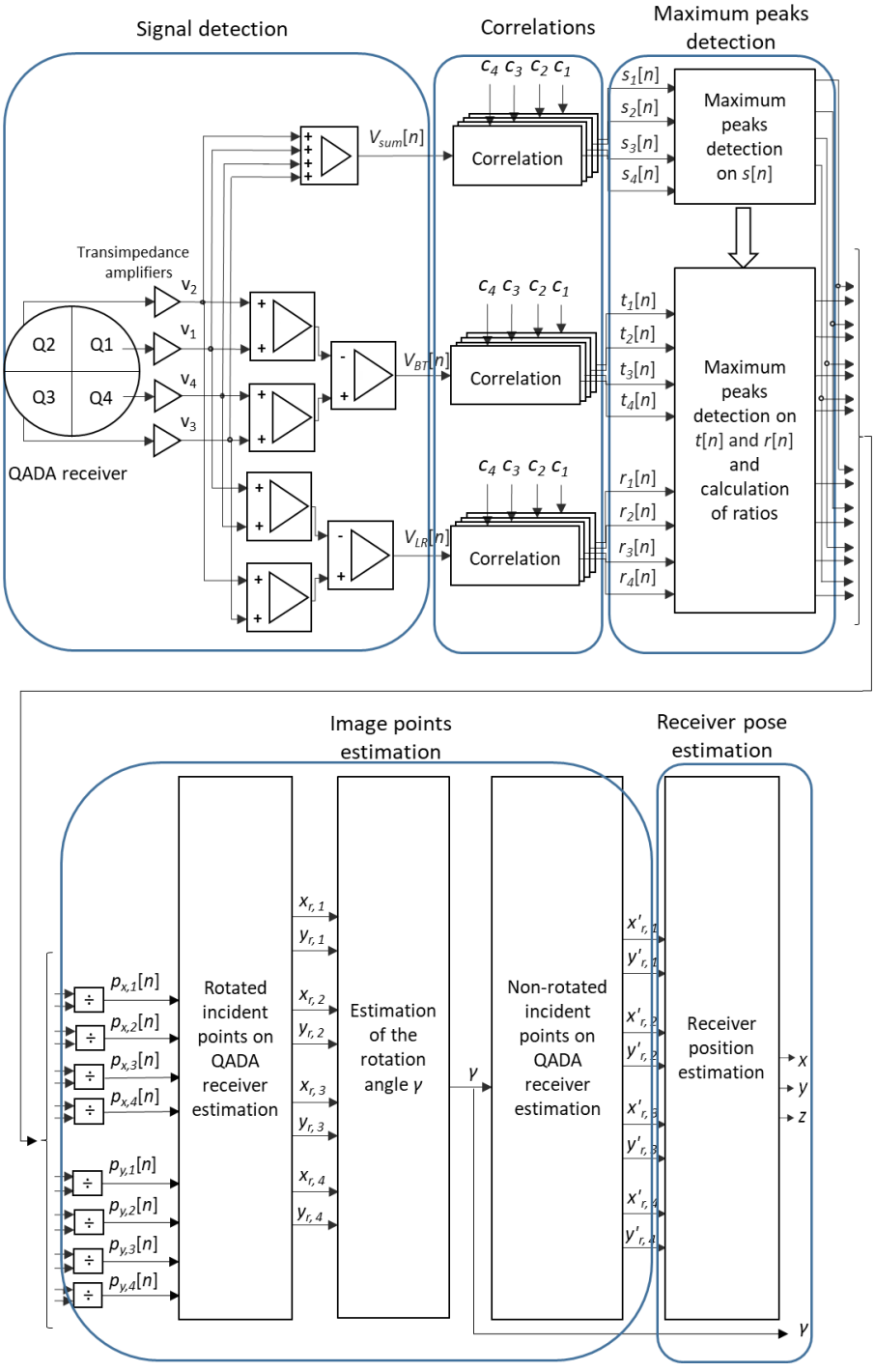

Figure 4.1: Global processing proposed for the receiver's position estimation.

After estimating every image point for each transmitter $(x_{r,i}, y_{r,i})$, the algorithm detects the rotation γ of the receiver around the Z axis. Since the transmitters are arranged in a square geometry, the image points on the QADA receiver should present the same shape. If the receiver is rotated a certain angle γ around the Z axis, the image points will be also rotated γ degrees around the Z axis. In this way,

trigonometric equations are used to estimate the current rotation angle γ by using the rotated image points $(x_{r,i}, y_{r,i})$.

Then, the image points $(x_{r,i}, y_{r,i})$ are rotated $-\gamma$ degrees to undo the rotation of the receiver and find the non-rotated image points $(x'_{r,i}, y'_{r,i})$. This step is crucial since the following algorithm does not operate properly whether the receiver is rotated.

Once the image points are rotated $-\gamma$, the positioning algorithm continues to the final estimation of the receiver's position in the proposed scenario. There are different approaches to estimate the receiver's position, in this chapter we present an AoA algorithm and different PnP solutions. Regarding the AoA algorithm, the positioning algorithm estimates the receiver's position (x, y) in the proposed scenario by means of a Least Squares Estimator (LSE). After estimating the receiver's position (x, y), the coordinate z is obtained by taking into account the trigonometric considerations that involve the incident angle and the distances between the estimated receiver's position and the projection of each transmitter i on the plane where the receiver is placed. On the other hand, regarding the homographic techniques, different PnP solutions, such as EPnP, IPPE and RPnP, can be directly applied to estimate the pose of the receiver in the proposed scenario. The input of these algorithms are the image points $(x_r, y_r)_i$, the focal length h_{ap} and the beacons' position $(x_t, y_t, z_t)_i$, whereas the output of the PnP solutions is the complete 3D pose of the receiver $(x, y, z, \alpha, \beta, \gamma)$.

4.2 Proposed Image Points Estimation at the Receiver

The principle of operation in the proposal is based on the fact that the light coming from the LEDs goes through the square aperture, and lights the QADA photoreceiver (see Fig. 4.2).

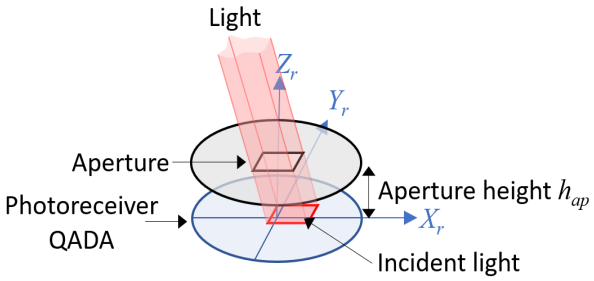

Figure 4.2: Geometrical representation of the incident light in the QADA sensor.

Note that the aperture is fully aligned with the QADA sensor, and the centre of the aperture perfectly matches the centre of the QADA. The central point of the illuminated area is of special interest and corresponds to the ray that crosses the center of the aperture. The analysis described hereinafter is detailed for one LED i, although it can be similarly extended to the rest of them.

According to the incidence angle, different areas are illuminated by each one of the different photodiodes. Fig. 4.3 shows the four quadrants $k = \{1,2,3,4\}$ and their areas A_k covered by the beam of light that passes through the aperture for the case of an incident ray with a central impact point (x_r, y_r).

The incident light generates four different currents $i_k(t)$, one for every quadrant $k = \{1,2,3,4\}$ that are combined to provide the sum of all quadrant signals (v_{sum}) and two difference signals, bottom minus top for the Y axis (v_{BT}) and left minus right for the X axis (v_{LR}). Note that all quadrants must be illuminated in order to estimate the incident point.

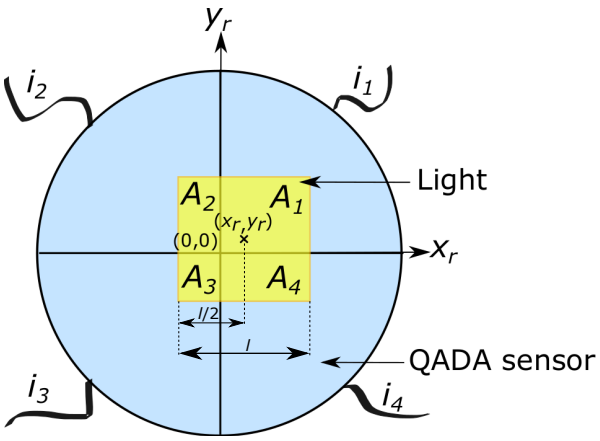

Figure 4.3: Incident light in the QADA sensor.

Without noise, the currents $i_k(t)$ generated by each quadrant k can be considered proportional to the lighted areas A_k(t) from the different quadrants. In this way, the ratios $p_x(t)$ and $p_y(t)$ can be defined as a function of the areas $A_k(t)$ from every quadrant k, as denoted in (4.1) and (4.2).

$$p_x(t) = \frac{v_{LR}(t)}{v_{sum}(t)} = \frac{A_2(t) + A_3(t) - A_1(t) - A_4(t)}{A_1(t) + A_2(t) + A_3(t) + A_4(t)}, \forall x \tag{4.1}$$

$$p_y(t) = \frac{v_{BT}(t)}{v_{sum}(t)} = \frac{A_3(t) + A_4(t) - A_1(t) - A_2(t)}{A_1(t) + A_2(t) + A_3(t) + A_4(t)}, \forall y \tag{4.2}$$

Where $v_{sum}(t) = \sum_{k=1}^{4} v_k(t)$; $v_{LR}(t) = (v_2(t) + v_3(t)) - (v_1(t) + v_4(t))$; and $v_{BT}(t) = (v_3(t) + v_4(t)) - (v_1(t) + v_2(t))$. Note that these output voltages provided by the QADA receiver are coming from the currents i_k(t) obtained by the different photodiodes, transformed into the voltages v_k(t) by means of transimpedance amplifiers.

Once these three signals are obtained, the system correlates the acquired signals with the transmitted codes c_i in the discrete time, so that every signal coming from each transmitter can be identified, while minimizing other impairment signals (noise, ambient light, incoming sunlight, etc.). It is worth noting that the receiver detects all the transmitted codes simultaneously.

In addition to (4.1) and (4.2), the ratios p_x and p_y can also be obtained by combining the maximum values of the correlated signals $s_i[n]$, $t_i[n]$ and $r_i[n]$, as presented in (4.3) and (4.4).

$$p_x = \frac{max(r_i[n])}{max(s_i[n])} \tag{4.3}$$

$$p_y = \frac{max(t_i[n])}{max(s_i[n])} \tag{4.4}$$

Where $t_i[n]$ is the correlation between the received signal v_{LR} and the LS sequence $c_i[n]$; $s_i[n]$ is the correlation between the received signal v_{sum} and the sequence $c_i[n]$; and $r_i[n]$ is the correlation between the received signal $v_{LR}[n]$ and the sequence $c_i[n]$ for every LED i, respectively. Note that since $s_i[n]$, $t_i[n]$ and $r_i[n]$ are the correlated signals, their maximum peaks are a representation of the energy received from each transmitter i for the three received signals v_{sum}, v_{BT} and v_{LR}, respectively.

Fig. 4.4 shows an example of the theoretical above-mentioned correlations at a particular point of the space near LED $i = 1$ with the position of the LEDs $i = \{1, 2, 3, 4\}$ given by Table 4.1. It can be observed

how the correlations differ from one transmitter i to another depending on the transmitter location. Those LEDs located at further distances from the receiver provide worse correlation functions (see, for instance, Fig. 4.4.b for LED $i = 3$). That means that the maximum peak may not be clearly detected. In order to minimize that possibility, in the proposed algorithm, maximum peaks are initially selected in the correlation function $s_i[n]$, since this function always presents higher amplitudes than the others, thus making the correlation peaks easier to be identified. Afterwards, the other correlation peaks in functions $r_i[n]$ and $t_i[n]$ are located, just by taking into account where they should be accordingly to the displacements of the transmissions carried out previously. Therefore, this method of determining the correlation peaks provides the system with a significant robustness against very low SNR, and multipath and near-far effects.

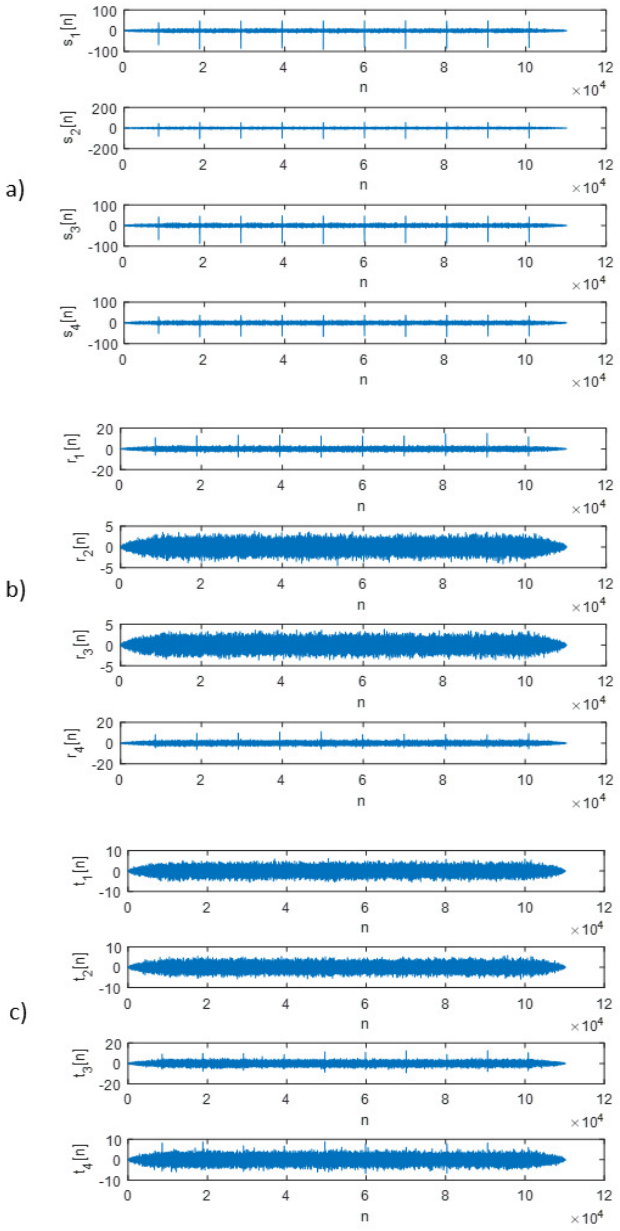

Figure 4.4: Example of the correlation functions computed at the reception: a) $r_i[n]$; b) $t_i[n]$; and c) $s_i[n]$ for each LED i.

Table 4.1: LED's coordinates considered in simulations.

LED i	**Coordinates** $(x_{t,i}, y_{t,i}, z_{t,i})$
LED 1	(1.33 m, 0.66 m, 3.40 m)
LED 2	(1.33 m, 1.33 m, 3.40 m)
LED 3	(0.66 m, 1.33 m, 3.40 m)
LED 4	(0.66 m, 0.66 m, 3.40 m)

It is worth mentioning that Eqs. (4.1) and (4.2) are linear when the illuminated areas A_k in the QADA sensor are always within the photodiodes' areas. This linearity is fulfilled when the diagonal of the used aperture is equal to or smaller than the radius of the QADA (r = 3.9 mm), and, therefore, the side of the aperture is equal to or smaller than $l = \sqrt{\frac{r^2}{2}} = 2.75$ mm, as can be observed in Fig. 4.5, where the ratio p_x in Eq. 4.1 is plotted for different sizes of the aperture l. This analysis can similarly be extended for p_y.

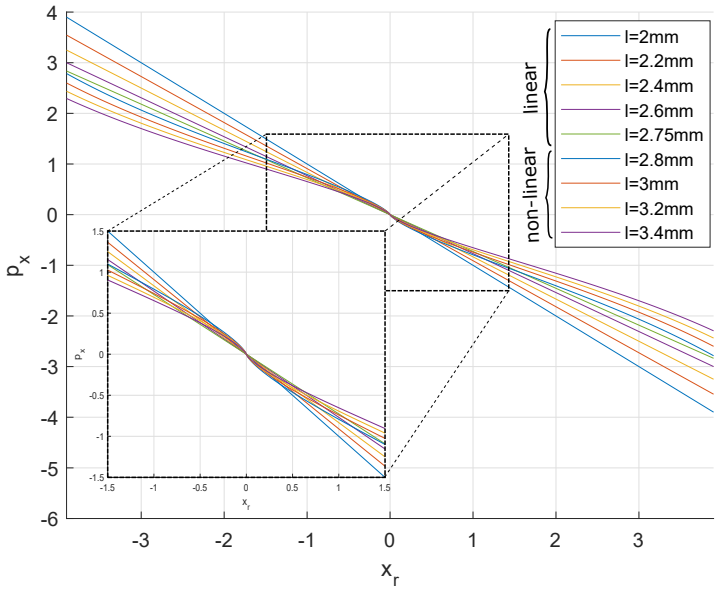

Figure 4.5: Representation of the ratio p_x according to the aperture side l for $-r < x_r < r$.

In addition, Fig. 4.6 presents the global coverage volume, where the black crosses are the transmitters' position detailed in Table 4.1 and the coloured map represents the maximum height at which the receiver can be placed, while still receiving emissions from the four transmitters with a particular beam angle of 150°.

The maximum height at which the receiver can be placed is obtained by the estimation of the maximum distance, from the receiver centre, at which the incident wave impacts the photoreceiver after it passes the aperture. This is determined by using ray tracing from the transmitters to the photoreceiver. We analyze two cases: the most general, in which it is enough that the ray that passes through the centre of the aperture impacts inside the sensitive area of the photoreceiver and, one more restrictive, in which all the rays passing through the aperture impact on the sensitive area. In this way, for the first case mentioned, when the aperture side is equal to the diameter of the photoreceiver ($l = 7.8$ mm),

the coverage volume is presented in Fig. 4.6.a). On the other hand, for the sencond case, when using an aperture side length of $l = 2.75\,\text{mm}$, the coverage volume is smaller, as presented in Fig. 4.6.b). For all the test area, the receiver can be placed at heights from the floor up to 2 m (first case) and up to 0.5 m (second case). There is a trade-off between minimizing the aperture size and maximizing the FoV (Field-of-View), since a smaller aperture size results in a smaller FoV (see Fig. 4.6). In particular, for $l = 2.75\,\text{mm}$, the QADA receiver will only detect angles of incidence lower than 36.87°. Note that diffraction effects are not considered, since the wavelength of the emission is small compared to the aperture side $l = 2.75\,\text{mm}$.

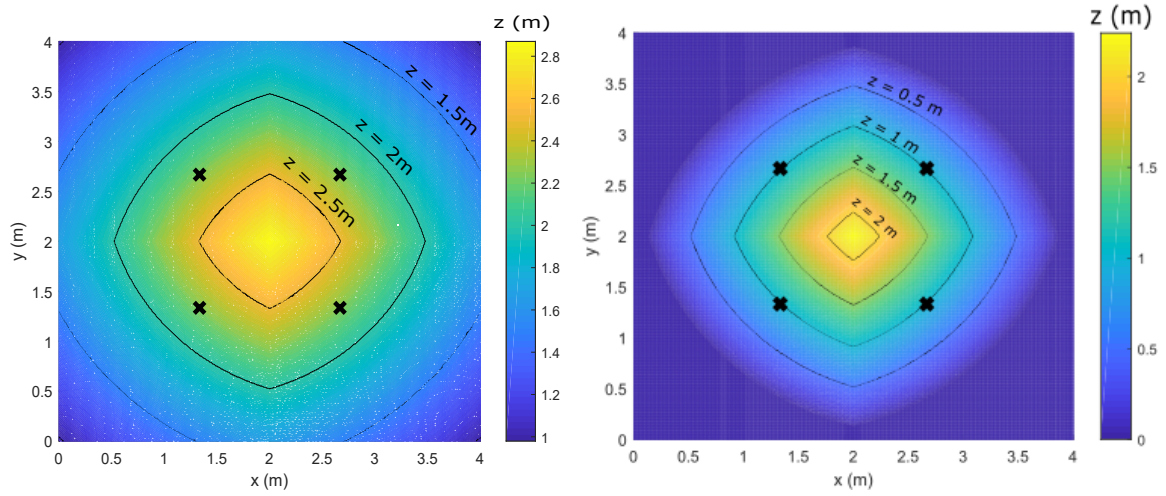

Figure 4.6: Coverage particularized for a beam angle $\alpha = 150°$ with the four transmitters at XY planes ($z = \{1.5\,\text{m}, 2\,\text{m}, 2.5\,\text{m}\}$): a) without aperture size constraint; b) with an aperture side length $l = 2.75\,\text{mm}$.

4.2.1 Non-Linear Image Point Estimation at the Receiver

In order to achieve a higher coverage volume, a full usage of the area of the photodiodes is required, thus, the side of the square aperture is set equal to the diameter of the photoreceptor (l = 7.8 mm). In this way, when the center of the light beam impacts at the coordinates ($x_r = 0$, $y_r = 0$), QADA's center, all the area from the four quadrants is lighted on.

The image point (x_r, y_r), where light passing through the center of the aperture impacts, is estimated by Non-Linear Least Squares Estimator (NLSE) using the Gauss-Newton algorithm. Before applying NLSE, two tables with theoretical predefined ratios p_x and p_y are characterized for the plane where the receiver is placed, in a range [-r, r] at intervals of 1 μm, thus performing a geometrical characterization of the receiver's areas as detailed in the following (note that r = 3.9 mm).

The calculation of the different areas A_k for p_x are calculated in the first quadrant, (x_r,y_r) ϵ [0, r] (4.5)-(4.9), where $r = 3.9\,\text{mm}$ is the radius of the photoreceiver QADA. Similarly, this study can be extended to the other quadrants and, also, to perform the analysis for p_y. Note that the third quadrant has an area $A_3(t)$ that depends on the position at which the projection of the aperture is located in the photoreceptor, as is shown in Fig. 4.7 and is detailed in (4.7) and (4.8) for the two cases $A_{3,1}$ and $A_{3,2}$, respectively.

$$A_1 = \frac{\pi \cdot r^2}{4} \tag{4.5}$$

$$A_2 = \frac{\pi \cdot r^2}{4} - \frac{1}{2} \cdot \left(\frac{r^2}{2} \cdot (\rho - \sin\rho) \right) \tag{4.6}$$

$$A_{3,1} = (r - x_r) \cdot (r - y_r) \tag{4.7}$$

$$A_{3,2} = \frac{\pi \cdot r^2}{4} - \frac{1}{2} \cdot \left(\frac{r^2}{2} \cdot (\rho - \sin\rho) \right) - \frac{1}{2} \cdot \left(\frac{r^2}{2} \cdot (\rho' - \sin\rho') \right) \tag{4.8}$$

$$A_4 = \frac{\pi \cdot r^2}{4} - \frac{1}{2} \cdot \left(\frac{r^2}{2} \cdot (\rho' - \sin\rho') \right) \tag{4.9}$$

Where r is the radius of the receiver; and $\rho = 2 \cdot \arccos\left(1 - \frac{x_r}{r}\right)$ and $\rho' = 2 \cdot \arccos\left(1 - \frac{y_r}{r}\right)$ are the angles that define the circular segments represented in Fig. 4.7. The conditions that must be met in order to use (4.8) instead of (4.7) when calculating the area A_3 are (4.10) and (4.11). Note that both equations are modifications on the circle equation: $(x_r - r)^2 \leq r^2 - (y_r - r)^2$.

$$x_r \leq 2 \cdot r - \left(\sqrt{-y_r^2 + 2 \cdot y_r \cdot r} + r\right) \tag{4.10}$$

$$y_r \leq 2 \cdot r - \left(\sqrt{-x_r^2 + 2 \cdot x_r \cdot r} + r\right) \tag{4.11}$$

If both conditions (4.10) - (4.11) are not met, the projection of the incident light in A_3 will be calculated as (4.7).

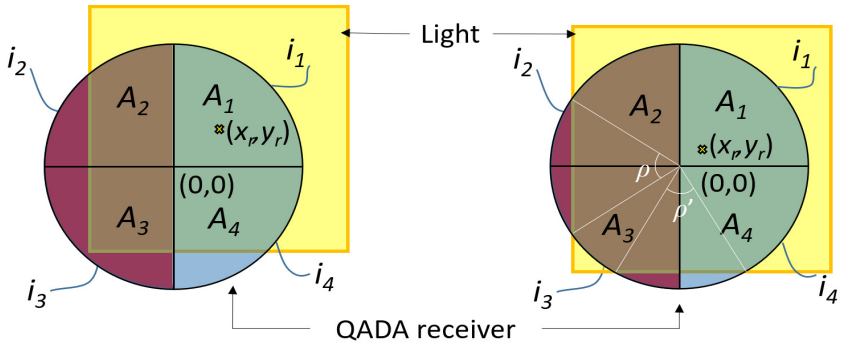

Figure 4.7: Projection of the incident light onto the QADA receiver through an aperture for $A_{3,1}(t)$ (left) and $A_{3,2}(t)$ (right).

It can be mentioned that the area $A_1(t)$ depends neither on x_r nor on y_r, $A_2(t)$ only depends on x_r, $A_4(t)$ only depends on y_r, whereas $A_3(t)$ depends both on x_r and y_r.

It is worth noting that this geometrical characterization does not involve certain approximations as in [Cin18a], taking into account an accurate round shape of the QADA receiver instead. In addition, these tables can be calibrated to consider practical deviations of some intrinsic parameters of the receiver (i.e. aperture height). As can be observed in Fig. 4.8.a) where p_x is represented, there is a wide range around the centre of the QADA receiver where the values for p_x are hard to be directly extracted from the graph, since they are extremely similar for different y_r values (low derivative).

To avoid this lack of sensitivity, these aforementioned ratio tables are actually calculated as the square root of the absolute value of the ratios p_x and p_y, still considering the sign of the ratios p_x and p_y, respectively, as can be observed in Fig. 4.8.b) for the case of p_x. As a result, a greater slope in the centre of the QADA ($x_r = 0$, $y_r = 0$) (see zoomed plots in Fig. 4.8) is obtained. It is worth noting that only those ratio tables related to the ratio p_x, depending on x_r for all the ranges in y_r (Eq. 4.1), are plotted in Fig. 4.8. Similarly, tables about ratio p_y provide the corresponding information.

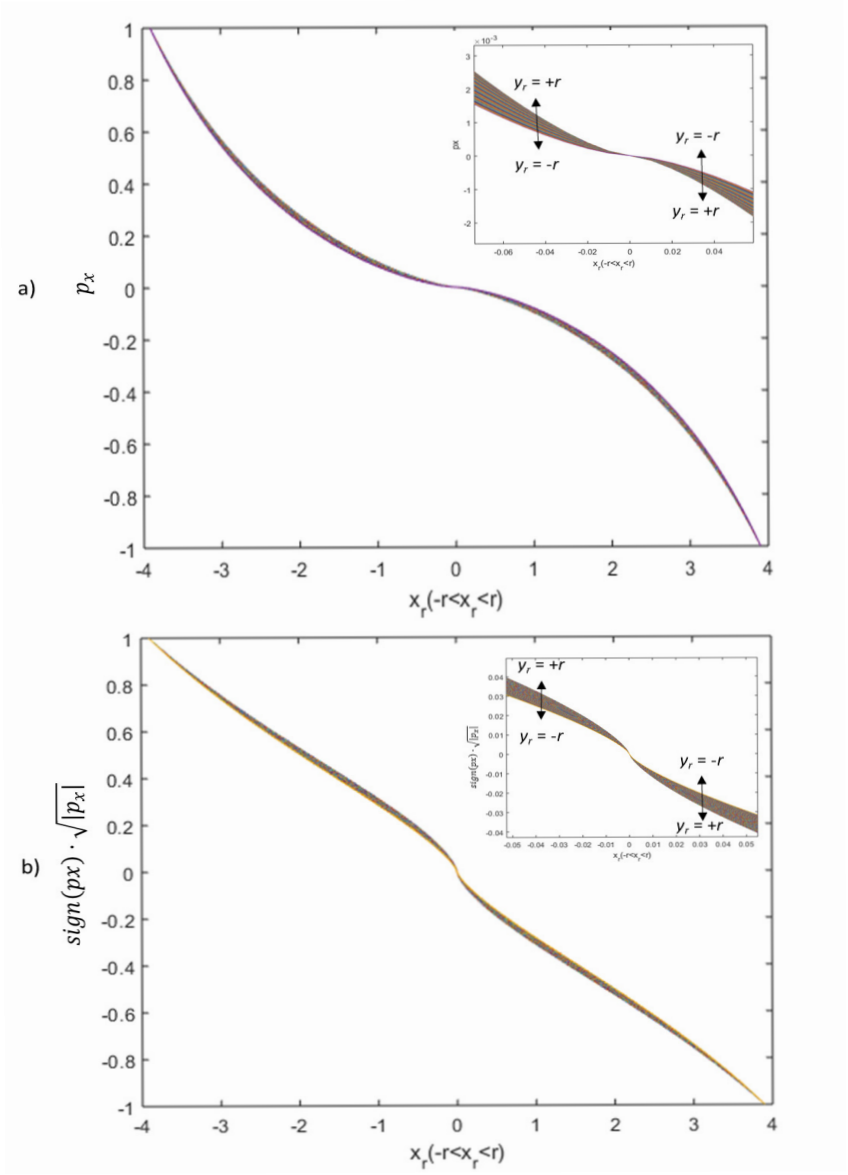

Figure 4.8: Ratio p_x depending on the coordinate x_r for a range of values in y_r; $x_r \epsilon$ [-r, r], $y_r \epsilon$ [-r, r] a) Ratio p_x; b) Square root of the absolute value of the ratio p_x, still considering the sign of p_x: $sign(p_x) \cdot \sqrt{|p_x|}$.

The algorithm involved in the calculation of the position (x_r, y_r) starts with the initialization of a threshold u, which is actually the maximum error allowed by the iterative algorithm; in this case, it is fixed at $u = 1\,\mu$m. While the threshold u is lower than the detected errors $\epsilon_{s,1}$ for x_r and $\epsilon_{s,2}$ for y_r at a certain iteration s, the algorithm will continue iterating. A predefined Jacobian matrix is obtained in (4.12), by means of the above-mentioned tables, according to (x_r, y_r).

$$\mathbf{J} = \begin{bmatrix} \frac{\delta p_x}{\delta x_r} & \frac{\delta p_x}{\delta y_r} \\ \frac{\delta p_y}{\delta x_r} & \frac{\delta p_y}{\delta y_r} \end{bmatrix} \tag{4.12}$$

Where the finite derivatives $\frac{\delta p_x}{\delta x_r}$, $\frac{\delta p_x}{\delta y_r}$, $\frac{\delta p_y}{\delta x_r}$ and $\frac{\delta p_y}{\delta y_r}$ are calculated as an approximation of the first-order derivative (4.13)-(4.16). Note that the constant n is considered to be $1\,\mu$m, which is the step between intervals considered in the tables for ratios p_x and p_y.

$$\frac{\delta p_x}{\delta x_r} = \frac{4 \cdot p_x(x_r + n) - 3 \cdot p_x(x_r) - p_x(x_r + 2 \cdot n)}{2 \cdot n} \tag{4.13}$$

$$\frac{\delta p_x}{\delta y_r} = \frac{4 \cdot p_x(y_r + n) - 3 \cdot p_x(y_r) - p_x(y_r + 2 \cdot n)}{2 \cdot n} \tag{4.14}$$

$$\frac{\delta p_y}{\delta x_r} = \frac{4 \cdot p_y(x_r + n) - 3 \cdot p_y(x_r) - p_y(x_r + 2 \cdot n)}{2 \cdot n} \tag{4.15}$$

$$\frac{\delta p_y}{\delta y_r} = \frac{4 \cdot p_y(y_r + n) - 3 \cdot p_y(y_r) - p_y(y_r + 2 \cdot n)}{2 \cdot n} \tag{4.16}$$

The algorithm starts by searching for the values of the first position $(x_r, y_r)_1$ into the ratio tables, and the corresponding errors $\epsilon_{s,1}$ and $\epsilon_{s,2}$ are calculated (4.17). The initial position $(x_r, y_r)_0$ is set at (0, 0).

$$\begin{bmatrix} \epsilon_{s,1} \\ \epsilon_{s,2} \end{bmatrix} = \begin{bmatrix} p_x \\ p_y \end{bmatrix} - \begin{bmatrix} p_x \\ p_y \end{bmatrix}_s \tag{4.17}$$

Where p_x and p_y are the measured values from the correlation peaks (4.3) and (4.4); and $p_{x,s}$ and $p_{y,s}$ are the values obtained from the search, at each iteration, in the ratio tables for the desired predefined values of the ratios p_x and p_y for the position $(x_r, y_r)_s$. After the errors $\epsilon_{s,1}$ and $\epsilon_{s,2}$ are calculated, the previous solution $(x_r, y_r)_s$ is updated (4.18) for the next iteration.

$$\begin{bmatrix} x_r \\ y_r \end{bmatrix}_{s+1} = \begin{bmatrix} x_r \\ y_r \end{bmatrix}_s + (\mathbf{J}^T \begin{bmatrix} x_r \\ y_r \end{bmatrix}_s \cdot \mathbf{J} \begin{bmatrix} x_r \\ y_r \end{bmatrix}_s)^{-1} \cdot \mathbf{J}^T \begin{bmatrix} x_r \\ y_r \end{bmatrix}_s \cdot \begin{bmatrix} \epsilon_{s,1} \\ \epsilon_{s,2} \end{bmatrix}_s \tag{4.18}$$

Where $\mathbf{J}\begin{bmatrix} x_r \\ y_r \end{bmatrix}_s$ is the Jacobian matrix $\mathbf{J}$ for the current estimated position $(x_r, y_r)_s$; and $\mathbf{J}^T\begin{bmatrix} x_r \\ y_r \end{bmatrix}_s$ is the transposed of the Jacobian matrix $\mathbf{J}$ for the current estimated position $(x_r, y_r)_s$. The new position $(x_r, y_r)_{s+1}$ will enter again in the NLSE algorithm until the convergence of the algorithm, when the error is lower than the threshold, i.e. $\sqrt{(\epsilon_1^2 + \epsilon_2^2)_s} < u$. It is worth mentioning that the iterative algorithm stops when that convergence criteria is met or when the algorithms reaches 100 iterations. Furthermore, the procedure has been modified to avoid any out-of-range result (outlier), so the column and/or row indexed by the position $(x_r, y_r)_s$ in the ratio tables always remains inside their dimensions. Whether the algorithm searches for a column/row outside the dimensions of the ratio tables, it will be readdressed to a column/row contained in the table. Note that, although it is an infrequent event, it may occur when the point of incidence is near the border of the QADA receiver. For a better understanding of the aforementioned NLSE algorithm, a flowchart is presented in Fig. 4.9. The iterative cycle starts at $(x_r, y_r)_s$, whereas the transpose is indicated by the block T and the inverse is denoted as $()^{-1}$.

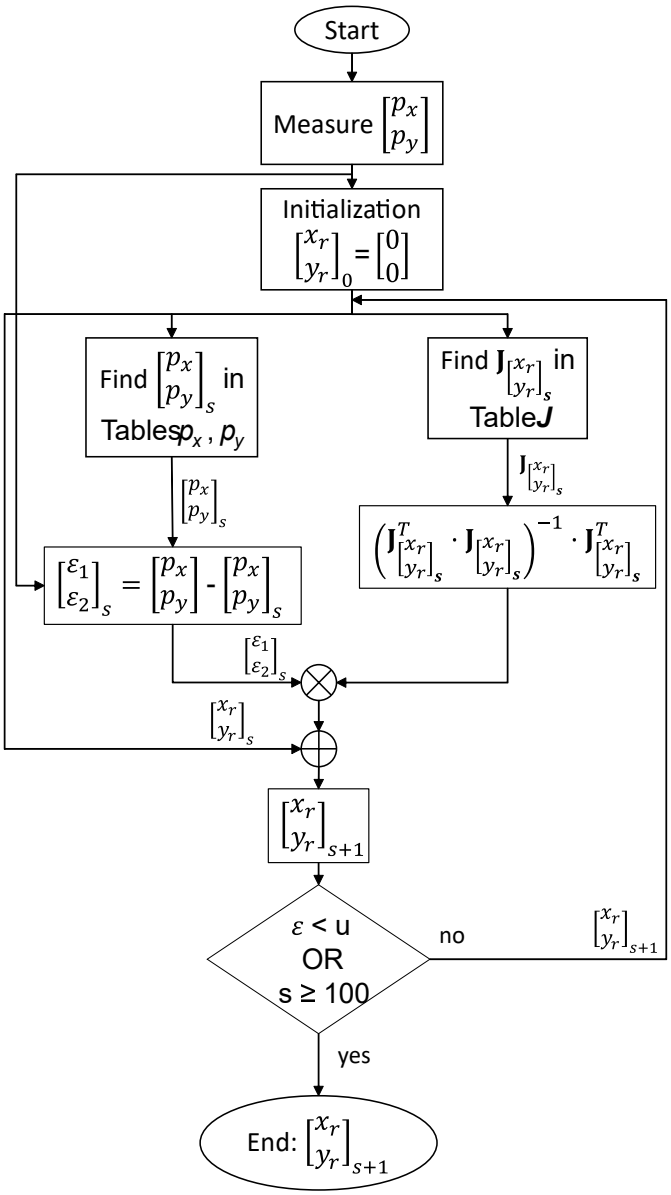

Figure 4.9: Flowchart of the proposed NLSE algorithm.

4.2.2 Linear Image Point Estimation at the Receiver

On the other hand, and in order not to have any boundaries (i.e., non-linearity in the calculation of p_x and p_y), we propose a square aperture, smaller than the one used in the previous subsection (see Fig. 4.32.a), which assures that the illuminated areas A_k on the QADA sensor are always confined inside the photodetector's sensitive areas ($l = 2.75\,\text{mm}$). Eqs. (4.19) - (4.22) define the illuminated areas A_k when the image point is located at any generic point (x_r, y_r).

$$A_1 = (l/2 + x_r) \cdot (l/2 + y_r) \tag{4.19}$$

$$A_2 = (l/2 - x_r) \cdot (l/2 + y_r) \tag{4.20}$$

$$A_3 = (l/2 - x_r) \cdot (l/2 - y_r) \tag{4.21}$$

$$A_4 = (l/2 + x_r) \cdot (l/2 - y_r) \tag{4.22}$$

Combining Eqs. (4.1) - (4.2) with Eqs. (4.19) - (4.22), the centre of the light incidence can be defined as (4.23). Note that different terms are cancelled out so that x_r and y_r only depend on p_x and p_y, respectively.

$$\begin{bmatrix} x_r \\ y_r \end{bmatrix} = \frac{-l}{2} \cdot \begin{bmatrix} p_x \\ p_y \end{bmatrix} \tag{4.23}$$

It is worth mentioning that there are other parameters that have an impact on the estimation of the image point (x_r, y_r), which are the intrinsic parameters of a pin-hole system. Since the proposed system relies on the accurate location of the aperture onto the QADA receiver, the parameters under consideration are: the optical centre (x_c, y_c), which is defined as the centre of the square aperture placed on top of the QADA receiver; the height h_{ap} at which the aperture is located (in other words, the focal length); the aperture misalignment δ, which is defined as the rotation of the aperture with respect to the photoreceiver axis; and the length of the aperture l (see Fig. 4.10). Note that it is possible to introduce the intrinsic parameters in the image points estimation thanks to the simplification of the equations as a result of their linearization.

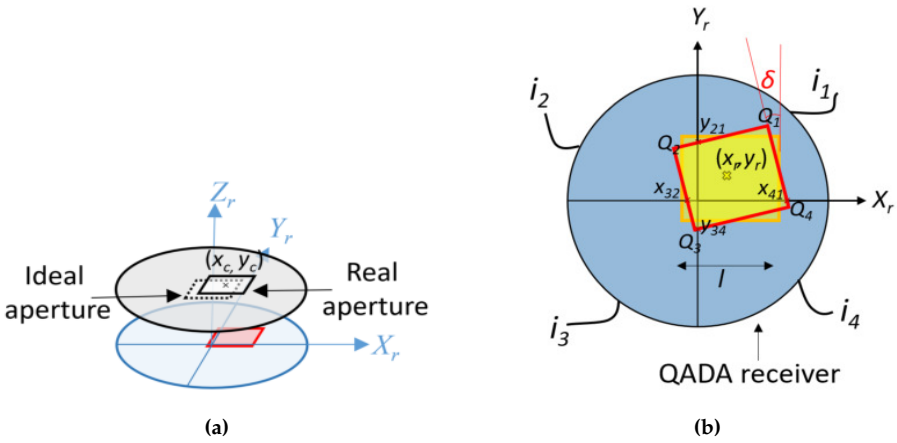

Figure 4.10: Parameters to calibrate in the aperture of the QADA: a) optical centre; b) aperture misalignment.

The optical centre (x_c, y_c) and the correction of the focal distance h_{ap} can be adjusted in the central image point $\left(\begin{bmatrix} x_{r,\lambda,c} \\ y_{r,\lambda,c} \end{bmatrix} \right)$ according to (4.24), where λ is the relation between the expected focal length h_{ap} and the actual focal length h'_{ap}: $\lambda = \frac{h'_{ap}}{h_{ap}}$.

$$\begin{bmatrix} x_{r,\lambda,c} \\ y_{r,\lambda,c} \end{bmatrix} = \frac{-l}{2} \cdot \lambda \cdot \begin{bmatrix} p_x \\ p_y \end{bmatrix} + \begin{bmatrix} x_c \\ y_c \end{bmatrix} \tag{4.24}$$

A more in-depth analysis is required to obtain the aperture misalignment δ (see Fig. 4.10.b), where the corners of the tilted aperture (red square in Fig. 4.10.b) are denoted as $\mathbf{Q_1}$, $\mathbf{Q_2}$, $\mathbf{Q_3}$ and $\mathbf{Q_4}$ (4.25 - 4.28).

$$\mathbf{Q_1} = \left(x_r + \frac{l}{\sqrt{2}} \cdot cos(45+\delta), y_r + \frac{l}{\sqrt{2}} \cdot sin(45+\delta)\right) \tag{4.25}$$

$$\mathbf{Q_2} = \left(x_r + \frac{l}{\sqrt{2}} \cdot cos(135+\delta), y_r + \frac{l}{\sqrt{2}} \cdot sin(135+\delta)\right) \tag{4.26}$$

$$\mathbf{Q_3} = \left(x_r + \frac{l}{\sqrt{2}} \cdot cos(225+\delta), y_r + \frac{l}{\sqrt{2}} \cdot sin(225+\delta)\right) \tag{4.27}$$

$$\mathbf{Q_4} = \left(x_r + \frac{l}{\sqrt{2}} \cdot cos(315+\delta), y_r + \frac{l}{\sqrt{2}} \cdot sin(315+\delta)\right) \tag{4.28}$$

These equations can be simplified into (4.29 - 4.32), by taking into account some straightforward trigonometric considerations and assuming small values of δ, so $\sin(\delta) \approx \delta$ and $\cos(\delta) \approx 1$.

$$\mathbf{Q_1} = (x_1, y_1) = \left(x_r + \frac{l}{2} \cdot (1-\delta), y_r + \frac{l}{2} \cdot (1+\delta)\right) \tag{4.29}$$

$$\mathbf{Q_2} = (x_2, y_2) = \left(x_r + \frac{l}{2} \cdot (-1-\delta), y_r + \frac{l}{2} \cdot (1-\delta)\right) \tag{4.30}$$

$$\mathbf{Q_3} = (x_3, y_3) = \left(x_r + \frac{l}{2} \cdot (-1+\delta), y_r + \frac{l}{2} \cdot (-1-\delta)\right) \tag{4.31}$$

$$\mathbf{Q_4} = (x_4, y_4) = \left(x_r + \frac{l}{2} \cdot (1+\delta), y_r + \frac{l}{2} \cdot (-1+\delta)\right) \tag{4.32}$$

As can be observed in Fig. 4.10.b), the intersection points of the X axis with the line from $\mathbf{Q_4}$ to $\mathbf{Q_1}$ and with the line from $\mathbf{Q_3}$ to $\mathbf{Q_2}$ are denoted as x_{41} and x_{32}, respectively. Similarly, the intersection points of the Y axis with the line from $\mathbf{Q_2}$ to $\mathbf{Q_1}$ and with the line from $\mathbf{Q_3}$ to $\mathbf{Q_4}$ are denoted as y_{21} and y_{34}, respectively.

$$x_{41} = \frac{x_1 - x_4}{y_1 - y_4} \cdot (-y_1) + x_1 = -\delta \cdot \left(-y_r - \frac{l}{2} \cdot (1+\delta)\right) + \left(x_r + \frac{l}{2} \cdot (1-\delta)\right) \tag{4.33}$$

$$x_{32} = \frac{x_2 - x_3}{y_2 - y_3} \cdot (-y_2) + x_2 = -\delta \cdot \left(-y_r - \frac{l}{2} \cdot (1-\delta)\right) + \left(x_r - \frac{l}{2} \cdot (1+\delta)\right) \tag{4.34}$$

$$y_{21} = \frac{y_1 - y_2}{x_1 - x_2} \cdot (-x_2) + y_2 = \delta \cdot \left(-x_r + \frac{l}{2} \cdot (1+\delta)\right) + \left(y_r + \frac{l}{2} \cdot (1-\delta)\right) \tag{4.35}$$

$$y_{34} = \frac{y_4 - y_3}{x_4 - x_3} \cdot (-x_3) + y_3 = \delta \cdot \left(-x_r + \frac{l}{2} \cdot (1-\delta)\right) + \left(y_r - \frac{l}{2} \cdot (1+\delta)\right) \tag{4.36}$$

Finally, the centre ($x_{r,\delta}$, $y_{r,\delta}$) of the illuminated square area when only the misalignment of the aperture is taken into account is obtained according to (4.37) and (4.38).

$$x_{r,\delta} = \frac{x_{41} + x_{32}}{2} = \delta \cdot y_r + x_r \tag{4.37}$$

$$y_{r,\delta} = \frac{y_{21} + y_{34}}{2} = -\delta \cdot x_r + y_r \tag{4.38}$$

Therefore, a final expression can be achieved by rewriting (4.24) and adding the effects of δ. Then, the image point considering all the parameters $\left(\begin{bmatrix} x_{r,\lambda,c,\delta} \\ y_{r,\lambda,c,\delta} \end{bmatrix}\right)$ is obtained according to (4.39).

$$\begin{bmatrix} x_{r,\lambda,c,\delta} \\ y_{r,\lambda,c,\delta} \end{bmatrix} = \frac{-l}{2} \cdot \lambda \cdot \begin{bmatrix} p_x + \delta \cdot p_y \\ -\delta \cdot p_x + p_y \end{bmatrix} + \begin{bmatrix} x_c \\ y_c \end{bmatrix} \tag{4.39}$$

For the ideal case, the aforementioned equations can be particularized as (4.40) and (4.41), whether $l = 2.75\,\text{mm}$, $\delta = 0$, $\lambda = 1$ and, $(x_c, y_c) = (0, 0)$. In a real case, the above-mentioned parameters are obtained by calibration (as will be seen later).

$$x_r = -\frac{11}{8} \cdot p_x \; mm \tag{4.40}$$

$$y_r = -\frac{11}{8} \cdot p_y \; mm \tag{4.41}$$

4.3 Positioning Algorithm

Once the image points in the QADA receiver $(x_r, y_r)_i$ have been estimated for each LED i, the local position of the receiver in the proposed scenario is analysed. For the sake of clarity, it is assumed that three or more image points (x_r, y_r) are known, as well as the locations of their corresponding transmitters i, so the receiver can estimate its own location. With regard to possible obstacles avoiding desirable LoS (Line-of-Sight) situations, note that, either the obstacle should cover at least two LEDs, or it should imply a specular reflection, thus deviating the path of the light onto a false image point (x_r, y_r) in the QADA receiver. It is worth noting that the positioning algorithm does not depend on how the image points have been obtained (using the linear or the non-lienar approach).

There are different approaches to estimate the receiver's position. In this chapter we present an Angle of Arrival (AoA) algorithm and different Perspective-n-Point (PnP) solutions. Regarding the AoA algorithm, the positioning algorithm estimates the final position of the receiver (x, y) by means of a Least Squares Estimator (LSE) and the coordinate z is obtained by means of trigonometric considerations that involve the incident angle and the distance between the receiver's position and the projection of each transmitter on the plane where the receiver is located. On the other hand, the proposed Local Positioning System (LPS) can be geometrically modelled to relate the beacon's 3D position with the sensor's 2D measurement as the perspective camera model (a.k.a the pin-hole camera). This model is widely used in photogrammetry and computer vision to solve problems that involve the 3D geometry of multiple views [Har04]. One such problem is known as the PnP problem. Given a collection of 3D-2D point correspondences between the scene and the image, the objective in PnP is to recover the receiver pose. We present recent PnP solutions that handle Planar-PnP, such as Efficient Perspective-n-Point Camera Pose Estimation (EPnP), Infinitesimal Plane-Based Pose Estimation (IPPE) and Robust Non-Iterative Solution of Perspective-n-Point (RPnP), to obtain the 6-DOF pose of the receiver.

The complete pose of the receiver is denoted as (x, y, z, α, β, γ), where α, β and γ are the rotation angles of the receiver around the X, Y and Z axis, respectively. However, if the receiver is placed on top of a mobile robot on the floor, α and β are equal to $0\,^{\circ}$. It is worth noting that in the AoA algorithms neither α nor β are obtained, meanwhile in the homographic solution, the complete pose can be estimated.

4.3.1 Positioning Algorithm with Angles of Arrival (AoA)

As has already be mentioned, it is considered that there is no angle of inclination (neither in the emitters nor in the QADA receiver), but there can be a certain rotation in the Z axis of the receiver (yaw angle γ). Furthermore, it is assumed that the X and Y axes of the LEDs and the X_r and Y_r axes of the QADA receiver are aligned when $\gamma = 0^{\circ}$.

The rotation angle γ_i shown in (4.42)-(4.45) are obtained by means of geometrical considerations, as detailed in Fig. 4.11.

$$\gamma_1 = \tan -1 \left(\frac{y_{r,1} - y_{r,2}}{x_{r,1} - x_{r,2}} \right) \tag{4.42}$$

$$\gamma_2 = \tan^{-1} \left(\frac{y_{r,2} - y_{r,3}}{x_{r,3} - x_{r,2}} \right) \tag{4.43}$$

$$\gamma_3 = \tan^{-1} \left(\frac{y_{r,4} - y_{r,3}}{x_{r,4} - x_{r,3}} \right) \tag{4.44}$$

$$\gamma_4 = \tan^{-1} \left(\frac{y_{r,1} - y_{r,4}}{x_{r,4} - x_{r,1}} \right) \tag{4.45}$$

Where γ_i is the rotation angle of the receiver with respect to the transmitter i; and $(x_r, y_r)_i$ are the coordinates of the impact points of the incident light onto the QADA receiver. Thus, it can be observed that the final rotation angle γ can be obtained as an average of the four different angles γ_i, as presented in (4.46).

$$\gamma = \overline{(\gamma_1, \gamma_2, \gamma_3, \gamma_4)} \tag{4.46}$$

Note that, although Fig. 4.11 represents the image points on the first quadrant, this algorithm can be easily extended to the four quadrants and it is not necessary that the image points $(x_r, y_r)_i$ are placed in the same quadrant for the algorithm to properly work. In addition, it is assumed that the rotation of the receiver is clockwise, thus the rotation of the image points is anticlockwise (see Fig. 4.11). It is worth mentioning that the incident points are geometrically distributed with a square shape, as the transmitters are placed in the ceiling forming a square.

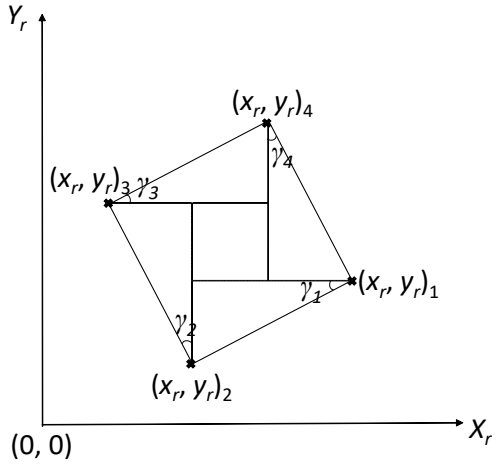

Figure 4.11: First quadrant of the QADA photoreceiver with four impact points $(x_r, y_r)_i$.

The proposed algorithm is based on the analysis of the rotation of the image points $(x_r, y_r)_i$, obtained for a certain rotation angle γ_i, with respect to the corresponding points of incidence without rotation $(x_r, y_r)'_i$ (assuming $\gamma_i = 0°$). Note that the rotation does not imply any change in the radius (defined at the distance of the incident point to the center of the square) of the points of incidence (see Fig. 4.12). The coordinates of the non-rotated impact point $(x_r, y_r)'_i$ are obtained as (4.47)-(4.48).

$$x'_{r,i} = r_i \cdot \cos(\theta_i) \tag{4.47}$$

$$y'_{r,i} = r_i \cdot \sin(\theta_i) \tag{4.48}$$

Where $\theta_i = \eta_i - \gamma_i$; and $\eta_i = tan^{-1}\left(\frac{y_r}{x_r}\right)_i$.

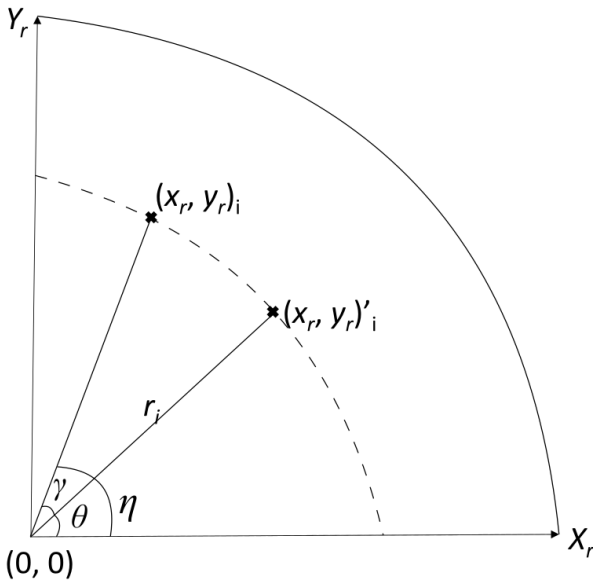

Figure 4.12: First quadrant of the QADA photoreceiver with an arbitrary impact point $(x_r, y_r)_i$ and its non-rotated impact point $(x_r, y_r)'_i$.

After the non-rotated coordinates $(x_r, y_r)'_i$ are obtained, the positioning algorithm continues to obtain the final coordinates $(x,\ y)$ of the receiver's position in the proposed scenario by means of the Least Squares Estimator (LSE). In this case, when considering the scenario proposed in Fig. 4.13, the point (x, y) is the 2D position of the receiver, $(x_{t,i}, y_{t,i})$ are the projections of the positions for every LED i, and κ_i are the angles between the transmitters i and the X axis. Thus, note that the positioning algorithm is actually based on triangulation techniques.

From Fig. 4.13, the geometrical expression (4.49) can be written as (4.50).

$$\tan(\kappa_i) = \frac{\sin(\kappa_i)}{\cos(\kappa_i)} = \frac{\delta y}{\delta x} = \frac{y - y_{t,i}}{x - x_{t,i}} \tag{4.49}$$

$$-x \cdot \sin(\kappa_i) + x_{t,i} \cdot \sin(\kappa_i) = -y \cdot \cos(\kappa_i) + y_{t,i} \cdot \cos(\kappa_i) \tag{4.50}$$

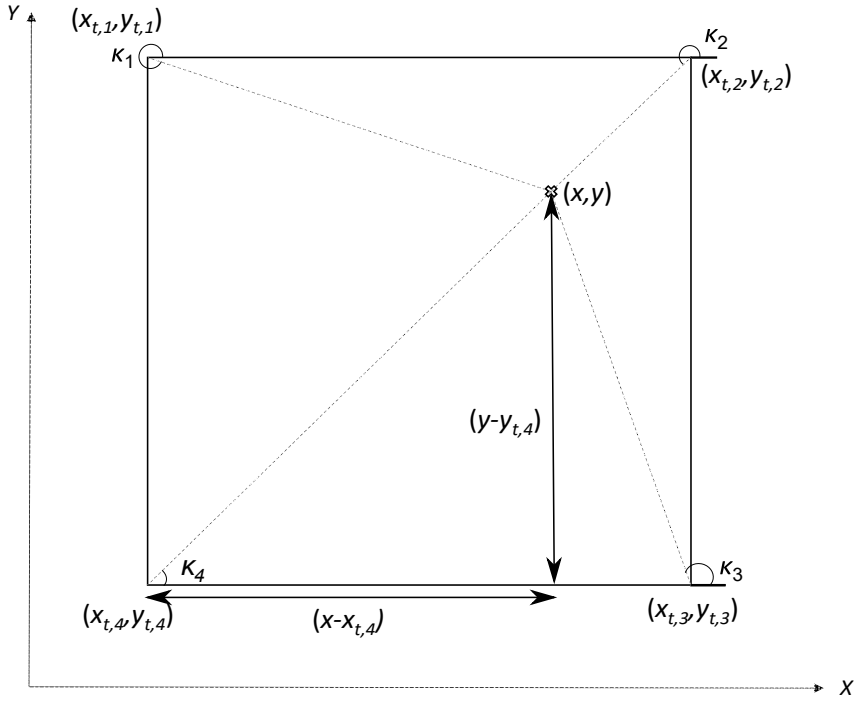

Figure 4.13: 2D geometrical analysis of the proposed system.

Keeping in mind the geometrical distribution of the QADA receiver and its aperture shape in Fig. 4.14, it is possible to obtain (4.51), similarly to (4.49). Since the receiver is neither rotated nor tilted, then $\kappa_i = \theta_i$, so Eqs. (4.50) and (4.51) can be combined according to (4.52).

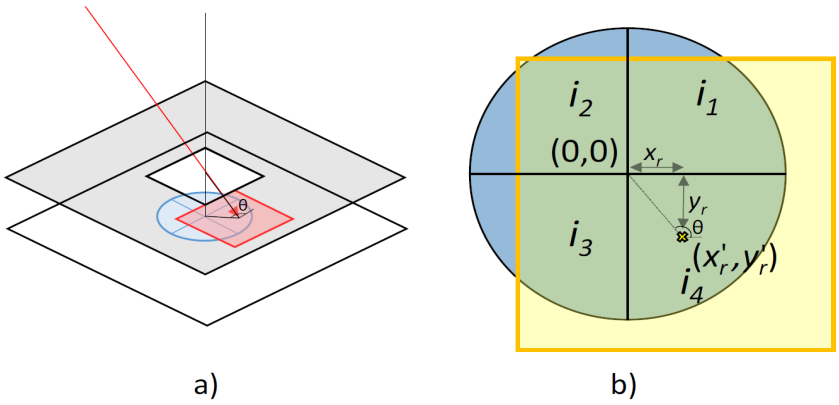

Figure 4.14: a) Incident light in the photoreceiver; b) Geometrical analysis of the receiver.

$$\tan(\theta_i) = \frac{\sin(\theta_i)}{\cos(\theta_i)} = \frac{y'_{r,i}}{x'_{r,i}} \tag{4.51}$$

$$-x \cdot y'_{r,i} + x_{t,i} \cdot y'_{r,i} = -y \cdot x'_{r,i} + y_{t,i} \cdot x'_{r,i} \tag{4.52}$$

Eq. (4.52) can be transformed into a matrix form **A**·**X**=**b**, where the least squares method estimates the global coordinates (x, y) of the receiver (4.53).

$$(x, y) = (\mathbf{A}^T \cdot \mathbf{A})^{-1} \cdot \mathbf{A}^T \cdot \mathbf{b} \tag{4.53}$$

$$\text{Where } \mathbf{A} = \begin{bmatrix} -y'_{r,1} & x'_{r,1} \\ -y'_{r,2} & x'_{r,2} \\ -y'_{r,3} & x'_{r,3} \\ -y'_{r,4} & x'_{r,4} \end{bmatrix} \text{ and } \mathbf{b} = \begin{bmatrix} y_{t,1} \cdot x'_{r,1} - x_{t,1} \cdot y'_{r,1} \\ y_{t,2} \cdot x'_{r,2} - x_{t,2} \cdot y'_{r,2} \\ y_{t,3} \cdot x'_{r,3} - x_{t,3} \cdot y'_{r,3} \\ y_{t,4} \cdot x'_{r,4} - x_{t,4} \cdot y'_{r,4} \end{bmatrix}.$$

After estimating the location $(x,\ y)$ of the receiver in 2D, the third dimension z is obtained by means of the triangulation relationship detailed in Fig. 4.15. The non-rotated image points $(x'_r, y'_r)_i$ allows the angle of incidence ψ_i to be geometrically estimated (see Fig. 4.14), by taking into account the corresponding geometrical considerations about the aperture height h_{ap}, as denoted in (4.54), or the geometrical relationship between the emitters' and the receiver's position, as denoted in (4.55). Note that ψ_i is the angle at which the light beam passing through the centre of the aperture impacts on the array of photodiodes for each LED i. Combining Eqs. (4.54) and (4.55), we can estimate the coordinate z as the averaged value from the result obtained from each LED.

$$\psi_i = \tan^{-1}\left(\frac{\sqrt{x'^2_{r,i} + y'^2_{r,i}}}{h_{ap}}\right) \tag{4.54}$$

$$\psi_i = \tan^{-1}\left(\frac{\sqrt{(x_{t,i} - x)^2 + (y_{t,i} - y)^2} + \sqrt{x'^2_{r,i} + y'^2_{r,i}}}{z_{t,i} - z}\right) \tag{4.55}$$

$$z = \frac{\sum_{i=1}^{4} z_{t,i} - h_{ap} \cdot \left(1 + \sqrt{\frac{(x_{t,i}-x)^2 + (y_{t,i}-y)^2}{x'^2_{r,i} + y'^2_{r,i}}}\right)}{4} \tag{4.56}$$

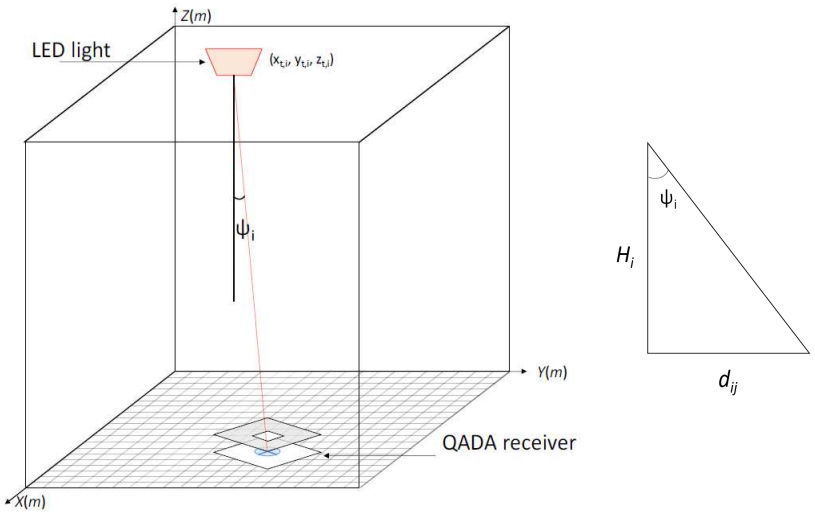

Figure 4.15: Scenario of the positioning analysis for the distance H_i between a transmitter i and the receiver. Note that elements are not to scale.

Experiments and Results

For the simulation results, the proposed optical positioning system is based on a set of four transmitters placed at certain points in the environment (see Table 4.2), so that they cover an area where the receiver can detect all the transmissions and, therefore, estimate its position. A general schematic of the proposal

is presented in Fig. 4.16. It is considered that the LEDs emit a 1023-bit Kasami sequence with a displacement of 5 samples and, in the reception, the QADA has an aperture length of $l = 7.8$ mm. Hereinafter, a Gaussian Noise has been added in the received signal in order to have a Signal-to-Noise Ratio (SNR) of 10 dB, as detailed in Chapter 3. It is assumed that the four quadrants of the QADA receiver are exactly equal and that, under the same illuminating conditions, they generate the same currents. It is also assumed that there is no misalignment between the QADA surface and the aperture. Neither tilting in the transmitters nor in the receiver is considered, while the yaw angle γ is analysed. In addition, those situations where the LEDs illumination does not cover all the quadrants are not studied; therefore, the receiver is always considered to be inside the coverage area where at least three image points are received by the QADA.

Table 4.2: LED's coordinates considered in simulations.

LED i	**Coordinates** $(x_{t,i}, y_{t,i}, z_{t,i})$
LED 1	(1.33 m, 0.66 m, 2 m)
LED 2	(1.33 m, 1.33 m, 2 m)
LED 3	(0.66 m, 1.33 m, 2 m)
LED 4	(0.66 m, 0.66 m, 2 m)

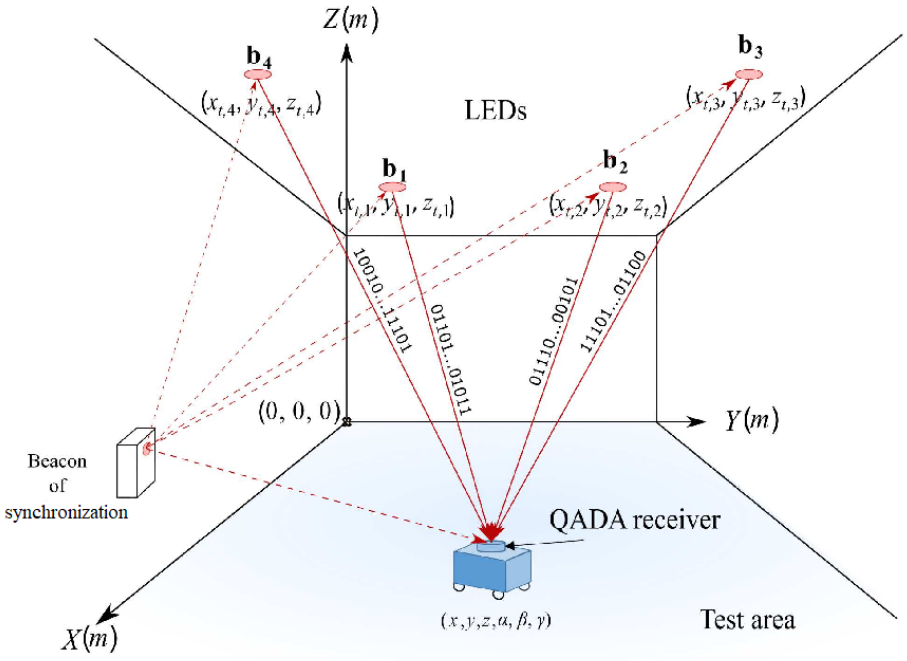

Figure 4.16: Global overview of the proposed system.

Firstly, some simulations are performed in order to determine the absolute error of the proposed algorithm in the calculation of the polar angle γ. Fig. 4.17 represents the cumulative distribution function (CDF) of the absolute errors of the polar angle for $\gamma = \{20\,°, 30\,°, 60\,°, 110\,°, 120\,°, 200\,°, 300\,°, 340\,°\}$. It has been analysed in a grid of 2×2 m every 10 cm with a hundred measurements at each point with the receiver is placed at $z = 0$ m. Note that those CDFs, whose angles verify $90\,° \cdot n \pm \gamma$ (n is an

integer), have similar results and, consequently, their absolute error is also similar. It can be obtained an absolute error of 1.2 ° in the 90 % of measures for a rotation angle $\gamma = \{20\,°, 110\,°, 200\,°, 340\,°\}$, and 0.8 ° in the 90 % of measures for a rotation angle $\gamma = \{30\,°, 60\,°, 120\,°, 300\,°\}$. Therefore, hereinafter only the first octant is analysed (from 0 ° to 45 °), since the results can be extended to the rest of the circumference.

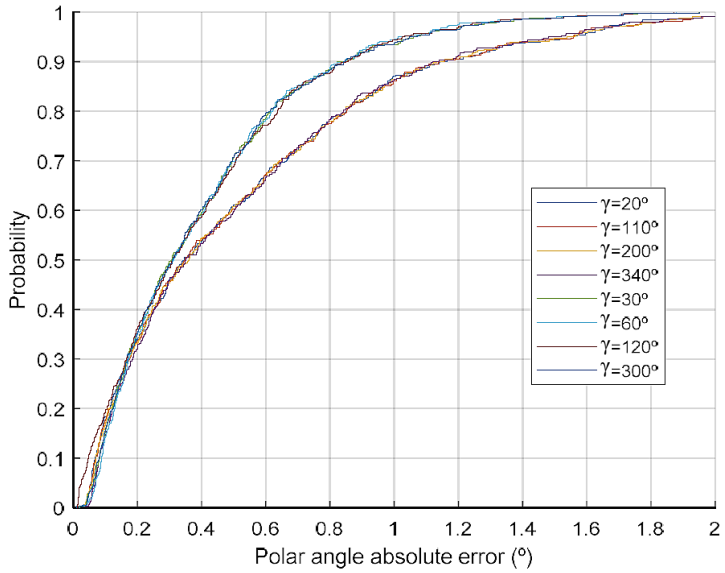

Figure 4.17: Absolute error in the estimation of the yaw angle γ for different values at $z = 0$ m with a SNR of 10 dB.

In Fig. 4.18 the absolute errors of the polar angle γ are detailed for angles in the range from 0 ° to 45 °. Furthermore, the global absolute error in the proposed scenario, for all possible angles γ, is detailed with a black line. This global error is 0.9 ° in 90 % of the cases. The worst performance of the algorithm occurs at $\gamma = 15\,°$ when an error of 1.25 ° is found in the 90 % of the measures, whereas the best performance is at $\gamma = 45\,°$ with a 0.25 ° of absolute error.

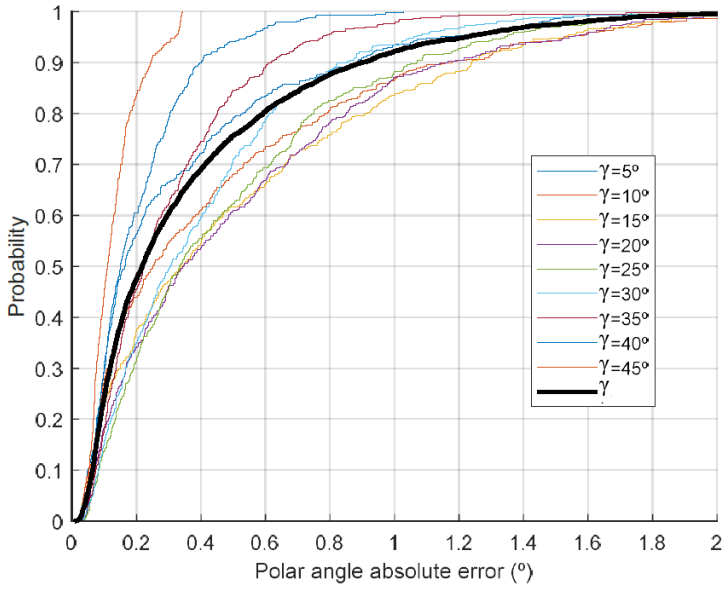

Figure 4.18: Absolute error in the estimation of the polar angle with a SNR of 10 dB for values γ={5 °, 10 °, 15 °, 20 °, 25 °, 30 °, 35 °, 40 °, 45 °} at $z = 0$ m.

Fig. 4.19 presents the error in the estimation of the polar angle for a particular value $\gamma = 30\,°$, depending on the receiver's position in the area under coverage. Two heights, $z = 0\,\text{m}$ and $z = 1\,\text{m}$, are considered, whereas the receiver is placed along the X and Y axes, always with the same angle $\gamma = 30\,°$. The red crosses represent the projected position of the transmitters in the XY plane. The polar angle $\gamma = 30\,°$ is selected due to its proximity to the global error CDF in Fig. 4.18. It is possible to distinguish a rotated cross in Fig. 4.19 where absolute errors are higher and close to $1\,°$. This cross is actually rotated $30\,°$, the same as the yaw angle $\gamma = 30\,°$. This is due to the fact that some uncertainty appears when coordinates x_r and/or y_r are close to 0, since in these cases the point of incidence in the QADA surface is near to the axes of the photoreceiver. Note that these higher errors are strongly dependent on the selected yaw angle γ and appear for any value of γ.

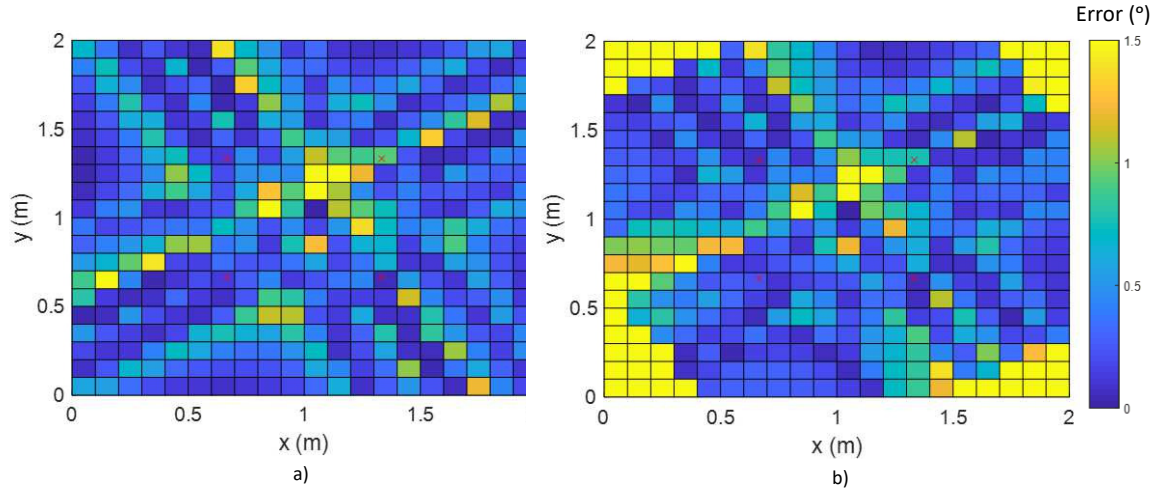

Figure 4.19: Absolute errors in the estimation of the polar angle, depending on the coordinates x_r and y_r, with $\gamma = 30\,°$ and a SNR of 10 dB at: a) $z = 0\,\text{m}$; b) $z = 1\,\text{m}$.

It is also possible to observe in Fig. 4.19.b) that no signal is detected in the corners and positioning is not possible. Therefore, the absolute errors of the estimated coordinates (x, y, z) are analysed by means of a CDF in Fig. 4.20 for a rotation angle γ in the first octant, every $5\,°$, at $z = 0\,\text{m}$. In 90 % of the measurements, the absolute error in the coordinates x and y is 0.12 m, whereas it is 0.32 m for the coordinate z. Note that those absolute values are the same for any polar angle γ considered since they converge in the CDFs for 90 % of the measurements in all cases considered here. Thus, it is worth mentioning that an increase of $1\,°$ in the absolute error of the polar angle (the difference between the worst and the best cases in Fig. 4.18) is negligible from the point of view of the positioning algorithm, with similar results in all the coordinates in Fig. 4.20.

Finally, a grid of $2 \times 2\ \text{m}^2$ in steps of 50 cm is detailed, with a total of 25 points of measurement represented as black crosses, as is shown in Fig. 4.21. The yaw angles considered here are $\gamma = \{5\,°, 10\,°, 15\,°, 20\,°, 25\,°, 30\,°, 35\,°, 40\,°, 45\,°\}$ at $z = 0\,\text{m}$. Thus, all the polar angles, from $0\,°$ up to $360\,°$, are considered, as previously demonstrated. Similarly, the absolute errors of the coordinates x, y and z for those points are detailed as CDF in Fig. 4.22.

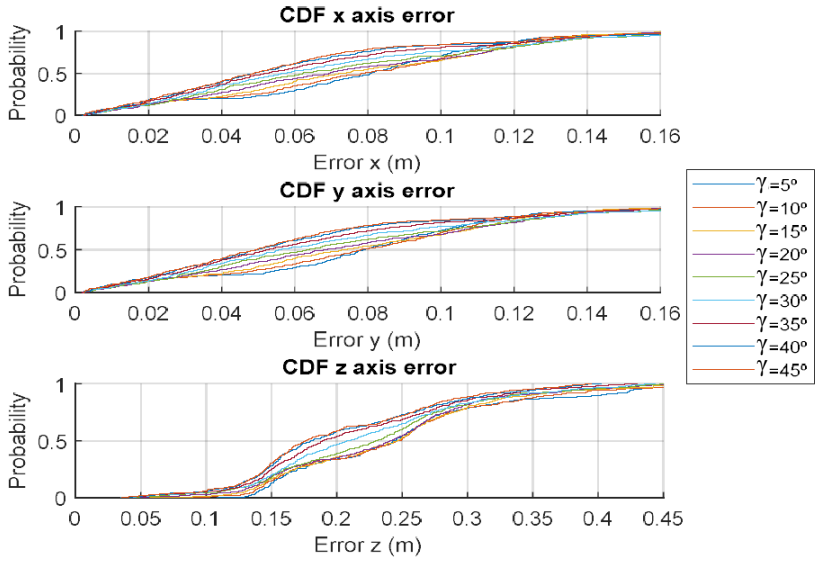

Figure 4.20: CDF of the absolute errors with a SNR of 10 dB for coordinates x, y and z at $z = 0$ m, depending on the yaw angle γ.

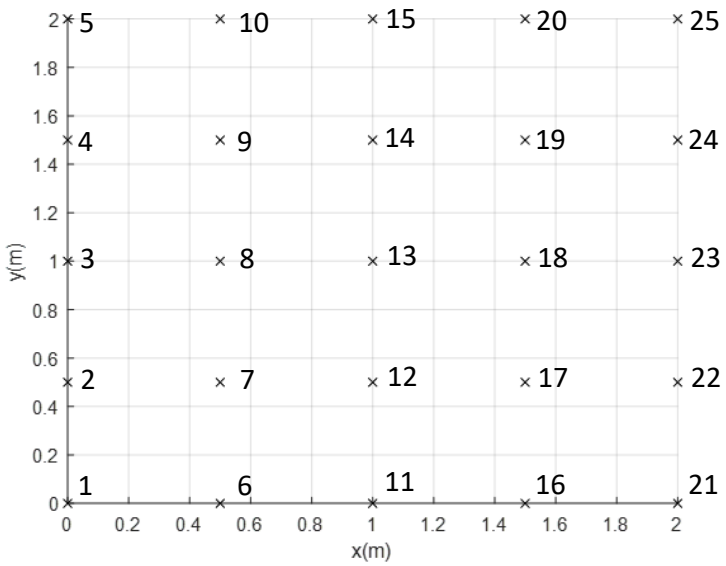

Figure 4.21: Scheme of the analysed points in a grid of 2×2 m^2.

Fig. 4.22 provides a good understanding of the positioning algorithm, which strongly depends on the position where the receiver is located. Those blue curves in the CDF of the absolute error for the coordinate x are the ones corresponding to those points in the centre of the X axis, and, therefore, they have the best performance with less than 4 cm of absolute error in 90 % of the measurements. On the other hand, the green and orange curves are those points in the region between the centre and the border of the X axis, reaching errors of around 8 cm for the coordinate x. Finally, the worst absolute errors are found at the corners of the X axis for red and pink curves. Coordinates y and z behave similarly to coordinate x. Note that there is a slight difference in the behaviour of the CDFs between Fig. 4.20 and

Fig. 4.22, due to the points considered in the simulation. In Fig. 4.20 all the points in the grid were simulated, whereas in Fig. 4.22 only 25 points are taken into account, with a majority of those in the borders of the grid.

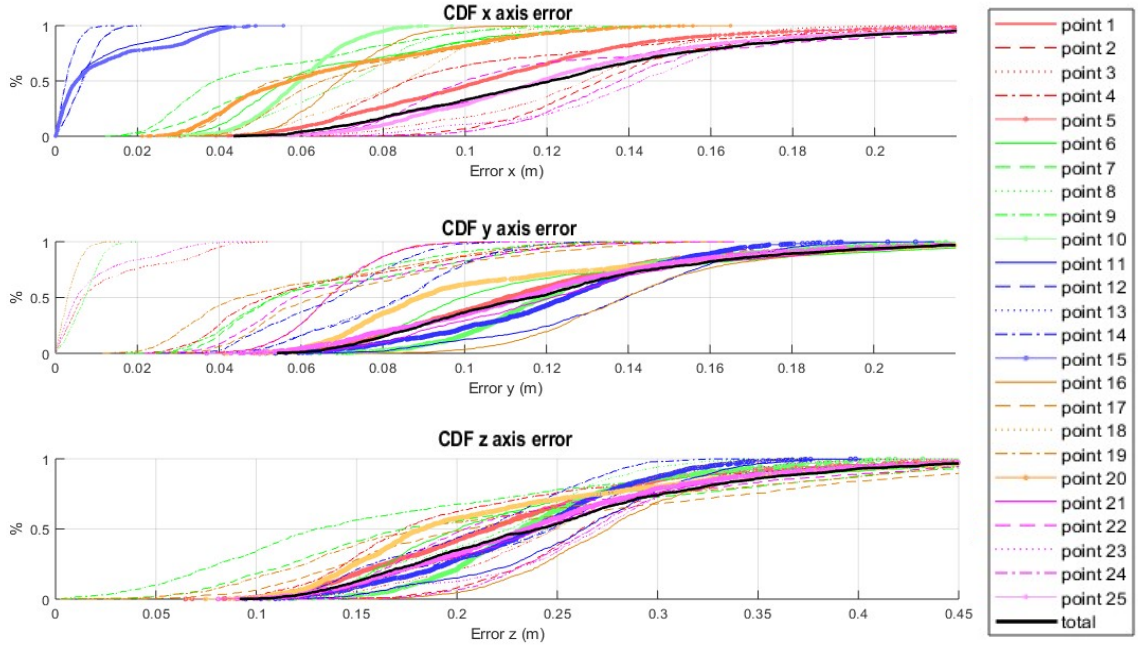

Figure 4.22: CDF of the absolute error of the coordinates x, y and z with a SNR of 10 dB for the 25 analysed points at $z = 0$ m.

4.3.2 Positioning Algorithm with PnP Solutions

The PnP problem has been thoroughly investigated in computer vision and mathematics. The minimal case occurs when $n = 3$, namely P3P, and yields four possible solutions [Gao03]. Closed-form solutions for the P3P problem are known for more than a century. For $n \leq 4$, the problem has a unique solution in general non-degenerate configurations. When the n points lie in a plane, the problem is known as Planar-PnP. Existing PnP solutions can be divided into iterative and non-iterative methods. Non-iterative PnP methods use convex relaxations that admit a closed-form solution [Lep09, Abd15] or are based on finding the roots of polynomial equations [Gao03, Li12]. Some representative Non-Iterative methods from the state-of-the-art are: Efficient Perspective-n-Point Camera Pose Estimation (EPnP) [Lep09], Robust Non-Iterative Solution of Perspective-n-Point (RPnP) [Li12] and Infinitesimal Plane-Based Pose Estimation (IPPE) [Col14], which exclusively solves Planar-PnP. EPnP is usually sub-optimal for $n < 5$, and requires a special configuration to work in the planar or quasi-planar case [Li12]. RPnP is accurate for both planar and non-planar cases. Finally, iterative PnP methods are often more accurate than non-iterative methods. They are based on optimizing a non-convex Maximum-Likelihood reprojection cost with iterative descent methods. These methods have a high computational cost and require to be initialized near the optimum, usually with a non-iterative method [Li12, Lep09].

In EPnP [Lep09], the n 3D points are defined as a weighted sum of four virtual control points. The algorithm estimates the 3D coordinates of these control points in the receiver coordinate system.

It expresses these coordinates as a weighted sum of the eigenvectors of a 12×12 matrix, and solves a small system of quadratic equations to select the appropriate weights. Furthermore, the solution can be used to initialize a Gauss-Newton refinement scheme in order to improve accuracy.

In the RPnP solution [Li12], the PnP problem is expressed as a least squares polynomial function F, derived from the classic P3P polynomial equations [Li11]. The minima of F are found as the roots of its derivative F', using the eigenvalue method. This method explores the properties of this function minima, and their geometric relationship with the degenerate configurations and the Planar-PnP case.

The IPPE solution [Col14] exclusively solves the Planar-PnP problem. First, it estimates the coefficients of the homographic transformation between the image coordinates and the 3D plane that contains the transmitters. Second, it finds the pose parameters from the homographic coefficients. This is a decomposition algorithm, that exploits redundancy in the homographic coefficients to find the pose in closed-form, maximizing the pose accuracy. This involves solving a local non-redundant 1^{st} order Partial Differential Equation (PDE). IPPE is very optimized in terms of computational complexity, being suitable to run in real-time in lightweight computing hardware.

Experiments and Results

Hereinafter, the EPnP, IPPE and RPnP algorithms are applied to the estimation of the receiver's pose using simulated data. Note that each algorithm is initially designed for certain conditions and particular cases and, therefore, their behaviour will be different regarding the proposed optical system, where a planar configuration with four transmitters is deployed ($n = 4$). It is worth mentioning that EPnP and RPnP handle both planar and non-planar configurations: EPnP is more suitable for $n \geq 4$ [Lep09], whereas RPnP presents a robust and high accuracy estimation of the pose when $n < 5$ [Li12].

In the following simulations, the volume under analysis is $2 \times 2 \times 3.4\,\mathrm{m}^3$. There is a distance of 3.4 m between the ceiling, where the transmitters are installed, and the floor, where the receiver is placed. This receiver is tested on a grid of points defined in the floor with an interval of 10 cm. The number of measurements per analysed point is 50 and a Gaussian Noise has been added in the received signal in order to have a Signal-to-Noise Ratio (SNR) of 10 dB. It is considered that the LEDs emit a 1151-bit LS sequence with a displacement of 10 samples and, in the reception, the QADA has an aperture length of $l = 2.75$ mm.

Note that the rotations considered in the receiver throughout these analysis are limited to the Z axis, $\gamma = \{0\,^\circ, 120\,^\circ, 240\,^\circ\}$. The mean absolute errors for each coordinate, and for the aforementioned EPnP, IPPE and RPnP algorithms, are plotted in Figs. 4.23 - 4.25 with $\gamma = 120\,^\circ$. It can be observed how the errors in the grid of considered points are linked to the distance between the transmitters and the receiver, thus providing slightly higher errors in the corners of the proposed scenario. Similar results are found for $\gamma = \{0\,^\circ, 240\,^\circ\}$.

For clarity's sake, a general analysis is detailed in Fig. 4.26, where the Cumulative Distribution Function (CDF) of the absolute pose error is presented for the EPnP, IPPE and RPnP algorithms with $\gamma = \{0\,^\circ, 120\,^\circ, 240\,^\circ\}$. These errors in the estimation of the 2D coordinates (x, y) are below 10 cm for the IPPE and EPnP algorithms and below 20 cm for the RPnP algorithm. In addition, the absolute error related to coordinate z is 3 cm, 7 cm and 30 cm for the IPPE, RPnP and EPnP algorithms, respectively. On the other hand, the errors in the estimation of the rotation angles α and β are below $1.5\,^\circ$ for the IPPE

and EPnP algorithms, whereas below 4 ° for RPnP. Finally, the absolute errors in the estimation of γ are 0.2 °, 0.4 ° and 10 ° for IPPE, RPnP and EPnP, respectively.

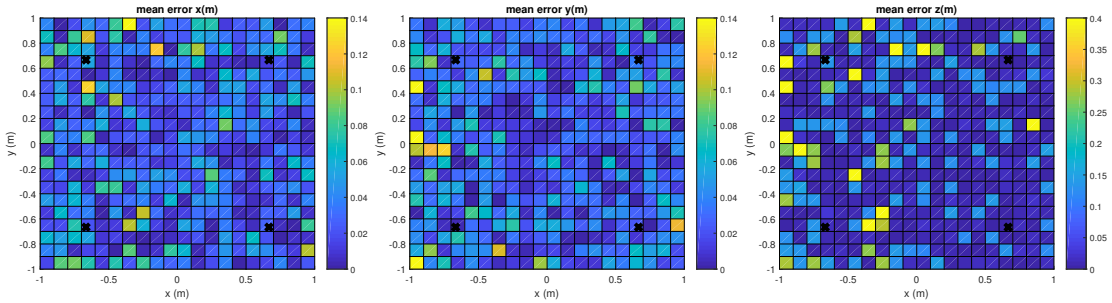

(a) coordinate x **(b)** coordinate y **(c)** coordinate z

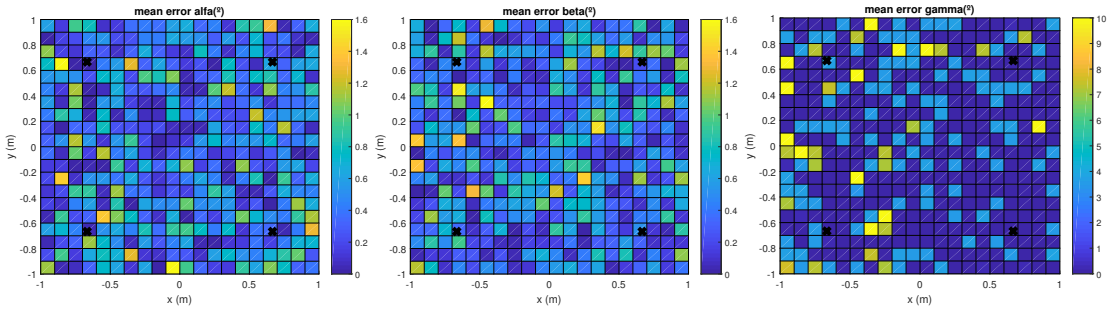

(d) α **(e)** β **(f)** γ

Figure 4.23: Mean absolute errors in the grid of considered points in the floor for the EPnP algorithm and a rotation in the Z axis γ =120 °.

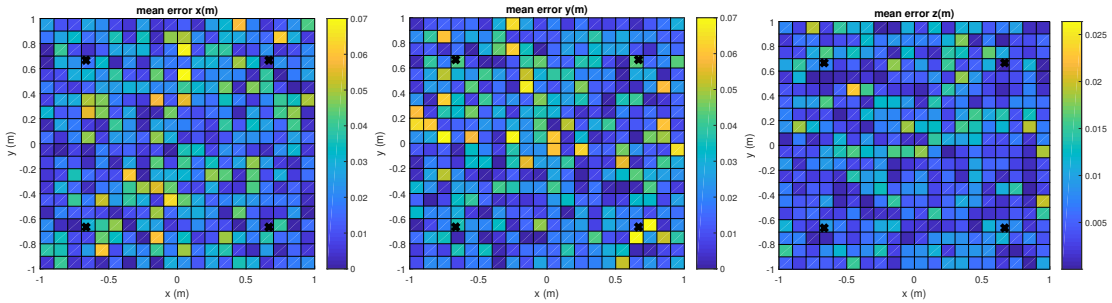

(a) coordinate x **(b)** coordinate y **(c)** coordinate z

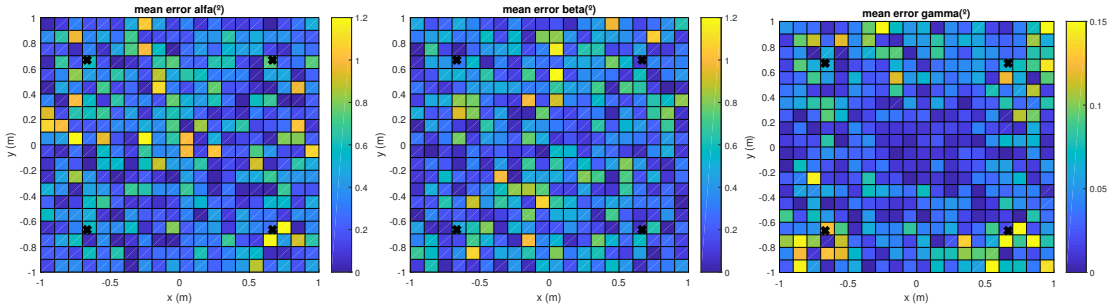

(d) α **(e)** β **(f)** γ

Figure 4.24: Mean absolute errors in the grid of considered points in the floor for the IPPE algorithm and a rotation in the Z axis γ =120 °.

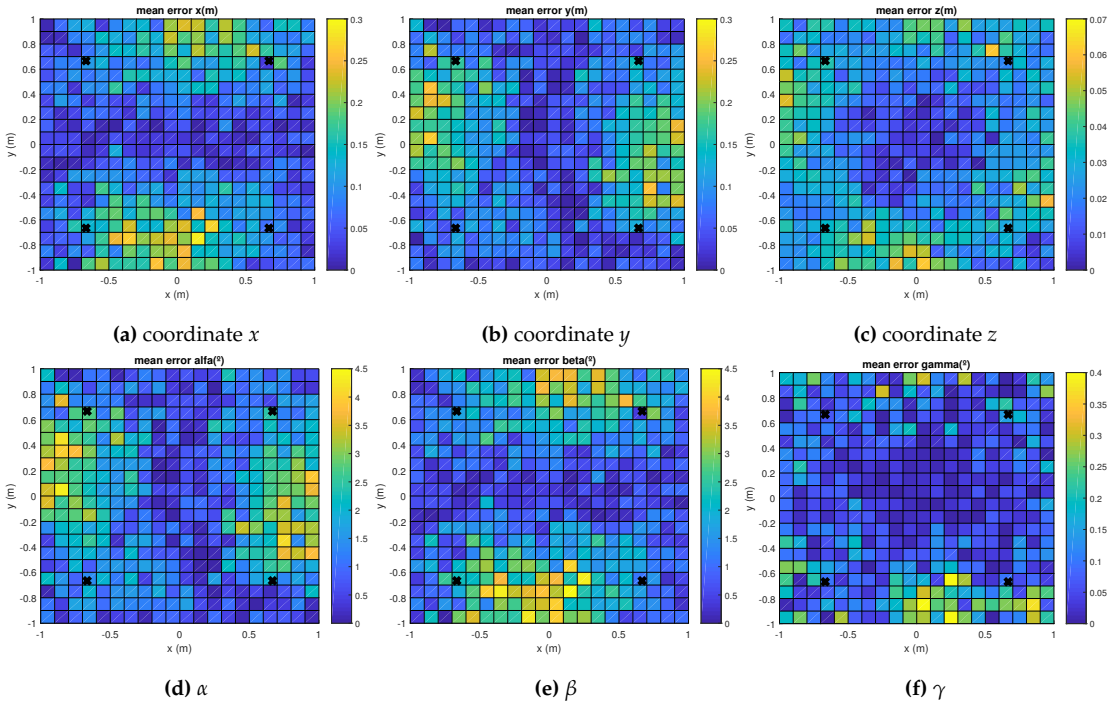

(a) coordinate x **(b)** coordinate y **(c)** coordinate z

(d) α **(e)** β **(f)** γ

Figure 4.25: Mean absolute errors in the grid of considered points in the floor for the RPnP algorithm and a rotation in the Z axis $\gamma = 120\,^{\circ}$.

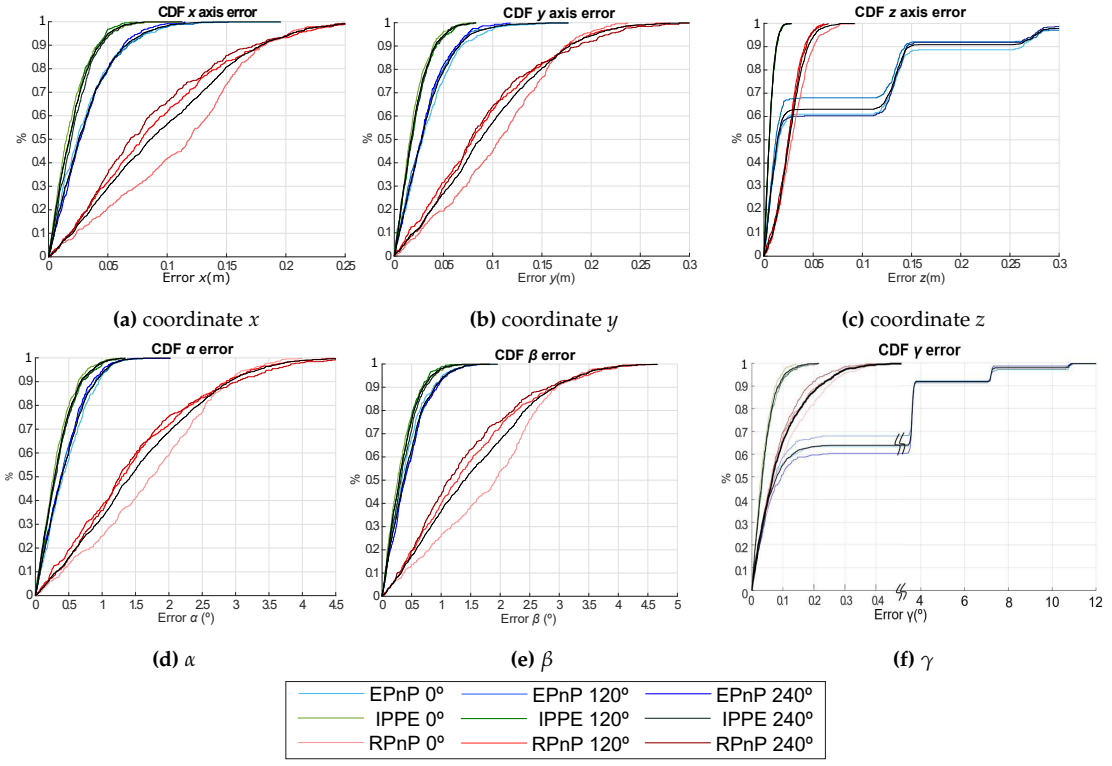

(a) coordinate x **(b)** coordinate y **(c)** coordinate z

(d) α **(e)** β **(f)** γ

Figure 4.26: CDF of the absolute pose errors for EPnP, IPPE and RPnP, according to the rotation in the Z axis $\gamma = \{0\,^{\circ}, 120\,^{\circ}, 240\,^{\circ}\}$.

In addition to the previous analysis, a particular CDF for nine points in the same scenario (see Fig. 4.27) is presented in Figs. 4.28 - 4.30 for the EPnP, IPPE and RPnP algorithms. These points are located in the first quadrant (see Table 4.3), as the rest of quadrants will have a similar behaviour given the symmetries of the positioning system, and consider variations in all the rotation angles (0 ° - 360 °) with a step of 10 °. The number of measurements per analysed point is 50 and the SNR is still 10 dB. This value has been selected since it has been checked, in the experimental tests, that typical values of SNR in the environment are around 10 dB. The obtained absolute errors are similar to those in Fig. 4.26. Note that the points in the corner of the area under analysis (points 3, 6, 7, 8, 9) present slightly higher errors than those in the center of the analysed scenario (points 1, 2, 4, 5). Moreover, although all the involved algorithms behave similarly, the IPPE presents better results for the proposed system in all the cases.

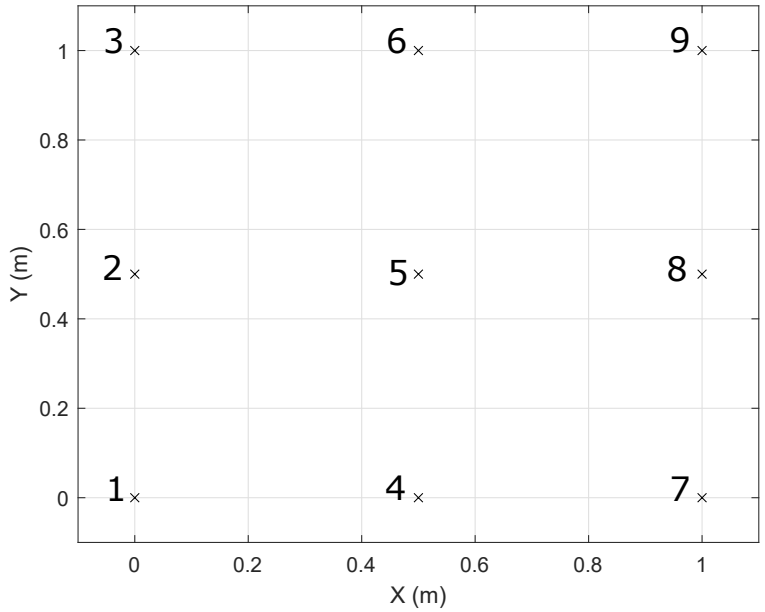

Figure 4.27: Scheme of the nine representative points considered in the first quadrant and detailed in Table 4.3.

Table 4.3: Coordinates of the nine representative points considered in the first quadrant for a further analysis.

Points	**Coordinates (m)**
Point 1	(0, 0)
Point 2	(0, 0.5)
Point 3	(0, 1)
Point 4	(0.5, 0)
Point 5	(0.5, 0.5)
Point 6	(0.5, 1)
Point 7	(1, 0)
Point 8	(1, 0.5)
Point 9	(1, 1)

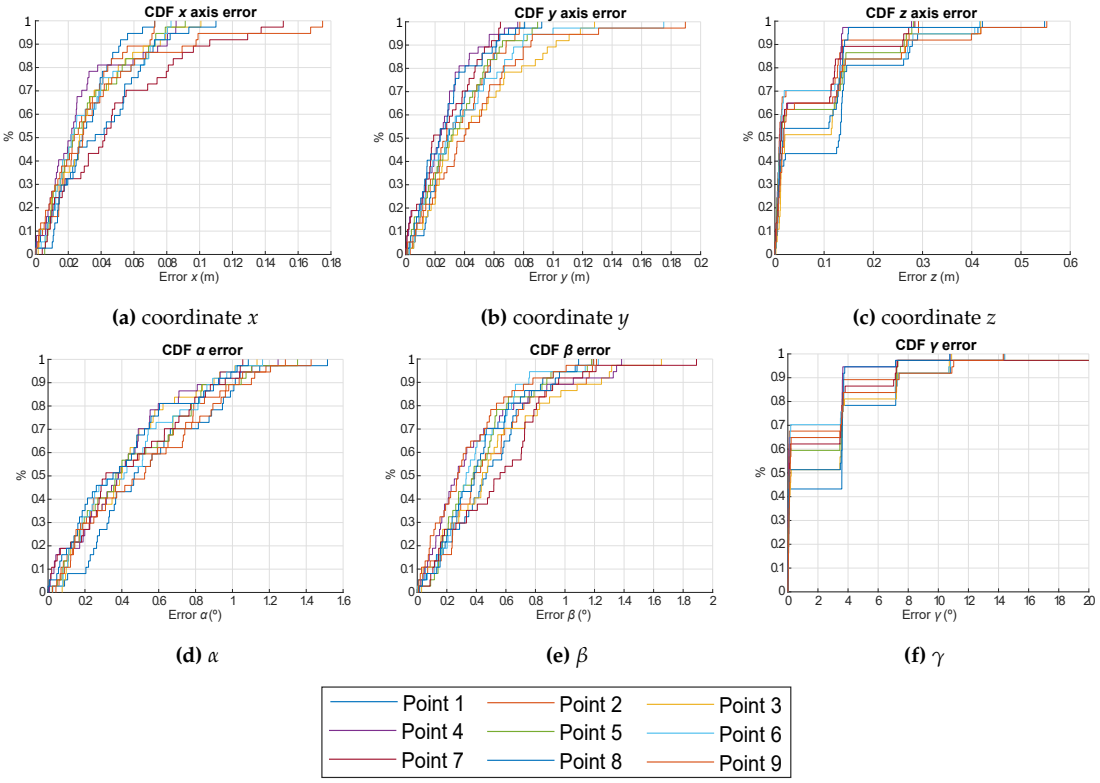

(a) coordinate x **(b)** coordinate y **(c)** coordinate z

(d) α **(e)** β **(f)** γ

Figure 4.28: CDF of the absolute pose errors for the nine representative points defined in Table 4.3 whether using the EPnP algorithm.

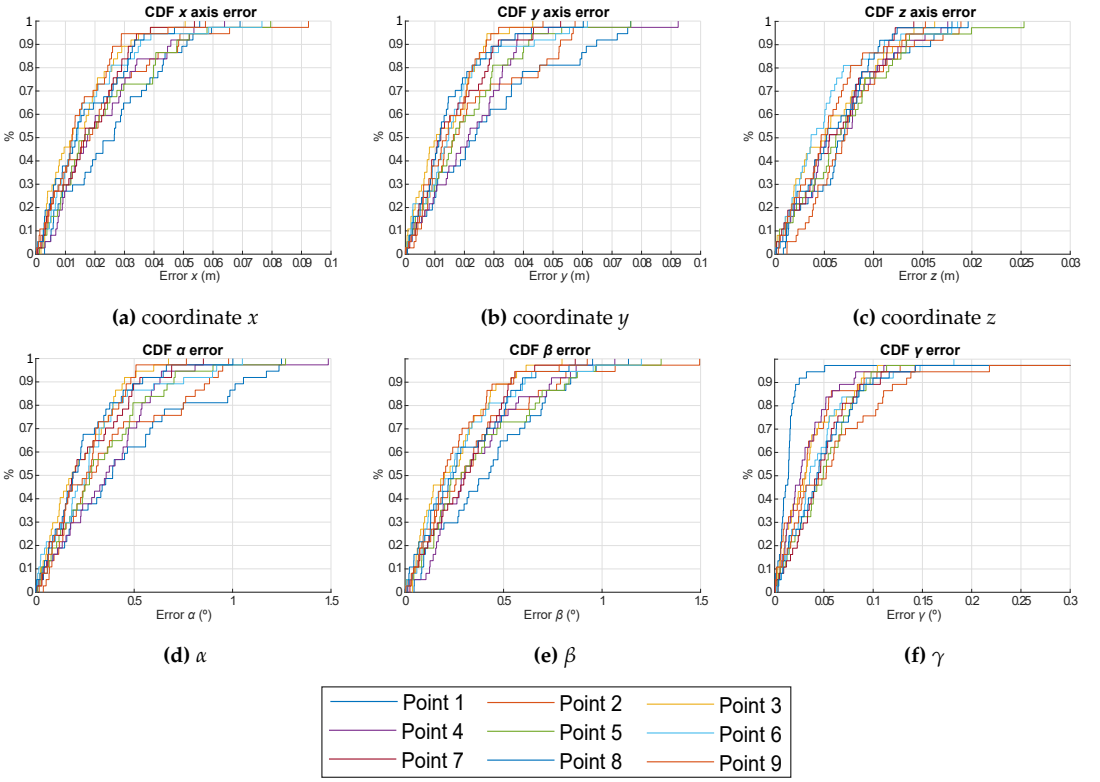

(a) coordinate x **(b)** coordinate y **(c)** coordinate z

(d) α **(e)** β **(f)** γ

Figure 4.29: CDF of the absolute pose errors for the nine representative points defined in Table 4.3 whether using the IPPE algorithm.

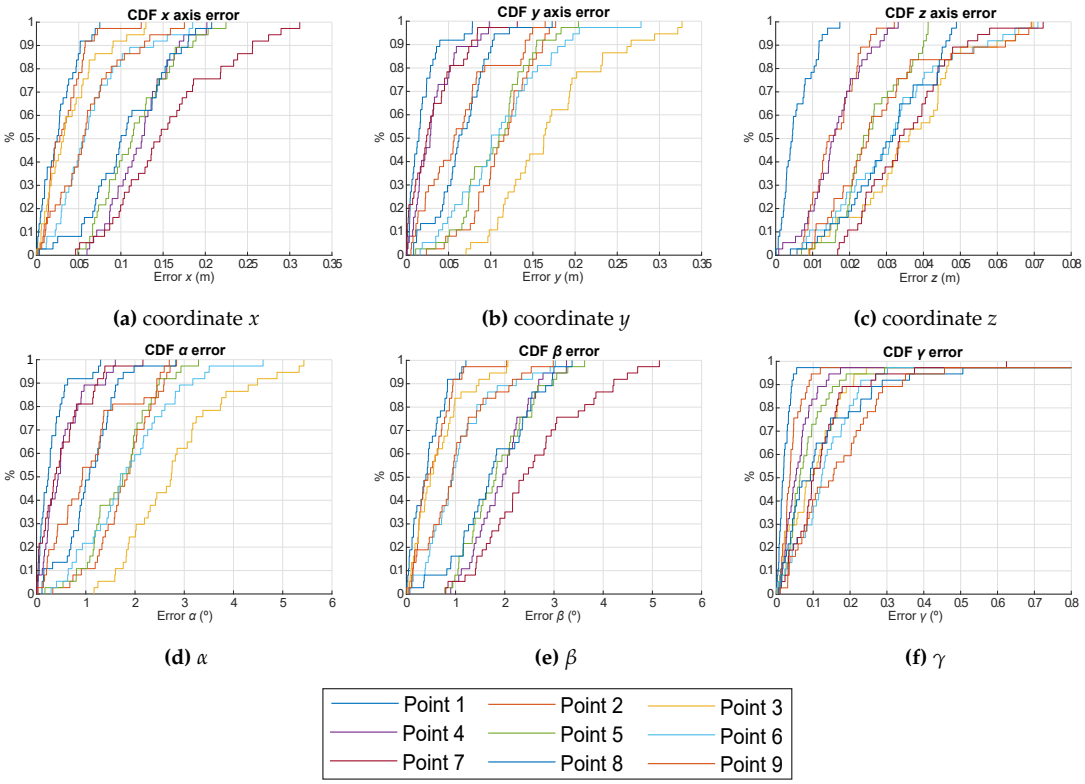

(a) coordinate x **(b)** coordinate y **(c)** coordinate z

(d) α **(e)** β **(f)** γ

Figure 4.30: CDF of the absolute pose errors for the nine representative points defined in Table 4.3 whether using the RPnP algorithm.

Furthermore, in order to clearly select the most suitable algorithm for the proposed system, we have analysed the robustness of the system in the estimation of the pose when varying the 3D location of one transmitter according to a Gaussian noise, $\{\sigma_x, \sigma_y, \sigma_z\} = 1\,\text{cm}$. These simulations have been performed under the same conditions as before, with a volume of $2 \times 2 \times 3.4\,\text{m}^3$ and a number of realization per point of 50. This analysis is detailed in Fig. 4.31, where the CDF of the absolute pose error is presented for the EPnP, IPPE and RPnP algorithms with $\gamma = \{0\,^\circ, 120\,^\circ, 240\,^\circ\}$. All the considered algorithms present a similar behaviour again, with a slightly better response of the IPPE algorithm. For IPPE, the absolute errors in the estimation of the 2D coordinates (x, y) are below 10 cm and the absolute error related to coordinate z is 3 cm, in 90% of cases. On the other hand, the absolute errors in the estimation of the rotation angles α and β are below $1.5\,^\circ$ for 90% of the cases, whereas γ is below $0.2\,^\circ$, also for 90% of the cases.

4.4 Calibration

The importance of a suitable calibration of the receiver is crucial to improve the obtained results by minimizing undesired misalignments, related to the optical centre (x_c, y_c), the height h_{ap} at which the aperture is located, the aperture misalignment δ and the length l of the aperture.

One of the most commonly used algorithms in camera calibration is the Zhang Method [Zha00], where several images are taken typically from a checkerboard. However, this method is unfeasible in this proposal since we only have 4 image points (the 4 transmitters) against the 49 image points that a checkerboard provides. Besides, this method does not calibrate the aperture misalignment δ, since

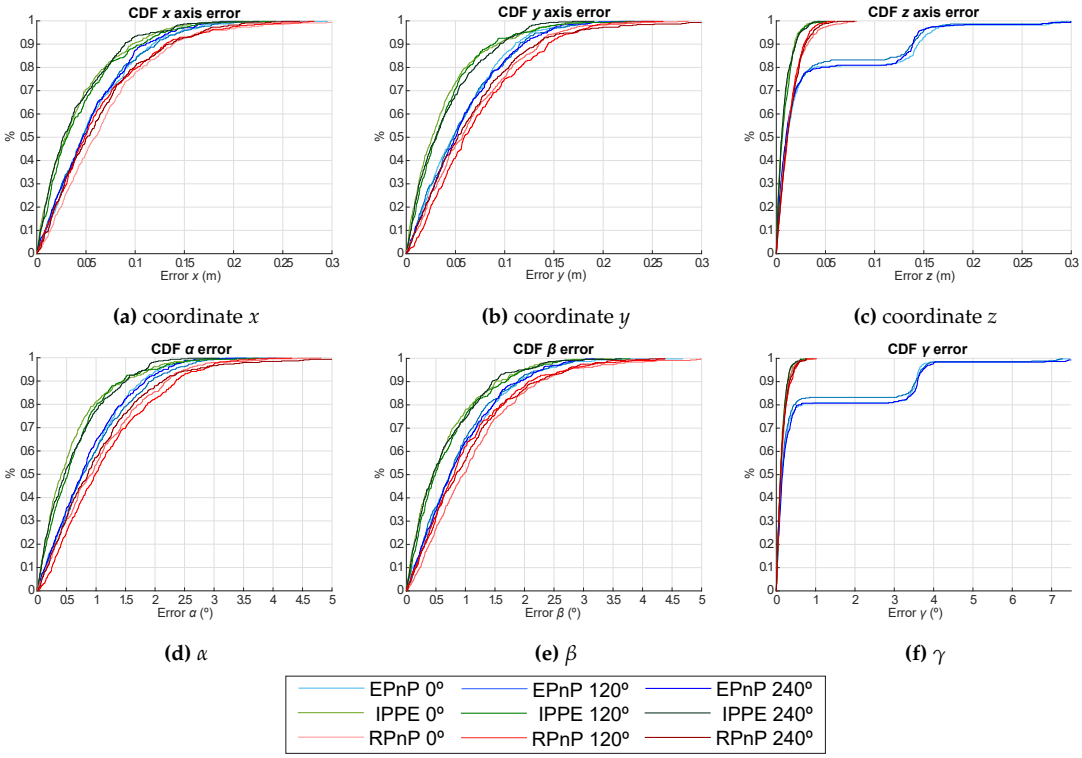

(a) coordinate x **(b)** coordinate y **(c)** coordinate z

(d) α **(e)** β **(f)** γ

Figure 4.31: CDF of the absolute pose errors for the EPnP, IPPE and RPnP algorithms and a rotation in the Z axis $\gamma = \{0\,°, 120\,°, 240\,°\}$, when varying the location of a transmitter with a Gaussian noise $\sigma = 1$ cm.

cameras involve lenses instead of apertures. Therefore, a novel calibration algorithm is proposed here, which combines iterative methods to obtain the optimized parameters in (4.39) (see the pseudocode 1 presented below).

In the first phase, the aperture height h_{ap}, or focal length in the optical system, has been estimated according to (4.57) (see Fig. 4.32), where D and d_r are the distances between pairs of transmitters obtained with a high precision system (such as Optitrack system [Opt21] or Leica total station [Geo14]) and pairs of image points, respectively; and H is the distance between the transmitter's and the receiver's plane.

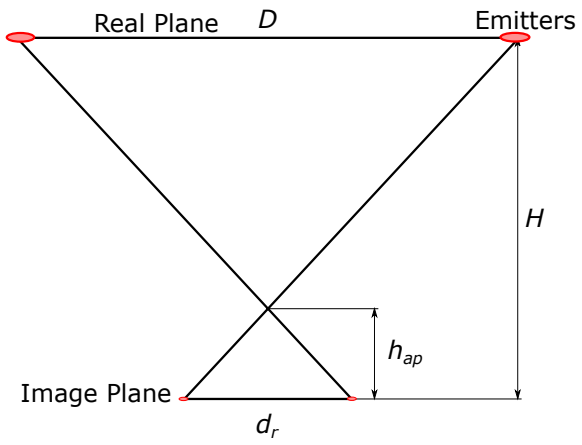

Figure 4.32: Calibration of the aperture height h_{ap} using the relation between distances in the real and image worlds.

Algorithm 1 Calibration algorithm pseudo-code

Phase 1 - Estimation of the aperture height

$h_{ap} = \frac{H}{\frac{D}{d_r}+1}$

Phase 2 - Estimation of the optical centre (x_c, y_c) using a Branch and Bound algorithm

while $step > tolerance$ **do**
  for $x_c = min_x : step : max_x$ **do**
    for $y_c = min_y : step : max_y$ **do**
      [x,y] = PositioningAlgorithm(x_c, y_c)
      $Grid(x_c, y_c)$ = std(x,y)
    end for
  end for
  [$value_x$, $value_y$] = find(max($Grid$))
  [min_x, min_y] = [$value_x$, $value_y$] - [$step$, $step$]
  [max_x, max_y] = [$value_x$, $value_y$] + [$step$, $step$]
  $step = step/2$
end while

Phase 3 - Estimation of the focal length adjustment λ using a Branch and Bound algorithm

while $step > tolerance$ **do**
  for $h_{ap} = min : step : max$ **do**
    z = PositioningAlgorithm(h_{ap})
    $Grid(h_{ap})$ = std(z)
  end for
  $value$ = find(max($Grid$))
  $min = value - step$
  $max = value + step$
  $step = step/2$
end while

Phase 4 - Estimation of the aperture misalignment δ using LLS

$\delta = pinv(\mathbf{J}) \cdot \begin{bmatrix} \mathbf{r_x} \\ \mathbf{r_y} \end{bmatrix}$

$$h_{ap} = \frac{H}{\frac{D}{d_r} + 1} \tag{4.57}$$

The second and third phases determine the optical centre (x_c, y_c) and the focal length adjustment λ, respectively, by applying a Branch and Bound algorithm that minimizes the experimental positioning error. The optical centre has been estimated by minimizing the 2D standard deviation, whereas the focal length adjustment λ has been determined by minimizing the standard deviation of coordinate z. The Branch and Bound algorithm recursively splits the search space into smaller spaces while keeping track of minimum and maximum bounds that reduce the search space and neglecting the solutions that are not optimal. In this proposal, the algorithm starts testing all the possible solutions within a search space. Then, it finds the value that minimizes the standard deviation and updates the maximum and minimum bounds as one step forward and backwards from that value. This method is recursively repeated by dividing by half the step at each iteration, until it reaches a certain tolerance.

In particular, in order to estimate the optical centre we have set (1, 1) mm and $(-1, -1)$ mm as the initial maximum and minimum bounds, respectively, and 0.1 mm as the initial step. The algorithm stops when the step is 0.025 mm, therefore, just three iterations are needed. On the other hand, in order to estimate the focal length adjustment, the initial maximum and minimum bounds are 2 and 0.5, respectively, and the step is set at 0.1. In this case, the algorithm stops when the step is 0.05, so that only two iterations are required. Note that the radius of the QADA sensor is 3.9 mm and a slightly off-centre aperture may imply high errors in the estimation of the receiver's position.

Finally, the fourth phase of the algorithm estimates the misalignment δ of the aperture by means of Linear Least Squares (LLS) with the Moore-Penrose Pseudoinverse to minimize the error in the estimation of the image points (4.39) using the experimental measurements, as well as the ground-truth of the measured points. The algorithm starts calculating the residuals $\begin{bmatrix} r_x \\ r_y \end{bmatrix}_{P_j,\gamma,i}$ by applying (4.58), where $\begin{bmatrix} \hat{x}_r \\ \hat{y}_r \end{bmatrix}_{P_j,\gamma,i}$ is the ideal image point for each transmitter i obtained for each point P_j and rotation γ; and $f(\mathbf{p}_{P_j,\gamma,i}, \delta)$ is defined in (4.59), where $\mathbf{p}_{P_j,\gamma,i}$ are the measured values of p_x and p_y for a particular point P_j and a rotation angle γ for each transmitter i. The ratios p_x and p_y are the measured values from the correlation peaks, as shown in (4.3) and (4.4). The length l of the aperture, the focal length adjustment λ and the optical centre (x_c, y_c) are obtained according to the above-mentioned phases of the calibration algorithm.

$$\begin{bmatrix} r_x \\ r_y \end{bmatrix}_{P_j,\gamma,i} = \begin{bmatrix} \hat{x}_r \\ \hat{y}_r \end{bmatrix}_{P_j,\gamma,i} - f(\mathbf{p}_{P_j,\gamma,i}, \delta) \tag{4.58}$$

$$f(\mathbf{p}_{P_j,\gamma,i}, \delta) = \frac{-l}{2} \cdot \lambda \cdot \begin{bmatrix} p_x + \delta \cdot p_y \\ -\delta \cdot p_x + p_y \end{bmatrix}_{P_j,\gamma,i} + \begin{bmatrix} x_c \\ y_c \end{bmatrix} \tag{4.59}$$

In addition, the Jacobian matrix for a certain transmitter i is defined in (4.60) for a particular point P with a certain rotation γ, according to δ.

$$\mathbf{J}_{P_j,\gamma,i} = \frac{\partial f(\mathbf{p}_{P_j,\gamma,i}, \delta)}{\partial \delta} = \frac{-l}{2} \cdot \lambda \cdot \begin{bmatrix} p_y \\ -p_x \end{bmatrix}_{P_j,\gamma,i} \tag{4.60}$$

After the residuals are obtained for all the points considered, the solution for the misalignment δ is obtained by means of an oversized system and using the pseudoinverse matrix (*pinv*), according to (4.61), being n the total number of points and m the total number of rotations γ.

$$\delta = pinv(\mathbf{J}) \cdot \begin{bmatrix} \mathbf{r_x} \\ \mathbf{r_y} \end{bmatrix} = pinv \left(\begin{bmatrix} \frac{-l}{2} \cdot \lambda \cdot p_{y_{1,1,1}} \\ \frac{-l}{2} \cdot \lambda \cdot p_{y_{1,2,1}} \\ \dots \\ \frac{-l}{2} \cdot \lambda \cdot p_{y_{n,m,4}} \\ \frac{-l}{2} \cdot \lambda \cdot (-p_{x_{1,1,1}}) \\ \frac{-l}{2} \cdot \lambda \cdot (-p_{x_{1,2,1}}) \\ \dots \\ \frac{-l}{2} \cdot \lambda \cdot (-p_{x_{n,m,4}}) \end{bmatrix} \right) \cdot \begin{bmatrix} r_{x_1} \\ r_{x_2} \\ \dots \\ r_{x_n} \\ r_{y_1} \\ r_{y_2} \\ \dots \\ r_{y_n} \end{bmatrix} \tag{4.61}$$

Chapter 6 will provide an experimental quantification of the improvement obtained due to the implementation of an accurate calibration.

4.5 Conclusions

In this chapter, the performance of the 3D Infrared or Visible Light Positioning system has been studied considering if the estimation of the image points follows a linear or a non-linear function and the positioning techniques. Here some partial conclusions are listed:

- In order to achieve a high coverage volume, a full usage of the area of the photodiode is defined by setting the side of the aperture equal to the diameter of the photoreceptor. In this configuration, a Non-Linear Least Squares Estimator (NLSE) using the Gauss-Newton algorithm is implemented to estimate the image points using a look-at-table with precalculated values of the non-linear function. On the other hand, the use of a small aperture assures the linearization of the involved algorithms, which simplifies them and improve the system performance.
- Regarding the estimation of the receiver's position, two solutions are proposed:
  - The first one, a triangulation technique, solved by LSE and some geometrical considerations achieving 3D positioning average errors in simulations below 13 cm and 5.5 cm when the separation in height between the emitters and the receiver is 2 m and 1 m respectively, and a general absolute error of 0.9 ° in the estimation of the polar angle γ (later on, in Chapter 6, real results will also be presented at heights of 3.4 m).
  - The second solution are different PnP approaches, such as EPnP, IPPE and RPnP. In general terms, the errors in the estimation of the 2D coordinates (x, y) are below 10 cm for the IPPE and EPnP algorithms and below 20 cm for the RPnP algorithm, when the separation in height between the emitters and the receiver is 3.4 m. The absolute error related to coordinate z is 3 cm, 7 cm and 30 cm for the IPPE, RPnP and EPnP algorithms, respectively. Simulations have verified that the PnP algorithm with a better behaviour in this proposal is the IPPE algorithm.

- The strong dependence of the system on the incidence light angle has also been proven, and consequently, the direct dependence on the location of the receiver in the proposed scenario for different rotation angles γ in the Z axis. In addition, a novel calibration algorithm has been defined and applied to the proposal, by combining trigonometric considerations for the aperture height, a Branch and Bound algorithm for the optical centre and the focal length adjustment, and a Linear Least Squares algorithm for the aperture misalignment.

The next chapter will detail a similar algorithm implementation but with a different configuration, as well as some simulated results that will be also presented and discussed.

Chapter 5

Centralized Local Positioning System

In Chapter 4 we presented a positioning system focused on privacy-oriented applications, where the receivers were located on board the person, object, or whatever to be positioned and the transmitters were placed at fixed locations in the scenario. On the contrary, this chapter focuses on the implementation and validation of a centralized Local Positioning System, based on a rigid set of mobile emitter LEDs, and at least two fixed receivers at know positions in the room.

Note that the fact that the receivers are static in pre-established positions simplifies some processes and is less constraining for the electronic modules to be used. This simplification is directly related to how the positioning algorithm is implemented as well as to the hardware involved. The minimum required hardware are 1 LED and 2 QADAs, although since the equations and algorithms proposed here are calculated independently for each pair of LED-QADA, more LEDs and QADAs can be easily added to have a more robust system, if needed. In addition, there is no restriction on the rotational angles that the moving LEDs can have, allowing the system to position 3D mobile objects such as drones using minimal hardware.

This system is intended for long-distance measurements (over 4 m) using Visible or Infrared Light signals and includes an ad hoc synchronization module only to allow the receiver module to acquire when new data is available, thus facilitating real-time operation. The 3D pose of the transmitters is obtained by the implementation of a Least Squares Estimator (LSE). In addition, geometrical considerations of the transmitter deployments can also be added to the LSE algorithm to increase the robustness of the link. It is worth noting the possibility of adding more advanced fusion techniques such as the Extended Kalman Filter (EKF), to further refine the minimisation of the equations.

This chapter is organized as follows: the first section provides an introduction to the proposed system; the second section describes the algorithm developed to estimate the final coordinates of the receiver using an AoA algorithm and an EKF, as well as the simulated results that verify the proposal; and the last section discusses some conclusions.

5.1 Proposed System

The proposed optical positioning system is based on a set of LEDs located at 3D unknown positions $\mathbf{b}_i$ within the coverage area, as well as at least two receivers located at known places on a certain plane and a synchronization module. It should be noted that the suggested system does not need synchronization,

but its usage facilitates real-time operation. The overall system is shown in Fig. 5.1 where (X, Y, Z) are the global axes of the system and $(X_r, Y_r, Z_r)_p$ are the local axes of the mobile target p. It is worth mentioning that although the system can estimate the 3D pose $(x, y, z)_p$ with just 1 LED and 2 receiver modules, for some scenarios (when working at large distances with low SNR, when it is difficult to maintain the LoS between transmitter and receivers, etc.) it may be interesting to add more LEDs, to increase the robustness of the positioning algorithm and/or estimate the complete pose of the object $(x, y, z, \alpha, \beta, \gamma)_p$. For instance, only one LED is needed to estimate the 3D pose $(x, y,z)_p$, two LEDs to estimate the 3D pose and one degree of freedom $(x, y, z, \gamma)_p$ (i.e. mobile robot in a planar plane), and three or more LEDs to estimate the complete 3D pose with three degrees of freedom $(x, y, z, \alpha, \beta, \gamma)_p$ (i.e. drone). Although we will hereinafter assume the ceiling as the plane where the receivers are deployed in this Chapter, all the proposed algorithms can be adapted to other planes (i.e. walls).

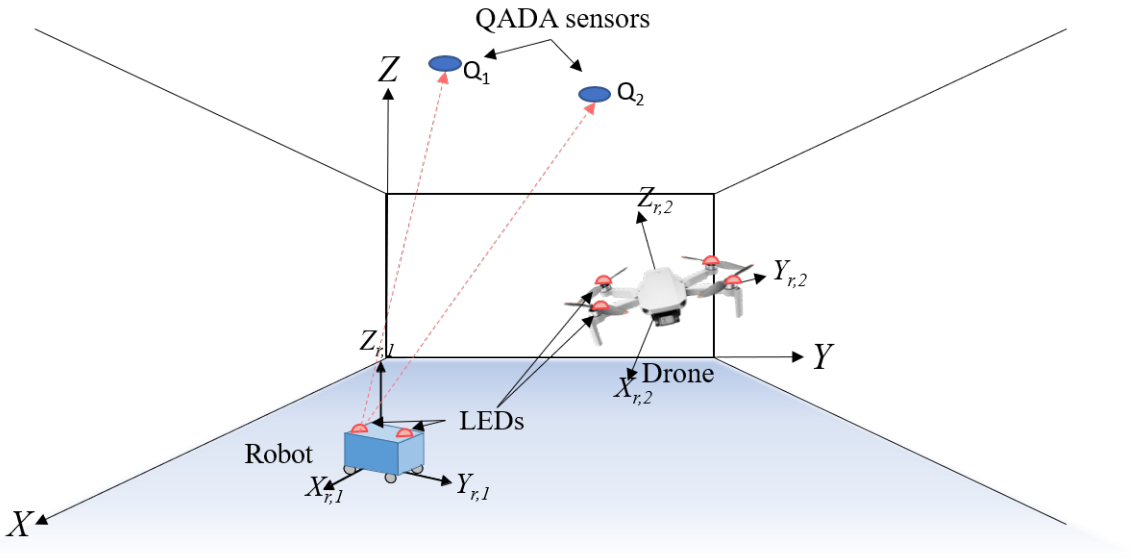

Figure 5.1: General diagram of the proposed positioning system.

The implemented receiver, transmitter and synchronisation modules are those presented in Chapter 3.1; a general overview is presented in Fig. 5.2, where the transmitters LED are located on board of the mobile to be positioned (i.e. a drone), while the receivers are located in a certain plane (i.e. the ceiling). The synchronization beacon emits a 1 ms pulse every 0.5 s. When the synchronization pulse is captured by the beacons and the receiver modules, transmission and acquisition start simultaneously. The beacons emit a 1151-bit LS sequence with a BPSK modulation and a square carrier signal with a carrier frequency of $f_c = 25$ kHz. Each LED has its unique code. The transmission has been defined by using an oversampling of $M = f_s/f_c = 10$ samples for a carrier cycle (sampling frequency of $f_s = 250$ kHz) and sequence shifting of 10 samples, which improves the cross-correlation properties of the codes at the receiver by minimising the Multiple Access Interference (MAI) effect, produced by the simultaneous transmission and reception of all the sequences. The receiver consists of a quadrant circular photoreceptor (QADA) with a square aperture placed on top of it, a filtering system, a synchronization signal detector and an acquisition system STM32F469I Discovery. The acquired signals come from the signals measured by the QADA after filtering and are then stored in a micro-SD for further processing on a computer. The positioning system does not need to be synchronized.

The synchronization beacon is only included in the design to facilitate the acquisition of the emitted sequences.

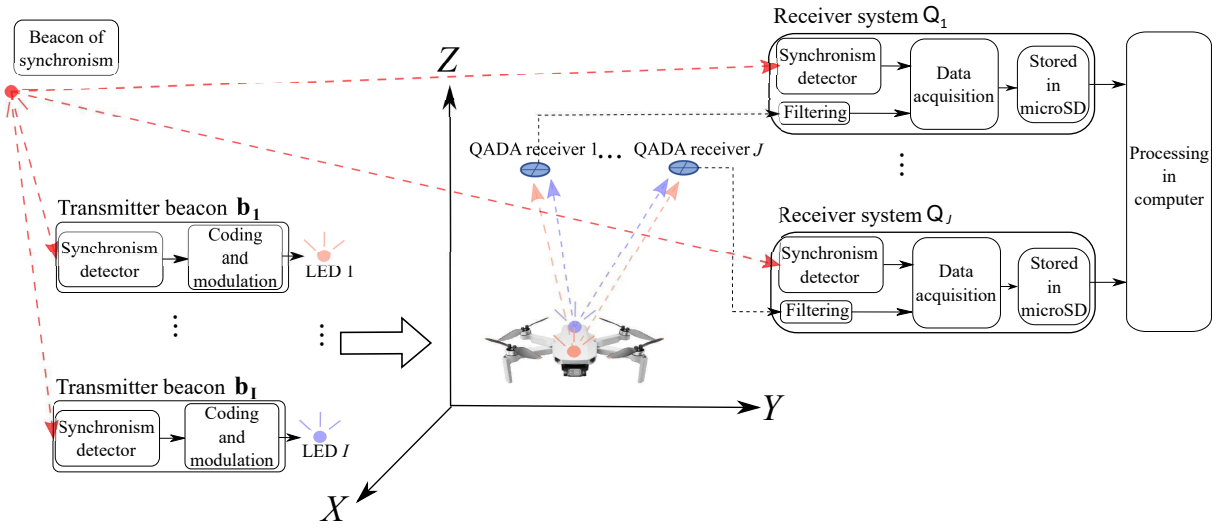

Figure 5.2: General overview of the proposed centralized positioning system.

5.2 Positioning System

The positioning system starts with the correlation of the acquired signals with the emitted codes to later determine the value of the maximum peaks from the correlation signals and finally estimate the image points in the QADA receiver. The image points in the QADA receiver $(x_{r,i,j}, y_{r,i,j})$ are estimated following the calculations carried out in Section 4.2 for each LED i on each QADA j as defined in Eq. (5.1). The intrinsic parameters under consideration in Eq. (5.1) are the optical center (x_c, y_c), which is defined as the center of the square aperture placed on top of the QADA receiver; the height h_{ap} at which the aperture is located (in other words, the focal length); the aperture misalignment δ, which is defined as the rotation of the aperture with respect to the photoreceiver axis; and the length of the aperture l.

$$\begin{bmatrix} x_{r,i,j} \\ y_{r,i,j} \end{bmatrix} = \frac{-l_j}{2} \cdot \lambda_j \cdot \begin{bmatrix} p_{x,i,j} + \delta_j \cdot p_{y,i,j} \\ -\delta_j \cdot p_{x,i,j} + p_{y,i,j} \end{bmatrix} + \begin{bmatrix} x_{c,j} \\ y_{c,j} \end{bmatrix} \tag{5.1}$$

The image points in Eq. (5.1) are geometrically related with the transmitter's 3D coordinates (x_t, y_t, z_t) as follows:

$$\begin{bmatrix} x_{r,i,j} \\ y_{r,i,j} \\ z_{r,i,j} \end{bmatrix} = \Big[\mathbf{R}|\mathbf{t}\Big] \cdot \begin{bmatrix} x_t \\ y_t \\ z_t \end{bmatrix} \tag{5.2}$$

where $\Big[\mathbf{R}|\mathbf{t}\Big]$ concatenates the rotation matrix $\mathbf{R} = \mathbf{R}(\alpha, \beta, \gamma)$ and the translation matrix $\mathbf{t} = (x, y, z)^\top$, which is defined as the receiver's location.

Once the image points in the QADA receiver $(x_{r,i,j}, y_{r,i,j})$ have been estimated, the positioning algorithm continues to obtain the final coordinates $(x_{t,i}, y_{t,i}, z_{t,i})$ of the i-th transmitter's position in the proposed scenario by means of the Least Squares Estimator (LSE). The proposed 2D scenario is detailed

in Fig. 5.3.a), where the point (x_j, y_j) is the 2D position of the j-th QADA receiver; $(x_{t,i}, y_{t,i})$ is the 2D position of the LED beacon i; $\kappa_{i,j}$ is the angle between the transmitter and the X axis for each LED i and QADA j; and $\theta_{i,j}$ is the angle between the image point $(x_{r,i,j}, y_{r,i,j})$ of each LED i and the X_r axis of each QADA j. Thus, note that the proposed positioning algorithm is based on triangulation techniques.

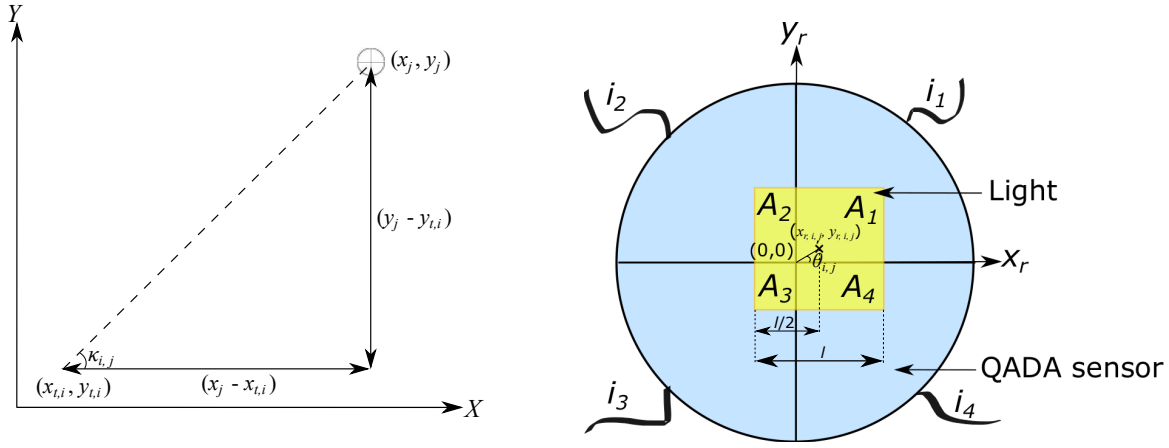

Figure 5.3: Geometrical analysis of the proposed system with QADA j and LED i: a) 2D projection on global coordinates; b) 2D projection on the receiver local coordinates.

From Fig. 5.3, the geometrical expression (5.3) can be written as (5.4).

$$\tan(\kappa_{i,j}) = \frac{\sin(\kappa_{i,j})}{\cos(\kappa_{i,j})} = \frac{\delta y}{\delta x} = \frac{y_j - y_{t,i}}{x_j - x_{t,i}} \tag{5.3}$$

$$-x_{t,i} \cdot \sin(\kappa_{i,j}) + x_j \cdot \sin(\kappa_{i,j}) = -y_{t,i} \cdot \cos(\kappa_{i,j}) + y_j \cdot \cos(\kappa_{i,j}) \tag{5.4}$$

Keeping in mind the geometrical distribution of the QADA receiver and its aperture shape in Fig. 5.3.b), it is possible to obtain (5.5), similarly to (5.3). Since the receivers are neither rotated nor tilted (they are actually fixed in the ceiling aligned with the global axes of the system), then $\kappa_{i,j} = \theta_{i,j}$, and Eq. (5.4) can be simplified according to (5.6).

$$\tan(\theta_{i,j}) = \frac{\sin(\theta_{i,j})}{\cos(\theta_{i,j})} = \frac{y_{r,i,j}}{x_{r,i,j}} \tag{5.5}$$

$$-x_{t,i} \cdot y_{r,i,j} + x_j \cdot y_{r,i,j} = -y_{t,i} \cdot x_{r,i,j} + y_j \cdot x_{r,i,j} \tag{5.6}$$

Eq. (5.6) can be transformed into a matrix form $\mathbf{A}\cdot\mathbf{X}=\mathbf{b}$, where the least squares estimator (LSE), using the Levenberg-Marquardt method, estimates the global 2D coordinates $(x_{t,i}, y_{t,i})$ of the transmitter beacon i (5.7).

$$(x_{t,i}, y_{t,i}) = (\mathbf{A}^T \cdot \mathbf{A})^{-1} \cdot \mathbf{A}^T \cdot \mathbf{b} \tag{5.7}$$

Where, $\mathbf{A} = \begin{bmatrix} -y_{r,i,j} & x_{r,i,j} \end{bmatrix}$ and $\mathbf{b} = \begin{bmatrix} y_j \cdot x_{r,i,j} - x_j \cdot y_{r,i,j} \end{bmatrix}$ for each QADA sensor j and each LED i.

An example of a complete deployment, where 4 QADAs and 4 LEDs are used, is given by $\mathbf{A} = \begin{bmatrix} -y_{r,1,1} & x_{r,1,1} \\ -y_{r,1,2} & x_{r,1,2} \\ \dots & \\ -y_{r,4,4} & x_{r,4,4} \end{bmatrix}$ and $\mathbf{b} = \begin{bmatrix} y_1 \cdot x_{r,1,1} - x_1 \cdot y_{r,1,1} \\ y_2 \cdot x_{r,1,2} - x_2 \cdot y_{r,1,2} \\ \dots \\ y_4 \cdot x_{r,4,4} - x_4 \cdot y_{r,4,4} \end{bmatrix}$.

After estimating the 2D location of the transmitters ($x_{t,i}$, $y_{t,i}$), the coordinate $z_{t,i}$ is obtained by means of the triangulation relationship detailed in Section 4.3 (see Fig. 4.15) as denoted in (5.8).

$$z_{t,i,j} = z_j - h_{ap} \cdot \left(1 + \sqrt{\frac{(x_{t,i} - x_{r,i,j})^2 + (y_{t,i} - y_{r,i,j})^2}{x'^2_{r,i,j} + y'^2_{r,i,j}}}\right)$$
$$z_{t,i} = \frac{1}{\sum_{j=1}^{j} d^2_{i,j}} \cdot \sum_{j=1}^{j} \left(d^2_{i,j} \cdot z_{t,i,j}\right) \tag{5.8}$$

Thus, the coordinate $z_{t,i}$ is obtained as the weighted averaged value from the differences between the height z_j of the receivers $j = \{1, 2, ..., J\}$ and the geometrically calculated height h_j (see Fig. 4.15), where $d_{i,j}$ is the distance between the estimated beacons' position ($x_{t,i}$, $y_{t,i}$) and the projection of each receiver j in the plane where the transmitters are placed.

Once the 3D coordinates are estimated, the rotation angles (α, β, γ) can be estimated by knowing the geometry of the beacons on the mobile robot/drone. Note that at least 3 beacons are needed to estimate the complete pose.

In addition to (5.7), where only the angles of arrival equations are considered, the geometry of the system can also be included in the LSE minimization to increase the robustness of the proposal. In particular, in Eq. (5.9) the Euclidean distance between transmitters is presented for LEDs $i = \{1, 2\}$. Similar equations can be derived for the rest of the deployed emitters. Note that since it is a non-linear equation, the Non-Linear Least Squares Estimator (NLSE) is applied instead of the LSE.

$$d_{1,2} = \sqrt{(x_{t,1} - x_{t,2})^2 + (y_{t,1} - y_{t,2})^2 + (z_{t,1} - z_{t,2})^2} \tag{5.9}$$

To increase the robustness of the link, fusion filters such as the Kalman Filter (KF) or the Extended Kalman Filter (EKF), as well as homographic techniques such as those implemented in Section 4.3, can also be implemented.

5.2.1 Positioning Algorithm with Fusion Filters

Regarding the fusion filters, one must first consider whether the equations to be used are non-linear or linear. Note that the estimation of the image points (5.1) as well as the LSE approach (5.6) are linear equations. On the other hand, Eq. (5.9) is a non-linear equation. In addition, we can also differentiate between loosely and tightly coupled systems. In this proposal we implement a tightly coupled algorithm in a non-linear system that uses the ratios $\mathbf{p}_x$ and $\mathbf{p}_y$ (4.3 - 4.4) and the geometry of the transmitters' arrangement to estimate the final coordinates of the transmitters ($x_{t,i}, y_{t,i}, z_{t,i}$) using an EKF.

The EKF provides estimates for non-linear systems, relying on the covariance matrices of the input and output noises of the process. The EKF uses Jacobian matrices to linearise the equations and thus solve non-linear problems in two steps: prediction and update. The estimation may not be optimal (as for the Kalman Filter, KF), but it has enough precision for most applications. The state model of the EKF is presented in (5.10), where $\mathbf{X}_k = (x_{t,i}, y_{t,i}, z_{t,i})_k$ is the estimated position of the transmitters on the current state k; w_k is the process noise; $\mathbf{Z}_k$ is the array of measurements given by the estimated ratios $\mathbf{p}_x$ and $\mathbf{p}_y$ from the correlation functions and the distances between transmitters; and v_k is the measurements noise.

$$\begin{aligned} \mathbf{X}_k &= f(\mathbf{X}_{k-1}) + w_k \\ \mathbf{Z}_k &= h(\mathbf{X}_k) + v_k \end{aligned} \tag{5.10}$$

After initializing the vector of position $\mathbf{X}_0$ and the transition matrix $\mathbf{P}_0$, the recursive loop between predictions and updates starts until convergence to the estimated final position. Eq. (5.11) presents the prediction step that estimates the a priori state vector $\hat{\mathbf{X}}_k^-$ and its covariance $\mathbf{P}_k^-$; and Eq. (5.12) shows the update step which updates the state vector $\hat{\mathbf{X}}_k$, its covariance $\mathbf{P}_k$ and the Kalman gain $\mathbf{K}$.

$$\begin{aligned} \hat{\mathbf{X}}_k^- &= f(\hat{\mathbf{X}}_{k-1}) \\ \mathbf{P}_k^- &= \mathbf{A}_k \cdot \mathbf{P}_{k-1} \cdot \mathbf{A}_k^T + \mathbf{Q} \end{aligned} \tag{5.11}$$

$$\begin{aligned} \mathbf{K} &= \mathbf{P}_k^- \cdot \mathbf{H}_k^T \cdot (\mathbf{H}_k \cdot \mathbf{P}_k \cdot \mathbf{H}_k^T + \mathbf{R})^{-1} \\ \hat{\mathbf{X}}_k &= \hat{\mathbf{X}}_k^- + \mathbf{K} \cdot (\mathbf{Z}_k - h(\hat{\mathbf{X}}_k^-)) \\ \mathbf{P}_k &= (\mathbf{I} - \mathbf{K} \cdot \mathbf{H}_k) \cdot \mathbf{P}_k^- \end{aligned} \tag{5.12}$$

Where $\mathbf{K}$ is the Kalman Filter gain that minimizes the residual error; $\mathbf{Q}$ and $\mathbf{R}$ are the process and measurement noise error covariance matrices, respectively; $\mathbf{A}_k$ is the derivative of $f(\hat{\mathbf{X}}_{k-1})$ with respect to the state vector $\hat{\mathbf{X}}_k^-$; and $\mathbf{H}_k$ represents the derivative of $h(\hat{\mathbf{X}}_k^-)$ with respect to the state vector $\hat{\mathbf{X}}_k^-$. It is given as:

$$\mathbf{A}_k = \left. \frac{\partial f(\hat{\mathbf{X}}_{k-1})}{\partial \hat{\mathbf{X}}_k^-} \right|_{X_k} \tag{5.13}$$

$$\mathbf{H}_k = \left. \frac{\partial h_k(\hat{\mathbf{X}}_k^-)}{\partial \mathbf{X}_k^-} \right|_{X_k} \tag{5.14}$$

The covariance matrices of the process and measurement are fixed experimentally. In particular, the measurement noise matrix $\mathbf{R}_{ij}$ is fixed experimentally as $\mathbf{Q}_i/10$ as defined in (5.15) and (5.16), where σ^2 are the variances of the measured positions.

$$\mathbf{Q}_i = \begin{pmatrix} \sigma_i^2 & 0 & 0 \\ 0 & \sigma_i^2 & 0 \\ 0 & 0 & \sigma_i^2 \end{pmatrix}, \quad \mathbf{Q} = \begin{pmatrix} \sigma_1^2 & 0 & 0 & \cdots & 0 & 0 & 0 \\ 0 & \sigma_1^2 & 0 & \cdots & 0 & 0 & 0 \\ 0 & 0 & \sigma_1^2 & \cdots & 0 & 0 & 0 \\ \vdots & \vdots & \vdots & \ddots & \vdots & \vdots & \vdots \\ 0 & 0 & 0 & \cdots & \sigma_i^2 & 0 & 0 \\ 0 & 0 & 0 & \cdots & 0 & \sigma_i^2 & 0 \\ 0 & 0 & 0 & \cdots & 0 & 0 & \sigma_i^2 \end{pmatrix} \tag{5.15}$$

$$\mathbf{R}_{ij} = \begin{pmatrix} \sigma_{ij}^2/10 & 0 & 0 \\ 0 & \sigma_{ij}^2/10 & 0 \\ 0 & 0 & \sigma_{ij}^2/10 \end{pmatrix}, \quad \mathbf{R} = \begin{pmatrix} \sigma_{1,1}^2/10 & 0 & 0 & \cdots & 0 & 0 & 0 \\ 0 & \sigma_{1,1}^2/10 & 0 & \cdots & 0 & 0 & 0 \\ 0 & 0 & \sigma_{1,1}^2/10 & \cdots & 0 & 0 & 0 \\ \vdots & \vdots & \vdots & \ddots & \vdots & \vdots & \vdots \\ 0 & 0 & 0 & \cdots & \sigma_{ij}^2/10 & 0 & 0 \\ 0 & 0 & 0 & \cdots & 0 & \sigma_{ij}^2/10 & 0 \\ 0 & 0 & 0 & \cdots & 0 & 0 & \sigma_{ij}^2/10 \end{pmatrix} \tag{5.16}$$

Note that **A** and **Q** are diagonal matrices of order $3 \cdot i$, since we aim to estimate the 3D coordinates (x, y, z) for each LED i. Similarly, **R** is a diagonal matrix with an order of $2 \cdot i \cdot j$; since we consider both ratios p_x and p_y per QADA j per LED i. The dimension of **R** increases when adding the geometrical considerations included in Eq. (5.9). For instance, if we have four QADAs and four LEDs with four geometrical equations, then, **A** and **Q** are matrices with order 12 and **R** is a matrix of order 36.

The a priori state $h(\hat{\mathbf{X}}_k^-)$ is defined as (5.17). We have added the geometrical considerations for 2 LEDs but it can be extended with as many equations as needed to cover all the deployed transmitters.

$$h(\hat{\mathbf{X}}_k^-) = \begin{bmatrix} \mathbf{p}_x \\ \mathbf{p}_y \\ \sqrt{(x_{t,1} - x_{t,2})^2 + (y_{t,1} - y_{t,2})^2 + (z_{t,1} - z_{t,2})^2} \end{bmatrix} \tag{5.17}$$

Combining Eq. (5.1) - (5.2), the ratios p_x and p_y for a certain LED i and a QADA j can be defined as (5.18 - 5.19) if no rotation is considered in any axis ($\alpha = \beta = \gamma = 0\,°$).

$$p_{x,i,j} = \frac{2 \cdot x_c - 2 \cdot \delta \cdot y_c - \frac{2 \cdot h_{ap} \cdot (x_j - x_{t,i})}{z_j + z_{t,i}} + \frac{2 \cdot \delta \cdot h_{ap} \cdot (y_{t,i} - y_{t,i})}{z_j + z_{t,i}}}{l \cdot \lambda \cdot (\delta^2 + 1)} \tag{5.18}$$

$$p_{y,i,j} = \frac{2 \cdot y_c + 2 \cdot \delta \cdot x_c - \frac{2 \cdot h_{ap} \cdot (y_j - y_{t,i})}{z_j + z_{t,i}} - \frac{2 \cdot \delta \cdot h_{ap} \cdot (x_j - (x_{t,i}))}{z_j + z_{t,i}}}{l \cdot \lambda \cdot (\delta^2 + 1)} \tag{5.19}$$

Where the position of the receiver and the calibration parameters (δ, h_{ap}, λ, l) are pre-known values and, the transmitters' position is defined by the a priori solution ($\hat{\mathbf{X}}_k^-$).

Note that Eqs. (5.18) and (5.19) can be particularized as Eqs. (5.20) and (5.21) using ideal values for the calibration parameters ($\delta = 0$, $\lambda = 1$, $l = 2.75$ mm, $(x_c, y_c) = (0, 0)$ mm) with h_{ap} in millimeters.

$$p_{x,i,j} = -\frac{8 \cdot h_{ap} \cdot (x_j - x_{t,i})}{11 \cdot (z_j + z_{t,i})} \tag{5.20}$$

$$p_{y,i,j} = -\frac{8 \cdot h_{ap} \cdot (y_j - y_{t,i})}{11 \cdot (z_j + z_{t,i})} \tag{5.21}$$

5.2.2 Simulated Results

In the following, some simulated results are presented. Hereinafter, the area under analysis is a 4×4 m^2 plane with a grid of points every 10 cm performing 20 iterations at each point, the distance between transmitter and receivers is 3.4 m and no rotation in any axis is implemented ($\alpha = \beta = \gamma = 0\,°$). Gaussian noise of 10 dB has been added in the output signals of each QADA receiver. The transmitter has been placed at each of the points of the grid while different geometrical deployments of the QADA receivers are presented in Fig. 5.4. The geometrical deployments of the QADA receiver in Fig. 5.4 are: a) two QADAs aligned in the X axis; b) three QADAs distributed in the corners of an equilateral triangle; c) four QADAs distributed in the corners of a square; d) four non-aligned QADAs.

To detail how the errors are distributed in the test area, the mean absolute errors for each coordinate when using two receivers and a single transmitter is presented in Fig. 5.5. The deployment of the QADA receivers is the one presented in Fig. 5.4 a) with a distance $d = 10$ cm and their projections are represented in Fig. 5.5 with black crosses. Table 5.1 details their coordinates. It can be observed how the

errors in the grid of considered points are linked to the position of the receivers and therefore, to their image points, thus providing higher errors at those positions where the image point of the transmitter on both QADAs is the same. Eq. (5.7) presents a singularity that is responsible for these errors. The transmitter's position is estimated using AoA measurements with the LSE algorithm. No fusion filter has been considered in this simulation.

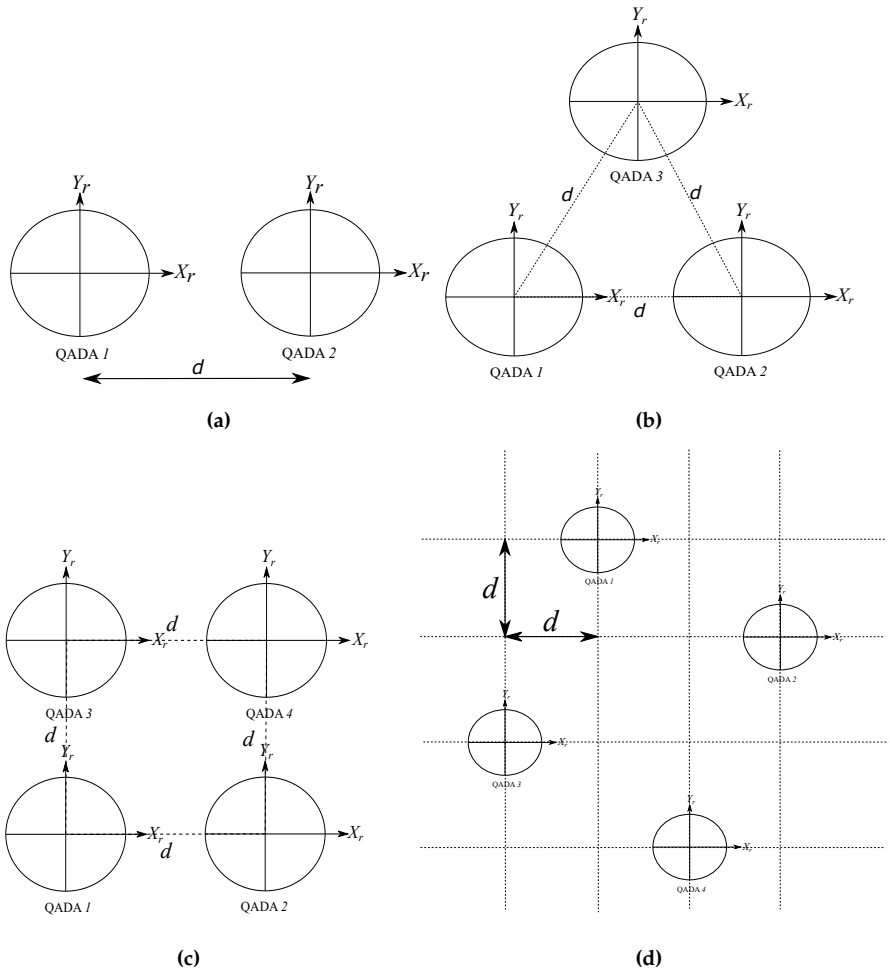

Figure 5.4: Geometrical distribution of the proposed system with a different number of QADAs j: a) distribution of QADAs $j = \{1, 2\}$; b) distribution of QADAs $j = \{1, 2, 3\}$; c) distribution of QADAs $j = \{1, 2, 3, 4\}$ located in the corners of a square; d) distribution of four non-aligned QADAs $j = \{1, 2, 3, 4\}$.

Table 5.1: Receiver's coordinates considered in Fig. 5.5.

QADA j	**Coordinates** (x_j, y_j, z_j)
QADA 1	(1.95 m, 2 m, 3.40 m)
QADA 2	(2.05 m, 2 m, 3.40 m)

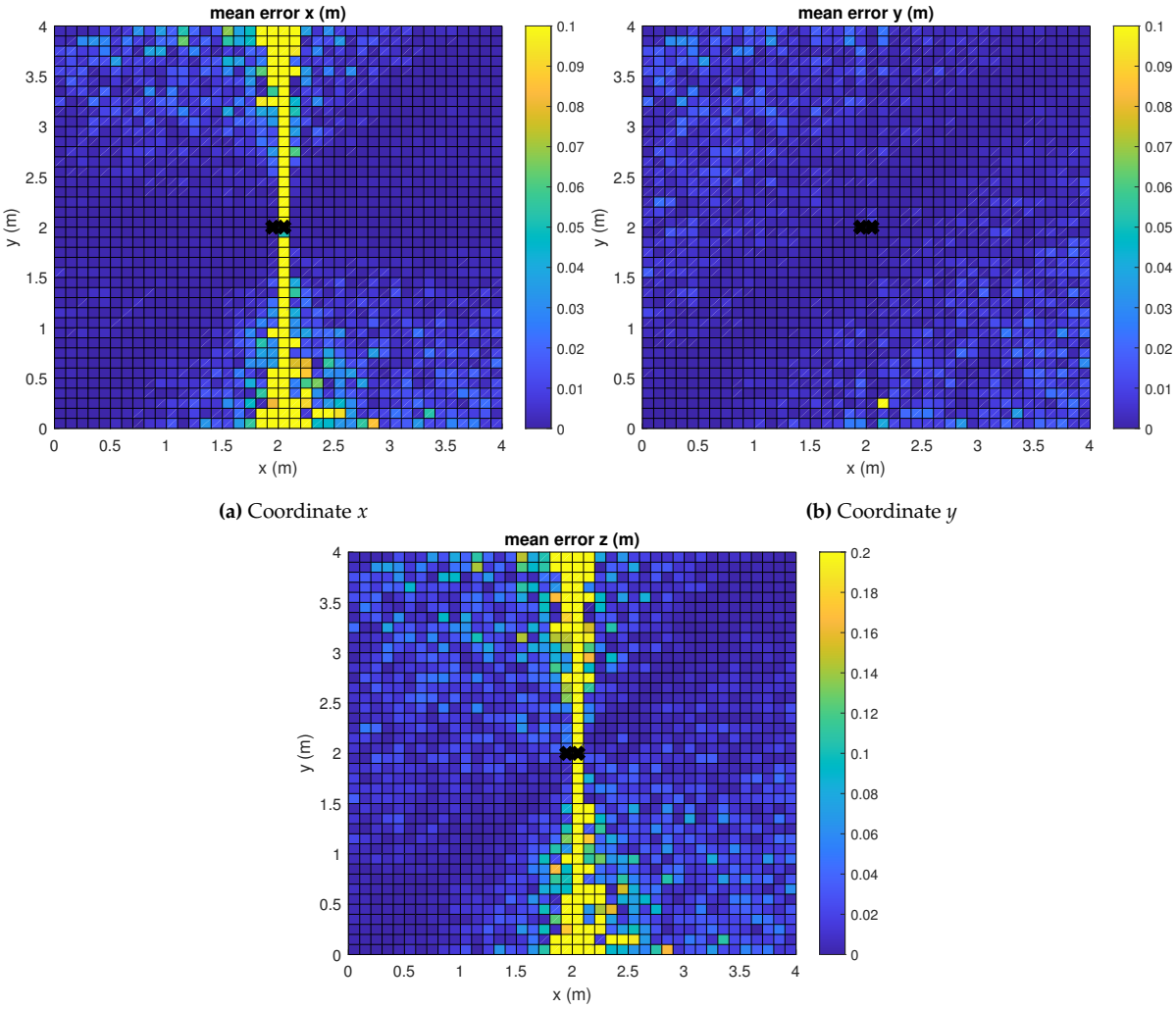

(a) Coordinate x

(b) Coordinate y

(c) Coordinate z

Figure 5.5: Mean absolute errors in the grid of considered points in the floor using two receivers QADA and a single transmitter.

It is interesting to analyse different solutions that may decrease these errors. Some of the proposed solutions are the use of more receivers, an increase of the distance between receivers and avoiding alignment between receivers. In Fig. 5.6 the CDF of the absolute pose errors is plotted for one transmitter and two to four receivers with the deployments presented in Fig. 5.4 a), b), c) and d) as blue, purple, green and red lines respectively, where the distances $d = \{5, 10, 20\}$ cm are plotted as a continuous line, a dashed line and a dotted line, respectively. The receivers are placed in the ceiling of the room with the centre of each geometrical distribution at coordinates (2, 2, 3.4) m. The transmitter's position is estimated using AoA measurements with the LSE algorithm. No fusion filter has been considered in this simulation.

As can be observed in Fig. 5.6 the best behaviour of the system is obtained when using a high number of receivers and a large distance between them ($10 - 20$ cm), achieving less than 1 cm of error in 90 % of cases. In addition, it can be observed the great improvement of the system performance when the 4 QADA receivers are not aligned (red lines).

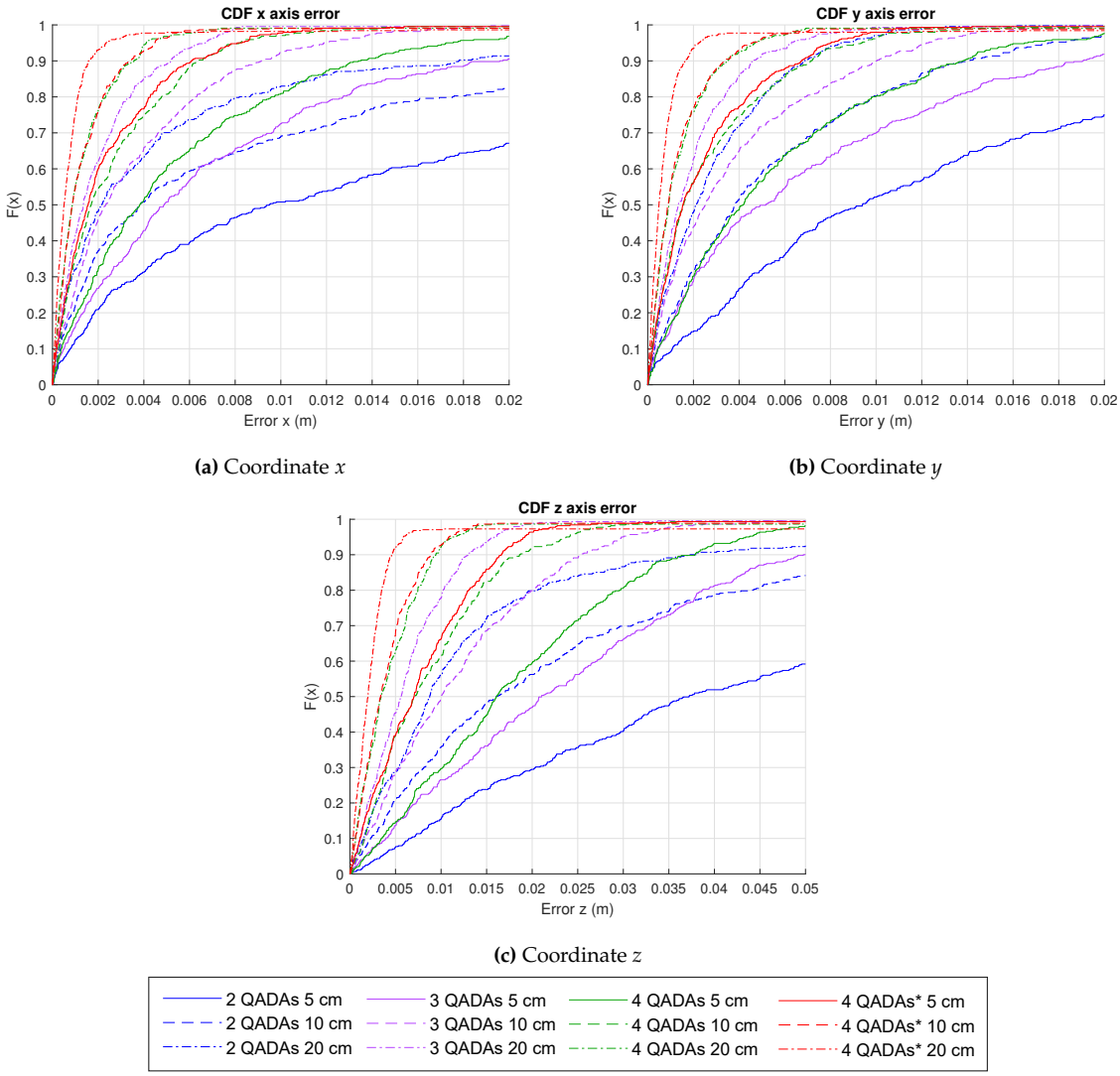

(a) Coordinate x

(b) Coordinate y

(c) Coordinate z

Figure 5.6: CDF of the absolute pose errors for a number of QADAs j from 2 to 4 and with a LED $i = 1$, according to the distance between QADAs $d = \{5, 10, 20\}$ cm.

Similar to Fig. 5.5, Fig. 5.7 presents the mean absolute errors for each coordinate when using four receivers distributed as presented in Fig. 5.4 d) with a distance between them of $d = 20$ cm, and a single transmitter. It is worth mentioning that, since the receivers are not aligned, none of the four QADAs will simultaneously have the same image point at any position, and thus, the achieved errors are much lower than those obtained using only two receivers (see Fig. 5.5).

In addition to the previous simulations, the behaviour of different algorithms is presented in Fig. 5.8. The CDF presents the absolute error in the estimation of the position of the transmitter $i = 1$ for each coordinate x, y and z. Similar results are obtained for the rest of the LEDs. In this analysis we have used the deployment of 4 QADAs presented in Fig. 5.4.d) with a distance between them of $d = 20$ cm and 4 LEDs placed in a square shape with a distance between them of 10 cm. The algorithms to be compared are the LSE without geometrical considerations, the NLSE with the geometrical equations and the EKF with the geometrical considerations. A threshold has been set so that, when the mean difference between the measurements ($\mathbf{Z}_k$) and the estimated observations from the a priori estate ($h_k(\mathbf{X}_k)$) is below 10^{-4}, the algorithm stops. If this threshold is never reached, the algorithm will stop after 20 iterations and the

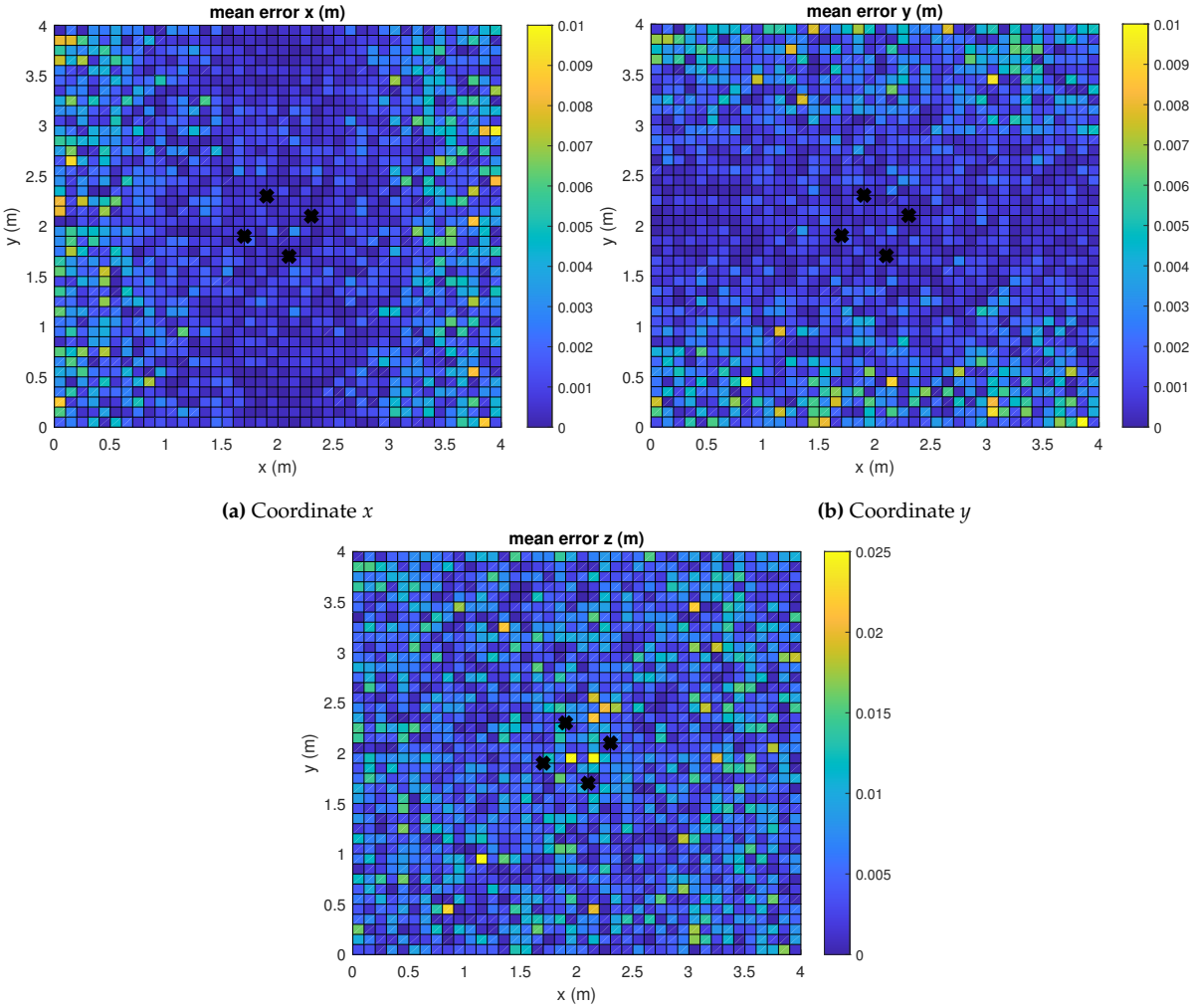

(a) Coordinate x

(b) Coordinate y

(c) Coordinate z

Figure 5.7: Mean absolute errors in the grid of considered points in the floor using four receivers QADA and a single transmitter.

last estimated update solution is the one considered to calculate the positioning error. The initial value considered in the NLSE and the EKF is a random value within the analysed area. The proposal achieves average absolute positioning errors in the coordinates x, y and z in 90% of cases below 0.76 mm, 0.93 mm and 2.00 mm; 4.04 mm, 1.67 mm and 1.12 mm; and 1.10 mm, 1.10 mm and 4.3 mm for the LSE, NLSE and for the implemented EKF, respectively.

There is a trade-off between increasing the number of QADAs and the distance between them and having a small, compact receiver module. In this way, and similar to Fig. 5.8, Fig. 5.9 analyses the behaviour of the proposed algorithms when using the geometrical distribution of two receivers (see Fig. 5.4.a) with a distance of 20 cm.

The proposal achieves average absolute positioning errors in the coordinates x, y and z in 90% of cases below 1.26 cm, 0.57 cm and 3.15 cm; 7.05 cm, 3.37 cm and 18.15 cm; and 0.61 mm, 0.58 mm and 0.11 mm for the LSE, NLSE and for the implemented EKF, respectively. As can be observed, the EKF presents much better results than the LSE or the NLSE. Thus, the use of one or another algorithm depends on the geometry of the deployed receivers.

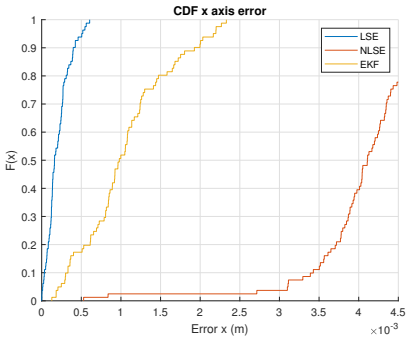

(a) Coordinate x

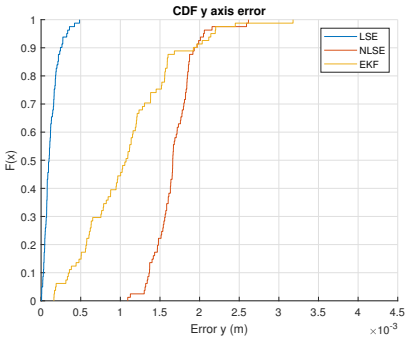

(b) Coordinate y

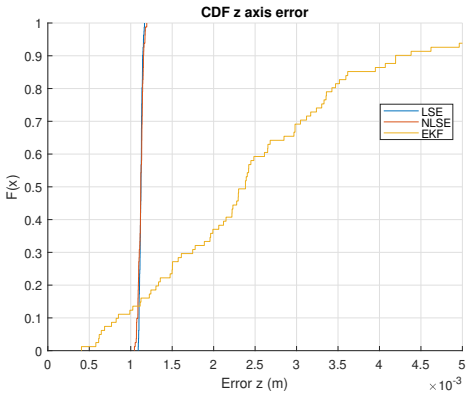

(c) Coordinate z

Figure 5.8: CDF of the absolute positioning errors with LED $i = 1$ when positioning with 4 QADAs and 4 LEDs, according to the different algorithms presented in this chapter.

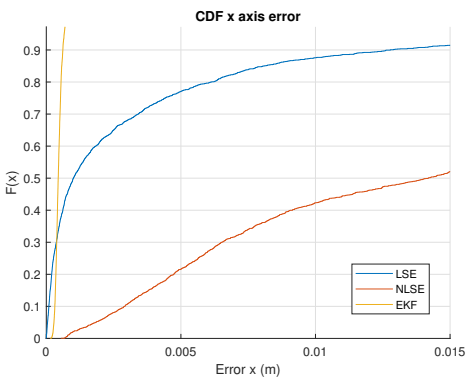

(a) Coordinate x

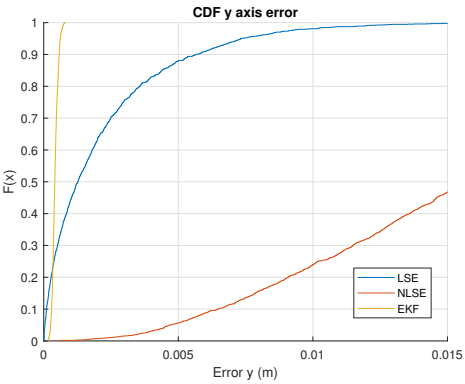

(b) Coordinate y

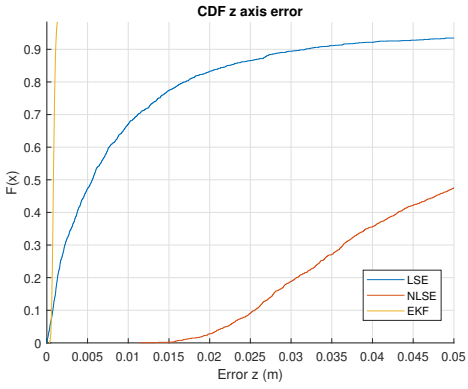

(c) Coordinate z

Figure 5.9: CDF of the absolute positioning errors with LED $i = 1$ when positioning with 2 QADAs and 4 LEDs, according to the different algorithms presented in this chapter.

5.3 Conclusions

In this chapter, the performance of a centralized 3D Infrared or Visible Light Local Positioning system has been studied according to the deployed LEDs or QADAs and different positioning techniques. Here some partial conclusions are listed:

- To achieve a high coverage volume, the positioning system is based on at least two receivers QADA working on the linear region (aperture length of $l \leq 2.75$ mm) and several LEDs located at the mobile to locate (mobile robot, drone...). In this configuration, a linear least squares estimator in combination with the Levenberg-Marquardt method and some trigonometric considerations are implemented to estimate the position of the mobile (x, y, z). The geometry of the transmitters has also been included in the algorithm by using a non-linear least squares estimator. In addition, an EKF has been implemented to increase the robustness of the proposal.

- The geometrical distribution of the QADA receivers has been studied. Different arrangements and distances between receivers ($d = \{5, 10, 20\}$ cm) have been analysed by plotting the absolute pose errors in a CDF in simulations with a SNR = 10 dB, finding that the best behaviour of the system is when using 4 non-aligned QADAs and a distance of 20 cm between receivers. There is a trade-off between increasing the number of receivers, thus, decreasing the positioning error and having a small, compact receiver module.

- The simulation tests have compared the estimation of the position of 4 transmitters using 4 QADAs with a distance of 20 cm between them in a large area of 4×4 m^2 using a linear and non-linear least squares estimator and an extended kalman filter. The proposal achieves average absolute positioning errors in the coordinates x, y and z in 90% of cases below 4 mm for all the coordinates and algorithms.

The next chapter will detail and discuss the experimental results obtained for all the different configurations and algorithms presented in Chapters 3 - 5.

Chapter 6

Experimental Results

In this chapter, some experimental results are presented using the algorithms, techniques and hardware described and evaluated in simulations. Two different scenarios in the School of Engineering at the University of Alcalá have been used to apply the described direct 3D configuration in Chapters 3 and 4 and validate it experimentally. The first location is a small area in a laboratory used to test the reliability of this configuration and the experimental challenges derived from it, such as the use of point-like light sources, reception of strong undesired multipath signals, and the MAI effect from simultaneous transmission of the encoded sequences. Then, the second location is a large room on the second floor, used to test the reliability of the configuration in large scenarios with a low SNR as well as the influence of the rotation of the receiver in the final estimation of its position. Finally, a preliminary evaluation of a loosely-coupled fusion approach is described to merge two different LPS based on optical and ultrasonic technologies. To produce a more robust solution, the position estimates from both LPS are fused using a Kalman filter (KF).

This chapter is organized as follows: the first section provides an introduction to the experimental set-up and the two deployed scenarios; the second section presents the experimental results that verify the AoA and the IPPE algorithms in the direct configuration; the third section shows some preliminary results of the fusion approach to merge an IR and an US LPS; and the last section discusses some conclusions.

6.1 Scenarios and Experimental Set-Up

Two scenarios have been deployed to verify the proposed algorithms presented in previous chapters. Fig. 6.1 presents both. Scenario no. 1 is a space of 2×2 m^2 located in the laboratory on the third floor of the building. The LEDs are distributed in the four corners of a square with a 0.60 m long side at $z = 1$ m or $z = 2$ m high, while the QADA receiver is placed on the floor at plane $z = 0$ m. Fig. 6.1.a) shows this set-up when the LEDs were placed at $z = 2$ m. As described in Chapter 3, they emit a 1023-bit Kasami with a displacement of 5 samples or a 1151-bit LS sequence with a displacement of 10 samples and a BPSK modulation using visible or infrared light.

The scenario no. 2, on the other hand, is a large 4×4 m^2 room located in another laboratory on the second floor of the building, as shown in Fig. 6.1.b). The beacons in this case are distributed in the four corners of a square with a 1.25 m long side and are located on the ceiling at a height of $z = 3.4$ m.

They emit a 1151-bit LS sequence with a displacement of 10 samples and a BPSK modulation using infrared light as detailed in Chapter 3. It is worth mentioning that, since the receiver is located on the floor of the room, the distance between the transmitters and the receiver is longer than 3.4 m. A synchronization beacon has been included in this scenario so that the emission of the different BPSK modulated sequences c_i, as well as their acquisition in the QADA sensor, are all simultaneous. The positioning system does not need to be synchronized. The beacon of synchronization is only included in the design to facilitate the acquisition of the emitted sequences.

In both cases, the receiver is a QADA receiver QP50-6-18u-TO8 with a radius $r = 3.9\,\text{mm}$ [Inc12] and a square aperture placed on top of the sensor at a distance of $h_{ap} = 2.6\,\text{mm}$ with an aperture side of $l = 3.9\,\text{mm}$. In scenario no. 2, the side of the aperture has also been set at $l = 2.75\,\text{mm}$. The main difference between using an aperture length of $l = 2.75\,\text{mm}$ or $l = 3.9\,\text{mm}$ is whether or not the illuminated areas are always confined inside the photodetector's sensitive areas, and, thus, the need of using the linear or non-linear approach as discussed in Section 4.2.

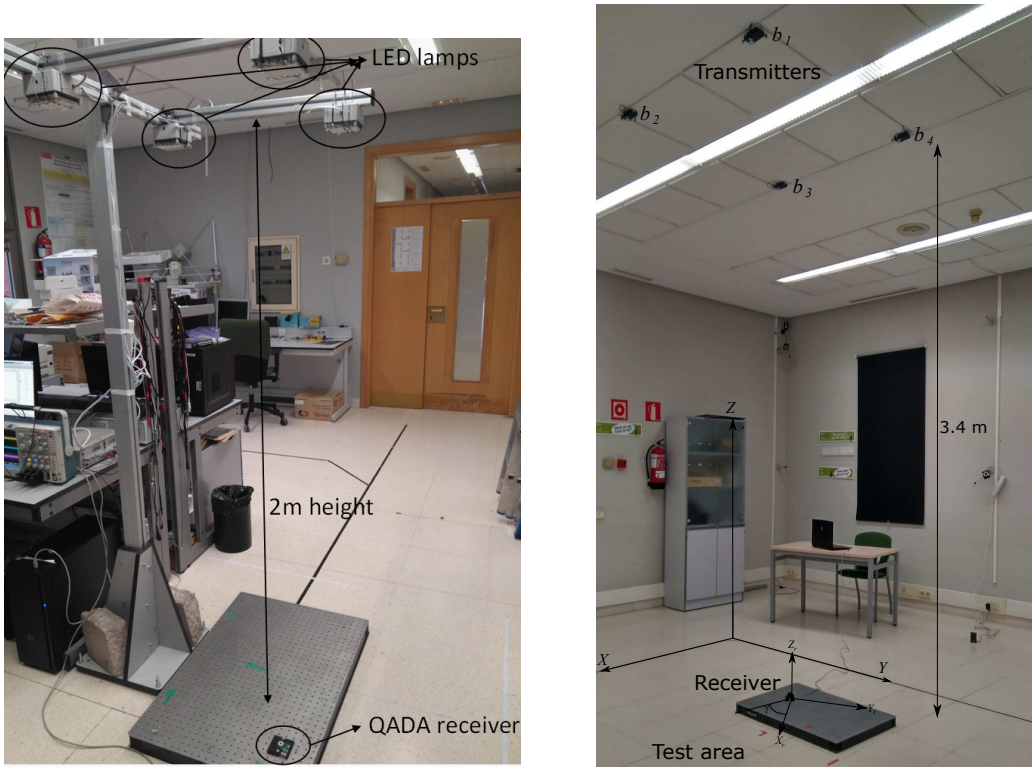

Figure 6.1: Experimental set-up in the proposed scenario: a) Scenario no. 1, b) Scenario no. 2.

As can be observed in Fig. 6.1, measurements were taken under normal artificial and natural light conditions. The ambient light and incoming sunlight from the windows are assumed to be equal on the entire receiver surface and will thus be eliminated using the correlation functions computed with the transmitted codes c_i and the normalization of the differential signals with respect to the total amount of energy received. Therefore, no variations due to this noise will affect the estimation of the receiver's position if the system is not saturated.

The transmitter's modules for the visible light and the infrared light set-up are presented in Fig. 6.2. The visible light emitters are five modules OVM12F3W7 [Tec16] connected in parallel, and

the infrared light emitters are ILH-IW01–85NL–SC201-WIR200 modules [Osl15]. In addition, the receiver module consists of a QADA circular photoreceptor QP50–6–18u–TO8 [Inc12], a filtering system, a synchronization signal detector, and an acquisition system STM32F469I Discovery [STM15]. It is presented in Fig. 6.3 when using a square aperture of $l = 2.75\,\text{mm}$.

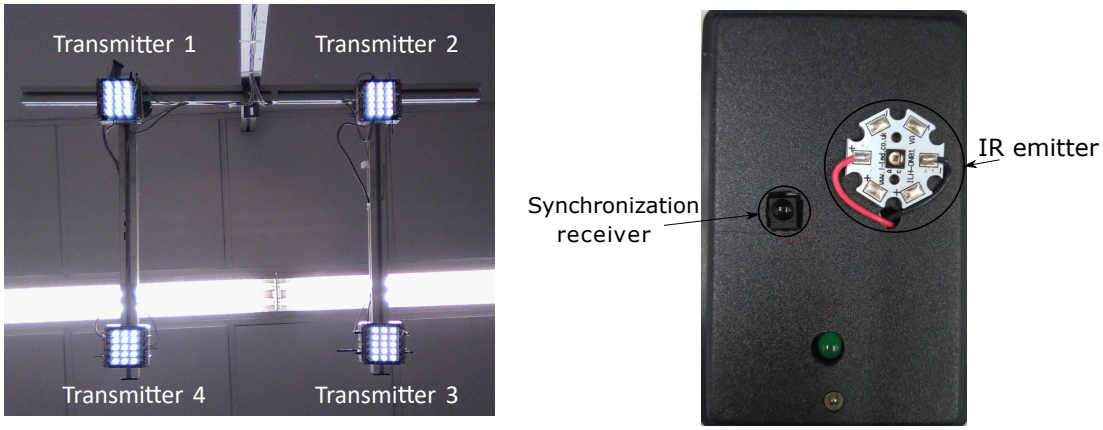

Figure 6.2: Detail of the deployed LED beacons using a) visible light, b) infrared.

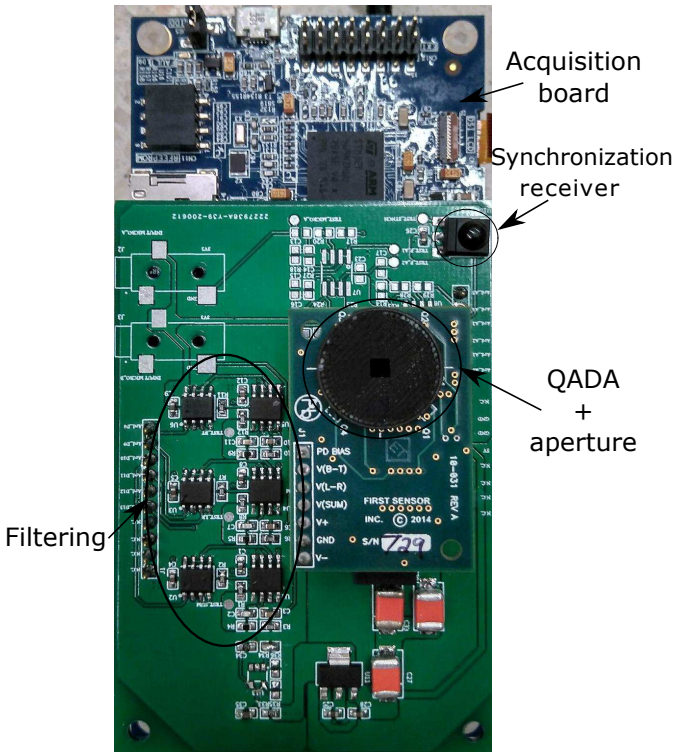

Figure 6.3: Detail of the receiver acquisition system: quadrant photodiode with square aperture of $l = 2.75\,\text{mm}$, filtering system and acquisition board.

6.2 Evaluation

6.2.1 AoA Algorithm with a Fixed Target in Scenario no. 1

Using Visible Light and Kasami Sequences

The experimental tests that verify the AoA algorithm have been conducted in both scenarios under normal light and noise conditions (see Fig. 6.1). In the following, we present the experimental tests carried out in scenario no. 1 with a fixed target and using visible light to transmit the Kasami sequences. The receiver has been placed in a grid of nine points in the area bellow the emitters on the floor, and the corresponding positions have been obtained up to 50 times per point. Fig. 6.4 plots these experimental results, where the red crosses are the ground-truth; the black crosses represent the projection of the LED beacons; and, the coloured point clouds are the positions obtained for the receiver. For each of the nine measured points in the plane XY, an error ellipse is also plotted with a 95% confidence level. It is worth mentioning that when the SNR is low (at the corners of the cell and when placing the transmitters at z =2 m), the dispersion of the measured points is very high. The overall absolute error in the XY plane is found to be less than 4 cm for a distance of 1 m and 8 cm for a distance of 2 m.

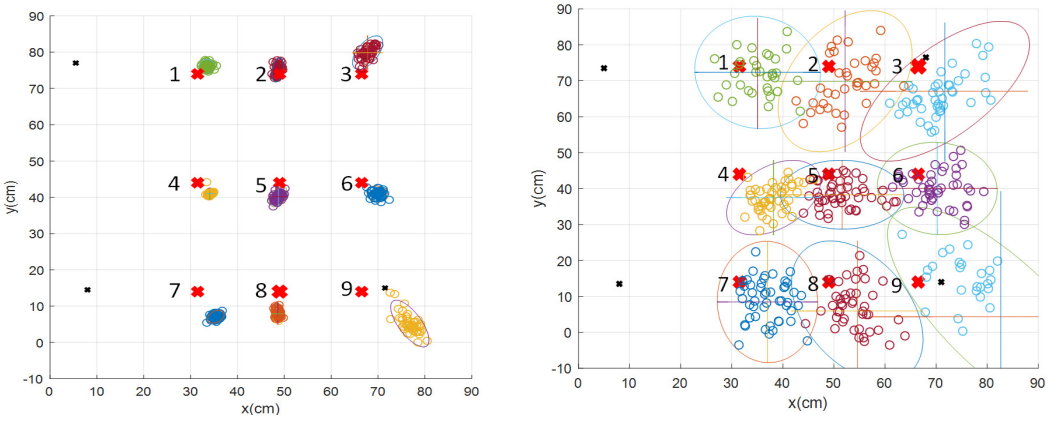

Figure 6.4: Experimental position estimates using visible light when the transmitters are placed at a) $z = 1$ m; b) $z = 2$ m. The red crosses are the ground-truth; the black crosses represent the projection of the LED beacons; the coloured point clouds are the positions obtained for the receiver; and, the ellipses at each point are error ellipses with a 95% confidence level.

A CDF for the absolute error of the receiver's coordinates (x, y, z) when the transmitters are located at planes $z = \{1, 2\}$ m is presented in Fig. 6.5. The absolute error for each coordinate hereinafter is defined as the distance error of each estimated point coordinate with respect to the measured ground-truth. In 90% of the measures at $z = 1$ m and $z = 2$ m, the absolute error in x and y is less than 8 cm and 14 cm, respectively. It is worth noting the high errors found at $z = 2$ m where less light intensity impacts the photoreceiver and, as a result, the algorithm fails at some specific points when measuring the correlation peaks from the signals. Furthermore, the importance of light intensity and angles of incidence can be observed in the coordinate z. The 90% of the measures are less than 15 cm and 8 cm when the transmitters are placed at $z = 2$ m and $z = 1$ m, respectively. The average absolute error and the average standard deviation obtained in the experimental positions are estimated for the nine

considered points as detailed in Table 6.1. Furthermore, it has been noted that those points in the centre of the cell are not comparable to those points in the corners due to the strong dispersion of these last points. Table 6.2 details particular information on points 3 and 4 for further comparison.

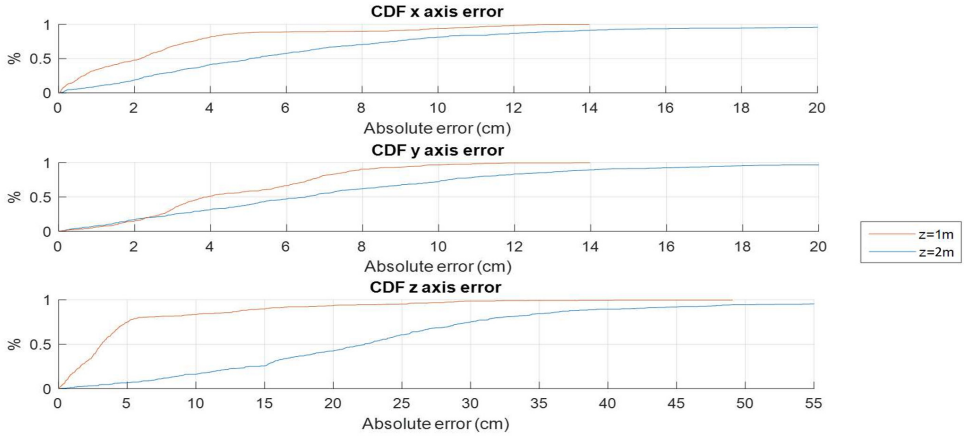

Figure 6.5: CDF for the absolute error of the positioning error in the receiver's coordinates (x, y, z) when the transmitters are located at $z = 1$ m, 2 m in the experimental results.

Table 6.1: Average absolute errors and standard deviations for the nine points considered in the experimental results from Fig. 6.4.

Axis	$z = 1$ m		$z = 2$ m	
	Average absolute error	Average standard deviation	Average absolute error	Average standard deviation
X axis	2.80 cm	0.78 cm	6.43 cm	4.88 cm
Y axis	4.62 cm	1.14 cm	7.28 cm	6.31 cm
Z axis	5.57 cm	2.50 cm	24.16 cm	18.77 cm

Table 6.2: Average absolute errors and standard deviations for points 3 and 4 considered in the experimental results from Fig. 6.4.

Axis		$z = 1$ m		$z = 2$ m	
		Average absolute error	Standard deviation	Average absolute error	Standard deviation
Point 3	X axis	2.99 cm	2.03 cm	6.07 cm	5.91 cm
	Y axis	6.93 cm	1.71 cm	8.87 cm	6.96 cm
	Z axis	11.97 cm	6.81 cm	27.10 cm	22.15 cm
Point 4	X axis	2.61 cm	0.35 cm	6.66 cm	3.28 cm
	Y axis	3.05 cm	0.57 cm	6.53 cm	3.71 cm
	Z axis	8.49 cm	1.74 cm	21.11 cm	9.21 cm

As expected, point 4 presents higher errors than point 3. It is of particular interest the error difference between them in coordinate y (more than 2 cm) and in coordinate z (more than 12 cm) in both scenarios, when the transmitters are located at $z = 1$ m and $z = 2$ m. Note than the SNR is higher in the centre of the room (point 4) compared to the corner of the room (point 3) and thus, errors are lower in the centre of the room.

The Euclidean distance error E_d of the estimation with respect to the measured ground-truth is the metric used to estimate the total absolute error for the nine points considered in Fig. 6.4. The error

function is given by (6.1), where $(\widehat{x}, \widehat{y}, \widehat{z})$ are the estimated positions and (x, y, z) are the ground-truth coordinates. The experimental tests achieve absolute errors below 5.5 cm for a distance of 1 m and 13 cm for a distance of 2 m.

$$E_d = \sqrt{(\widehat{x} - x)^2 + (\widehat{y} - y)^2 + (\widehat{z} - z)^2} \tag{6.1}$$

It is worth mentioning that the obtained dispersion is higher in the corners of the cell, so that the obtained errors reduce the positioning system to areas close to the centre of the cell at distances of 2 m between transmitter and receiver or to the whole grid when z =1 m. Note that higher distances imply lower SNR. Then, a higher emitting power from the transmitters, as well as the consideration of the real dimensions of the transmitters instead of point-like, may decrease the dispersion in Fig. 6.4. The effect of non-point-like light sources has already been analysed in [Cin19], where it is concluded that increasing the size of the LED beacons largely increases the positioning error in the limits of the analysed scenario.

Using Infrared Light and Kasami Sequences

To solve some of these issues, hereinafter the transmitters are point-like IR LED sources, as can be observed in Fig. 6.2.b). In addition, since the maximum responsivity of the QADA receiver is in the near-infrared region, the use of an IR emitter improves the response of the photodiodes compared to a visible light LED.

In this way, and in addition to the previous experimental tests, a certain rotation angle γ in the Z axis has been set for each point; in particular, the rotation angles γ considered are 5° and 45°, since it can be derived from Fig. 4.18 in Section 4.3 that the worst performance is obtained for $\gamma = 5°$ whereas the best one is for $\gamma = 45°$. Note that the IR emitters are aligned with the X and Y axes (see Fig. 6.1). Furthermore, it was proven in Section 4.3 that angles that meet $90° \cdot n \pm \gamma$, where n is an integer and γ is the rotation angle of the receiver, achieve similar performance results and, thus, the study of the rotation of the receptor can be simplified to a single octant. The six points considered in Fig. 6.6 actually represent the behaviour of the algorithm in one quadrant of the proposed space. It is possible to extend the following results to the rest of the octants of the grid.

Measurements have been acquired up to 50 times per rotation angle $\gamma = \{5°, 45°\}$ and per point when the transmitters are located in plane $z = 2$ m and the receiver is placed in the plane $z = 0$ m. Those points corresponding to $\gamma = 5°$ are plotted in blue, whereas those for $\gamma = 45°$ are in purple. The black crosses represent the transmitters' projected position in the XY plane, while the red crosses represent the ground-truth. For each point in the XY plane, an error ellipse with a 95% confidence level is also plotted. The best position estimates are obtained when the QADA axes are not aligned with two of the transmitters. Therefore, the area around the centre requires lower rotation angles γ to achieve similar positioning errors than in the borders of the surface for higher rotational angles.

It is worth mentioning that the systematic error existing in Fig. 6.6 is caused by a multiple-access interference (MAI), coming from the simultaneous transmissions by the LEDs, whose cross correlations interfere in the positioning algorithm. This issue can be overcome by fully separating the transmitted emissions, so any MAI effect can be discarded. Similarly to Fig. 6.6, this case has been simulated and is depicted in Fig. 6.7, verifying that no systematic errors appear when there is no MAI.

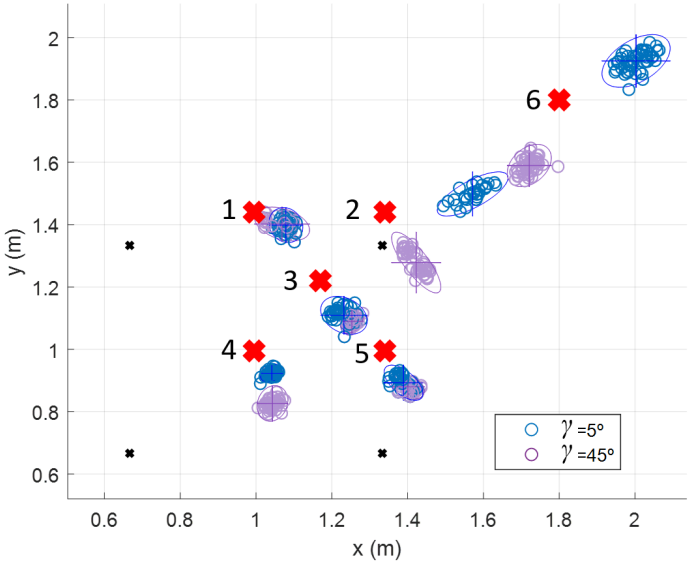

Figure 6.6: Experimental position estimates for $\gamma = \{5°, 45°\}$, when the infrared LEDs are located in plane $z = 2$ m. The red crosses are the ground-truth, the black crosses represent the projection of the LED beacons and the ellipses at each point are error ellipses with a 95% confidence level.

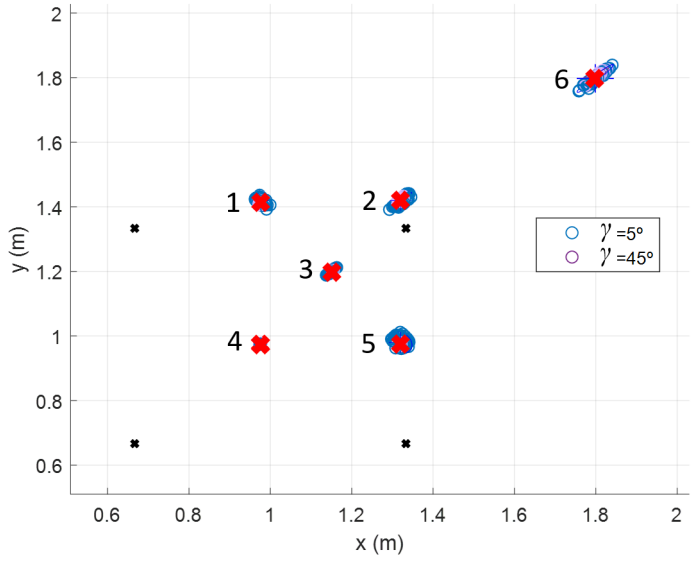

Figure 6.7: Estimation of simulated positions for $\gamma = \{5°, 45°\}$, when the infrared LEDs are located in plane $z = 2$ m and no MAI effect is present. The red crosses are the ground-truth, the black crosses represent the projection of the LED beacons and the ellipses at each point are error ellipses with a 95% confidence level.

At this point, it is convenient to remember that all the previous results were obtained for an aperture height $h_{ap} = 2.6$ mm. Nevertheless, the accuracy obtained in the determination of this height is key for the estimation of coordinate z, which is carried out by means of geometrical considerations as presented in Section 4.3. In order to analyse this influence, the errors obtained for the coordinate z at different aperture heights h_{ap} are detailed in Fig. 6.8. It is possible to observe that different aperture heights h_{ap} should be considered in order to achieve minimum errors in the coordinate z for different angles and points.

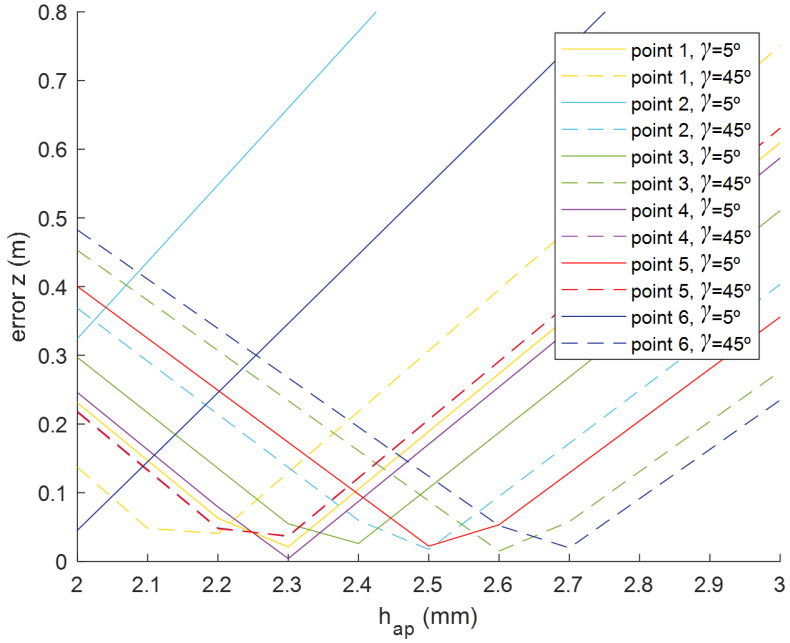

Figure 6.8: Absolute error in the estimation of coordinate z, depending on the aperture height h_{ap}.

The aperture height that minimize the error in coordinate z is $h_{ap} = 2.37$ mm. This value has been obtained as the average between all the aperture heights h_{ap} that minimize the error z for each point and angle, except of the ones obtained for point 2, $\gamma = 5°$ and point 4, $\gamma = 5°$. Those points are excluded since their minimum aperture height are far from the average. Table 6.3 details the averaged absolute errors and the standard deviation obtained for points in Fig. 6.6 with an aperture height $h_{ap} = 2.37$ mm.

Table 6.3: Averaged absolute error and standard deviation for the considered points, assuming $h_{ap} = 2.37$ mm.

		Average absolute error			**Standard deviation**		
Points	γ(°)	***X (cm)***	***Y (cm)***	***Z (cm)***	***X (cm)***	***Y (cm)***	***Z (cm)***
Point 1	5°	10.38	2.27	6.78	1.60	2.00	3.61
	45°	4.92	1.18	10.79	1.04	1.47	4.14
Point 2	5°	15.47	13.10	21.14	6.59	11.08	29.46
	45°	10.27	14.14	4.96	2.32	3.48	4.67
Point 3	5°	8.93	9.92	9.92	2.10	2.70	3.41
	45°	10.29	11.00	2.67	1.06	1.38	2.56
Point 4	5°	6.67	5.16	4.14	1.06	0.99	4.01
	45°	6.83	14.83	4.20	1.45	2.04	5.70
Point 5	5°	5.47	6.11	5.77	1.29	0.95	7.42
	45°	8.07	9.50	2.94	1.55	1.41	3.81
Point 6	5°	20.28	12.50	41.68	3.21	3.02	6.63
	45°	7.90	21.04	25.58	2.08	2.43	4.81
Total		10.43	12.49	15.24	1.92	1.97	3.79

All the points present a low standard deviation, with values around 2 cm, except for points 2 and 6 with a polar angle of 45° for coordinate z. Point 6 presents the highest errors due to the fact that it is the one located near the corner of the grid, where the transmissions reach the highest angle of incidence. Note that the averaged absolute error and the standard deviation of the results obtained for coordinate z are strongly dependent on the aperture height h_{ap}, as well as on the incident angle; therefore, a small error in the measurement will provide large errors in this coordinate as detailed in Fig. 6.8. Fig. 6.9 plots the CDF of the experimental results detailed in Table 6.3. Most points are below 10 cm of absolute error at 90% of the cases.

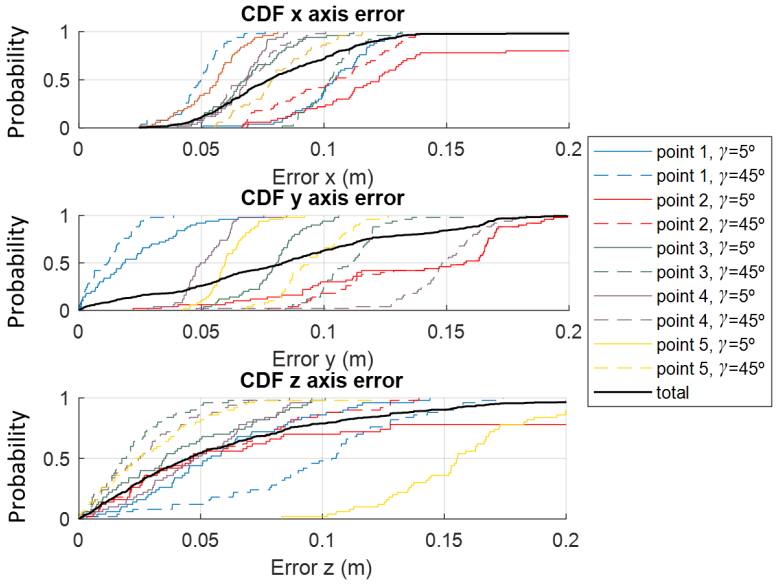

Figure 6.9: CDF of the absolute error of the coordinates x, y and z for the five experimentally analysed points.

Using Infrared Light and LS Sequences

In Figs. 6.6 and 6.7, we showed that there was a systematic error due to the MAI effect and that it could be solved with a full separation of the transmissions. Another solution to decrease the MAI effect is to implement a sequence with suitable cross-correlation properties, as presented in Section 3.2. In particular, when the LS sequence was used in the transmission, the absolute errors in the estimation of the different coordinates were highly decreased. In this way, we implement a 1151-bit LS sequence in scenario no.1 to estimate the position of the same points in Fig. 6.6 as detailed in Fig. 6.10.

The values of the average absolute error and the standard deviation for the five points analysed for each of the rotation angles is further detailed in Table 6.4. It can be checked the low values of the standard deviation that are in the range of millimetres. On the other hand, as can be observed in Fig. 6.1.a), the experimental scenario is highly favourable to have reflections in some surfaces that surround the receiver. These reflections appear in the estimation of the receiver's coordinates in Fig. 6.10, where it is worth mentioning how there is a slight displacement of all the measurements in the same direction. A posterior calibration process was conducted to reduce the influence of other parameters, as will be seen in the next sections.

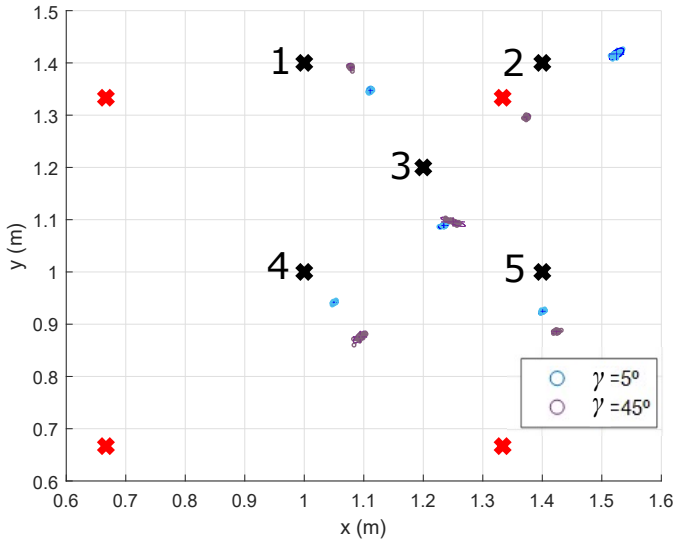

Figure 6.10: Experimental position estimates for $\gamma = \{5°, 45°\}$ with the transmission of a 1151-bit LS sequence with a displacement of 10 samples. The black crosses are the ground-truth, the red crosses represent the projection of the LED beacons and the ellipses at each point are error ellipses with a 95% confidence level.

Table 6.4: Experimental average absolute error and standard deviation for the analysed points with a transmission of 1151-bit LS sequence.

		Average absolute error			**Standard deviation**		
Points	γ(º)	*X (cm)*	*Y (cm)*	*Z (cm)*	*X (cm)*	*Y (cm)*	*Z (cm)*
Point 1	5º	11.08	4.77	23.49	0.19	0.24	1.27
	45º	7.80	0.32	40.37	0.17	0.22	1.87
Point 2	5º	17.47	1.71	64.17	0.43	0.40	1.93
	45º	2.38	10.39	0.24	0.18	0.22	0.76
Point 3	5º	3.44	11.11	37.33	0.29	0.19	0.77
	45º	5.01	10.41	29.41	0.72	0.31	0.78
Point 4	5º	4.99	5.84	35.60	0.19	0.15	0.60
	45º	9.40	12.43	39.99	0.41	0.41	0.45
Point 5	5º	5.05	7.55	4.38	0.21	0.17	1.31
	45º	7.39	11.39	15.52	0.26	0.16	1.31
Total		7.40	7.59	29.05	0.30	0.25	1.11

6.2.2 AoA Algorithm with a Fixed Target in Scenario no. 2

In order to decrease any undesired reflections from the surrounding furniture, the following tests are carried out in scenario no. 2 using a LS sequence. Considering the square formed by the projections of the emitters on the floor, the experimental measurements were obtained hereinafter in seven points (P1 to P7) on the floor ($z = 0$ m) distributed in one of the octants of this square. In particular, points P1, P2 and P5 were located inside this square and P3, P4, P6 and P7 outside of it. Fig. 6.11 shows the estimated positions for each of the points analyzed with the receiver rotated at angles $\gamma = \{5°, 15°, 30°, 45°\}$. The projections of the transmitters on the ground are represented by black crosses, the different positions of the receiver are represented by red crosses and the point cloud represents the 100 measurements taken

for every point and angle. An error ellipse with a confidence of 95% has also been drawn. Note that each subfigure is plotted with a different scale to provide a better insight of the dispersion at each location. The aperture side placed on top of the receiver QADA is 3.9 mm, so that the non-linear approach detailed in Chapter 4 is used.

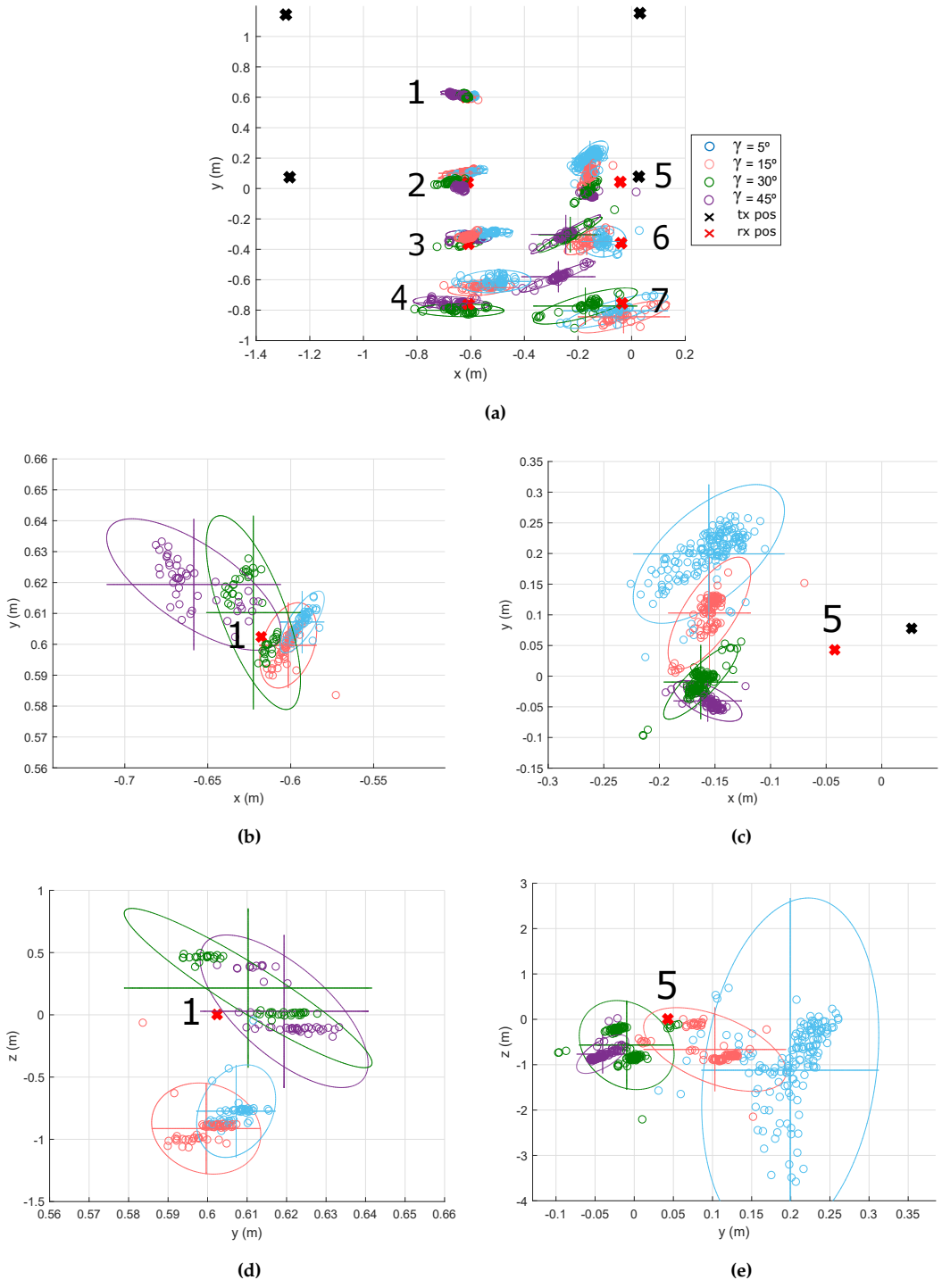

Figure 6.11: Estimated positions and ground-truth in points P1 to P7 after 100 trials: (a) general view; (b) zoom in point P1 of the XY plane; (c) zoom in point P5 of the XY plane; (d) zoom in point P1 of the YZ plane; (e) zoom in point P5 of the YZ plane. The red crosses are the ground-truth, the black crosses represent the projection of the LED beacons and the ellipses at each point are error ellipses with a 95% confidence level.

An Optitrack system is a high accuracy motion capture system that was used to obtain the real positions (ground-truth) of the transmitting beacons and the different positions at which the receiver was placed [Opt21]. It is considered as a way to determine the real positions of transmitters and receiver, but not as an alternative method for comparison. This system presents a much more complex architecture than the proposal described here, since it is based on a set of cameras distributed all over the room that allow to obtain the position of the desired object with an accuracy of 0.1 mm. Note that the measurements with the Optitrack system are not simultaneous with the IRLPS (they are made sequentially), as the IR emitters used by the Optitrack system saturates the QADA receiver.

Fig. 6.12 shows a CDF of the experimental points presented in Fig. 6.11. The system has a higher precision and less dispersion in the center of the exploration area (P1), in contrast with the results obtained below a transmitting beacon (P5) or in the corner of the grid (P7). Table 6.5 shows the numerical results obtained and presented in Figs. 6.11 and 6.12. The average errors obtained are 1.5 and 10 cm, and the standard deviation is less than 1 and 1.5 cm in the XY plane at P1 and P5, respectively. It can also be observed that the angle of rotation where the greatest errors are obtained in the XY plane is $\gamma = 45°$ for P1 and $\gamma = 5°$ for P5. The greatest errors appear where the transmitting beacons and the axes of the QADA photoreceiver are aligned. It has a particularly negative impact on coordinate z, which exhibits exceptionally high errors (greater than 1 m) at certain locations where the QADA axis is aligned with two transmitters.

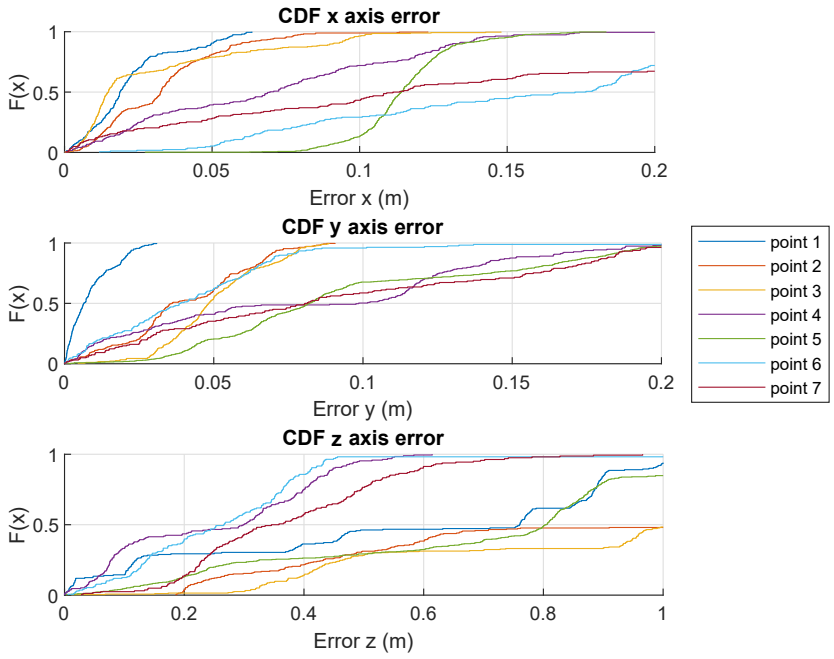

Figure 6.12: CDF of the experimental position estimates for points 1 to 7 including all rotational angles $\gamma = \{5°, 15°, 30°, 45°\}$ in Fig. 6.11.

These results match those found in simulations (see Fig. 4.20 of Section 4). For a 2×2 grid with the transmitters located at 3.4 m, the absolute error in coordinates x and y was 12 cm, whereas it was 32 cm for the coordinate z, in 90 % of the measurements. In addition, in Fig. 4.22 it was shown how those points in the centre of the grid (P1) reached absolute errors in plane XY below 4 cm, those points in the region between the centre and the border of the grid (P2) reached errors of around 8 cm in 90 % of the measurements, while the worst absolute errors were found at the corners of the grid (P3-P7).

Table 6.5: Absolute average and standard deviation errors, at each coordinate, for the real results obtained in the analyzed points P1 to P7.

		Average absolute error			**Standard deviation**		
Points	γ(°)	***X (cm)***	***Y (cm)***	***Z (cm)***	***X (cm)***	***Y (cm)***	***Z (cm)***
Point P1	5°	2.47	0.48	67.64	0.48	0.36	13.30
	15°	1.63	0.28	81.60	0.61	0.49	13.09
	30°	0.48	0.79	11.20	1.02	1.12	22.88
	45°	4.07	1.70	8.03	1.88	0.76	21.92
	Total (all angles)	2.16	0.81	42.12	1.00	0.68	17.80
Point P2	5°	0.47	6.06	39.90	2.69	1.06	35.08
	15°	2.97	6.09	57.17	2.84	1.23	43.31
	30°	5.95	0.39	48.36	2.17	1.03	8.04
	45°	2.77	3.15	175.50	0.97	0.76	3.53
	Total (all angles)	3.04	3.92	80.23	2.17	1.02	22.49
Point P3	5°	7.70	7.35	30.24	3.14	0.83	9.89
	15°	0.09	4.77	156.50	1.36	0.85	3.15
	30°	0.39	2.91	96.48	2.61	1.67	22.71
	45°	0.00	4.73	63.01	3.03	1.43	29.71
	Total (all angles)	2.05	4.94	86.56	2.54	1.20	16.37
Point P4	5°	9.60	14.99	31.82	4.89	2.66	8.42
	15°	4.71	10.93	20.48	4.42	1.89	11.88
	30°	2.92	3.96	5.34	5.77	1.50	10.13
	45°	6.39	0.86	1.18	5.07	1.53	15.65
	Total (all angles)	5.91	7.69	14.71	5.04	1.90	11.52
Point P5	5°	11.33	15.64	102.85	2.43	4.05	135.80
	15°	11.27	6.01	57.14	1.33	3.26	32.99
	30°	12.05	5.26	47.34	1.19	2.17	35.10
	45°	11.43	8.33	67.39	1.10	1.19	15.22
	Total (all angles)	11.52	8.81	68.68	1.51	2.67	54.78
Point P6	5°	6.43	1.13	1.25	2.96	3.68	170.52
	15°	12.79	1.11	3.86	2.98	3.14	9.50
	30°	18.96	5.48	12.32	4.24	4.17	31.21
	45°	20.62	5.78	19.13	4.64	4.56	56.02
	Total (all angles)	14.70	3.38	9.14	3.71	3.89	66.81
Point P7	5°	2.38	4.89	38.96	6.96	4.13	11.15
	15°	0.56	8.84	46.26	6.12	3.79	11.26
	30°	13.71	1.76	23.24	6.93	4.25	13.08
	45°	23.76	17.49	9.72	4.94	3.63	8.27
	Total (all angles)	10.10	8.25	29.55	6.24	3.95	10.94
P1 to P7	Total (all angles)	7.07	5.40	47.28	3.17	2.19	28.67

Evaluation of the Influence of the Calibration and Aperture Length in the Proposed IRLPS

In the following, we analyse the influence of the calibration presented in Section 4.4 in the proposed IRLPS at $z_t = 3.4$ m. Furthermore, instead of $l = 3.9$ mm (as in Fig. 6.11) the aperture side placed on top of the receiver QADA is set to $l = 2.75$ mm, so that the linear algorithm detailed in Section 4.2 is used to estimate the image points. Three experimental points from Fig. 6.10 have been selected due to their particular locations: point 1 is between the projections of two transmitters in the side of the test area (grid) considered; point 2 is below a transmitter in the corner of the grid; and point 4 is near of the centre of the grid. In that way, they are placed in representative points of an octant of the system. The following analysis and considerations can be extended to the rest of the octants of the grid, due to the symmetries existing in the transmitters' arrangement. In the same way, the rotation angles $\gamma = \{0°, 120°, 210°, 300°\}$ are selected to verify that very different orientations of the sensor at each point behave similarly. The ground-truth of the measurements has been obtained using the Optitrack system.

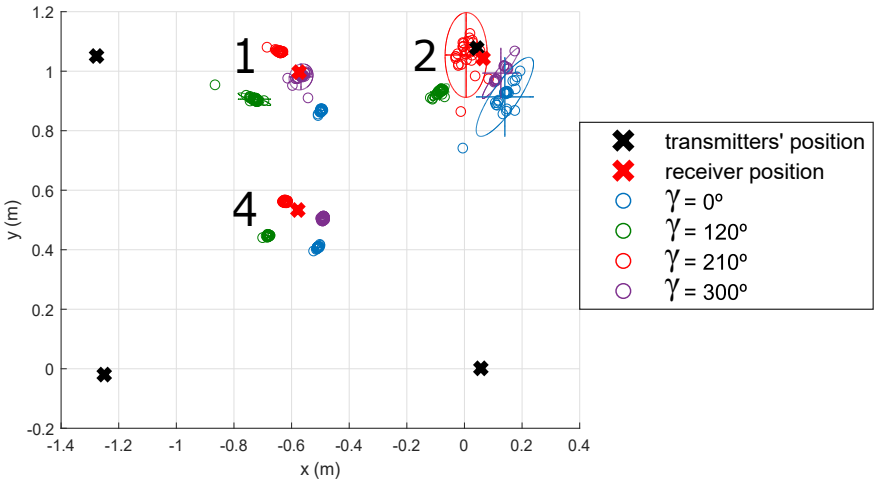

Figure 6.13: Experimental position estimates for $\gamma = \{0°, 120°, 210°, 300°\}$ without calibration at points P1, P2 and P4. The red crosses are the ground-truth, the black crosses represent the projection of the LED beacons and the ellipses at each point are error ellipses with a 95% confidence level.

While performing the experimental tests, the importance of a suitable previous calibration emerged (see Fig. 6.13). Before calibration, the global average absolute error obtained for coordinates x and y is 8.5 cm and the standard deviation is 1.6 cm. Coordinate z achieves an average absolute error of 1 m and a standard deviation of 30 cm. These errors are mainly coming from undesired misalignments in the experimental set-up, related to the optical centre (x_c, y_c), the height h_{ap} at which the aperture is located, the aperture misalignment δ and the length l of the aperture. In this way, after performing the receiver's calibration detailed in Section 4.4 all the intrinsic parameters are known. These parameters are obtained by minimizing the positioning error using iterative methods such as the Branch and Bound algorithm and the Linear Least Squares algorithm, as presented in Chapter 4. The aperture height is set at $h_{ap} = 2.55$ mm, the optical centre is located at $(x_c, y_c) = (0.055, -0.035)$ mm, the focal length adjustment is $\lambda = 1.25$, the aperture misalignment is $\delta = 0.1$ rad, and the aperture length is $l = 2.75$ mm. Note that the radius of the QADA sensor is 3.9 mm and a slightly off-center aperture may imply high errors in the estimation of the receiver's position.

With those calibration parameters and, similarly to the analysis performed in Fig. 6.13, points 1, 2 and 4 have been experimentally analysed in Fig. 6.14 for the polar angles $\gamma = \{0°, 120°, 210°, 300°\}$. The average absolute error, the median absolute error and the standard deviation for the three analysed points and the corresponding polar angles $\gamma = \{0°, 120°, 210°, 300°\}$ are further detailed in Table 6.6. After 50 measurements performed at each point, the obtained results for coordinates x, y and z are 3.50 cm, 7.34 cm and 23.32 cm for the total average absolute error, and 1.42 cm, 3.63 cm and 33.60 cm for the standard deviation.

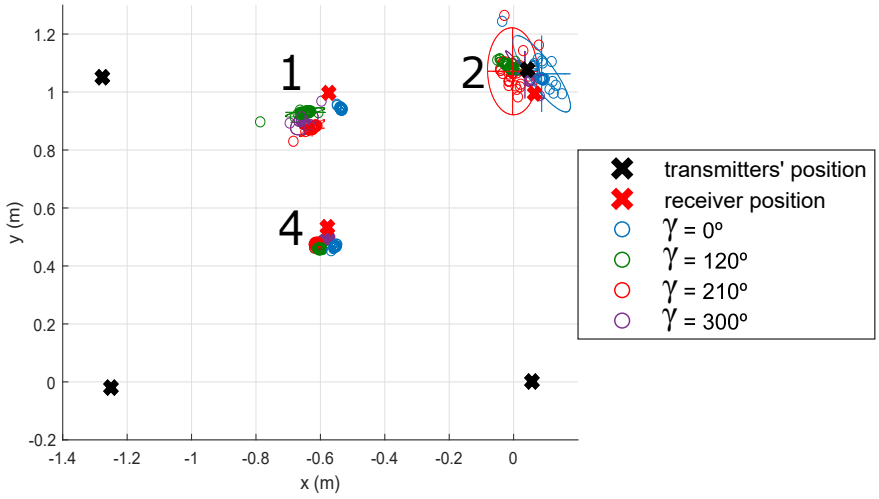

Figure 6.14: Experimental position estimates for $\gamma = \{0°, 120°, 210°, 300°\}$ after calibration. The red crosses are the ground-truth of the receiver, the black crosses represent the projection of the LED beacons and the ellipses at each point are error ellipses with a 95% confidence level.

Table 6.6: Experimental average absolute error, median absolute error and standard deviation for the analysed points with a 1151-bit LS sequence with an aperture length of $l = 2.75$ mm and after performing a calibration of the receiver.

		Average absolute error			**Median absolute error**			**Standard deviation**		
Points	**γ(°)**	***X (cm)***	***Y (cm)***	***Z (cm)***	***X (cm)***	***Y (cm)***	***Z (cm)***	***X (cm)***	***Y (cm)***	***Z (cm)***
Point 1	0°	0.47	10.63	52.97	0.47	10.62	52.36	0.31	0.30	4.73
	120°	4.92	3.68	8.01	4.85	3.71	31.65	0.44	0.27	132.14
	240°	0.98	3.05	1.90	1.13	3.15	4.26	0.49	0.41	14.35
	300°	2.87	7.90	0.95	2.88	7.89	2.31	0.43	0.42	10.62
Point 2	0°	2.62	11.82	117.64	2.65	11.74	118.51	0.40	0.48	2.92
	120°	10.57	3.64	12.74	10.27	3.73	17.11	2.04	0.64	13.66
	240°	1.02	6.09	4.76	1.22	1.38	3.15	1.71	25.60	24.78
	300°	4.52	7.41	3.87	4.37	7.13	1.38	1.52	1.25	34.49
Point 4	0°	0.72	11.21	1.75	0.91	9.81	1.41	3.23	4.64	26.33
	120°	10.72	6.53	2.34	10.34	6.01	4.76	1.30	1.09	15.94
	240°	2.19	5.53	14.41	2.27	4.91	5.41	2.89	5.41	88.79
	300°	0.37	10.58	58.47	1.00	12.61	73.27	2.24	3.04	34.39
Total		3.50	7.34	23.32	3.53	6.89	26.30	1.42	3.63	33.60

For clarity's sake, a CDF of the absolute errors in the estimation of the receiver's position is presented in Fig. 6.15. Points 1 and 2, which are located near the corners, present higher errors than the point 4, near the centre of the grid. The results obtained in Figs. 6.13, 6.14, and 6.15 show the importance of an accurate calibration, since the global positioning error has decreased more than 5 cm for coordinate x, 1 cm for coordinate y and 80 cm for coordinate z. A CDF presenting the comparison between the calibrated and non-calibrated results is detailed in Fig. 6.16.

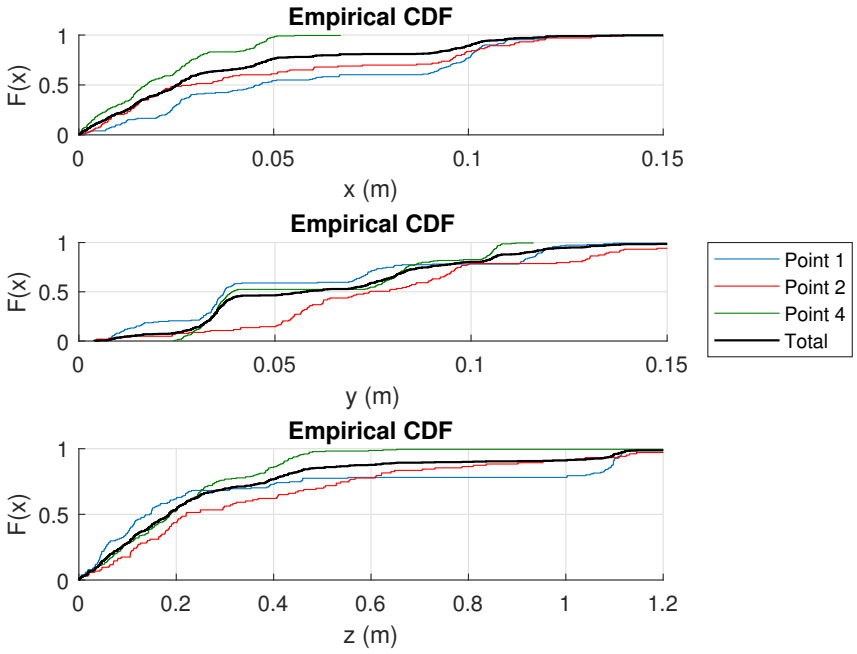

Figure 6.15: CDF of the absolute errors of every calibrated experimental point for $\gamma = \{0°, 120°, 210°, 300°\}$.

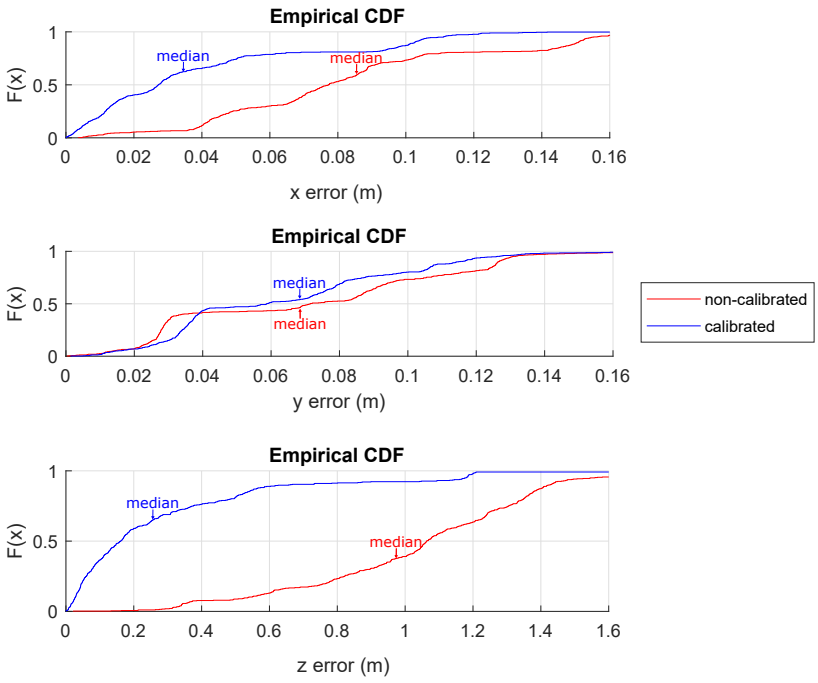

Figure 6.16: CDF of the absolute errors with and without calibration for all points and angles.

6.2.3 PnP Algorithms with a Fixed Target in Scenario no. 2

The experimental tests that verify the PnP algorithms have been conducted in scenario no. 2 under normal light and noise conditions (see Fig. 6.1.b). It has been verified in simulations in Chapter 4, that the most suitable algorithm in this proposal is the IPPE algorithm; therefore, hereinafter, in the experimental tests, only this algorithm has been considered to estimate the pose of the receiver.

The receiver has been calibrated, so that all the intrinsic parameters are known. These parameters are obtained as presented in Chapter 4 and are the same as the ones used in the previous section. In addition, an Optitrack system [Opt21] has been applied to obtain the real positions (ground-truth) of the transmitting beacons and the receiver. Three points have been experimentally analysed, as shown in Fig. 6.17 for $\gamma = \{0\,°, 120\,°, 210\,° \text{ and } 300\,°\}$. These angles are selected to verify that all the quadrants behave similarly.

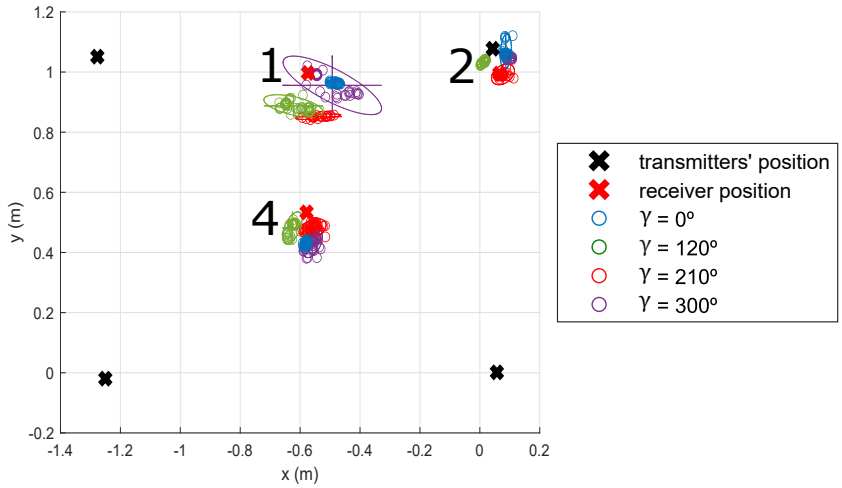

Figure 6.17: Experimental position estimates at $z = 0$ m for $\gamma = \{0\,°, 120\,°, 210\,° \text{ and } 300\,°\}$ with the IPPE algorithm.

Table 6.7 details the average and median absolute errors, as well as the standard deviation, for the analysed points with $\gamma = \{0\,°, 120\,°, 210\,° \text{ and } 300\,°\}$, performing 50 realizations at each point. The obtained results for coordinates x, y and z are 4.33 cm, 3.51 cm and 28.90 cm for the total average absolute error, and 1.84 cm, 1.17 cm and 19.80 cm for the standard deviation, respectively. In addition, the obtained results for the rotation angles α, β and γ are 5.36 °, 8.53 ° and 6.87 ° for the total average absolute error, and 3.07 °, 4.22 ° and 0.63 ° for the standard deviation, respectively. It is worth mentioning that points beyond $3\,\sigma$ are treated as outliers and are not taken into consideration in the analysis. Note that $3\,\sigma$ includes the 99.73 % of all the data.

Fig. 6.18 shows the CDF of the absolute errors of the receiver pose estimation. Those points located near the corners of the room (points 1 and 2) present slightly higher errors than point 4, which is located near the centre of the room. Note that the rotation angle γ presents a 4 ° absolute error offset that may be due to a slight δ miscalibration or to the ground-truth estimation.

In simulations (see Fig. 4.29), the obtained errors were below 5 cm for the 2D coordinates (x, y), 1.5 cm for the coordinate z, 1 ° for the rotation angles α and β and, 0.1 ° for γ, in 90% of cases. It can be seen how the 2D positioning errors (x, y) in Fig. 6.18 are in the same range as the expected errors from simulations. Regarding the errors in coordinate z or those related to the rotation angles, it is worth noting

that the experimental tests may include a miscalibration of the receiver's intrinsic parameters, and/or the ground-truth estimation of the transmitters' or receiver's ground-truth pose. Fig. 4.31 shown an analysis of the influence of the transmitters location on the receiver's pose estimation.

Table 6.7: Experimental average, median and standard deviation of the absolute error for the three analysed points, with $\gamma = \{0°, 120°, 210°$ and $300°\}$, using the IPPE algorithm.

		Average absolute error						Median absolute error						Standard deviation					
Points	γ(°)	*X (cm)*	*Y (cm)*	*Z (cm)*	α(°)	β(°)	γ(°)	*X (cm)*	*Y (cm)*	*Z (cm)*	α(°)	β(°)	γ(°)	*X (cm)*	*Y (cm)*	*Z (cm)*	α(°)	β(°)	γ(°)
Point 1	0°	5.59	3.17	20.65	1.41	9.55	5.54	5.53	2.86	19.09	1.03	11.07	5.57	0.47	0.77	7.48	1.22	2.63	0.15
	120°	1.79	1.16	7.74	2.78	13.02	4.82	1.61	0.59	8.29	1.05	13.27	4.51	1.16	1.22	13.71	2.70	5.37	0.65
	240°	7.64	0.67	27.06	3.26	18.49	5.93	8.38	0.49	31.22	1.63	20.14	5.99	1.58	1.35	13.36	3.48	4.65	0.49
	300°	5.80	3.86	34.91	5.22	9.52	5.32	5.61	3.45	35.59	4.86	7.80	5.20	1.42	1.43	9.43	3.27	5.45	0.42
Point 2	0°	9.50	3.14	123.29	8.73	9.64	7.57	9.92	3.15	126.22	9.46	10.30	7.55	1.07	0.31	6.55	1.89	1.62	0.18
	120°	2.25	4.32	9.73	5.08	2.42	7.84	4.50	4.03	19.79	4.62	9.35	7.77	3.80	1.06	23.08	2.38	4.24	0.54
	240°	3.77	6.52	22.02	9.22	3.90	7.94	2.09	6.29	31.67	9.09	3.96	7.26	2.94	0.77	25.62	4.70	3.55	1.22
	300°	7.05	2.14	3.92	5.62	2.32	6.47	3.44	1.18	9.81	4.08	26.30	6.55	6.31	2.70	48.32	3.83	3.21	0.97
Point 4	0°	1.90	6.84	8.54	3.63	0.44	7.48	1.94	6.07	7.48	1.66	1.36	7.36	0.62	2.06	31.86	4.24	5.17	0.75
	120°	4.52	5.26	69.42	3.88	13.98	9.43	4.29	5.35	70.01	4.09	14.32	9.61	0.57	0.84	4.12	1.26	2.80	0.53
	240°	0.46	0.21	2.37	6.65	9.03	8.69	0.51	0.36	1.13	6.82	11.64	8.69	1.36	1.16	27.16	3.99	6.80	0.37
	300°	1.66	4.88	17.16	8.82	10.11	5.39	1.13	4.86	10.06	10.58	13.48	4.49	0.81	0.39	26.92	3.92	5.13	1.29
Total		4.33	3.51	28.90	5.36	8.53	6.87	4.08	3.22	30.86	4.92	11.92	6.71	1.84	1.17	19.80	3.07	4.22	0.63

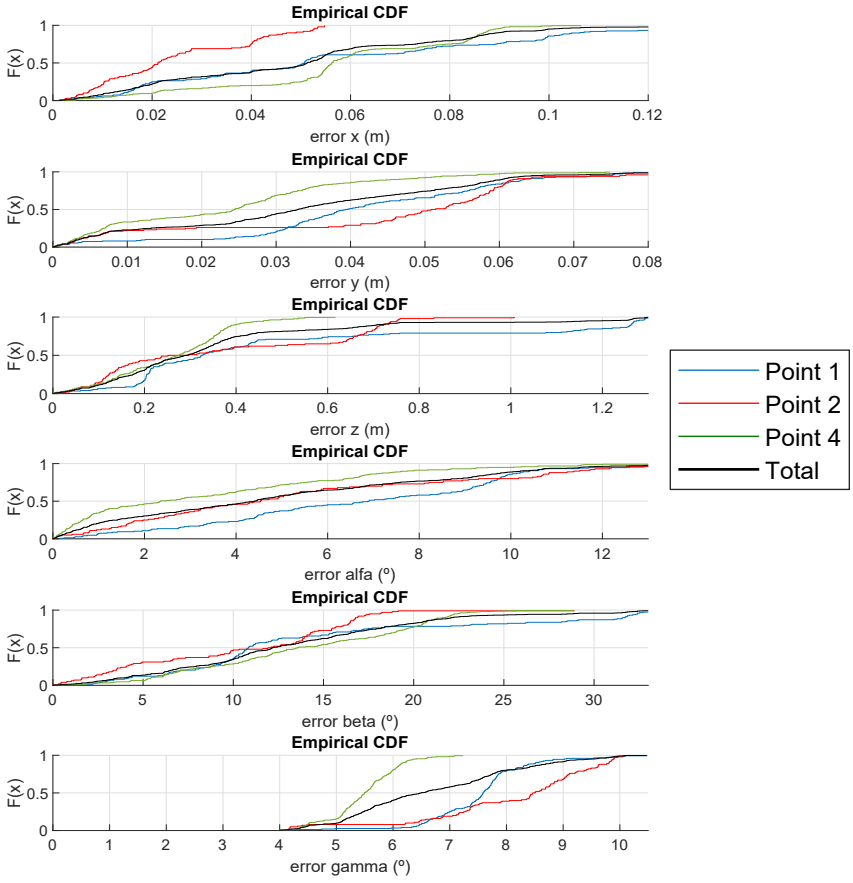

Figure 6.18: CDF of the absolute errors for every experimental point at $z = 0$ m for $\gamma = \{0°, 120°, 210°$ and $300°\}$, with IPPE algorithm.

6.3 Evaluation of an IR and US Multi-Sensory Positioning Fusion Method with a Moving Target in Scenario no. 2

In this section, we evaluate a loosely-coupled fusion method for merging two different LPS based on optical and ultrasonic technologies that cover the same area and are measured simultaneously. Merging both systems enhances the coverage area with a higher reliability and availability. The IR positioning system uses angles-of-arrival measurements to estimate the receiver position as presented in Chapter 4, while the US positioning system uses times-of-flight measurements. The position estimates coming from both are fused using a Kalman Filter (KF) to provide a more robust estimated position.

6.3.1 Experimental Set-Up and Description of the Proposed IR and US Systems

The experimental tests have been carried out in scenario no. 2 with the infrared beacons located at the centre of the room and the ultrasonic beacons placed at the corners of the room. The infrared (IR) and ultrasound (US) receivers are placed on a line-following robot on the room floor, as shown in Fig. 6.19. The ground-truth of the analysed trajectories is determined by using a Leica TS60 total station and a 360º mini prism. This is a high-precision system, which allows the 3D position of the desired object to be obtained with an accuracy of 1.5 mm. Note that, thanks to the use of the Leica total station, the IR, US and ground-truth measurements are simultaneous.

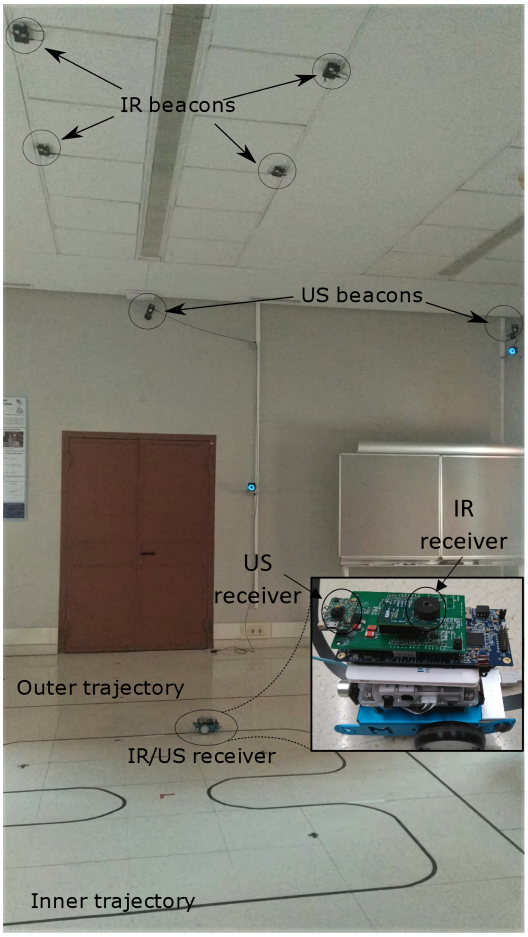

Figure 6.19: Experimental validation scenario for the proposed positioning systems.

The Ultrasonic Local Positioning System (ULPS) consists of a set of emitting beacons, together with a block of synchronization. Every beacon transmits a different Kasami code with a length of 255 bits, also BPSK modulated with a carrier of 41.667 kHz [Ure18]. Note that the modulation symbol consists of two carrier periods. The ultrasonic receiver includes a MEMS microphone SPU0414HR5H-SB [Kno12], connected to an analog input of the STM32F103 microcontroller to acquire the incoming signal at $f_s = 100$ kHz with 8 bits. All these elements, both ultrasonic beacons and receiver, are synchronized through an IR synchronization block, based on the LPC1768 microcontroller. The beacon of synchronization is the same one from the previous IRLPS, so that both positioning systems (US and IR) emit and receive simultaneously. Fig. 6.20 shows a general scheme of the proposed ultrasonic LPS.

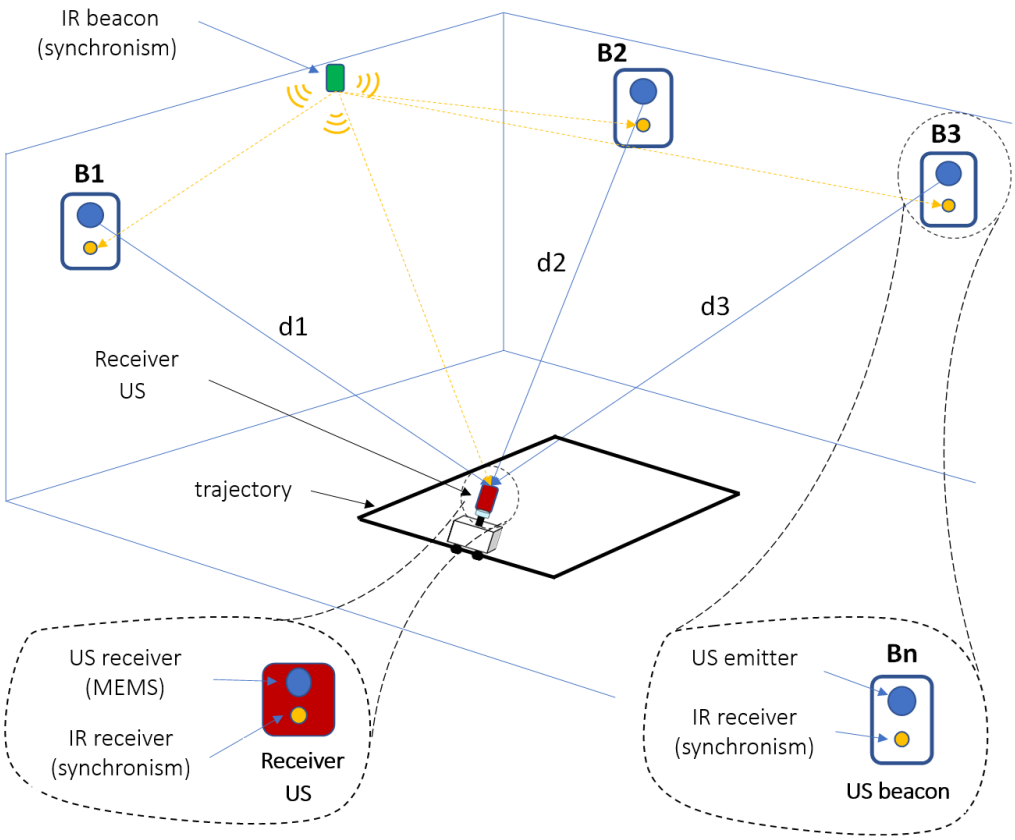

Figure 6.20: Proposed ULPS.

To estimate the receiver's position based on the distances measured by the ToFs, the trilateration equation system is solved using the Gauss-Newton algorithm. This is an iterative approach for solving the system of non-linear equations resulting from the distance measurements derived from the ToFs between the receiver and the beacons. As before, these distances are determined again from the matched filtering between the received signal and the emitted Kasami codes. In spherical trilateration, with the location of the beacons in the plane of the ceiling, only three correct measurements are needed to estimate the receiver's position. Whether more measurements are available, the algorithm dynamically adapts and solves an oversized system. More details can be found in [Ure18], where the ultrasonic LPS with large coverage is described.

6.3.2 Implementation of the Kalman Filter (KF)

The state model of the Kalman Filter is presented in Eq. (6.2), where $\mathbf{X}_k = (x, y)_k$ is the estimated position on the current state k; $\mathbf{A}$ and $\mathbf{H}$ are constant transition matrices; $\mathbf{X}_{k-1}$ is the estimated position on the previous state; $\mathbf{Z}_k$ is the measurements array given by the estimated IR and US positions; w_k is the process noise; and v_k is the measurement noise.

$$\begin{aligned} \mathbf{X}_k &= \mathbf{A} \cdot \mathbf{X}_{k-1} + w_k \\ \mathbf{Z}_k &= \mathbf{H} \cdot \mathbf{X}_k + v_k \end{aligned} \tag{6.2}$$

A summary of the KF is presented in the flowchart in Fig. 6.21.

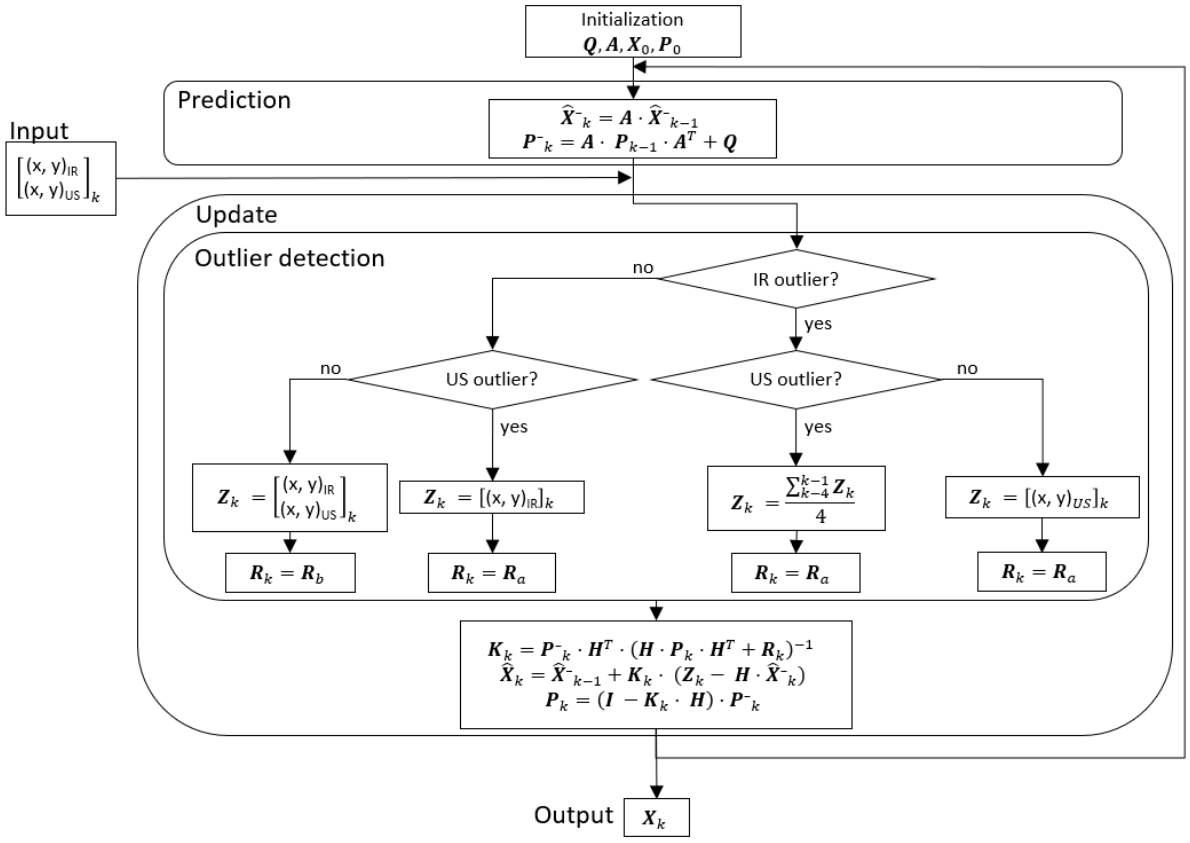

Figure 6.21: Flowchart of the proposed KF for fusing the estimated ultrasound and infrared positions. After the initialization, the KF begins with the prediction steps where $\hat{\mathbf{X}}_k^-$ and $\mathbf{P}_k^-$ are estimated. The algorithm then proceeds to the update step, where it firstly determines whether the input measures are outliers and sets the values of $\mathbf{Z}_k$ and $\mathbf{R}_k$ before estimating the receiver's position.

The initialization matrices are defined in Eqs. (6.3)-(6.5), with the variances of the measured positions $\sigma^2 = 10^{-2}$.

$$\mathbf{Q} = \begin{pmatrix} \sigma^2 & 0 \\ 0 & \sigma^2 \end{pmatrix} \tag{6.3}$$

$$\mathbf{A} = \begin{pmatrix} 1 & 0 \\ 0 & 1 \end{pmatrix} \tag{6.4}$$

$$\mathbf{R}_a = \begin{pmatrix} \sigma^2/10^2 & 0 \\ 0 & \sigma^2/10^2 \end{pmatrix}, \quad \mathbf{R}_b = \begin{pmatrix} \sigma^2/10^2 & 0 & 0 & 0 \\ 0 & \sigma^2/10^2 & 0 & 0 \\ 0 & 0 & \sigma^2/10^4 & 0 \\ 0 & 0 & 0 & \sigma^2/10^4 \end{pmatrix} \tag{6.5}$$

After initializing the initial position vector $\mathbf{X}_0 = (x, y)_{US,0}$ and the transition matrix $\mathbf{P}_0 = \begin{pmatrix} \sigma^2 & 0 \\ 0 & \sigma^2 \end{pmatrix}$, the recursive loop between predictions and updates starts. Eqs. (6.6) and (6.7) present the prediction and the update steps for the proposed system, where $\mathbf{K}_k$ is the Kalman Filter gain that minimizes the residual error; $\mathbf{Q}$ and $\mathbf{R}$ are the process and measurement noise error covariance matrices, respectively; and $\mathbf{P}_k$ is the a posteriori estimate covariance matrix.

$$\begin{aligned} \hat{\mathbf{X}}_k^- &= \mathbf{A} \cdot \hat{\mathbf{X}}_{k-1} \\ \mathbf{P}_k^- &= \mathbf{A} \cdot \mathbf{P}_{k-1} \cdot \mathbf{A}^T + \mathbf{Q} \end{aligned} \tag{6.6}$$

$$\begin{aligned} \mathbf{K}_k &= \mathbf{P}_k^- \cdot \mathbf{H}^T \cdot (\mathbf{H} \cdot \mathbf{P}_k \cdot \mathbf{H}^T + \mathbf{R})^{-1} \\ \hat{\mathbf{X}}_k &= \hat{\mathbf{X}}_{k-1}^- + \mathbf{K}_k \cdot (\mathbf{Z}_k - \mathbf{H} \cdot \mathbf{X}_k^-) \\ \mathbf{P}_k &= (\mathbf{I} - \mathbf{K}_k \cdot \mathbf{H}) \cdot \mathbf{P}_k^- \end{aligned} \tag{6.7}$$

In the update state, the KF detects if the estimated receiver's position using the IRLPS or the ULPS is an outlier. It is considered an outlier when the difference between the position of the receiver and the previous KF solution is higher than a certain threshold. In this case, that value is neglected, and it will not enter in the KF. In particular, a threshold of 35 cm is selected. On the other hand, if both measurements are outliers, the average of the previous four KF solutions is considered as the initial estimation for the KF. Note that, this is a particular situation that only occurs in the 6.37% and 0.82% of the total measurements for the outer and the inner trajectories, respectively. This method assures that the criteria for discarding an outlier is equal for both systems. The matrix $\mathbf{R}$ is also updated according to $\mathbf{Z}$ so that if both IR and US systems are considered, the ultrasound estimated position has more weight than the infrared estimated position (see Fig. 6.21).

6.3.3 Evaluation

Two trajectories are analyzed in the experimental tests: the first one is a square with a side of 3 m (outer trajectory), whereas the second is a trajectory in an area of 2×2 m^2 (inner trajectory). Figs. 6.22 and 6.23 show the experimental measurements obtained in the XY plane using either IR or US measurements, as well as using a KF that merges both IR and US measurements. The ground-truth (GT) of the two trajectories is also plotted in a black line, and the projections of the IR and US beacons are presented with a triangle and a square, respectively. The average speed of the mobile robot during the experimental tests is 15 cm/s. Note that, since the length of the IR and US coded signals are 46.3 ms and 12.24 ms, respectively, no great influence is associated with the speed of the robot in the acquisition of the transmitted signals.

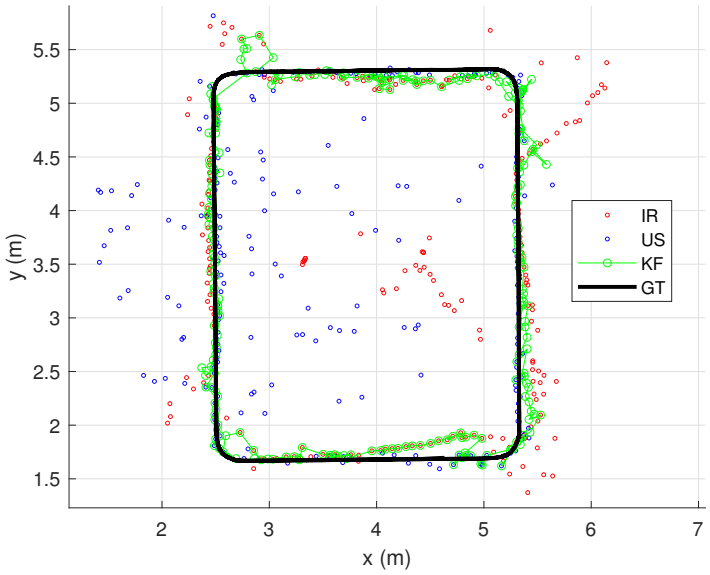

Figure 6.22: Estimated positions for the outer trajectory with IR and US measurements, as well as the merged solution from the KF and the ground-truth.

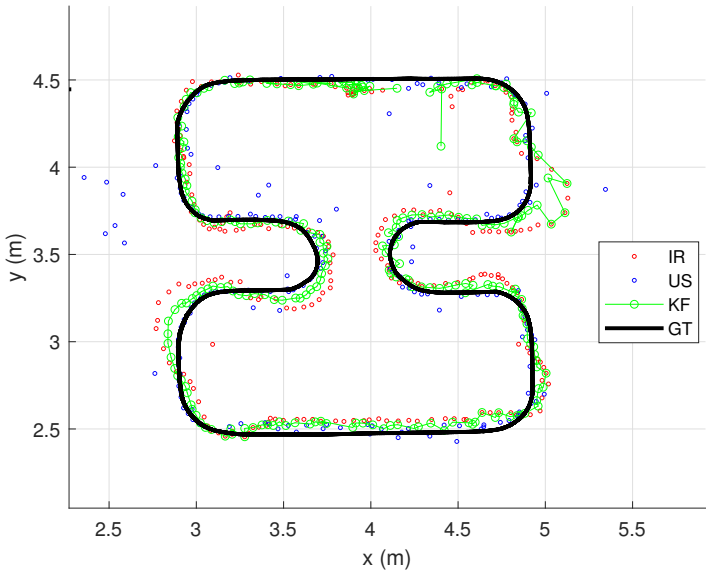

Figure 6.23: Estimated positions for the inner trajectory with IR and US measurements, as well as the merged solution from the KF and the ground-truth.

The estimated coordinates x and y are plotted for both trajectories in Figs. 6.24 and 6.25, respectively, for the estimated position using the ULPS and the IRLPS, as well as the merged solution from the KF. It can be verified that the estimated position using the KF decreases the number of outliers and increases the availability of the total system.

Finally, Figs. 6.26 and 6.27 show the Cumulative Distribution Functions (CDFs) of the absolute errors obtained in the XY plane for the position estimation, considering both positioning systems for the outer and the inner trajectories. The absolute error has been determined as the distance between each estimated point and the nearest ground-truth point [Pé19]. The absolute errors obtained in 90% of cases for the KF approach are lower than 13 cm and 7 cm in the outer and inner trajectories, respectively. It

can also be observed that higher errors are obtained at the corners of the room for the IR system, where there is a longer distance between the transmitters and the receiver. Both systems have errors in the same range in the inner path, where the coverage conditions are similar (although it should be remarked that the ultrasound beacons are further away as they were installed at the corners of the room).

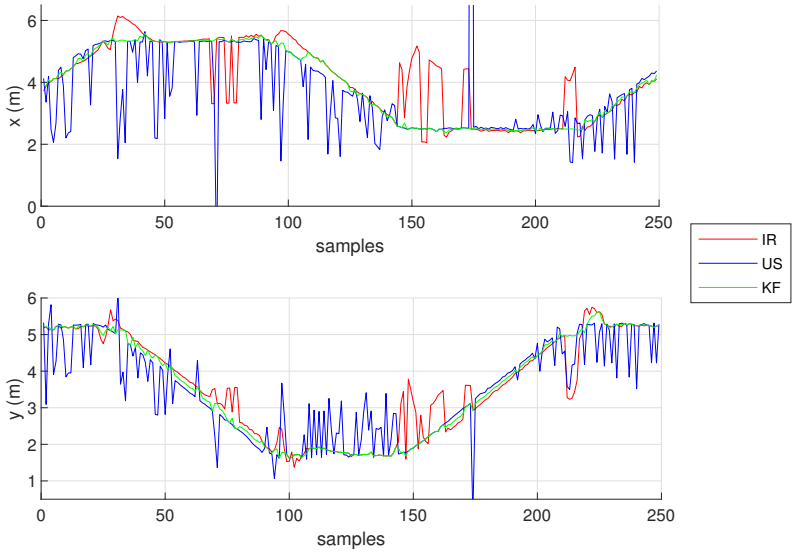

Figure 6.24: Estimated (x, y) positions for the outer trajectory with IR and US measurements, as well as the merged solution from the KF.

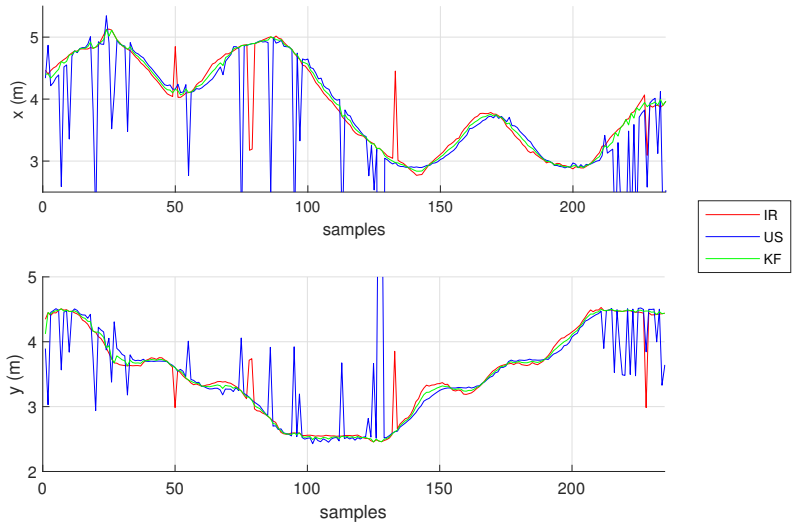

Figure 6.25: Estimated (x, y) positions for the inner trajectory with IR and US measurements, as well as the merged solution from the KF.

Furthermore, for both analysed trajectories, there are sections where the performance of positioning systems degrades (this is where discarded outliers accumulate). This is due to particular issues in the signals' transmission (multipath conditions, low SNR, etc.). Combining the results from both systems with the KF provides a clear improvement in terms of positioning availability along the whole trajectory. It should be noted that no integration of odometry from the mobile robot has been done at this stage, although it could also help filter or mitigate the dispersion of values along the path.

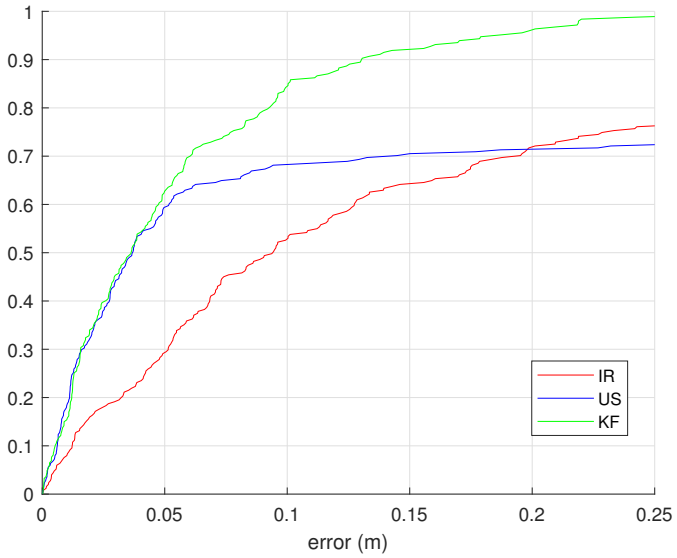

Figure 6.26: CDF of the absolute positioning errors for IR, US and KF measurements in the outer trajectory.

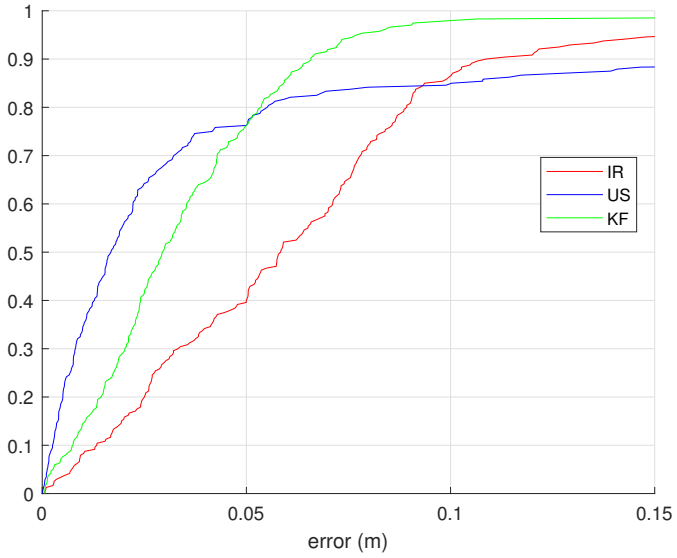

Figure 6.27: CDF of the absolute positioning errors for IR, US and KF measurements in the inner trajectory.

6.4 Conclusions

This chapter have presented the experimental results using AoA or PnP algorithms that verify the direct configuration of the proposed optical positioning system based on visible or infrared light. Different experimental tests have been carried out involving two scenarios: scenario no. 1 is a space of 2×2 m^2 and scenario no. 2 is a room of 4×4 m^2. A summary is presented in Table 6.8. Here some partial conclusions are listed:

- The experimental tests carried out in scenario no. 1 verify the AoA algorithm using visible light LEDs emitting 1023-bit Kasami sequences. The receiver has been placed at each one of nine points, and the corresponding positions have been obtained up to 50 times per point. When the height

separation between the emitters and the receiver is 2 m and 1 m, it achieves 3D positioning average errors below 13 cm and 5.50 cm, respectively.

- The strong dependence of the alignment of the receiver QADA axis and the transmitters has also been proven, and consequently, different rotation angles γ result in different positioning errors depending on the receiver's location in the test grid. The receiver has been placed at six points with $\gamma = \{5°, 45°\}$ covering one quadrant of the grid, and each position has been obtained up to 50 times per point. Errors in the range of $5 - 10$ cm are achieved with standard deviations of 2 cm with a distance of 2 m between the emitters and the receiver. It has been detected that the MAI effect may cause some of these errors.

- Therefore, we have implemented for the same six points a sequence with suitable cross-correlation properties in order to decrease the MAI effect. In particular, a 1151-bit LS sequence has been implemented, achieving average experimental absolute errors and standard deviations of 7.40 cm, 7.60 cm and 29 cm; and 0.30 cm, 0.25 cm and 1.11 cm in the x, y and z coordinates, respectively. Although the MAI effect has been highly reduced with the use of LS sequences, it can be appreciated how the reception of reflections still implies a degradation of the system performance.

- To decrease the effect of undesired reflections in the evaluation of this proposal, further tests were carried out in scenario no. 2 with a distance between the transmitters and the receiver of at least 3.40 m. The estimation of the position of the receiver in that environment for seven particular points (P1 to P7), with P1 at the center of the emitters' projection on the floor and the others covering one of the octants of this projection with $\gamma = \{5°, 15°, 30°, 45°\}$, has been performed for one hundred realizations, using an Optitrack system to determine the ground-truth. The obtained absolute average errors, considering all the points, are 7.10, 5.40, and 47.30 cm in the X, Y and Z axes, respectively. It is worth noting the large dispersion achieved in some of the seven measured points, as well as the high errors in coordinate z.

- A linearization of the image points estimation algorithm as well as the implementation of a calibration algorithm has been key to improve the system performance and simplifying the involved algorithms. The receiver's position was estimated for three points with $\gamma = \{0°, 120°, 210°, 300°\}$, performing 50 realizations per point and using the Optitrack system as ground-truth. The achieved average absolute errors and standard deviations are 3.50, 7.34, and 23.32 cm; and 1.42, 3.63, and 33.60 cm in the coordinates x, y, and z, respectively.

- Further results in scenario no. 2 were related to the evaluation of the PnP techniques. The position of the receiver was estimated for the same three points with $\gamma = \{0°, 120°, 210°, 300°\}$, using 50 realizations per point and the Optitrack system as ground-truth. The IPPE algorithm achieved average absolute errors of 4.33 cm, 3.51 cm and 28.90 cm and standard deviations of 1.84 cm, 1.17 cm and 19.80 cm in coordinates x, y and z, respectively. It allows obtaining also the rotation angles in all axis (α, β, γ) achieving average absolute errors of 5.36°, 8.53° and 6.87° and standard deviations of 3.07°, 4.22° and 0.63°, respectively.

- Finally, this chapter have presented a comparison based on experimental tests of two different technologies used to design indoor local positioning systems. They were tested and compared in

scenario no. 2 over two trajectories that covered an area of 3×3 m^2 using a Leica total station as ground-truth. The infrared solution presents a greater restriction in the provided coverage, which causes the performance to be reduced earlier when moving away from the room's central area (this would be mitigated by installing a larger number of IR emitters). On the other hand, their accuracy is higher than ultrasounds in the central area, perhaps also due to the distance of the ultrasonic emitters. Overall, the position errors achieved when merging both proposals with a KF are less than 10 cm in 90% of cases, while increasing the availability of the positioning system.

Table 6.8: Summary of the experimental results presented in this Chapter.

Scenario	l_{ap} (mm)	Sequence	Algorithm	Distance	Rotation γ	Average absolute error [x / y / z] (cm)	Standard deviation [x / y / z] (cm)
no. 1	3.90	1023-bit Kasami	AoA	1 m	0º	2.80 / 4.62 / 5.57	0.78 / 1.14 / 2.50
				2 m	0º	6.43 / 7.28 / 24.16	4.88 / 6.31 / 18.77
					5º, 45º	10.43 / 12.49 / 15.24	1.92 / 1.97 / 3.79
		1151-bit LS				7.40 / 7.59 / 29.05	0.30 / 0.25 / 1.11
no. 2	2.75			3.4 m	5º, 15º, 30º, 45º	7.07 / 5.40 / 47.28	3.17 / 2.19 / 28.67
					0º, 120º, 210º, 300º	3.50 / 7.34 / 23.32	1.42 / 3.63 / 33.60
			IPPE			4.33 / 3.51 / 28.90	1.84 / 1.17 / 19.80
			KF (IR + US)		Trajectory	outer / inner: 13 / 7 cm (p 90)	-

Comparing Table 6.8 with the works studied in Chapter 2, it can be concluded that the proposed system can estimate the complete 3D pose (x, y, z, α, β, γ) of a static or moving target on large scenarios (3×3 m^2 with 3.4 m of height). Also, the proposal presents a linear algorithm using AoA and encoding techniques that increases the robustness of the system achieving average positioning errors below 5 cm on plane XY, coordinate z errors below 30 cm and, rotation angle errors below 8°.

Chapter 7

Conclusions and Future Works

In this chapter, the most important conclusions of this work are shown together with the claims to novelty and future lines of research. Finally, the publications derived from this thesis will be listed.

7.1 Conclusions

The motivation of this thesis is the contribution to the development of an optical LPS that can replace or be complementary to the Global Navigation Satellite System (GNSS) in the absence of its signals or in locations where this system is not available (e.g. indoor environments). To do so, a 3D optical indoor positioning system is designed and implemented, deploying different configurations using various emitters and receivers. Different algorithms have been implemented to estimate the position of the desired target in large distances up to 5 m using encoded sequences and achieving centimetric accuracies.

Throughout the thesis, a series of partial conclusions have been gathered that allow corroborating the aforementioned global conclusion. Each of these partial conclusions drawn in the previous chapters are detailed below.

- Chapter 2 details the importance of developing a system that overcomes the weaknesses of GNSS in indoor scenarios. Some proposed solutions rely on optical, mechanical, magnetic, acoustic, and radio frequency signals. Among them, optical systems can provide significant advantages, such as the accuracy achieved. Nevertheless, there is still a number of research challenges, mainly related to the robustness of the technology.

  Regarding the positioning techniques, the most commonly used in VLPS or IRLPS are fingerprinting, triangulation and trilateration or multilateration with times-of-flight measurements, signal attenuation measurements or angles-of-arrival measurements. The main advantages of angles-of-arrival measurements are its robustness against source and environmental fluctuations, as well as the fact that synchronisation between transmitters is not necessary. Also, it only requires three measurements to position in three dimensions although obstruction in the LoS may deteriorate the link.

  Summing it up, there is an interest in having a 3D optical system covering large distances, capable of working in non-ideal situations to locate people, robots, drones, etcetera. In addition, having a

small and compact modular structure is key to facilitate the system's deployment in a room. For this purpose, it is crucial to have centimetric accuracies using a low number of beacons and the fact of not including other types of sensors that might compromise the latency of the proposal.

- Chapter 3 analyses the implementation of the transmitter and the receiver in the proposed system. The reception module consists of a QADA photoreceptor, a filtering system and an acquisition system. The filtering system eliminates undesired signals below 2 kHz and beyond 75 kHz. Regarding the acquisition system, the circuit gain is adjusted with a digital potentiometer controlled by a SPI bus to maximize the dynamic range of the used acquisition module.

  On the other hand, the transmitter system is based on four beacons, each one of them emitting a particular BPSK modulated signal using either Kasami or LS sequences. The carrier frequency has been established at 25 kHz, which is much higher than the frequency detectable by human eyes (200 Hz), in order to eliminate any possible flickering.

  The behaviour of different sequences has been analysed to improve the performance of the proposal without greatly increasing the emission time. In particular, the SMR, IFW and sequence shifting have been studied for Kasami and LS sequences to improve the cross-correlation properties of the codes. It has been found that a 1023-bit Kasami sequence with a displacement of 5 samples and a 1151-bit LS sequence with a displacement of 10 samples are a suitable trade-off between minimizing the positioning error and having a simultaneous transmission.

- Chapter 4 has studied the performance of a privacy-oriented 3D Optical Positioning system that has the transmitters fixed at a known location and the receiver placed at the object to position.

  In the aim of increasing the coverage volume, a full usage of the area of the photodiode is defined by setting the side of the aperture equal to the diameter of the photoreceptor. In this configuration, a Non-Linear Least Squares (NLS) is implemented to estimate the image points using a look-at-table with precalculated values of the non-linear function. On the other hand, the use of a smaller aperture assures the linearization of the involved algorithms, which simplifies them and improves the overall system performance.

  Regarding the estimation of the receiver's position, two solutions are proposed: a triangulation technique, solved by LSE and some geometrical considerations, that estimates the receiver's position (x, y, z, γ), and different PnP approaches (EPnP, IPPE and RPnP) that estimates the complete pose of the receiver (x, y, z, α, β, γ). Simulations have verified that the PnP algorithm with a better behaviour in this proposal is the IPPE algorithm.

  In addition, a calibration algorithm has been defined and applied to the proposal to estimate the intrinsic parameters of the receiver: optical centre, the height at which the aperture is located, the aperture misalignment and the length of the aperture. This parameters have been obtained by combining trigonometric considerations with a Branch and Bound algorithm and a LSE algorithm.

- Chapter 5 has studied the performance of a centralized 3D Optical Positioning system according to the deployed LEDs or QADAs, as well as different positioning techniques.

  The positioning system is based on at least two fixed receivers QADA and several LEDs located at the mobile to locate. With this configuration, three positioning algorithms are

implemented: 1) a LSE in combination with the Levenberg-Marquardt method and some trigonometric considerations; 2) a NLSE to include the geometry of the transmitters and; 3) an EKF to increase the robustness of the proposal.

There is a trade-off between increasing the number of receivers, thus, decreasing the positioning error and having a small, compact receiver module. In this way, the geometrical distribution of the QADA receivers has been studied including different arrangements and distances between receivers, finding that the best behaviour of the system is when using 4 non-aligned QADAs with a distance of 20 cm between them.

- Chapter 6 has presented the experimental results using AoA or PnP algorithms that verify the proposed privacy-oriented 3D Optical Positioning system. Various experimental tests have been carried out in two scenarios using visible or infrared light; LS or Kasami sequences; two different aperture lengths; different distances between transmitters and receiver; different positioning algorithms and various rotations of the receiver.

  It can be concluded that the proposed system can estimate the complete 3D pose $(x, y, z, \alpha, \beta, \gamma)$ of a static or moving target on large scenarios. Also, the proposal presents a linear algorithm using AoA and encoding techniques that increases the robustness of the system, achieving average positioning errors below 5 cm on plane XY, coordinate z errors below 30 cm and, rotation angle γ errors below 8°.

7.2 Claims to Novelty

The main claim to novelty of this thesis is the design and implementation of two configurations of a 3D optical indoor positioning system using encoding techniques. The following list enumerates each of the claims to novelty of this thesis:

- Two positioning system designs for estimating the 3D pose of mobile assets, people, robots or objects:
  - A privacy-oriented system where there is a mobile quadrant-type receiver (QADA photodiode) and at least three visible or infrared light static emitters in the environment.
  - A centralized system where there are at least three visible or infrared light mobile emitters and at least two static quadrant-type receivers (QADA photodiode) in the environment.
- A modulation and coding scheme using binary sequences that enables simultaneous transmission from all LED emitters in the environment, and their discrimination and identification by means of correlation techniques (coupled filtering) in the QADA receivers.
- The calculation of the angles of arrival of the light beams coming from each LED emitter, by applying a quadrangular aperture to the QADA receivers, which enables the discrimination of the illuminated area in each quadrant of the QADA photodiode according to its geometrical configuration. Two algorithms are derived depending on the length of the aperture:
  - When using the full area of the photodiode, the aperture length is set equal to the diameter of the photoreceptor. In this configuration, a Non-Linear Least Squares (NLS) is implemented

to estimate the image points using a look-at-table with precalculated values of the non-linear function.

  - When using a smaller aperture. The linearization of the involved algorithms is assured. In this configuration, the calibration parameters (optical centre, misalignment of the aperture, aperture length, and aperture height) are also included.

- The calibration method that estimates the intrinsic parameters of the QADA receiver: optical centre, misalignment of the aperture, aperture length, and aperture height. It combines iterative methods (Branch and Bound algorithm and LLS) and trigonometric considerations to obtain the optimized parameters.

- The calculation of the position of the 3D pose of the asset (person or object) from the angles of arrival estimated in the QADA receivers, by means of triangulation for the two 3D positioning designs:

  - In the privacy-oriented system, two positioning algorithms are implemented: 1) LSE and trigonometric considerations and; 2) various PnP approaches (EPnP, IPPE, RPnP).
  - In the centralized system, three positioning algorithms are implemented: 1) LSE and some trigonometric considerations; 2) NLSE to include the geometry of the transmitters and; 3) an EKF to increase the robustness of the proposal.

- The proposed system can estimate the complete 3D pose (x, y, z, α, β, γ) of a static or moving target in large scenarios with a low SNR, achieving average positioning errors on plane XY below 5 cm, coordinate z errors below 30 cm, and rotation angle γ errors below 8°.

7.3 Future Works

Based on the results of this thesis, and in line with the conclusions previously drawn, the following actions and future works to be carried out are proposed:

- The implementation of the centralized Local Positioning System is key to experimentally verify the proposal. Also, it is interesting to analyse the influence of deploying the receivers not only on the ceiling, but also on one or more walls to increase the robustness of the system. The odometry of the moving object (i.e., robot) can also be included in the EKF.

- The current carrier and sampling frequencies are set at 25 kHz and 250 kHz making it difficult to determine the real-time position of a fast moving object. As a result, increasing both frequencies will reduce the required emission time, allowing the system to position moving objects at greater speeds (i.e., drones).

- The proposed cell for the privacy-oriented LPS is based on four transmitters and a QADA. It would be interesting to increase the number of transmitters in order to assess the system in larger scenarios (a warehouse or a long corridor). The proposed algorithm would be the same, with the exception of the receiver going from one cell to another to estimate its position using the transmitters located in its current cell.

- We need to process the obtained signals on a computer, even if the current system can work in real time (a wired connection between receiver and computer is needed). A wireless approach is to first store the acquired signals in a micro-SD card for further post-processing on the computer. However, this last solution does not allow real-time implementations. Implementing the positioning algorithm in an FPGA (Field-Programmable Gate Array) device, for example, would allow real-time implementations as well as more freedom of movement at the receiver. These enhancements could expand the current system's real-time applications to include controlling a drone or a robot in a large indoor environment, such as an industrial warehouse.
- Nowadays, the implementation of machine learning methods is highly increasing due to the vast majority of developed work. Assessing the proposed systems using those methods would be interesting because no information about the transmitters' position or intrinsic properties would be required. These methods, on the other hand, have the disadvantage of requiring multiple training points, being extremely dependent on the scenario, and not being typically real-time compatible.

7.4 Publications derived from this Thesis

7.4.1 International Journals

- [Apa20b] E. Aparicio-Esteve, Á. Hernández, J. Ureña, J.M. Villadangos. 'Visible Light Positioning System Based on a Quadrant Photodiode and Encoding Techniques'. *IEEE Transactions on Instrumentation and Measurement*. vol. 69 (8), pp. 5589–5603, 2020. doi:10.1109/TIM.2019.2962563.
- [Apa20d] E. Aparicio-Esteve, Á. Hernández, J. Ureña, J.M. Villadangos, S. Lluva, M.C. Pérez-Rubio. 'Detecting Relative Amplitude of IR Signals with Active Sensors and Its Application to a Positioning System'. *Applied Sciences*. vol. 10 (18), pp. 1-12, 2020. doi:10.3390/app10186412.
- [Apa21a] E. Aparicio-Esteve, Á. Hernández, J. Ureña. 'Design, Calibration, and Evaluation of a Long-Range 3-D Infrared Positioning System Based on Encoding Techniques'. *IEEE Transactions on Instrumentation and Measurement*. vol. 70, pp. 1–13, 2021. doi:10.1109/TIM.2021.3089223.
- [Apa21c] E. Aparicio-Esteve, J. Ureña, Á. Hernández, D. Pizarro, D. Moltó. 'Using Perspective-n-Point Algorithms for a Local Positioning System Based on LEDs and a QADA Receiver'. *Sensors*. vol. 21 (19), pp. 1-16, 2021. doi:10.3390/s21196537.

7.4.2 International Conferences

- [Apa19a] E. Aparicio-Esteve, Á. Hernández, J. Ureña, J.M. Villadangos, F. Ciudad. 'Estimation of the Polar Angle in a 3D Infrared Indoor Positioning System based on a QADA receiver'. *Proc. of 2019 International Conference on Indoor Positioning and Indoor Navigation (IPIN 2019)*. pp. 1–8, Pisa (Italy), 2019.
- [Apa20a] E. Aparicio-Esteve, Á. Hernández, J. Ureña. 'Evaluation of MAI Effect in Encoding Techniques for an Infrared Positioning System'. *IEEE International Instrumentation & Measurement Technology Conference (I2MTC 2020)*. pp. 1–6, Dubrovnik (Croatia), 2020.

- [Apa21d] E. Aparicio-Esteve, J.M. Villadangos, Á. Hernández, J. Ureña. 'Experimental Evaluation of an IR and US Multi-Sensory Positioning Fusion Method'. *Proc. of 2021 International Conference on Indoor Positioning and Indoor Navigation (IPIN 2021)*. pp. 1–13, Lloret del Mar (Spain), 2021.

7.4.3 National Conferences

- [Apa19b] E. Aparicio-Esteve, Á. Hernández, J. Ureña, J.M. Villadangos, R. Nieto, F. Ciudad. 'Implementación de un Sistema de Posicionamiento con Luz Visible basado en focos LEDs y un receptor QADA'. *Seminario Anual de Automática, Electrónica Industrial e Instrumentación (SAAEI 2019)*. pp. 414–419, Córdoba (Spain), 2019.

- [Apa20c] E. Aparicio-Esteve, Á. Hernández, J. Ureña, J.M. Villadangos, S. LLuva, J.J. Vicente-Real. 'Implementación de un Sistema de Posicionamiento Local 3D Síncrono basado en Luz Infrarroja'. *Seminario Anual de Automática, Electrónica Industrial e Instrumentación (SAAEI 2020)*. pp. 38–43, Ciudad Real (Spain), 2020.

- [Apa21b] E. Aparicio-Esteve, J. Ureña, J.M. Villadangos, Á. Hernández. 'Evaluación de un Sistema de Posicionamiento con Medidas Simultáneas de Ultrasonidos e Infrarrojos'. *Seminario Anual de Automática, Electrónica Industrial e Instrumentación (SAAEI 2021)*. pp. 1–6, Ciudad Real (Spain), 2021.

7.4.4 Patents

- [Ureew] J. Ureña, Á. Hernández, E. Aparicio-Esteve, J.M. Villandangos, J.J. Garcíia, A. Jiménez, M.C. Pérez. 'SISTEMA Y PROCEDIMIENTO DE POSICIONAMIENTO DE ALTA VELOCIDAD CON EMISORES MÓVILES TIPO LEDS Y RECEPTORES ESTÁTICOS TIPO FOTODIODOS EN CUADRANTES', Spain Patent P202131028, 02-11-2021 (Under Review).

Bibliography

[Abd14] A. Abdelgawad. 'Localization system for indoor robot using RFID'. In *2014 IEEE Symposium on Industrial Electronics Applications (ISIEA)* (2014) pp. 157–160.
doi:10.1109/ISIEA.2014.8049890

[Abd15] Y.I. Abdel-Aziz, H. Karara, M. Hauck. 'Direct linear transformation from comparator coordinates into object space coordinates in close-range photogrammetry'. *Photogrammetric Engineering & Remote Sensing*. vol. 81 (2), pp. 103–107, 2015.

[Agu16] T. Aguilera Benítez. *Desarrollo de un Sistema de Posicionamiento Local Acústico para Dispositivos Móviles con Modulación de Espectro Expandido*. Ph.D. thesis, Universidad de Extremadura, 2016.

[Agu17] D. Aguirre, R. Navarrete, I. Soto, S. Gutierrez. 'Implementation of an emitting LED circuit in a Visible Light communications positioning system'. In *2017 First South American Colloquium on Visible Light Communications (SACVLC)* (Santiago, Chile, 2017) pp. 1–4.
doi:10.1109/SACVLC.2017.8267602

[Ala19] F. Alam, M.T. Chew, T. Wenge, G.S. Gupta. 'An Accurate Visible Light Positioning System Using Regenerated Fingerprint Database Based on Calibrated Propagation Model'. *IEEE Transactions on Instrumentation and Measurement*. vol. 68 (8), pp. 2714–2723, 2019.
doi:10.1109/TIM.2018.2870263

[Alm19] Y. Almadani, M. Ijaz, S. Bastiaens, S. Rajbhandari, W. Joseph, D. Plets. 'An Experimental Analysis of the Effect of Reflections on the Performance of Visible Light Positioning Systems in Warehouses'. In *2019 IEEE 2nd British and Irish Conference on Optics and Photonics (BICOP)* (London, UK, 2019) pp. 1–4.
doi:10.1109/BICOP48819.2019.9059580

[Apa19a] E. Aparicio-Esteve, Á. Hernández, J. Ureña, J.M. Villadangos, F. Ciudad. 'Estimation of the Polar Angle in a 3D Infrared Indoor Positioning System based on a QADA receiver'. In *Proc. of 2019 International Conference on Indoor Positioning and Indoor Navigation (IPIN 2019)* (Pisa, Italy, 2019) pp. 1–8.

[Apa19b] E. Aparicio-Esteve, Á. Hernández, J. Ureña, J.M. Villadangos, R. Nieto, F. Ciudad. 'Implementación de un Sistema de Posicionamiento con Luz Visible basado en focos LEDs y un receptor QADA'. In *Seminario Anual de Automática, Electrónica Industrial e Instrumentación* (Córdoba, Spain, 2019) pp. 414–419.

[Apa20a] E. Aparicio-Esteve, Á. Hernández, J. Ureña. 'Evaluation of MAI Effect in Encoding Techniques for an Infrared Positioning System'. In *IEEE International Instrumentation & Measurement Technology Conference* (Dubrovnik, Croatia, 2020) pp. 1–6.

[Apa20b] E. Aparicio-Esteve, Á. Hernández, J. Ureña, J.M. Villadangos. 'Visible Light Positioning System Based on a Quadrant Photodiode and Encoding Techniques'. *IEEE Transactions on Instrumentation and Measurement*. vol. 69 (8), pp. 5589–5603, 2020.
doi:10.1109/TIM.2019.2962563

[Apa20c] E. Aparicio-Esteve, Á. Hernández, J. Ureña, J.M. Villadangos, S. LLuva, J.J. Vicente-Real. 'Implementación de un Sistema de Posicionamiento Local 3D Síncrono basado en Luz Infrarroja'. In *Seminario Anual de Automática, Electrónica Industrial e Instrumentación* (Ciudad Real, Spain, 2020) pp. 38–43.

[Apa20d] E. Aparicio-Esteve, Á. Hernández, J. Ureña, J.M. Villadangos, S. Lluva, M.C. Pérez-Rubio. 'Detecting Relative Amplitude of IR Signals with Active Sensors and Its Application to a Positioning System'. *Applied Sciences*. vol. 10 (18), pp. 1–12, 2020.
doi:10.3390/app10186412

[Apa21a] E. Aparicio-Esteve, Á. Hernández, J. Ureña. 'Design, Calibration, and Evaluation of a Long-Range 3-D Infrared Positioning System Based on Encoding Techniques'. *IEEE Transactions on Instrumentation and Measurement*. vol. 70, pp. 1–13, 2021.
doi:10.1109/TIM.2021.3089223

[Apa21b] E. Aparicio-Esteve, J. Ureña, J.M. Villadangos, Á. Hernández. 'Evaluación de un Sistema de Posicionamiento con Medidas Simultáneas de Ultrasonidos e Infrarrojos'. In *Seminario Anual de Automática, Electrónica Industrial e Instrumentación* (Ciudad Real, Spain, 2021) pp. 1–6.

[Apa21c] E. Aparicio-Esteve, J. Ureña, Á. Hernández, D. Pizarro, D. Moltó. 'Using Perspective-n-Point Algorithms for a Local Positioning System Based on LEDs and a QADA Receiver'. *Sensors*. vol. 21 (19), pp. 1–16, 2021.
doi:10.3390/s21196537

[Apa21d] E. Aparicio-Esteve, J. Villadangos, Á. Hernández, J. Ureña. 'Experimental Evaluation of an IR and US Multi-Sensory Positioning Fusion Method'. In *Proc. of 2021 International Conference on Indoor Positioning and Indoor Navigation (IPIN 2021)* (Lloret del Mar, Spain, 2021) pp. 1–13.

[App21] I. Apple. 'iBeacon', 2021.
https://developer.apple.com/ibeacon/

[Atl21] I. Atlas. 'Overview Magnetic Positioning System', [online] Available: https://www.indooratlas.com, 2021.

[Ber08] P. Berglez. 'Development of a GPS, Galileo and SBAS receiver'. In *2008 50th International Symposium ELMAR*, vol. 2 (Zadar, Croatia, 2008) pp. 573–576.

[Ber12] G. Berkovic, E. Shafir. 'Optical methods for distance and displacement measurements'. *Adv. Opt. Photon. (OSA)*. vol. 4 (4), pp. 441–471, 2012.
doi:10.1364/AOP.4.000441

[Ber20] E. Bernardes, S. Viollet, T. Raharijaona. 'A Three-Photo-Detector Optical Sensor Accurately Localizes a Mobile Robot Indoors by Using Two Infrared Light-Emitting Diodes'. *IEEE Access*. vol. 8, pp. 87490–87503, 2020.
doi:10.1109/ACCESS.2020.2992996

[Bes19] N.P. Bester, A. Hoffman. 'Kalman Filter based RFID tag velocity estimation in the presence of frequency hopping'. In *2019 IEEE International Conference on RFID Technology and Applications (RFID-TA)* (2019) pp. 488–493.
doi:10.1109/RFID-TA.2019.8892213

[Bis09] V. Bistrovs, A. Kluga. 'Combined Information Processing from GPS and IMU using Kalman Filtering Algorithm'. *Elektronika ir Elektrotechnika*. pp. 1392–1215, 2009.

[Buf17] A. Buffi, P. Nepa, R. Cioni. 'SARFID on drone: Drone-based UHF-RFID tag localization'. In *2017 IEEE International Conference on RFID Technology Application (RFID-TA)* (Warsaw, Poland, 2017) pp. 40–44.
doi:10.1109/RFID-TA.2017.8098872

[Cai17] Y. Cai, W. Guan, Y. Wu, C. Xie, Y. Chen, L. Fang. 'Indoor High Precision Three-Dimensional Positioning System Based on Visible Light Communication Using Particle Swarm Optimization'. *IEEE Photonics Journal*. vol. 9 (6), 2017.
doi:10.1109/JPHOT.2017.2771828

[Cha19] N. Chaudhary, L.N. Alves, Z. Ghassemblooy. 'Feasibility Study of Reverse Trilateration Strategy with a Single Tx for VLP'. In *2019 2nd West Asian Colloquium on Optical Wireless Communications (WACOWC)* (Tehran, Iran, 2019) pp. 121–126.
doi:10.1109/WACOWC.2019.8770213

[Cha20] H.W. Chae, J.H. Choi, J.B. Song. 'Robust and Autonomous Stereo Visual-Inertial Navigation for Non-Holonomic Mobile Robots'. *IEEE Transactions on Vehicular Technology*. vol. 69 (9), pp. 9613–9623, 2020.
doi:10.1109/TVT.2020.3004163

[Che10] C. Chen, X. Zhang. 'Simulation Analysis of Positioning Performance of BeiDou-2 and Integrated BeiDou-2/GPS'. In *2010 International Conference on Communications and Mobile Computing*, vol. 2 (Shenzhen, China, 2010) pp. 505–509.
doi:10.1109/CMC.2010.149

[Che16] C. Chen, Y. Han, Y. Chen, K.J.R. Liu. 'Indoor GPS with centimeter accuracy using WiFi'. In *2016 Asia-Pacific Signal and Information Processing Association Annual Summit and Conference (APSIPA)* (2016) pp. 1–4.
doi:10.1109/APSIPA.2016.7820842

[Che18] G. Chen, S. Jian-Hua, K. Wei, Z. Chun-Yan. 'A Visible Light Indoor Positioning Algorithm Based on Fingerprint'. In *2018 4th Annual International Conference on Network and Information Systems for Computers (ICNISC)* (Wuhan, China, 2018) pp. 71–77.
doi:10.1109/ICNISC.2018.00022

[Cin18a] S. Cincotta, C. He, A. Neild, J. Armstrong. 'High angular resolution visible light positioning using a quadrant photodiode angular diversity aperture receiver (QADA)'. *Optics Express*. vol. 26 (7), pp. 9230–9242, 2018.
doi:10.1364/oe.26.009230

[Cin18b] S. Cincotta, C. He, A. Neild, J. Armstrong. 'QADA-PLUS: A Novel Two-Stage Receiver for Visible Light Positioning'. In *IPIN 2018 - 9th International Conference on Indoor Positioning and Indoor Navigation* (Nantes, France, 2018) pp. 24–27.
doi:10.1109/IPIN.2018.8533733

[Cin19] S. Cincotta, C. He, A. Neild, J. Armstrong. 'Indoor visible light positioning: Overcoming the practical limitations of the quadrant angular diversity aperture receiver (QADA) by using the two-stage QADA-plus receiver'. *Sensors (Switzerland)*. vol. 19 (4), 2019.
doi:10.3390/s19040956

[Col14] T. Collins, A. Bartoli. 'Infinitesimal Plane-Based Pose Estimation'. *International Journal of Computer Vision*. vol. 109 (3), pp. 252–286, 2014.
doi:10.1007/s11263-014-0725-5

[Dan12] C. Danakis, M. Afgani, G. Povey, I. Underwood, H. Haas. 'Using a CMOS camera sensor for visible light communication'. In *2012 IEEE Globecom Workshops* (2012) pp. 1244–1248.
doi:10.1109/GLOCOMW.2012.6477759

[Dec21] Decawave. 'Decawave 2021'. *Product Specification*, 2021.
https://www.decawave.com/

[DLLC21] Á. De-La-Llana-Calvo, J.L. Lázaro-Galilea, A. Gardel-Vicente, D. Salido-Monzú, I. Bravo-Muñoz, A. Iamnitchi, R. Gil-Vera. 'Weak Calibration of a Visible Light Positioning System Based on a Position-Sensitive Detector: Positioning Error Assessment'. *Sensors*. vol. 21 (11), 2021.
doi:10.3390/s21113924

[Do16a] T.H. Do, M. Yoo. 'An in-depth survey of visible light communication based positioning systems'. *Sensors*. vol. 16 (5), 2016.
doi:10.3390/s16050678

[Do16b] T.H. Do, M. Yoo. 'Performance Analysis of Visible Light Communication Using CMOS Sensors'. *Sensors*. 16 (3), 2016.
doi:10.3390/s16030309

[Fan17] J. Fang, Z. Yang, S. Long, Z. Wu, X. Zhao, F. Liang, Z.L. Jiang, Z. Chen. 'High-speed indoor navigation system based on visible light and mobile phone'. *IEEE Photonics Journal*. 9 (2), 2017.
doi:10.1109/JPHOT.2017.2687947

[Far17] Z.A. Farhat, M.H. Ahfayd, P.J. Mather, M.J.N. Sibley. 'Practical implementation of duobinary pulse position modulation using FPGA and visible light communication'. In *2017 IEEE 15th*

Student Conference on Research and Development (SCOReD) (Putrajaya, Malaysia, 2017) pp. 253–256.
doi:10.1109/SCORED.2017.8305383

[FCC21] U. Federal Communications Commission, 2021.
https://docs.fcc.gov/public/attachments/FCC-02-48A1.pdf

[Fer18] C.M.y.R.A. Ferguson R. 'mmWave radar: Enabling greater intelligent autonomy at the edge'. *Texas Instruments Incorporated*, 2018.

[Fri19] P.H. Frisch. 'RFID in Today's Intelligent Hospital Enhancing Patient Care amp; Optimizing Hospital Operations'. In *2019 IEEE International Conference on RFID Technology and Applications (RFID-TA)* (Pisa, Italy, 2019) pp. 458–463.
doi:10.1109/RFID-TA.2019.8892070

[G S17] G.Z. G. Simon, G. Vakulya. 'Lookup: Robust and Accurate Indoor Localization Using Visible Light Communication'. *IEEE Transactions on Instrumentation and Measurement*. pp. 2337–2348, 2017.

[Gao03] X.S. Gao, X.R. Hou, J. Tang, H.F. Cheng. 'Complete solution classification for the perspective-three-point problem'. *IEEE transactions on pattern analysis and machine intelligence*. vol. 25 (8), pp. 930–943, 2003.

[Gar12] E. García, J. Ureña, J.J. García, M.C. Perez, F.D. Ruiz, C. Diego, J. Aparicio. 'Multilevel LS sequences with flexible ZCZ length and their application to local positioning systems'. In *2012 IEEE International Instrumentation and Measurement Technology Conference Proceedings* (Graz, Austria, 2012) pp. 1665–1669.
doi:10.1109/I2MTC.2012.6229428

[Geo14] L. Geosystems. 'Leica Nova TS60'. *Product Specification*, 2014.
https://leica-geosystems.com/-/media/files/leicageosystems/products/datasheets/leica_nova_ts60_ds.ashx?la=en&hash=5C7BEB60644F956CFD103D64CE197073

[Gol10] E. Goldoni, A. Savioli, M. Risi, P. Gamba. 'Experimental analysis of RSSI-based indoor localization with IEEE 802.15.4'. In *2010 European Wireless Conference (EW)* (Lucca, Italy, 2010) pp. 71–77.
doi:10.1109/EW.2010.5483396

[Gua19] D. Gualda, J.M. Villadangos, J. Ureña, A.R.J. Ruiz, F.S. Granja, Á. Hernández. 'Indoor positioning in large environments: ultrasonic and UWB technologies'. In *IPIN 2019 - 10th International Conference on Indoor Positioning and Indoor Navigation* (Pisa, Italy, 2019) pp. 1–8.

[Hac14] C. Hackman, S.M. Byram, V.J. Slabinski, J.C. Tracey. 'USNO GPS/GLONASS PNT products: Overview, and GPS+GLONASS vs GLONASS only PPP accuracy'. In *2014 IEEE/ION Position, Location and Navigation Symposium - PLANS 2014* (2014) pp. 793–803.
doi:10.1109/PLANS.2014.6851444

[Hai19] A. Haider Malik, W. Yiqiao, S. Liu, S.H. Hwang. 'Pre- and Post-Processing Algorithms with Deep Learning Classifier for Wi-Fi Fingerprint-Based Indoor Positioning'. *Electronics*. vol. 8, p. 195, 2019.
doi:10.3390/electronics8020195

[Han11] G.P. Hancke. 'Practical Eavesdropping and Skimming Attacks on High-Frequency RFID Tokens'. *J. Comput. Secur.* vol. 19 (2), p. 259–288, 2011.

[Har04] R. Hartley, A. Zisserman. *Multiple View Geometry in Computer Vision* (Cambridge University Press, 2004), 2 ed.
doi:10.1017/CBO9780511811685

[Hav09] J. Haverinen, A. Kemppainen. 'A global self-localization technique utilizing local anomalies of the ambient magnetic field'. In *2009 IEEE International Conference on Robotics and Automation* (Kobe, Japan, 2009) pp. 3142–3147.
doi:10.1109/ROBOT.2009.5152885

[He19] H. He, X. Chen, L. Ukkonen, J. Virkki. 'Clothing-Integrated Passive RFID Strain Sensor Platform for Body Movement-Based Controlling'. In *2019 IEEE International Conference on RFID Technology and Applications (RFID-TA)* (Pisa, Italy, 2019) pp. 236–239.
doi:10.1109/RFID-TA.2019.8892118

[Hol05] S. Holm. 'Airborne ultrasound data communications: the core of an indoor positioning system'. In *IEEE Ultrasonics Symposium, 2005*, vol. 3 (Rotterdam, Netherlands, 2005) pp. 1801–1804.
doi:10.1109/ULTSYM.2005.1603217

[Hos20] H. Hosseinianfar, M. Brandt-Pearce. 'Performance Limits for Fingerprinting-Based Indoor Optical Communication Positioning Systems Exploiting Multipath Reflections'. *IEEE Photonics Journal*. vol. 12 (4), pp. 1–16, 2020.
doi:10.1109/JPHOT.2020.2991472

[Hu13] P. Hu, L. Li, C. Peng, G. Shen, F. Zhao. 'Pharos: Enable Physical Analytics through Visible Light Based Indoor Localization'. In *Proceedings of the Twelfth ACM Workshop on Hot Topics in Networks*HotNets-XII (Association for Computing Machinery, New York, USA, 2013) pp. 1–7.
doi:10.1145/2535771.2535790

[Hua21] Y. Huang, D. Shi, x. zhang, E.H. Aglzim, L. Shi. 'Environment-Aware RSSI Based Positioning Algorithm for Random Angle Interference Cancellation in Visible Light Positioning System'. In *Indoor Positioning and Indoor Navigation* (Lloret de Mar, Spain, 2021) pp. 1–8.
https://hal.archives-ouvertes.fr/hal-03328942

[Huy16] P. Huynh, M. Yoo. 'VLC-based positioning system for an indoor environment using an image sensor and an accelerometer sensor'. *Sensors (Switzerland)*. vol. 16 (6), 2016.
doi:10.3390/s16060783

[Inc03] M.T. Inc. 'Single/Dual Digital Potentiometer with SPIInterface'. *Product Specification*. pp. 1–32, 2003.
http://ww1.microchip.com/downloads/en/devicedoc/11195c.pdf

[Inc12] F.S. Inc. 'Series 6 Data Sheet Quad Sum and Difference Amplifier, Part Description QP50-6-18u-SD2, Product Specification', 2012.

[Jim05] A. Jiménez, F. Seco. 'Precise localisation of archaeological findings with a new ultrasonic 3D positioning sensor'. *Sensors and Actuators A-physical*. vol. 123, pp. 224–233, 2005.

[Kah97] J.M. Kahn, J.R. Barry. 'Wireless infrared communications'. *Proceedings of the IEEE*. vol. 85 (2), pp. 265–298, 1997.
doi:10.1109/5.554222

[Kal16] A.A. Kalbandhe, S.C. Patil. 'Indoor Positioning System using Bluetooth Low Energy'. In *2016 International Conference on Computing, Analytics and Security Trends (CAST)* (Pune, India, 2016) pp. 451–455.
doi:10.1109/CAST.2016.7915011

[Kan17] S.N.R. Kantareddy, R. Bhattacharyya, S.E. Sarma. 'Low-cost, automated inventory control of sharps in operating theaters using passive RFID tag-sensors'. In *2017 IEEE International Conference on RFID Technology Application (RFID-TA)* (Warsaw, Poland, 2017) pp. 16–21.
doi:10.1109/RFID-TA.2017.8098868

[Kar05] N. Karlsson, E. di Bernardo, J. Ostrowski, L. Goncalves, P. Pirjanian, M. Munich. 'The vSLAM Algorithm for Robust Localization and Mapping'. In *Proceedings of the 2005 IEEE International Conference on Robotics and Automation* (Barcelona, Spain, 2005) pp. 24–29.
doi:10.1109/ROBOT.2005.1570091

[Kaz14] F. Kazemzadeh, S.A. Haider, C. Scharfenberger, A. Wong, D.A. Clausi. 'Multispectral Stereoscopic Imaging Device: Simultaneous Multiview Imaging From the Visible to the Near-Infrared'. *IEEE Transactions on Instrumentation and Measurement*. vol. 63 (7), pp. 1871–1873, 2014.
doi:10.1109/TIM.2014.2307992

[Kes18] M.F. Keskin, O. Erdem, S. Gezici. 'Cooperative Localization in Visible Light Networks: Theoretical Limits and Distributed Algorithms'. *CoRR*. vol. abs/1804.00576, pp. 1–15, 2018.
http://arxiv.org/abs/1804.00576

[Kno12] L. Knowles Acoustics. 'Amplified "Ultra-Mini" SiSonicTM Microphone SpecificationWith MaxRF Protection'. *Product Specification*, 2012.

[Knu20] N. Knudde, W. Raes, J. De Bruycker, T. Dhaene, N. Stevens. 'Data-Efficient Gaussian Process Regression for Accurate Visible Light Positioning'. *IEEE Communications Letters*. vol. 24 (8), pp. 1705–1709, 2020.
doi:10.1109/LCOMM.2020.2990950

[Kol16] A. Kolomijeca, J.A. López-Salcedo, E.S. Lohan, G. Seco-Granados. 'GNSS applications: Personal safety concerns'. In *2016 International Conference on Localization and GNSS (ICL-GNSS)* (Barcelona, Spain, 2016) pp. 1–5.
doi:10.1109/ICL-GNSS.2016.7533861

[Kot15] M. Kotaru, K. Joshi, D. Bharadia, S. Katti. 'SpotFi: Decimeter Level Localization Using WiFi'. In *Proceedings of the 2015 ACM Conference on Special Interest Group on Data Communication*SIGCOMM '15 (Association for Computing Machinery, New York, USA, 2015) p. 269–282.
doi:10.1145/2785956.2787487

[Kov14] M. Kovalev. 'Indoor positioning of mobile devices by combined Wi-Fi and GPS signals'. In *2014 International Conference on Indoor Positioning and Indoor Navigation (IPIN)* (Busan, Korea, 2014) pp. 332–339.
doi:10.1109/IPIN.2014.7275500

[Kul00] K. Kulpa, E. Sliwa, J. Misiurewicz. 'Surface target tracking in WGS-84 coordinates'. In *13th International Conference on Microwaves, Radar and Wireless Communications. MIKON - 2000. Conference Proceedings (IEEE Cat. No.00EX428)*, vol. 2 (Wroclaw, Poland, 2000) pp. 619–622 vol.2.
doi:10.1109/MIKON.2000.914010

[Laz15] P. Lazik, N. Rajagopal, O. Shih, B. Sinopoli, A.G. Rowe. 'ALPS: A Bluetooth and Ultrasound Platform for Mapping and Localization'. *Proceedings of the 13th ACM Conference on Embedded Networked Sensor Systems*, 2015.

[Lee18] J.K. Lee, W. Jung. 'Vertical Position Estimation of a Constrained Link Using IMU Signals and Kinematic Constraint'. *2018 IEEE SENSORS*. pp. 1–4, 2018.

[Lep09] V. Lepetit, F. Moreno-Noguer, P. Fua. 'EPnP: An Accurate O(n) Solution to the PnP Problem'. *International Journal of Computer Vision*. vol. 81 (155), 2009.
doi:10.1007/s11263-008-0152-6

[Li11] S. Li, C. Xu. 'A Stable Direct Solution of Perspective-Three-Point Problem.' *IJPRAI*. vol. 25, pp. 627–642, 2011.
doi:10.1142/S0218001411008774

[Li12] S. Li, C. Xu, M. Xie. 'A Robust O(n) Solution to the Perspective-n-Point Problem'. *IEEE transactions on pattern analysis and machine intelligence*. vol. 34, 2012.
doi:10.1109/TPAMI.2012.41

[Li17] Z. Li, L. Feng, A. Yang. 'Fusion Based on Visible Light Positioning and Inertial Navigation using extended Kalman Filters'. *Sensors (Switzerland)*. vol. 17 (5), 2017.
doi:10.3390/s17051093

[Lib21] 'Polhemus Technology', [online] Available: http://www.polhemus.com/, 2021.

[Lin15] A. Lindo, E. García, J. Ureña, M.d.C. Pérez, Á. Hernández. 'Multiband Waveform Design for an Ultrasonic Indoor Positioning System'. *IEEE Sensors Journal*. vol. 15 (12), pp. 7190–7199,

2015.
doi:10.1109/JSEN.2015.2472978

[Liu17a] C. Liu, Z. Cheng, Y. Zhang, G. Wang. 'An indoor positioning system based on RFID with rotating antenna and passive tags'. In *2017 2nd International Conference on Robotics and Automation Engineering (ICRAE)* (Shanghai, China, 2017) pp. 455–459.
doi:10.1109/ICRAE.2017.8291429

[Liu17b] C. Liu, X. Jin, W. Zhu, M. Jin, Z. Xu. 'Demonstration of a low complexity ARM-based indoor VLC transceiver under strong interference'. In *2017 13th International Wireless Communications and Mobile Computing Conference (IWCMC)* (Valencia, Spain, 2017) pp. 622–627.
doi:10.1109/IWCMC.2017.7986357

[Lla20] Á. De la Llana Calvo. *Contribución al Posicionamiento en Interiores Basado en Emisores de Señal Óptica y Detectores PSD*. Ph.D. thesis, Universidad de Alcalá, 2020.

[Loc21] Locatify. 'UWB Indoor Positioning using Locatify', 2021.
https://locatify.com/blog/uwb-ultrawideband-indoor-positioning-for-visually-impaired/

[Lop14] S. Lopes. *In search of reliable centimeter-level indoor positioning: a smartphone-based approach*. Ph.D. thesis, Thesis in Eletrical Engineering, University of Aveiro, 2014.
doi:10.13140/RG.2.2.26076.62089

[Lv17a] H. Lv, L. Feng, A. Yang, P. Guo, H. Huang, S. Chen. 'High accuracy VLC indoor positioning system with differential detection'. *IEEE Photonics Journal*. vol. 9 (3), 2017.
doi:10.1109/JPHOT.2017.2698240

[Lv17b] H. Lv, L. Feng, A. Yang, P. Guo, H. Huang, S. Chen. 'High Accuracy VLC Indoor Positioning System With Differential Detection'. *IEEE Photonics Journal*. 9 (3), pp. 1–13, 2017.
doi:10.1109/JPHOT.2017.2698240

[Mau12] R. Mautz. *Indoor positioning technologies*. Ph.D. thesis, ETH Zurich, Zurich, 2012.
doi:10.3929/ethz-a-007313554

[Mor15] Mornsun. 'AC/DC LD05-20B12'. *Product Specification*, 2015.

[Mur18] S. Murano, M.C. Pérez, J. Ureña, C.J. Bleakley, C. De Marziani. 'Comparison of Zadoff-Chu Encoded Modulation Schemes in an Ultrasonic Local Positioning System'. In *2018 International Conference on Indoor Positioning and Indoor Navigation (IPIN)* (Nantes, France, 2018) pp. 206–212.
doi:10.1109/IPIN.2018.8533702

[Opt21] 'Optitrack motion tracking system', [online] Available: https://www.optitrack.com/, 2021.

[Osl15] Oslon. 'OSLON® 1 PowerStar IR, IGS Version'. *Product Specification*. pp. 1–7, 2015.

[Par15] Á. Parra-Cerrada, V. González-Posadas, J.L. Jiménez-Martín, Á. Blanco-del Campo, W. Hernandez, C. Calderón-Córdova. 'Low-Cost Measurement for a Secondary Mode S Radar Transmitter'. *IEEE Transactions on Instrumentation and Measurement*. vol. 64 (12), pp.

3217–3225, 2015.
doi:10.1109/TIM.2015.2450357

[Par18] J.A. Paredes, F.J. Álvarez, T. Aguilera, J.M. Villadangos. '3D Indoor Positioning of UAVs with Spread Spectrum Ultrasound and Time-of-Flight Cameras'. *Sensors*. vol. 18 (1), 2018.
doi:10.3390/s18010089

[Par21a] J.A. Paredes, F.J. Álvarez, M. Hansard, K.Z. Rajab. 'A Gaussian Process model for UAV localization using millimetre wave radar'. *Expert Systems with Applications*. vol. 185, p. 115563, 2021.
doi:https://doi.org/10.1016/j.eswa.2021.115563

[Par21b] J.A. Paredes Moreno. *Posicionamiento preciso de drones mediante cámara de tiempo de vuelo y radar de onda milimétrica*. Ph.D. thesis, Universidad de Extremadura, 2021.

[Pat15] P.H. Pathak, X. Feng, P. Hu, P. Mohapatra. 'Visible Light Communication, Networking, and Sensing: A Survey, Potential and Challenges'. *IEEE Communications Surveys and Tutorials*. vol. 17 (4), pp. 2047–2077, 2015.
doi:10.1109/COMST.2015.2476474

[Pen11] J. Peng, M. Zhu, K. Zhang. 'New Algorithms Based on Sigma Point Kalman Filter Technique for Multi-sensor Integrated RFID Indoor/Outdoor Positioning'. In *2011 International Conference on Indoor Positioning and Indoor Navigation (IPIN)* (Guimaraes, Portugal, 2011) .

[Per09] M.C. Pérez Rubio. *Generación y Correlación Eficiente de Códigos Binarios Derivados de Conjuntos de Secuencias Complementarias para Sistemas Ultrasónicos*. Ph.D. thesis, Universidad de Alcalá, 2009.

[Per14] A. Perttula, H. Leppäkoski, M. Kirkko-Jaakkola, P. Davidson, J. Collin, J. Takala. 'Distributed Indoor Positioning System With Inertial Measurements and Map Matching'. *IEEE Transactions on Instrumentation and Measurement*. vol. 63 (11), pp. 2682–2695, 2014.
doi:10.1109/TIM.2014.2313951

[Pé19] M.C. Pérez-Rubio, C. Losada-Gutiérrez, F. Espinosa, J. Macias-Guarasa, J. Tiemann, F. Eckermann, C. Wietfeld, M. Katkov, S. Huba, J. Ureña, J.M. Villadangos, D. Gualda, E. Díaz, R. Nieto, E. Santiso, P. del Portillo, M. Martínez. 'A realistic evaluation of indoor robot position tracking systems: The IPIN 2016 competition experience'. *Measurement*. vol. 135, pp. 151–162, 2019.
doi:https://doi.org/10.1016/j.measurement.2018.11.018

[Rab17] J. Rabadan, V. Guerra, R. Rodríguez, J. Rufo, M. Luna-Rivera, R. Perez-Jimenez. 'Hybrid visible light and ultrasound-based sensor for distance estimation'. *Sensors (Switzerland)*. vol. 17 (2), pp. 1–9, 2017.
doi:10.3390/s17020330

[Rae21] W. Raes, T. Dhaene, N. Stevens. 'On The Usage of Gaussian Processes for Visible Light Positioning With Real Radiation Patterns'. In *2021 17th International Symposium on Wireless*

Communication Systems (ISWCS) (2021) pp. 1–6.
doi:10.1109/ISWCS49558.2021.9562197

[Raj14] N. Rajagopal, P. Lazik, A. Rowe. 'Visual light landmarks for mobile devices'. In *IPSN-14 Proceedings of the 13th International Symposium on Information Processing in Sensor Networks* (Berlin, Germany, 2014) pp. 249–260.
doi:10.1109/IPSN.2014.6846757

[Rem21] Remcomsoftware. 'Detailed Indoor Channel Modeling with Diffuse Scattering for 5G Millimeter-Wave Wireless Networks', 2021.
https://www.remcom.com/archived-webinars/2017/4/17/detailed-indoor-channel-modeling-with-di

[Sam21] Samsung. 'Samsung Note 20'. *Product Specification*, 2021.
https://www.samsung.com/es/smartphones/galaxy-note20/

[Sch11] H.G. Schantz, C. Weil, A.H. Unden. 'Characterization of error in a Near-Field Electromagnetic Ranging (NFER) Real-Time Location System (RTLS)'. In *2011 IEEE Radio and Wireless Symposium* (2011) pp. 379–382.
doi:10.1109/RWS.2011.5725491

[Sch15] M. Scherhäufl, M. Pichler, A. Stelzer. 'UHF RFID Localization Based on Evaluation of Backscattered Tag Signals'. *IEEE Transactions on Instrumentation and Measurement*. vol. 64 (11), pp. 2889–2899, 2015.
doi:10.1109/TIM.2015.2440554

[Sch18] G. Schroeer. 'A Real-Time UWB Multi-Channel Indoor Positioning System for Industrial Scenarios'. *IPIN 2018 - 9th International Conference on Indoor Positioning and Indoor Navigation*. pp. 3–7, 2018.
doi:10.1109/IPIN.2018.8533792

[Sem17] N. Semiconductors. 'LPC1769 68 67 66 65 64 63 Product Datasheet'. *Product Specification*. pp. 1–90, 2017.

[Shi15] E. Shinwasusin, C. Charoenlarpnopparut, P. Suksompong, A. Taparugssanagorn. 'Modulation performance for Visible Light Communications'. In *2015 6th International Conference of Information and Communication Technology for Embedded Systems (IC-ICTES)* (Phetchaburi, Thailand, 2015) pp. 1–4.
doi:10.1109/ICTEmSys.2015.7110818

[Son21] B. Soner, S. Coleri. 'Visible Light Communication Based Vehicle Localization for Collision Avoidance and Platooning'. *IEEE Transactions on Vehicular Technology*. vol. 70 (3), pp. 2167–2180, 2021.
doi:10.1109/TVT.2021.3061512

[Ste17] H. Steendam, T.Q. Wang, J. Armstrong. 'Theoretical lower bound for indoor visible light positioning using received signal strength measurements and an aperture-based receiver'. *Journal of Lightwave Technology*. vol. 35 (2), pp. 309–319, 2017.
doi:10.1109/JLT.2016.2645603

[Ste18] H. Steendam. 'A 3-D Positioning Algorithm for AOA-Based VLP with an Aperture-Based Receiver'. *IEEE Journal on Selected Areas in Communications*. vol. 36 (1), pp. 23–33, 2018. doi:10.1109/JSAC.2017.2774478

[Ste19] N. Stevens. 'Bias Introduced by True Radiation Patterns in RSS-based Visible Light Positioning'. In *2019 IEEE SENSORS* (Montreal, Canada, 2019) pp. 1–4. doi:10.1109/SENSORS43011.2019.8956584

[STM13] STMicroelectronics. 'Omnifet VNP10N07FI'. *Product Specification*, 2013.

[STM15] STMicroelectronics. 'STM32F469IDiscovery'. *Product Specification*. pp. 1–40, 2015.

[Tec16] T.E. Technology. '3 LED Module (30 modules/string) OVM12F3x7 series'. *Product Specification*, 2016.

[Tec21] S.H. Technologies. 'Industry 4.0 Smart Manufacturing', 2021. https://www.hopelandrfid.com/industry-4-0-smart-manufacturing_n40

[Tel01] V. Telefunken. 'TSOP7000. IR Receiver for High Data Rate PCM at 455 kHz'. *Product Specification*. (82147), pp. 1–7, 2001. https://www.ret.hu/media/product/14704/437289/tsop7000.pdf

[Tie16] J. Tiemann, F. Eckermann, C. Wietfeld. 'ATLAS - an open-source TDOA-based Ultra-wideband localization system'. In *2016 International Conference on Indoor Positioning and Indoor Navigation (IPIN)* (Alcalá de Henares, Spain, 2016) pp. 1–6. doi:10.1109/IPIN.2016.7743707

[Ure18] J. Ureña, Á. Hernández, J.J. García, J.M. Villadangos, M.C. Pérez, D. Gualda, F.J. Álvarez, T. Aguilera. 'Acoustic Local Positioning with Encoded Emission Beacons'. *Proceedings of the IEEE*. vol. 106 (6), pp. 1042–1062, 2018. doi:10.1109/JPROC.2018.2819938

[Ureew] J. Ureña, Á. Hernández, E. Aparicio-Esteve, J.M. Villandangos, J.J. García, A. Jiménez, M.C. Pérez. 'SISTEMA Y PROCEDIMIENTO DE POSICIONAMIENTO DE ALTA VELOCIDAD CON EMISORES MÓVILES TIPO LEDS Y RECEPTORES ESTÁTICOS TIPO FOTODIODOS EN CUADRANTES', Spain Patent P202131028, 02-11-2021 (Under Review).

[Wan13a] T.Q. Wang, Y.A. Sekercioglu, J. Armstrong. 'Analysis of an Optical Wireless Receiver Using a Hemispherical Lens With Application in MIMO Visible Light Communications'. *Journal of Lightwave Technology*. vol. 31 (11), pp. 1744–1754, 2013. doi:10.1109/JLT.2013.2257685

[Wan13b] T.Q. Wang, Y.A. Sekercioglu, A. Neild, J. Armstrong. 'Position accuracy of Time-of-Arrival based ranging using Visible Light with Application in Indoor Localization Systems'. *Journal of Lightwave Technology*. vol. 31 (20), pp. 3302–3308, 2013. doi:10.1109/JLT.2013.2281592

[Wan14a] S. Wang, K. Liu, Y. Liu, X. Sun. 'Analysis for Low Cost Inertial Sensors Based Pedestrian Dead Reckoning'. *Lecture Notes in Electrical Engineering*. vol. 246, pp. 1029–1037, 2014.
doi:10.1007/978-3-319-00536-2_119

[Wan14b] T.Q. Wang, R.J. Green, J. Armstrong. 'Prism array-based receiver with application in MIMO indoor optical wireless communications'. In *2014 16th International Conference on Transparent Optical Networks (ICTON)* (Graz, Austria, 2014) pp. 1–4.
doi:10.1109/ICTON.2014.6876577

[Wan15a] C. Wang, L. Wang, X. Chi, S. Liu, W. Shi, J. Deng. 'The Research of Indoor Positioning based on Visible Light Communication'. *China Communications*. vol. 12 (8), pp. 85–92, 2015.
doi:10.1109/CC.2015.7224709

[Wan15b] Y.D. Wang, Y. Liu, X.J. Tian, X.H. Yang, W. Ye, C.T. Zheng. 'Development and performances of standalone visible light communication terminals using imitate infrared encoding technique'. *IET Communications*. vol. 9, 2015.
doi:10.1049/iet-com.2014.1148

[Xie18] C. Xie, W. Guan, Y. Wu, L. Fang, Y. Cai. 'The LED-ID Detection and Recognition Method Based on Visible Light Positioning Using Proximity Method'. *IEEE Photonics Journal*. vol. 10 (2), pp. 1–16, 2018.
doi:10.1109/JPHOT.2018.2809731

[Yan14] S.H. Yang, H.S. Kim, Y.H. Son, S.K. Han. 'Three-dimensional Visible light indoor localization using AOA and RSS with multiple optical receivers'. *Journal of Lightwave Technology*. vol. 32 (14), pp. 2480–2485, 2014.
doi:10.1109/JLT.2014.2327623

[Yan18] J.H. Yan, Y.J. Cheng, K.H. Lin, D.H. Chen, C.J. Chen, K.M. Feng. 'Multipath Interference Free Multi-LED Visible Light Communications with Gold Sequence Multiplexing'. In *Optical Fiber Communication Conference* (Optical Society of America, 2018) .
doi:10.1364/OFC.2018.Th2A.63

[Yas16] M. Yasir, S.W. Ho, B.N. Vellambi. 'Indoor position tracking using multiple optical receivers'. *Journal of Lightwave Technology*. vol. 34 (4), pp. 1166–1176, 2016.
doi:10.1109/JLT.2015.2507182

[You05] M. Youssef, A. Agrawala. 'The Horus WLAN Location Determination System'. In *Proceedings of the 3rd International Conference on Mobile Systems, Applications, and Services*MobiSys '05 (Association for Computing Machinery, New York, USA, 2005) p. 205–218.
doi:10.1145/1067170.1067193

[Zac16] G. Zachár, G. Vakulya, G. Simon. 'Long Distance VLC-based Beaconing for Indoor Localization Applications'. In *IPIN 2016 Seventh International Conference on Indoor Positioning and Indoor Navigation IEEE* (Alcalá de Henares, Spain, 2016) pp. 1–4.

[Zha00] Z. Zhang. 'A flexible new technique for camera calibration'. *IEEE Transactions on Pattern Analysis and Machine Intelligence*. vol. 22 (11), pp. 1330–1334, 2000.
doi:10.1109/34.888718

[Zha05] C. Zhang, X. Lin, M. HATORI. 'Novel Sequence Pair and Set with Three Zero Correlation Windows'. *IEICE Transactions on Communications*. vol. E88B, 2005.
doi:10.1093/ietcom/e88-b.4.1517

[Zha17] R. Zhang, W.D. Zhong, K. Qian, D. Wu. 'Image Sensor Based Visible Light Positioning System with Improved Positioning Algorithm'. *IEEE Access*. 5, pp. 6087–6094, 2017.
doi:10.1109/ACCESS.2017.2693299

[Zha19] P. Zhao, C.X. Lu, J. Wang, C. Chen, W. Wang, N. Trigoni, A. Markham. 'mID: Tracking and Identifying People with Millimeter Wave Radar'. In *2019 15th International Conference on Distributed Computing in Sensor Systems (DCOSS)* (Santorini, Greece, 2019) pp. 33–40.
doi:10.1109/DCOSS.2019.00028

[Zhu19] B. Zhu, Z. Zhu, Y. Wang, J. Cheng. 'Optimal Optical Omnidirectional Angle-of-Arrival Estimator With Complementary Photodiodes'. *Journal of Lightwave Technology*. vol. 37 (13), pp. 2932–2945, 2019.
doi:10.1109/JLT.2019.2907969